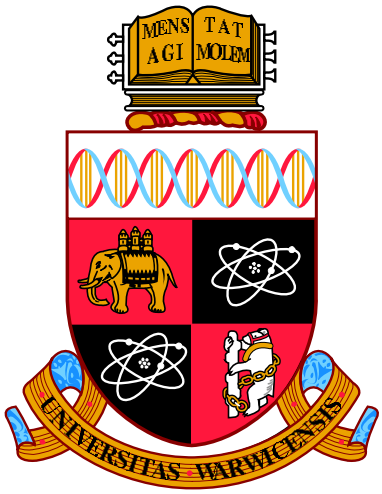

Growth, Characterization, and Functionalization of Wide Band Gap Oxide Alloys

by

Dae-Sung Park

Thesis

Submitted to the University of Warwick

in part fulfilment for the degree of

Doctor of Philosophy

Department of Physics

July 2015

THE UNIVERSITY OF WARWICK

Contents

Acknowledgements

I would first like to thank my supervisor Prof. Chris McConville, for welcoming me into his group at the University of Warwick, for his encouragement, enthusiasm, and regular advice of "You worry too much.". Particular thanks are owed to Dr. Gavin Bell for giving me PhD opportunity in Warwick and kind advice. I should thank to Dr. Sepehr Vasheghani Farahani, Dr. Marc Walker, Dr. Djelloul Seghier (Science institute in Iceland), and Prof. Chel-Jong Choi (Chonbuk National University in Republic of Korea) for their invaluable support, discussions, and friendship for the completion of this PhD project. My PhD study would not have been possible without their support. I am extremely grateful to Rob Johnston for his great technical help and immense technical expertise. Other present and previous members of Surface, Interface, and Thin Film Group include Dr. Nessa Fereshteh Saniee, Dr. James Mudd, Haiyuan Wang, Ebiyibo Collins Ouserigha, Badriya Al Hashmi, Dr. Mukul Misra, Dr. Hyunsik Kim, and Dr. Chris Burrows who are all thanked for their help, assistance, and warm friendship during the lonely PhD journey. I am very grateful to other Warwick research group members: Alexander Marsden, Geanina Apachitei, Prof. Marin Alexe, Dr. Akash Bhatnagar, Mingmin Yang, Hasan Tanvir Imam, and Dr. Reza Jalili Kashtiban for their kind help, advice, discussions, and friendship. Some of them improved my health a lot with playing badminton although I was very tired. Prof. Chang-Ju Youn (Chonbuk National University) and Prof. Woo-Seok Choi (Sungkyunkwan University) are acknowledged for the support of the thin film growth in Korea during my PhD studies.

Lastly, I would especially like to thank my family for the varied and extensive support and encouragement; I will forever be thankful.

Declarations

I declare that this thesis contains an account of my research work carried out at the Department of Physics, University of Warwick between October 2011 and April 2015 under the supervision of Prof. C. F. McConville. The research reported here has not been previously submitted, wholly or in part, at this or any other academic institution for admission to a higher degree.

All of the ZnO and $Be_xZn_{1-x}O$ samples were grown by RF-magnetron sputtering at Chonbuk National University, Republic of Korea. Dr. D. Seghier produced the photoluminescence data for the selected samples. Prof. C.-J. Choi is thanked for the TEM images presented in chapters 5, 6, and 7. Part of DFT calculations on ZnO and $Be_xZn_{1-x}O$ superstructures was performed by H. Wang. All other data and interpretation have been carried by the author.

Dae-Sung Park

July 2015

Several articles based on this research have been published or have been submitted for publication:

D.-S Park, J. J. Mudd, M. Walker, A. Krupski, D. Seghier, N. Fereshteh Saniee, C.-J. Choi, C. J. Youn, S. R. C. McMitchell, and C. F. McConville, *Pinning Effect on the Band Gap Modulation of Crystalline $Be_xZn_{1-x}O$ Alloy Films Grown on $Al_2O_3(0001)$*, CrystEngComm **16**, 2136 (2014).

D.-S Park, A. Krupski, A. M. Sanchez, C.-J. Choi, M.-S. Yi, H.-H. Lee, S. R. C. McMitchell, and C. F. McConville, *Optimal Growth and Thermal Stability of Crystalline $Be_{0.25}Zn_{0.75}O$ Alloy Films on $Al_2O_3(0001)$*, Appl. Phys. Lett. **104**, 141902 (2014).

D.-S Park, S. K. Vasheghani Farahani, M. Walker, J. J. Mudd, H. Wang, A. Krupski, E. B. Thorsteinsson, D. Seghier, C. J. Choi, C. J. Youn, and C. F. McConville, *Recrystallization of Highly-Mismatched $Be_xZn_{1-x}O$ Alloys: Formation of a Degenerate Interface Layer*, ACS Appl. Mater. Interfaces **6**, 18758 (2014).

D.-S Park, H. Wang, S. K. Vasheghani Farahani, M. Walker, A. Bhatnagar, D. Seghier, C.-J. Choi, J. H. Kang, and C. F. McConville, *Self-Assembled Passivation of Semiconducting Oxides*, (under review for publication).

D.-S Park, S. K. Vasheghani Farahani, H. Wang, D. Seghier, and C. F. McConville, *Localization and Transport Properties of Charge Carriers across a Phase Transition on Oxide Alloys*, (in preparation).

The work presented in this thesis has been presented at the following national and international conferences.

Formation of Secondary Phase Nanoparticles and Functionalization of Metastable Oxide Surfaces (poster presentation), ICMAT2015 & IUMRS-ICA2015 (MRS-S), Singapore (June 2015).

Enhancing Electronic Reconstruction at a Complex Oxide Interface (oral presentation), Materials Research Society (MRS), Fall Meeting, Boston, MA, USA (November 2013).

Pinning Effects on the Band Gap Modulation of $Be_xZn_{1-x}O$ Ternary Alloys Grown on Al_2O_3(0001) Substrates (poster presentation), Materials Research Society (MRS), Fall Meeting, Boston, MA, USA (November 2013).

Highly Conducting Interface Layer and Band Gap Renormalization in Highly-Mismatched Oxide Alloy Films induced by thermal recrystallization (oral presentation), International Symposium on the Physics of Semiconductor and Applications (ISPSA), Jeju, Republic of Korea (July 2013).

Control of Quasi Two-Dimensional Electron Gases at Conductive Oxide-Heterointerface (poster presentation), International Symposium on the Physics of Semiconductor and Applications (ISPSA), Jeju, Republic of Korea (July 2013).

Abstract

In recent years, oxide materials have received great interest due to their potentially superior properties, *e.g.*, high optical transparency and electrical conductivity, for next generation optoelectronics. To realize this, wide band gap semiconducting oxides are key components, not only as passive elements, but also as active components in several device architectures. Therefore, controlling the electrical conductivity, optical transparency, and band gap energy of the oxides is essential for the realization of oxide-based electronics. Moreover, the phase transition of oxides, including atomic diffusion and defect distribution can significantly alter their surface, interface, and bulk properties.

In this thesis, band gap modulation and growth features of a ZnO-based alloy, $Be_xZn_{1-x}O$, grown on Al_2O_3 substrates have been systematically studied by Be composition variations in the range of $0 \leq x \leq 0.77$ using a co-sputtering technique. Continuous lattice shrinkage from 5.23 to 4.80 Å and direct band gap shift from 3.24 to over 4.62 eV were achieved as the Be concentration increased. During the band gap modulation, significant particle pinning effects on the grain growth of the alloy films on highly-mismatched substrate were found together with variations in grain size, orientation, and composition. Such grain boundary decorated by Be particles cause structural fluctuations and compositional inhomogeneity in the alloy films. A correlation between the grain growth driving pressure and the particle pinning pressure was formulated by modelling the Be-induced particle pinning to elucidate the observed phase segregation. Furthermore, a comprehensive understanding of the thermodynamic characteristics of the $Be_xZn_{1-x}O$ thin films determines the optimized growth condition, *e.g.*, growth temperature of 400 °C, and sheds light on the effective band gap engineering with compositional homogeneity.

The thermodynamic characteristics of the phase transformation of metastable $Be_xZn_{1-x}O$ alloys have been extensively investigated. The induced phase transition initiates the formation of a highly conductive layer at the interface and secondary phase nanoparticles at the surface. The origin of the highly degenerate interface layers, which were identified by experimental data acquisition and mathematical modellings, has been addressed through a cation counter-diffusion mechanism with respect to the strain relaxation, atomic redistribution, and charge accumulation in the transformed alloy system. The highest interface conductivity, 1.4×10^3 S·cm^{-1}, is comparable to the highest conductivities recorded for highly-doped ZnO. The concurrence of transient diffusion and segregation of Be is responsible for the evolution of energetically favourable secondary phase nanoparticles as a result of solid-state reactions at the surface. The growth kinetics of the nanoparticles, the associated particle size-distribution, defect-mediated atomic compensations, and their environmentally-robust functionalities (thermal and chemical resistance) are taken into account based on the experimental observations and model calculations. This novel phase transformation has been highlighted as an effective passivation and functionalization of reactive oxide surfaces by the self-assembly of inert nanoparticles. Such spontaneous passivation allows the use of semiconducting oxides in a variety of electronic applications, while maintaining their inherent and intrinsic properties. This oxide phase transformation can provide new insights for the design of environmentally-robust oxide optoelectronics in many transparent device integrations.

Abbreviations and common symbols

2DEG	Two-dimensional electron gas
AFM	Atomic force microscopy
ARXPS	Angle-resolved X-ray photoemission spectroscopy
A^0X	Neutral acceptor-bound exciton
BGN	Band gap renormalization
BM	Burstein-Moss
BXE	Bound exciton emission
BZO	$Be_xZn_{1-x}O$
CB	Conduction band
CBM	Conduction band minimum
CNL	Charge neutrality level
CNT	Classical nucleation theory
CVD	Chemical vapour deposition
DAP	Donor-acceptor pair
DOS	Density-of-states
D^0X	Neutral donor-bound exciton
DBE	Deep band emission
DC	Direct current
DFT	Density functional theory
EDX	Energy dispersive X-ray spectroscopy
FB	Flat-band
FCC	Face-centered cubic
FET	Field-effect transistor
FFT	Fast-Fourier transform
FQHE	Fractional quantum Hall effect
FTIR	Fourier-transform infrared
FWHM	Full width at half maximum

FXE	Free-exciton emission
HEMT	High electron mobility transistor
H_i	Hydrogen interstitial
HRXRD	High resolution X-ray diffraction
IMFP	Inelastic mean free path
IR	Infrared
LAO	$LaAlO_3$
LD	Laser diode
LDA	Local density approximation
LED	Light emitting diode
LO	Longitudinal optical
LPP	Longitudinal optical phonon-plasmon
LSW	Lifshitz, Slyozov, and Wagner
MBE	Molecular beam epitaxy
MEB	Multi-emission band
ML	Monolayer
MOCVD	Metal-organic chemical vapour deposition
MTFA	Modified Thomas-Fermi approximation
MQW	Multi-quantum well
NBE	Near-band-edge
NIR	Near infrared
NP	Nanoparticle
OR	Ostwald ripening
PL	Photoluminescence
PLD	Pulsed laser deposition
PSD	Particle size distribution
PVD	Physical vapour deposition
QCE	Quantum confinement effect
QW	Quantum well
RF	Radio frequency

RMS	Root mean square
RS	Reactive sputtering
RSM	Reciprocal space map
RT	Room temperature
SEM	Scanning electron microscopy
SE	Secondary electron
SP	Surface plasmon
STEM	Scanning transmission electron microscopy
STO	$SrTiO_3$
sccm	Standard cubic centimetres per minute
TEM	Transmission electron microscopy
TES	Two-electron satellite
TO	Transverse optical
TOA	Take-off angle
UHV	Ultra-high vacuum
UPS	Ultraviolet photoemission spectroscopy
UV	Ultraviolet
ViGS	Virtual gap state
VB	Valence band
VC	Vacancy cluster
VBM	Valence band maximum
V_O	Oxygen vacancy
WZ	Wurtzite
XPS	X-ray photoemission spectroscopy
XRD	X-ray diffraction
Zn_i	Zinc interstitial

α	Absorption coefficient
a	In-plane lattice constant
a^*	Bohr radius
$\boldsymbol{B}$	Magnetic field

c	Out-of-plane lattice constant
Δ_{so}	Spin-orbit splitting
ΔG	Free energy change
D_{s}	Diffusion coefficient
d	Thickness
d_{hkl}	Lattice spacing
d_{n}	Detachment frequency of monomers
d_{s}	Sublimated thickness
$\boldsymbol{E}$	Electric field
E	Energy
E_{B}	Binding energy
E_{ES}	*Ehrlich-Schwoebel* barrier energy
E_{F}	Fermi level
E_f	Final state energy
E_{g}	Band gap energy
E_i	Initial state energy
E_{k}	Kinetic energy
$\bar{E}_{\mathrm{mid}}$	Averaged mid-gap energy
E_P	Energy parameter of the momentum matrix element
E_{p}	Plasmon energy
E_{sF}	Surface Fermi level
e	Electronic charge
eV	Electron volts (1.602×10^{-19} J)
ϵ	Strain
ϵ_0	Permittivity of vacuum
$\epsilon(0)$	Static dielectric constant
$\epsilon(\infty)$	High frequency dielectric constant
F	Lorentz force
f_{FD}	Fermi-Dirac distribution function
f_{n}	Attachment frequency of monomers

f_{S}	Lattice mismatch
G	Gibbs free energy
$\boldsymbol{G}$	Reciprocal lattice vector
$g(E)$	Density of states
Γ	Centre of the Brillouin zone
γ	Surface tension/interfacial energy
γ_{LO}	Longitudinal optical phonon damping
γ_{TO}	Transverse optical phonon damping
$\hat{\mathcal{H}}$	Hamiltonian
$\hbar$	$h/2\pi$
$h\nu$	Photon energy
I_{diff}	Diffusion distance
J	Nucleation rate
J_{G}	Growth rate of nanoparticles
j	Total angular momentum quantum number
k_{B}	Boltzmann constant
$\boldsymbol{k}$	Wavevector of electron
$\boldsymbol{k}_{\mathrm{F}}$	Angular wave number
$\boldsymbol{k}_{\mathrm{TF}}$	Thomas-Fermi screening angular wave number
L	De-Broglie wavelength of particles/Fermi length of Fermions
L_{T}	Terrace width
m_0	Free electron mass
m^*	Effective mass
m_0^*	Band edge effective mass
m_{av}^*	Averaged density-of-state electron effective mass
m_{d}	Dipole moment
N_{A}	Density of bulk ionized acceptor
N_{D}	Density of bulk ionized donor
n	Electron concentration
n_{r}	Nucleation rate

n_{B}	Bulk electron concentration
n_{H}	Hall electron concentration
n_{Int}	Interface electron concentration
n_{Mott}	Mott-transition carrier concentration
n'	Refractive index
n_{s}	Surface sheet density
ω_{p}	Plasma frequency
ω_{LO}	Longitudinal optical phonon frequency
ω_{TO}	Transverse optical phonon frequency
Φ	Work function
$\boldsymbol{P}_{\mathrm{s}}$	Spontaneous polarization
$\boldsymbol{p}$	Momentum operator
p	Hole concentration
q	Charge
$\boldsymbol{q}$	Imaginary component of wavevector
ρ	Density
$\boldsymbol{R}$, $\boldsymbol{r}$	Position vectors
R	Reflectance
R_{relax}	Relaxation factor
R_{S}	Sheet resistance
r^*	Critical radius of particles
$\tilde{r}$	Reflectivity
S	Supersaturation ratio
S_{e}	Entropy
T	Temperature
T_{A}	Annealing temperature
T_{g}	Growth temperature
T_{O}	Optical transmittance
τ_{a}	Residence time of adatoms
τ	Plasmon lifetime

u	Internal structural parameter
u_{P}	Poission′s ratio
V	Potential
V_H	Hall voltage
V_{d}	Band bending potential
v	Velocity of electron
ν	Frequency
μ	Mobility
$\boldsymbol{Z}$	Charge state
z	Atomic number

Chapter 1

Introduction

1.1 Overview

Oxide materials have attracted a great deal of attention due to their spectacular physiochemical properties in a versatile range of potential optoelectronic applications, *e.g.*, lighting applications (light emitting diodes, laser diodes, and optical sensors), high electron mobility transistors, photocatalytic applications, gas sensors, spintronics, and invisible electronics in many transparent materials and devices. These have provided a number of potential opportunities for the realization of highly-efficient device performance for next generation optoelectronic devices beyond the inherent limitations of group IV and III-V materials such as Si, GaAs and even GaN [1–4].

Recent progress in oxide-based optoelectronics has triggered the improvement in controlling oxide thin film growth, synthesis, and allowing the fabrication of various heterostructures, effective control of ionic polarities, intentional/unintentional doping, and band gap engineering of these materials [4–8]. The surface and interface properties of oxides give rise to a number of interesting physical and chemical phenomena, such as band bending, Fermi-level pinning, surface reconstruction, and highly accumulated/depleted charge carriers at oxide heterointerfaces [9–12]. These are primarily associated with the distribution of a number of neutral or charged point defects/impurities in distorted lattices, the removal of surface atoms, charge redistribution (charge screening), and structural defects such as various dislocations or planar defects/grain boundaries.

In principle, oxide materials can be generally categorized as highly mismatched compounds due to the large difference in the size and electronegativity between the cation (less electronegative atom) and oxygen (high electronegative atom) [13]. Such mismatch readily causes energetically favourable lattice defects

such as cation/anion vacancies and the creation of localized energy states within the band gap of oxide materials [8]. These strongly influence the electrical and optical properties of the oxides. The formation of preferential defects such as oxygen vacancies is predominantly dependent on the position of the Fermi level with respect to the charge neutrality level (the Fermi stabilization energy) [14]. In many semiconductors, hydrogen counteracts the majority carriers as either an interstitial donor (H^+) or an acceptor (H^-) [15, 16]. For example, interstitial H (H_i) and substituted hydrogen (H_O) act as a source of electrons in wide band gap oxides [17–20]. The formation of native defects such as cation interstitials and oxygen vacancies energetically lies on the character of the oxides or growth conditions, *e.g.*, cation- or anion-rich growth conditions) with respect to the position of the Fermi level. Therefore, a comprehensive understanding of the formation and balance of intrinsic/extrinsic defects in oxide materials as defect engineering is of particular importance to gain control over the properties of oxide materials to be functionalized in several oxide applications.

Oxide-based heterostructures are made possible by advances in heteroepitaxy and the growth of well-ordered atomic precision of oxide layers. These types of structures have shown a variety of functionalities due to their exotic interfacial properties together with their versatile electronic phases (metallic, insulating, semiconducting, superconducting phases, ferroelectrics, ferromagnets, *etc*) [6, 7, 21–23]. These artificial materials offer the possibility of discovering new physical phenomena and novel device concepts. For instance, two-dimensional properties have been observed at heterointerfaces confined between two band insulating complex oxides, polar pseudocubic $LaAlO_3$(LAO) and non-polar $SrTiO_3$(STO). Such polarity-mismatched interfaces manifest not only metallicity and a high mobility two-dimensional electron gases, 2DEGs, but also localized magnetism and superconductivity. These diverse set of coexisting physical properties occur at the heterointerface and are localized in a characteristically small length scale, 0.4 – 1 nm. Hence, the epitaxial growth control of thin films (atomic ordering) on the atomic scale with respect to underlying layers, is of prime importance to achieve atomically abrupt interfaces to study

artificially designed oxide heterostructures.

This reveals that an appropriate selection of similar materials is essential in conjunction with similar lattice sizes and other chemical properties, *e.g.*, thermal expansion coefficient, for the incorporation of these materials into the epitaxial heterostructures. However, in many cases, mismatched heterostructures, *e.g.*, GaN and ZnO films on Al_2O_3 or Si substrates, are inevitably employed for low-cost commercial applications [24, 25]. Such lattice mismatches between the film and substrate crucially affect growth dynamics and the resulting microstructural properties of the oxide [26, 27]. Substantial elastic strain arising from the high lattice mismatch readily leads to the formation of three-dimensional columnar structures, lattice point defects, and structural defects such as threading dislocations and planar defects to minimize the free energy during the growth process. Structural defects are normally formed at the interface to serve as a sink of point defects and extend throughout the upper film, which can produce defect states in the band gap.

For the case of n-type GaN, edge dislocation cores, which are usually negatively-charged, induce charge compensation and scattering effects acting as acceptor-like trap states, resulting in the decrease in free electron concentration and transport efficiency [28]. Moreover, most grain boundaries in ZnO-based films act as free-electron trapping centres (double-Schottky barriers), strongly degrading the carrier transport properties along the potential barriers and the electrochemical stability [29]. Therefore, the type and geometry of structural defects similar to point defects significantly influence the electric and optical properties of highly-mismatched oxide films. In addition, during the alloy synthesis process, strain from the high lattice mismatch hinders the solubility of a solute into the host oxide and the homogeneity of alloy composition. This results in the displacement/localization of solute atoms, corresponding compositional fluctuation, and phase separation in highly-mismatched alloys, predominantly due to a composition pulling effect to lower strain at the interface. In this work, the above strain effects and the resulting phase separation phenomena have been observed in highly-mismatched $Be_xZn_{1-x}O$ alloys grown on Al_2O_3 which will be discussed in Chapters 4 and 5.

Another significant aspect of oxide materials is the possibility of band gap engineering in a multitude of applications which requires for specific band gap energies and/or designing efficient quantum structures with appropriate alignment of the conduction and valence bands of the two different materials in the a heterojunctions. Such induced quantum effects such as quantum confinement effects and integer/fractional quantum Hall effects can be applied for the enhancement of optoelectronic performance, for example, in light emitting diodes (LEDs), laser diodes (LDs), solar cells, and heterojunction bipolar transistors [3, 30–32]. In principle, the tunability of the band gap of oxides can be achieved by; (*i*) the incorporation of other oxide species into the host as a varied chemical composition, (*ii*) strain-induced transition in their crystal structures and variations in the density-of-states, effective strain engineering, and (*iii*) size-dependent energy confinement on a nanoscale [33–36]. By compositional substitution in the host, the band gap energy, conduction/valence band orbitals, and chemical stability can be modulated to satisfy the criteria with respect to a phase miscibility gap. The conduction and valence bands for different chemical group compound materials are based on the ionization potential and electron affinity of the constituent elements.

For the case of a typical binary oxide semiconductor (non-transition metal oxides), the conduction band minimum (CBM) states are made of the spherically extended *s*-orbitals of the metal cations and their overlaps with neighboring metal *s*-orbitals, while anions (*p*-orbitals of O^{2-}) contribute more strongly to the valence band maximum (VBM) states [37]. The incorporation of different cations (anions) into the host oxide can greatly influence the conduction (valence) band and, hence, tailoring of the band gap of oxides is possible and composition-dependent. An increase (decrease) in the band gap energy of the host material is obtained by incorporating solute content of a larger (smaller) band gap material. For example, in a ternary alloy regime, the band gap energy of an $A_xB_{1-x}O$, $E_g(A_xB_{1-x}O)$, can be monotonically tailored to the band gap of the binary compound AO, E_g (AO), from that of the host BO,E_g (BO) as A composition, x, increases. A linear variation in the lattice constants of the $A_xB_{1-x}O$ alloys is typically a function of the A solute content

according to the Vegard law [38]. However, the band gap energy of the alloys varies non-linearly and, thus, a quadratic variation is typically used to include a bowing parameter, b, as follows

$$E_{\mathrm{g}}(\mathrm{A}_x\mathrm{B}_{1-x}\mathrm{O}) = xE_{\mathrm{g}}(\mathrm{AO}) + (1-x)E_{\mathrm{g}}(\mathrm{BO}) - bx(1-x) \tag{1.1}$$

Such non-linear (bowing) effects on the band gap variation occur mainly by structural and electronic factors: (*i*) the volume deformation as a result of the varied lattice constant which alters the electronic band structure based on Bloch theorem, (*ii*) the internal structural relaxation of the cation-anion bond lengths and bond angles caused by the different size of ions, and (*iii*) the electronegativity difference (changed lattice enthalpies/madelung energies in ionic solids) between the constituent elements which varies the electron distribution [39, 40]. Note that no band gap variation, *i.e.*, no band gap shift of a host material, occurs by impurity doping into the crystal structure of the material as impurities predominantly create local electronic energy states within the host band gap that trap/donate electrons. In optical experiments, such local impurity levels cause emission/absorption of photons at lower energies compared to the optically induced band-to-band transition in the host material [8, 41, 42]. In this thesis, doping effects of Be on the band gap tunability of ZnO-based alloys, $\mathrm{Be}_x\mathrm{Zn}_{1-x}\mathrm{O}$, are extensively investigated in conjunction with the corresponding variations in their physical, chemical, electronic and thermodynamic properties.

1.2 General properties of ZnO-based materials

Since the discovery of semiconducting zinc oxide (ZnO) by Fritsch in 1935 [43], the material has received great attention over past few decades because of a variety of promising properties; including a wide direct band gap ($\mathrm{E_g}$ = 3.37 eV), high transparency in near UV spectral range, and a large free exciton binding energy ($\approx$ 60 meV) [43, 44]. Beyond the success of III-nitrides (*e.g.* GaN) in optoelectronics, ZnO has also been expected to provide opportunities for the fabrication of highly efficient optoelectronic devices, especially light emitting diodes, transparent field effect transistors, and UV sensors. Moreover, intrinsic n-type electrical

properties of ZnO-based materials can be used as integrated materials in many transparent electronic applications [2, 45]. ZnO is also available in large-size bulk single crystals which can serve as substrates after the recent advances of crystal growth techniques [8]. These advantages have opened a window for the fabrication of homostructured ZnO devices and hence ZnO has been regarded as a complement or alternative to GaN in some optoelectronic applications.

Among the possible crystal phases (wurtzite structure, metastable zinc-blende and rocksalt structures), ZnO commonly crystallizes in the wurtzite crystal structure similar GaN, which is the most thermodynamically stable phase under ambient condition due to strong bond polarity (electrostatic interactions) between the Zn cation and O anion atoms. In the wurtzite structure (a hexagonal close packed Bravais lattice, $P6_3mc$ space group), each Zn cation is surrounded by four O anions, and vice versa in a tetrahedral coordination as shown in Fig. 1.1a. In the electronic band structure of covalent (ionic) ZnO binding, the valence band states are composed of the bonding hybridized sp^3: Zn $4s$ + O $2p$ orbitals or O $2p^3$ orbitals (mainly by $2p$ states of O^{2-}) and the conduction band is formed of the empty antibonding sp^3 orbitals: Zn $4s$ + Zn $4p$ (mainly by Zn $4s$ states of Zn^{2+}) [37]. The equilibrium in-plane and out-of-plane lattice parameters for wurtzite ZnO are $a = 3.2495$ Å and $c = 5.2069$ Å, respectively. The tetragonal ionic radii of Zn^{2+} and O^{2-} are 0.60 Å and 1.38 Å, respectively. Wurtzite ZnO has non-centrosymmetric crystal structure dominated by four low Miller surfaces: the nonpolar $(10\bar{1}0)$ and $(11\bar{2}0)$ surfaces, and the polar Zn-terminated (0001)-Zn and O-terminated $(000\bar{1})$-O surfaces (Fig. 1.1c) [46, 47]. These two polar surfaces are the terminating planes of a stacking sequence of hexagonal Zn and O layers along the crystallographic c-axis [0001] with alternating distances, $R_1 = 0.61$ Å and $R_2 = 1.99$ Å, which is the so-called "*Tasker-type III*": the unit cell is made of alternating layers of positive and negative ions. The two polar surfaces are energetically unstable. In an ionic model of ZnO with the charges $+Ze$ and $-Ze$ to the Zn and O ions, a dipole moment of $m_{\mathrm{d}} = NZe(1-2u)c/2$, where e is electronic charge, $u = 0.375$ is the internal structural parameter, and c is the out-of-plane lattice parameter of the wurtzite

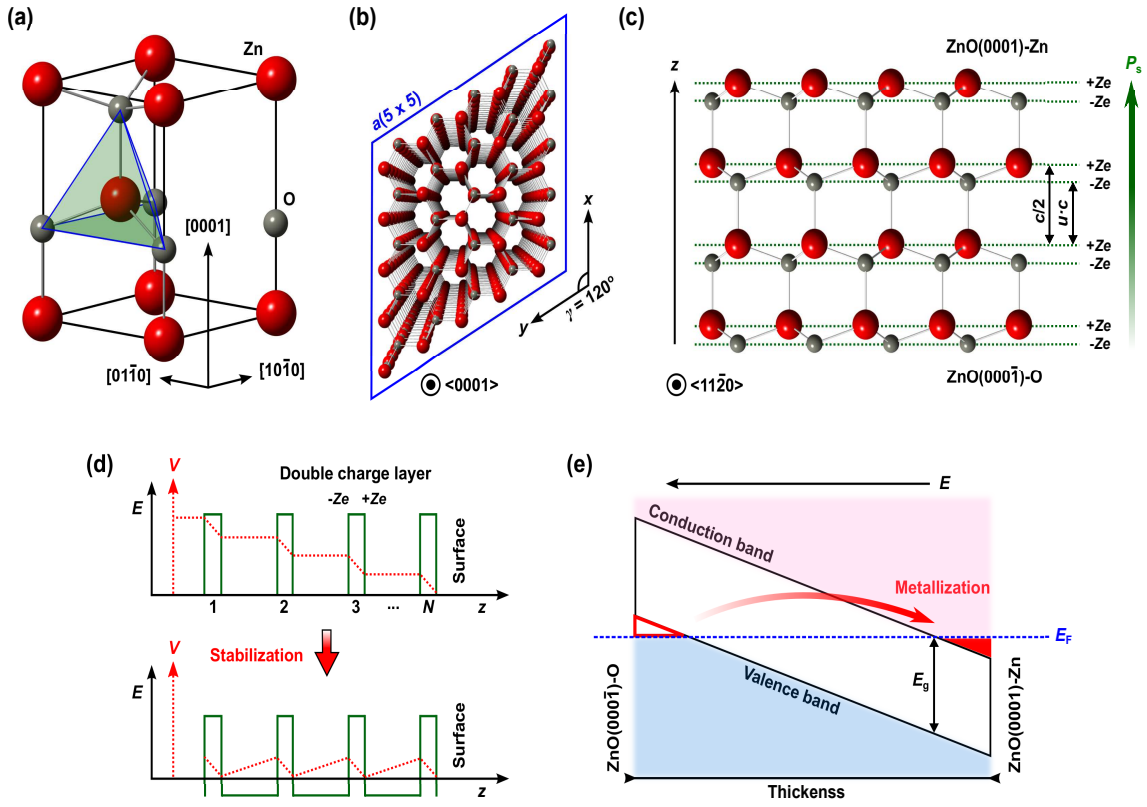

Figure 1.1: (a) Wurtzite ZnO unit cell including the tetrahedral coordination between Zn (red) atoms and the neighboring O (grey) atoms. (b) Representation of a 5×5 supercell structure for ZnO(0001)-Zn polar surface with lattice constant, a. Wurtzite symmetry elements, Zn and O, are shown with lattice parameters $a = b \neq c$ and the angle of the lattice vectors ($\alpha = \beta = 90°$ and $\gamma = 120°$). (c) Schematic side view of the Zn-terminated (0001) and O-termianted ($000\bar{1}$) polar surfaces of wurtzite ZnO along the z-axial direction and the $<11\bar{2}0>$ zone axis. ZnO has a non-centrosymmetric crystal structure that is composed of alternate layers of positive and negative ions by a stacking sequence along the z-axis with different distances, causing a spontaneous polarization, $\boldsymbol{P}_s$. A net dipole moment across N double layers occurs within the slab. (d) Spatial variations of the induced electrostatic field, $\boldsymbol{E}$, and potential, V, in the slabs generated along the polar direction before (upper graph) and after (lower graph) surface relaxation. (e) Schematic illustration of the tilted band structure by the induced internal electric field and the subsequent fractional charge transfer from the O- to Zn-terminated surface of the slab. This corresponds to the reduction of the ionicity of the Zn and O ions at each surface layer and the metallic polar surfaces depending on the band gap, E_g and the slab thickness, d.

lattice, occurs across the slab of N double layers. The corresponding spontaneous polarization is $\boldsymbol{P}_{\rm s} = Ze(1-2u)$ and the electric field inside the slab is $\boldsymbol{E}$ = -4$\pi\boldsymbol{P}_{\rm s}$. This gives rise to a diverging electrostatic potential within the slab thickness. Thus, a shift of the electronic levels (a tilt of the band structure) relative to the Fermi level arises, *i.e.*, the uppermost valence band energy state close to the O-terminated surface becomes higher than the lowest conduction band state at the Zn-terminated surface. Consequently, a fractional charge transfer of half an electron occurs from the valence band at the O-terminated side to the conduction band at the Zn-terminated side, corresponding to a reduction of $Zn^{+3/2}$ and $O^{3/2-}$ [46,48]. This is referred to as "*the metallization of polar surfaces*". However, such a surface stabilization phenomena by the formation of a metallic surface state has not yet been observed/verified experimentally as an infinite potential difference between both surfaces is unrealistic just as an oversimplistic ionic model. The energy cost is also quite high. In most practical cases, the stabilization processes of the polar surfaces to compensate their ionic excess charges usually occur through: (*i*) a modification of surface layer composition as a surface reconstruction, *e.g.*, removal of 1/4 Zn atoms at the Zn-terminated surface, or (*ii*) adsorption of impurities such as water molecule, *e.g.*, 1/4-monolayer O^{2-} or 1/2-monolayer OH-group at the surface [46, 48, 49]. In this work, similar stabilization behaviors have been observed at the polar surface of the ZnO and $Be_xZn_{1-x}O$ alloy films. X-ray photoemission spectroscopy results have been carefully considered to take into account atomic removal, chemical adsorption, and the associated atomic composition of the stabilized polar surfaces.

ZnO normally shows n-type characteristics due to the presence of intrinsic/extrinsic defects such as Zn interstitials (Zn_i), O vacancies (V_O), n-type H_i although the origin and interpretation of shallow donor defects are a long-standing controversy [8]. The n-type conductivity of undoped ZnO is strongly dependent on the degree of unintentional doping from experimental conditions, *e.g.*, growth conditions or post treatments. Therefore, controlling the intrinsic conductivity of semiconducting or degenerate ZnO has remained a major issue in many optoelectronic devices. A fundamental understanding of the role of native defects in ZnO is there-

fore deemed essential. For example, V_O defects have long been considered the most probable donor source in ZnO. However, recent theoretical and experimental studies using density functional theory (DFT) calculations and electron paramagnetic resonance measurements, found that oxygen vacancies cannot contribute electrons to the conduction band due to their energy position deep in the band gap [50]. D. C. Look suggested that Zn_i create shallow defect levels around 31 – 37 meV below the conduction band edge possibly acting as a shallow donor in ZnO [51,52]. Others (C.G. Van de Walle and D. M. Hofmann) also predicted that the most relevant shallow donor is hydrogen introducing a defects level $\approx$ 35 meV below the conduction band edge [17,53]. H_i are usually unintentionally present in the ZnO lattice during growth processes and most likely form as OH bonds along side O atoms. In many theoretical studies, the formation energy of donor-like defects in *n*-type ZnO is lower compared to that of acceptor-like defects. As a simple example, in the Zn-rich (O-rich) condition, the formation of V_O (V_{Zn}) becomes dominant. The formation of *n*-type defects in ZnO is correlated with the position of the charge neutrality level (CNL), *i.e.*, the energy at which defect states change from donor-type to acceptor-type with reference to the Fermi level. This causes the persisting difficulty to *p*-type doped ZnO due to the self-compensation effect by residual donor-like defects. This has led to critical obstacles in achieving highly efficient and reproducible ZnO-based optoelectronics [54–56].

Band gap engineering and designing quantum structures in ZnO are of profound importance. An effective quantum confinement effect can be achieved by the formation of quantum wells by subsequent stacking of energy barriers and well layers. The band gap energy change is dependent on the size and chemical property of the substituted cations whose *s*-orbitals predominantly shift the conduction band states [57]. Hence, the band gap energy of ZnO can be larger (smaller) by alloying with MgO and BeO (CdO) as shown in Fig. 1.2a. To obtain wider band-gap energies in ZnO-based materials, A. Ohtomo *et al.* first proposed that the band gap energy (E_g) of $Mg_xZn_{1-x}O$ could be tuned from 3.3 (ZnO) to 7.8 eV (MgO) by substitution of Mg into Zn lattice sites in the wurtzite structure [33]. The alloying process,

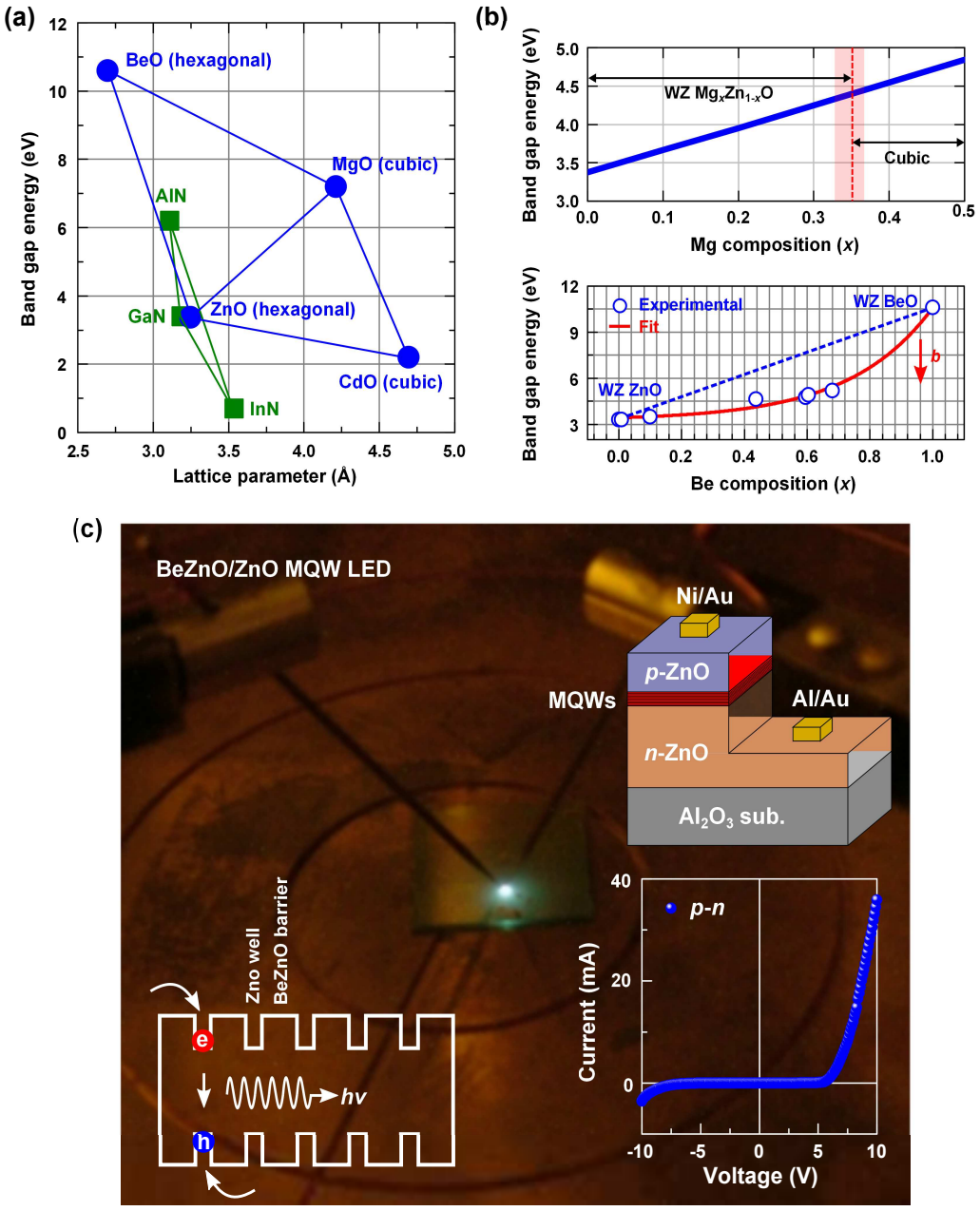

Figure 1.2: (a) Band gap energies, lattice parameters, and crystal structures of selected II-VI compounds (CdO, MgO, and BeO) for the band gap engineering of ZnO compared to that of GaN. (b) Phase separation in $Mg_xZn_{1-x}O$ at the Mg mole fraction of around $x = 0.36$, shown in the upper graph. The lower panel shows variations in the band gap energy of wurtzite ZnO up to that of WZ BeO as a function of Be concentration. The non-linear band gap energy change of $Be_xZn_{1-x}O$ as a function of Be composition is due to the bowing effect with the bowing constant, b. (c) A photograph image of light emission generated from a ZnO-based LED with a turn-on voltage of ≈6 V (the rectifying current-voltage curve in the bottom-right inset) and injection current of 100 mA. The corresponding device structure schematically shown in the inset is designed by n-type ZnO (Ga-doped ZnO)/active layer (multi-quantum wells, MQWs, by a stacking sequence of $Be_{0.2}Zn_{0.8}O$ and ZnO layers as energy barriers and well layers for carrier confinement)/p-type ZnO (As-doped ZnO). Different multi-layered metals of Al/Au (Ni/Au) are applied to achieve Ohmic contacts on the n-type (p-type) ZnO layer. The bottom-left inset illustrates a light ($h\nu$) emission mechanism generated by the recombination of confined electrons, e, and holes, h, inside the BeZnO/ZnO MQWs. The charge carriers in the MQWs are supplied by the n- and p-type ZnO layers in an applied electric field.

however, was limited to $x \leq 0.36$ due to a phase transition from the hexagonal structure of ZnO to the rocksalt structure of MgO at higher concentrations (see the upper panel in Figure 1.2b).

Ryu *et al*. suggested that the E_g could be fully modulated by alloying with BeO ($E_g = 10.6$ eV) without a structural phase transition owing to the fact that the two materials have the same hexagonal symmetry (see the lower panel in Fig. 1.2b) [58]. Subsequently, a $Be_xZn_{1-x}O$-based multi-quantum-well structure was designed by periodically stacking ZnO wells with $Be_{0.2}Zn_{0.8}O$ barriers, resulting in UV light emission generated from a conventional LED structure (Fig. 1.2c) [58]. After this demonstration, Klingshirn *et al*. highlighted possible compositional fluctuations and local segregation of Be to the ZnO interfaces in the quantum well device structures [59]. While there are relatively few growth studies, in previous studies, growth of $Be_xZn_{1-x}O$ ternary thin films using various growth methods resulted in poor quality crystals due to the tetrahedral ionic radius of Be^{2+} (0.27 Å) being much smaller than that of Zn^{2+} (0.60 Å) [60–63]. This size difference possibly leads to a change in the crystal space group from hexagonal ($P6_3mc$) to other crystal symmetries, *e.g*. orthorhombic ($Pmn2_1$ or $Pna2_1$) or zinc-blende (F43m) [64]. Additionally, a miscibility gap in the $Be_xZn_{1-x}O$ alloy system can lead to thermodynamic instabilities such as compositional fluctuations or phase segregation [65]. Finally, considerable strain arises from the lattice mismatch between the epilayer film and the substrate. The interface normally favours a three-dimensional (3D) growth mode, resulting in columnar growth, mixed orientations, and a relatively rough surface morphology [66, 67]. Although some studies predicted such phase instabilities on $Be_xZn_{1-x}O$ alloys, only limited studies have been reported to date. Hence, a deeper understanding of the fundamental nature on $Be_xZn_{1-x}O$ alloy system is required in many physical points of view for their potential applications.

1.3 Organization of the thesis

In this thesis, $Be_xZn_{1-x}O$ alloys are investigated from the point of view of the band gap engineering, phase stability, defect formation, and functional phase

transformations. Following this introduction, Chapter 2 reviews the general background of the nucleation theory, epitaxial growth, and growth mechanisms of thin films. An overview of the theoretical approximations to the formation of electronic bands, their defect- or dopant-induced variations, and space-charge-associated accumulation layers and the resulting band bending are also introduced. Chapter 3 outlines the experimental techniques (growth and characterization methods) used in this work and the computational methods for theoretical simulations. Chapters 4 and 5 present the band gap engineering and growth kinetics of $Be_xZn_{1-x}O$ thin films in conjunction with the potential impact on the thermodynamic phase transformations. In Chapter 6, thermally induced phase transformation and the resulting formation of a charge accumulation layer in metastable $Be_xZn_{1-x}O$ alloy films are extensively explored. Hereafter, all of the transformed $Be_xZn_{1-x}O$ alloys are referred to as BZO in this thesis. Chapter 7 details the growth kinetics and particle size distribution of secondary phase oxide nanoparticles formed in phase-transformed BZO films along with the functionalization of reactive oxide surfaces. Chapter 8 summarizes the contributions of this work with a view to future studies.

Chapter 2

Theoretical Background

2.1 Crystal growth

2.1.1 Introduction

This thesis is concerned with the growth of oxide thin films and their physical properties such as structural, optical, electrical, electronic, etc. Understanding of the growth kinetics and formation of the oxide thin films in terms of thermodynamics and phase transformations is profoundly important to control the surface morphology, crystallinity, defect distribution, and the variations in their physical properties. Therefore, this chapter attempts to provide details and theoretical background of the nucleation-and-growth, and the epitaxial growth mechanisms of thin films, with particular focus on strain engineering in dissimilar materials.

2.1.2 Thermodynamics and the nucleation theory

A fundamental understanding of the thermodynamics of materials is essential for the study of phase transformations in many material systems. This typically gives us a phase diagram of the system which is associated to the thermodynamic stability in various states, *e.g.*, temperature versus pressure coordinates [68–70]. The approaches also provide insights for the depiction of physiochemical reactions and kinetics especially in solid-state materials. In 1876, J. W. Gibbs postulated that the growth of a new phase from an existing phase is initiated by the formation and subsequent spontaneous growth of the smallest stable new-phase cluster [68,71]. The formation of the smallest stable clusters (or critical nuclei) is a result of the so-called nucleation. The phase transformation from an initial state in thermodynamic equilibrium occurs by a change in the variables such as pressure and temperature, resulting in the lowest total energy configuration of the final state in a given sys-

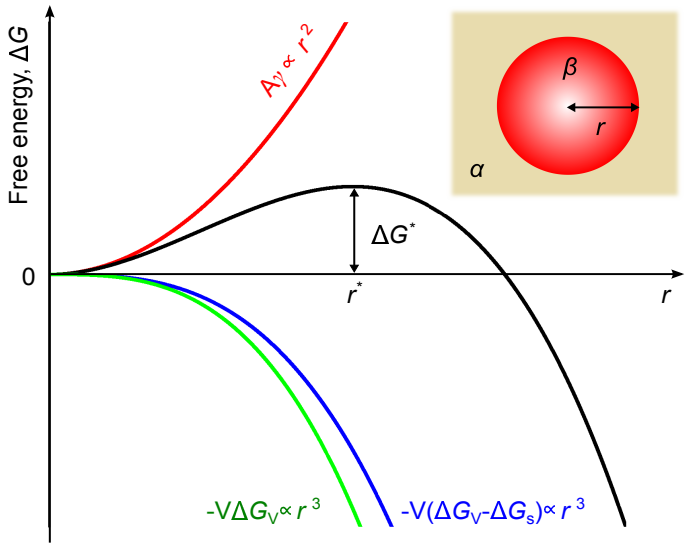

Figure 2.1: The variation of ΔG as a function of nuclei size, r, for a homogeneous nucleus. ΔG^* and r^* are the activation barrier and critical size for the nucleus, respectively. $A\gamma$ is the interface energy, $V\Delta G_{\mathrm{V}}$ is the volume free energy, and $V\Delta G_{\mathrm{s}}$ is the misfit strain energy.

tem [72, 73]. Additionally, other phase configurations in the so-called *metastable equilibrium* states occur by a local minimization in the total free energy of the system. As mentioned above, any transformation results in a decrease in the Gibbs free energy, G, following the necessary criterion; $\Delta G_{\alpha\beta} = G_\alpha - G_\beta < 0$, where G_α and G_β are the free energies of the initial and final states, respectively. In general, a change in G of a given system is described by variations in temperature T, pressure P, and molar quantities of the solutes, n_i, as

$$dG = -(\partial G/\partial T, S_{\mathrm{e}})_{P,n_i} dT + (\partial G/\partial P, V)_{T,n_i} dP + \Sigma(\partial G/\partial n_i)_{T,P,n(i\neq j)} dn_i, \quad (2.1)$$

where S_{e} is the entropy of the system and V is the volume. A negative entropy implies that G decreases with increasing T at a rate given by S_{e}, whereas G increases with P. If T and P are constant, Eq. 2.1. can be rearranged as

$$dG = \Sigma(\partial G/\partial n_i)_{T,P,n(i\neq j)}, \quad (2.2)$$

where the constant of proportionality, $(\partial G/\partial n_i)_{T,P,n(i\neq j)}$ is the partial molar quantity, namely, the partial molar free energy of i, dn_i, added to a large amount of the phase at a constant T and P. This is known as chemical potential, μ_i.

In the classical nucleation theory, the formation of a secondary phase typically results from nucleation or spinodal decomposition [68]. The difference (decrease) in the free energy between two distinct phases, *e.g.*, the condensation of vapour to form liquid and solidification of vapour or liquid to a solid crystal, provides the driving force for such phase transformations. In the solid state, the majority of phase transformations occur by thermally activated atomic movements regarded as atomic diffusion. During the initial stage of the nucleation processes, a small amount of the new phase is formed, which is called the embryo [74]. Embryos or smaller clusters are unstable with increasing G until they reach a critical particle size (so-called nuclei) due to their their high surface-to-volume ratio [75, 76]. Beyond the critical size, where the energy stabilizes, the size of the particles becomes bigger through further growth. This is driven by atomic diffusion in which atoms migrate across the interface between the newly-formed and initial microstructures and form into a more stable new phase. Therefore, the characteristics of the nucleation and subsequent growth are dependent on the reaction kinetics including: (*i*) reaction time; (*ii*) temperature; (*iii*) stress between new and initial phases; (*iv*) composition; atomic volume; and shape of the new phase; (*v*) orientation relations, and (*vi*) energetic stabilization.

There are two representative types of nucleation, namely, homogeneous and heterogeneous. Homogeneous nucleation is the spontaneous formation of critical nuclei from isolated atoms (monomers) of the initial phase, while heterogeneous nucleation is the occurrence of the new phase nuclei on other solutes (impurities) at pre-existing surfaces to minimize the free energy in a given system. The homogeneous nucleation takes place in the interior of a uniform phase within a solid by a spherical nucleus of a radius, r, to simplify the theoretical derivation. The interface at the boundaries of initial (α) and new (β) phases is formed when the β phase is nucleated. The change in the total free energy ($\Delta G_{\alpha\beta}$) associated with the nucleation process can be determined by [68]

$$\Delta G_{\alpha\beta} = -\frac{4\pi r^3}{3}(\Delta G_{\mathrm{V}} - \Delta G_{\mathrm{s}}) + 4\pi r^2 \gamma_{\alpha\beta}, \tag{2.3}$$

where ΔG_{V} is the change in the Gibbs energy per volume during the transition from

α to β, $\gamma_{\alpha\beta}$ is the isotropic interfacial energy, and $\Delta G_{\rm s}$ is the misfit strain energy per unit volume of β. The associated strain energy, $\Delta G_{\rm s}$, is proportional to the volume of both coherent and incoherent β phase inclusions, which do not fit perfectly in the space originally occupied by the matrix. The strain energy can also be estimated according to the relation: $\Delta G_{\rm s} = 6\eta_\alpha X f^2$ [$X{\equiv}3\epsilon_\beta/(3\epsilon_\beta{+}4\eta_\alpha)$], where ϵ_β and η_α are the bulk modulus of the β phase and shear modulus of α phase, respectively [77]. f is the misfit strain originated from the difference in the lattice constants of the α and β phases. The change in the free energy is shown as a function of r in Fig. 2.1. The minimization of ΔG with respect to r yields the critical size of the nuclei (equilibrium size of $r = r^*$). From the condition, $d\Delta G_{\alpha\beta}/dr = 0$, the critical size, r^*, and the activation energy of formation, $\Delta G_{\alpha\beta}$, of such nuclei for the phase transition can be determined by

$$r^* = 2\gamma/(\Delta G_{\rm V} - \Delta G_{\rm s}), \tag{2.4}$$

$$\Delta G_{\alpha\beta} = 16\pi\gamma^3/3(\Delta G_{\rm V} - \Delta G_{\rm s})^2. \tag{2.5}$$

According to this energy configuration, the critical size of the nuclei is defined by the counterbalance of the decrease in $\Delta G_{\alpha\beta}$ due to the formation of the secondary phase β, and the increase in $\Delta G_{\alpha\beta}$ due to the increase in the boundary surface and misfit strain between α and β phases. Note that the effect of the misfit strain energy is related to the effective driving force for the transformation to $(\Delta G_{\rm V} - \Delta G_{\rm s})$.

In most solid-state transformations, nucleation occurs heterogeneously and the preferential nucleation sites are non-equilibrium defects such as atomic vacancies (especially at high temperature), grain boundaries, dislocations, stacking faults, inclusions, free surfaces, *etc* (Fig. 2.2a). These lattice and planar defects increase the free energy of a material considering the variation in their enthalpies and entropies [68, 78]. Hence, the creation of heterogeneous nuclei annihilates the non-equilibrium defects, lowering the activation energy barriers and facilitating the nucleation processes. The change of the free energy, $\Delta G_{\alpha\beta}$, associated with the heterogeneous nucleation is given by

$$\Delta G_{\alpha\beta}({\rm Het}) = -V(\Delta G_{\rm V} - \Delta G_{\rm s}) + A\gamma_{\alpha\beta} - \Delta G_{\rm d}, \tag{2.6}$$

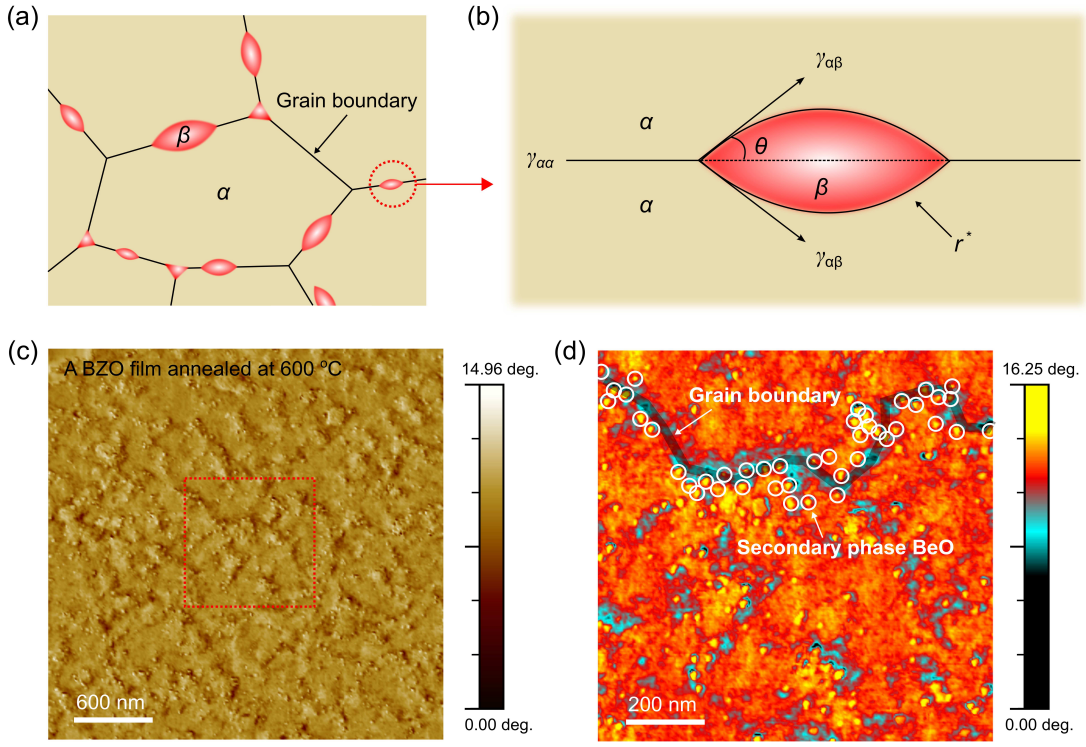

Figure 2.2: (a) A Schematic of the heterogeneous nucleation of β precipitates out of the matrix, α. (b) The critical nucleus size, r^*, for heterogeneous grain boundary nucleation. During the nucleation process to minimize the surface free energy (see Eqs. 2.6 and 2.7), the α/α grain boundary is destroyed with a relation of $\gamma_{\alpha\alpha} = 2\gamma_{\alpha\beta}\cos\theta$. Here, $\gamma_{\alpha\alpha}$, $\gamma_{\alpha\beta}$, and θ are the α/α grain boundary energy, the α/β interfacial energy, and a wetting angle of the two spherical caps. (c) and (d) AFM tapping phase images of a BZO film annealed at 600 °C. The red-dot square area in (c) corresponds to (d). Most heterogeneous nucleation-and-growth of the secondary phase BeO nanoparticles (white circles) occurs along the grain boundaries (black-shadow lines).

where A is the area of the β/α interface and ΔG_{d} is the released free energy by the removal of defects, which are favourable sites for the nucleation. Here, we examine a heterogeneous nucleation at the grain boundaries in a solid. Apart from the effect of any misfit strain energy, the optimum embryo shape should be formed by the minimization of the total interfacial free energy. Assuming $\gamma_{\alpha\beta}$ to be isotropic and equal for both grains, the shape of an incoherent grain boundary nucleus is two spherical caps with a wetting angle θ as shown in Fig. 2.2b. The excess of the free energy associated with the embryo is therefore given by

$$\Delta G_{\alpha\beta}(\mathrm{Het}) = -V(\Delta G_{\mathrm{V}} - \Delta G_{\mathrm{s}}) + A_{\alpha\beta}\gamma_{\alpha\beta} - A_{\alpha\alpha}\gamma_{\alpha\alpha}, \tag{2.7}$$

where V is the volume of the embryo, $A_{\alpha\beta}$ is the area of the α/β interface with the

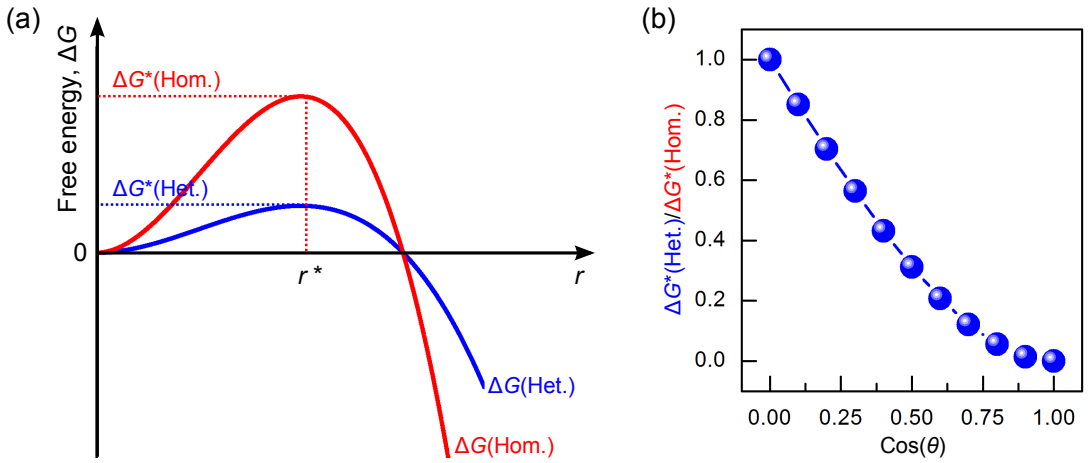

Figure 2.3: (a) A comparison in the excess free energy of nucleus, which is required for homogeneous, ΔG(Hom), and heterogeneous, ΔG(Het), nucleation. The activation energy barrier for the heterogeneous nucleation, ΔG^*(Het), is smaller than that for the homogeneous nucleation, ΔG^*(Hom), but the critical nucleus radius, r^*, is independent. (b) The wetting angle dependent activation energy for heterogeneous nucleation relative to homogeneous nucleation.

interfacial energy $\gamma_{\alpha\beta}$, and $A_{\alpha\alpha}$ is the area of the α/α grain boundary of energy $\gamma_{\alpha\beta}$, which is annihilated by the grain boundary nucleation processes. The activation energy barrier for the heterogeneous nucleation can be given by $\Delta G^*(\text{Het}) = \Delta G^*(\text{Hom})$ $S(\theta)$, where S is a shape factor. Note that the critical radius of the spherical capes, $r^* = (2\gamma_{\alpha\beta}/\Delta G_{\text{V}})$, is independent on the α/α grain boundary. It is because the equilibrium across the curved α/β interface is unaffected by the α/α grain boundary. Furthermore, the model breaks down as the wetting angle becomes zero, $\theta = 0°$. According to the wetting-angle-(cosθ)-dependent free energy of the heterogeneous grain boundary nucleation compared to homogeneous type, $\Delta G^*(\text{Het})/\Delta G^*(\text{Hom})$, grain boundaries (or grain edges and corners) are, therefore, active heterogeneous nucleation sites for incoherent precipitates with lower $\gamma_{\alpha\beta}$ and lower activation barrier energy [see Figs. 2.2c,d and 2.3]. These heterogeneous nucleation phenomena and the subsequent growth of secondary phase particles along the grain boundaries are observed experimentally and discussed in Chapters 6 and 7.

The nucleation of particles is influenced mainly by: the total number, n_0, of arriving atoms at nucleation sites per volume of the system; thermally activated adatoms; and the excess free energy associated with the formation of the nucleus

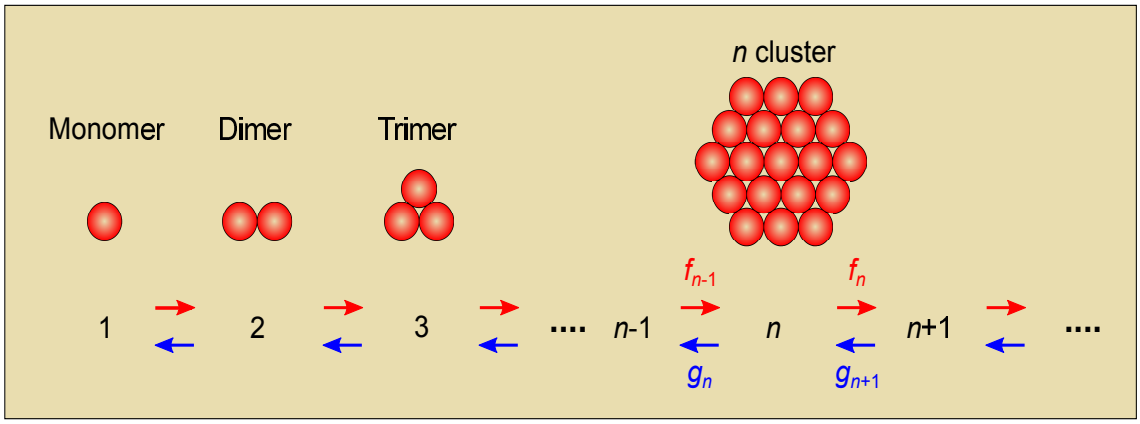

Figure 2.4: Diffusion of monomers to form dimer, trimer, and eventually critical sized clusters composed by n atoms. Here, f_n and g_n are the attachment (red-arrow) frequency and detachment (blue-arrow) frequency of the monomers.

onto immobile clusters [68,74,79]. The formation of the nuclei or clusters is a result of encountering thermally-diffused other atoms and attachments and detachments of atoms. In Volmer and Weber's theory, the nucleation rate, n_r, under supersaturation condition was estimated to be [68,80];

$$n_r = f_c n_0 \exp(-\Delta G_c / k_B T), \tag{2.8}$$

where f_c and G_c are the attachment frequency of monomers to the critical-size nuclei and the formation energy of the critical-size nucleus. This relationship can be only valid for $r < r^*$ as clusters bigger than the critical nucleus size form stable nuclei. Moreover, n_r decreases exponentially with ΔG_c, and thus the probability of bigger nuclei forming decreases. As a result, $n_0 \exp(-\Delta G_c / k_B T)$ represents the equilibrium number of the nuclei with a critical size, r^*. During the nucleation processes based on further developed models of the classical nucleation theory (by Farkas, Becker, Döring, Zeldovich, and Frenkel), the formation of the nuclei or clusters is modelled by monomer fluctuations as shown in Fig. 2.4

During the nucleation processes, clusters of n atoms are formed by the growth and shrinkage of clusters, namely, the growth of clusters of n-1 atoms and the shrinkage of clusters of n+1 atoms. The clusters of n atoms disappear by both growth and decay into the clusters of n+1 atoms and clusters of n-1 atoms, respectively.

Hence, the time-dependent density, $N_n(t)$, of clusters of n atoms is given by

$$\frac{dN_n(t)}{dt} = D_n(t) - D_{n+1}(t), \tag{2.9}$$

where D_n (t) is the net flux of clusters described as

$$D_n(t) = f_{n-1}N_{n-1}(t) - f_nN_n(t) + g_{n+1}N_{n+1}(t) - g_nN_n(t), n = 2, 3, ..., \tag{2.10}$$

where f_n (g_n) is the attachment (detachment) frequency or rate of monomers to (from) the clusters composed of n atoms. In Eq. 2.10, evaporation (or re-evaporation for the case of depositions), direct impingement of arriving atoms onto clusters, or coalescence of clusters are neglected. When the attachment and detachment frequencies are the same, a steady-state density of the clusters occurs as D_n (t) = D_{n+1} (t). Here, it should be noted that while Volmer-Weber theory considers the density of critical-size nucleus under the equilibrium state (the formation of the critical-size clusters by monomer fluctuations), the Becker-Döring theory also takes into account the nucleus density during the steady-state nucleation reactions (considering the detachment of monomers from the critical-size cluster and the resulting formation of subcritical-size clusters) [81]. Consequently, the nucleation rate is expressed by adding a kinetic prefactor, X, to Eq. 2.8,

$$n_r = f_{\mathrm{c}}n_0X\exp(-\Delta G_{\mathrm{c}}/k_{\mathrm{B}}T), \tag{2.11}$$

where $X = (-\frac{1}{2\pi k_{\mathrm{B}}T}\frac{\partial^2 \mathrm{G}}{\partial n^2})^{0.5}$ is the Zeldovich factor [82]. The Zeldovich factor accounts for the fact that the critical-size cluster has an equal probability of either growth or shrinkage with respect to the multiple crossing and re-crossing of the free energy barrier. This is because the flatter free energy region near the energy barrier has more diffusive nucleation dynamics and lower nucleation rate. The Bocker-Döring theory is corrected by Kampmann and Wagner taking into account the incubation time, which is approximated from the supersaturating parent phase to the formation of new-phase clusters of the critical size [83].

In this solid-state classical nucleation theory (CNT), the thermodynamic driving force for spontaneous phase transition is the exothermicity of lattice formation [84]. The diffused/segregated monomers, therefore, can predominantly react with other monomers/clusters to form a more thermodynamically stable phase.

This results in the effective formation of the nuclei at energetically favourable sites such as defective surface and grain boundaries to minimize their free energies.

Kinetics of the particle nucleation reaction can be described by the steady-state rate of nucleation in the Arrhenius form of $J \approx \exp(\text{-}E_\text{a}/k_\text{B}T)\cdot\exp(\text{-}\Delta G(r)/k_\text{B}T)$. The first exponential term reflects the kinetic barriers with activation energy (E_a) for the atomic rearrangements and disolvation [84,85]. The kinetic factor is typically varied by temperature to influence the nucleation kinetics. The second term is the thermodynamic energy barrier or the total free energy change, $\Delta G(r)$. Thus, the critical free energy, ΔG_c, and radius of the nucleus, r^*, can be defined as

$$\Delta G_\text{c} = \frac{16}{3}\frac{\pi\gamma^3}{\Delta G_\text{V}^2}, \tag{2.12a}$$

$$r^* = -2\gamma\Delta G_\text{V} = \frac{2\gamma v_\text{m}}{k_\text{B}Tln(S)}, \tag{2.12b}$$

where v_m is the molar volume of the bulk crystal. The CNT explains that the kinetics of particle nucleation originate from the induced supersaturation of solutes at the surface and the ensuing energetically stable chemical reactions. The subsequent growth stage of the particles can be approximated by various growth dynamics of the particles [86–89]. The critical radius, r^*, represents the minimum size of stable nuclei with a critical free energy that can endure and grow further: values below r^* resulting in the dissociation of the particles. Due to an inverse proportionality between supersaturation, S, and r^* in Eqs. 2.12a and b, the particle radius increases with decreasing S as temperature increases. This leads to a shift in the critical particle radius toward larger particles, and a decrease of the particle growth rate. Such nucleation-and-growth has been addressed by several mechanisms such as burst nucleation by diffusion growth and simultaneous nucleation, *i.e.* nucleation occurs rapidly by the injection of solutes (monomers) and continue until the temperature and solute concentration drop below a critical energy barrier, the growth/dissolution, and coarsening (Ostwald ripening: OR) mechanisms, the aggregation and/or oriented attachment of smaller particles [90, 91]. In the classical description of OR derived from Lifshitz, Slyozov, and Wagner (LSW) theory for the particle growth under low supersaturation and quasi-steady-state limit, the driving

force of OR is a decrease in the solubility of particles with increasing their radius, r, described by the Gibbs-Thomson relation: [92, 93]

$$C_{\mathrm{r}} = C_{\mathrm{B}}^{0}\exp[\frac{2\gamma v_{\mathrm{m}}}{\Re T r}] \approx C_{\mathrm{B}}^{0}[1 + \frac{2\gamma v_{\mathrm{m}}}{\Re T r}], \tag{2.13}$$

where C_{r}, C_{B}^{0}, and $\Re$ are the solubility of the particle, the corresponding solid bulk, and the universal gas constant, respectively. The coefficient, is the so-called capillary length, $2\gamma v_{\mathrm{m}}/\Re T$, which is a measure of the size effect on the chemical potential of a particle (curvature-induced solubility) [94]. This equation indicates that OR processes are driven by the size discrepancy of the particles as the growth of larger particles is at the expense of smaller dissolving particles due to the high solubility and surface energy of the smaller particles. In the LaMer mechanism [92, 95], the nucleation-and-growth of particles follows two dominant mechanisms: (i) the transport of arriving monomers from the bulk onto the crystal surface, "*diffusion-controlled growth*", and (ii) the curvature-induced surface reaction of the particles, "*reaction-controlled growth*"based on OR. In the former, all monomers participate in the nucleation processes and thus the mean NP size is dependent on S (Eq. 2.15), while the latter mechanism is particle size-dependent. The size-dependent growth rate of the spherical particle with the radius, r, is generally given by

$$\frac{d\tilde{r}}{d\tau_{\mathrm{g}}} = \frac{S - \exp(1/\tilde{r})}{\tilde{r} + K\exp(\alpha/\tilde{r})}, \tag{2.14}$$

where

$$\tilde{r} = \frac{\Re T}{2\gamma v_{\mathrm{m}}} r, \tag{2.15a}$$

$$\tau_{\mathrm{g}} = \frac{\Re^{2} T^{2} D_{r} C_{\mathrm{B}}^{0}}{4\gamma^{2} v_{\mathrm{m}}} t, \tag{2.15b}$$

$$K = \frac{\Re T}{2\gamma v_{\mathrm{m}}} \frac{D_{r}}{k}. \tag{2.15c}$$

Here, α is the transfer coefficient for the precipitation/dissolvation reaction ($0 < \alpha < 1$); $\tilde{r}$ and τ are the dimensionless particle radius and time, respectively; K is the so-called Damköhler number and a dimensionless kinetic-limiting factor which indicates whether diffusion rate (D_r) or reaction rate (k) dominates the growth reaction.

Therefore, two distinct growth modes, diffusion-controlled growth and surface reaction-controlled growth, can be determined primarily by the S and K factors in conjunction with the particle size distribution (PSD). Monomer diffusion is the rate-liming step with $S \gg 1$ and/or $K \ll 1$ as the monomers transported from the bulk of the film rapidly bind onto the surface of the particles. The smaller particles grow much faster than the larger ones, leading to the narrowing of the size distribution. On the other hand, when $S \ll 1$ and/or $K \gg 1$, curvature-induced surface reaction of the particles is dominant as the smaller particles are thermodynamically less stable according to Gibbs-Thomson effect and in turn they are shrinking and eventually disappear. This usually results in a broad size distribution (broadening) of the paricles.

Such nucleation-and-growth of particles and distinct particle size distribution depending on growth kinetic parameters has been observed during the phase transition of metastable $Be_xZn_{1-x}O$ alloys. The associated growth mechanism of the secondary phase particles are discussed in Chapter 7.

2.1.3 Thin film growth

Thin films applicable for the fabrication of electronic devices are required to be atomically smooth and flat at their surfaces and interfaces. The formation of such films along with the underlying solid-state substrate strongly relies on the growth kinetics and subsequent crystallization considering the thermodynamic equilibrium, atomic diffusion, nucleation, epitaxial relation between an upper film and underlying layer, and so on [70]. Therefore, an atomistic approach to the growth kinetics is required to associate variables such as substrate temperature, deposition rate, and critical film thickness. In the thermodynamic aspects, heterogeneous nucleation of a solid on a bare surface of planar substrate is considered. The structural formation begins with forming atoms (adsorbates) in the vapour phase, creating aggregates composed of dense clusters which can either grow in size or dissociate as shown in Fig. 2.5.

During vapour-phase processes, two independent processes, which are nucle-

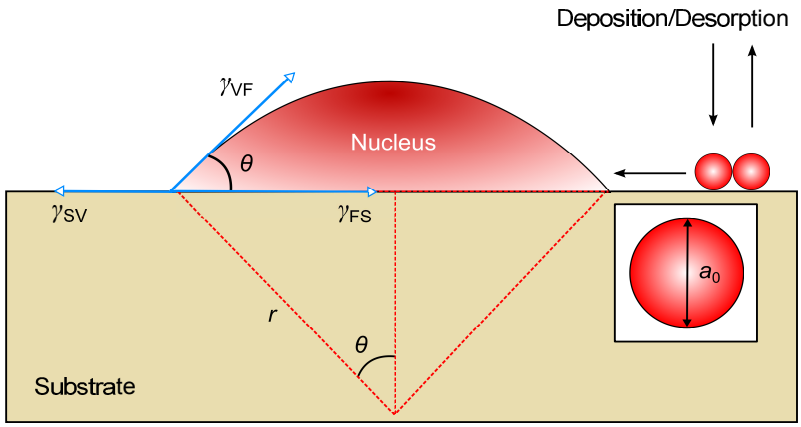

Figure 2.5: A schematic of nucleation of spherical cap on a planar substrate via basic atomistic processes. During the vapour deposition, adatoms of a dimension, a_0, are poised to attach to the circumferential belt. The cap-shaped nucleus of mean dimension, r, on the surface of the substrate is formed with a wetting angle, θ, by the balance of the interfacial tensions, γ, including the free energies of vapour/film (VF), film/surface (FS), and surface/vapour (SV) interfaces.

ation and growth of clusters, play a major role and occur at non-equilibrium states. The change in the free energy of the nucleus with an average size, r, is given by

$$\Delta G = \mathrm{a}_1 r^3 \Delta G_\mathrm{V} + r^2(\mathrm{a}_2\gamma_\mathrm{VF} + \mathrm{a}_3\gamma_\mathrm{FS} - \mathrm{a}_3\gamma_\mathrm{SV}), \tag{2.16}$$

where ΔG_V is the volume free energy change for the formation of a nucleus, which drives the condensation reaction when it is a negative value. $\mathrm{a}_1 r^3$, $\mathrm{a}_2 r^2$, and $\mathrm{a}_3 r^2$ are the volume of the nucleus (spherical cap), the curved area of nucleus exposed to vapour, and contact area between the nucleus and substrate, respectively. The interfacial tensions, γ, are identified by subscripts, VF, FS, and SV, which represent the free energies of vapour-film, film-surface, and surface-vapour interfaces, respectively. The first two energies are positive as they originate from the interfaces during the nucleation process. However, the last one is due to the annihilation of the vapour (liquid)/substrate interface under the nucleus, leading to a negative energy contribution. The corresponding geometric constants are $\mathrm{a}_1 = \pi(2–3\cos\theta + \cos^3\theta)/3$, $\mathrm{a}_2 = 2\pi(1–\cos\theta)$, and $\mathrm{a}_3 = \pi\sin^2\theta$, respectively.

For a given volume of the nucleus, the mechanical equilibrium (the minimization of total free energy) of the interfacial tensions can be described by Young′s equation which states that the tensions, γ_VF, γ_FS, and γ_SV are balanced along the

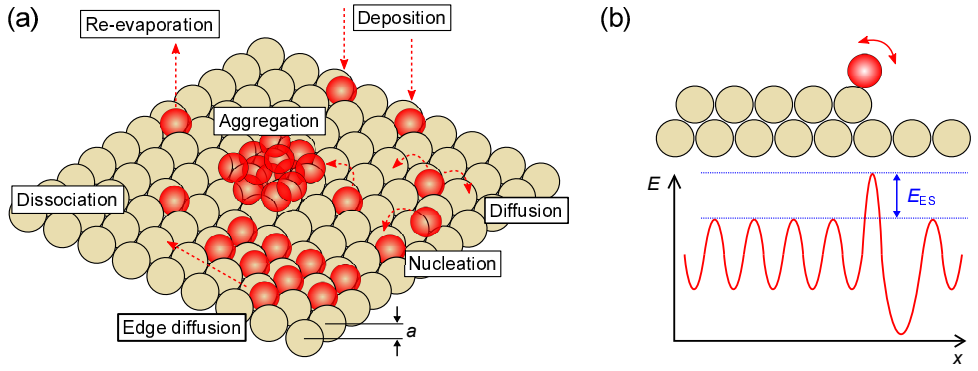

Figure 2.6: Schematic illustrations of (a) atomic movements on a surface of atomically defined substrates during growth processes and (b) the Ehrlich-Schowoebel energy barrier (E_{ES}) that atom on the surface has to bridge into a low-coordinated site at a step edge as an interlayer jump in addition to the diffuse barrier (E_{diff}) on the terrace in order to cross the edge of stage and descend to the lower terrace [96].

plane of the substrate:

$$\cos\theta = (\gamma_{SV} - \gamma_{FS})/\gamma_{VF}. \tag{2.17}$$

Hence, the contact/wetting angle (θ) is dependent on the surface properties of the materials involved, and distinguishes three representative film growth modes by different balancing of the interfacial energies. The three different growth modes are schematically depicted in Fig. 2.7. For island growth, $0 < \cos\theta < 1$ [the so-called Volmer-Weber growth mode], the relationship between the interfacial energies is given by $\gamma_{SV} \leq \gamma_{VF} + \gamma_{FS}$. In this case, the non-wetting films occur along the underlying layer/substrate as the strain energy per unit area of film over growth, γ_{FS}, increases, resulting in the formation of three-dimensional (3D) islands (see Fig. 2.7a).

For the layer-by-layer growth mode [Frank-van der Merwe growth model; Fig. 2.7(b)], the strain energy, γ_{FS}, is lower than the surface energy of the vapour/film interface, γ_{VF} ($\cos\theta \approx 1$): $\gamma_{SV} \geq \gamma_{VF} + \gamma_{FS}$. This condition is the case for ideal homoepitaxy, indicating the wetted film along the substrate with strong atomic bonding. In heteroexpitaxial growth, the Stranski-Krastanov growth mode (Fig. 2. 7c), is the most commonly observed, in which the growth mode changes from the layer-by-layer growth to island growth. This transition is associated with the distribution of strain energy by lattice mismatch, which gives rise to an increase in the elastic

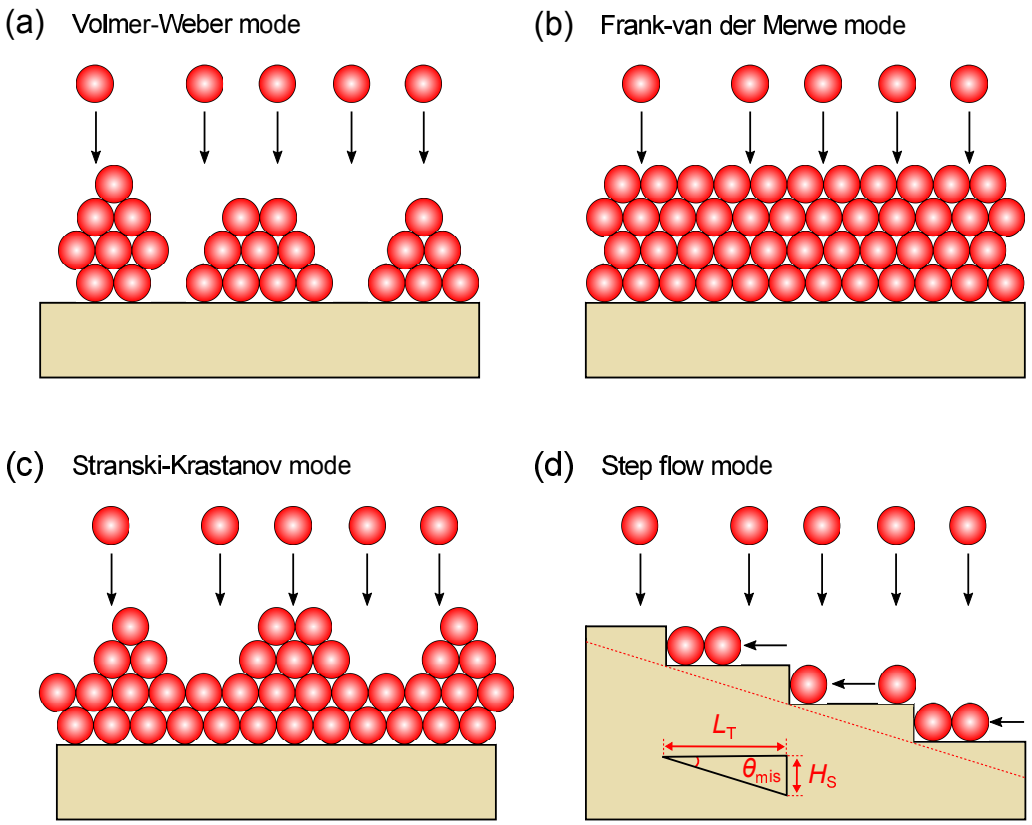

Figure 2.7: Film growth modes: (a) island (3D growth); (b) layer-by-layer (2D growth); (c) mode transition from 2D to 3D growth; and (d) step flow growth. In the inset of (d), L_T, H_S, θ_{mis} are terrace width, step height, and miscut angle of a vicinal substrate, respectively.

energy with increasing the layer thickness. The biaxial strain energy, either compressive or tensile, being lower (higher) than the interfacial energy, γ_{VF}, yields the characteristics of layer growth (island growth) for an initial stage (later stage) of the film grown on a mismatched substrate or a underlying layer. Furthermore, this strain-induced energy configuration gives rise to the formation of misfit dislocations near the film/substrate interfaces to release and/or minimize the strain energy as the film thickness is beyond the critical thickness. Hence, the strain-associated misfit dislocations are the so-called equilibrium defects. The transition between growth modes and the resulting formation of islands (or columnar structures) along highly-mismatched substrates have been discussed throughout this thesis.

Lastly, in epitaxial thin films, growth along a vicinal substrate, which contains the train of atomic-height steps relying on a miscut angle (θ_{mis}), is step-flow growth

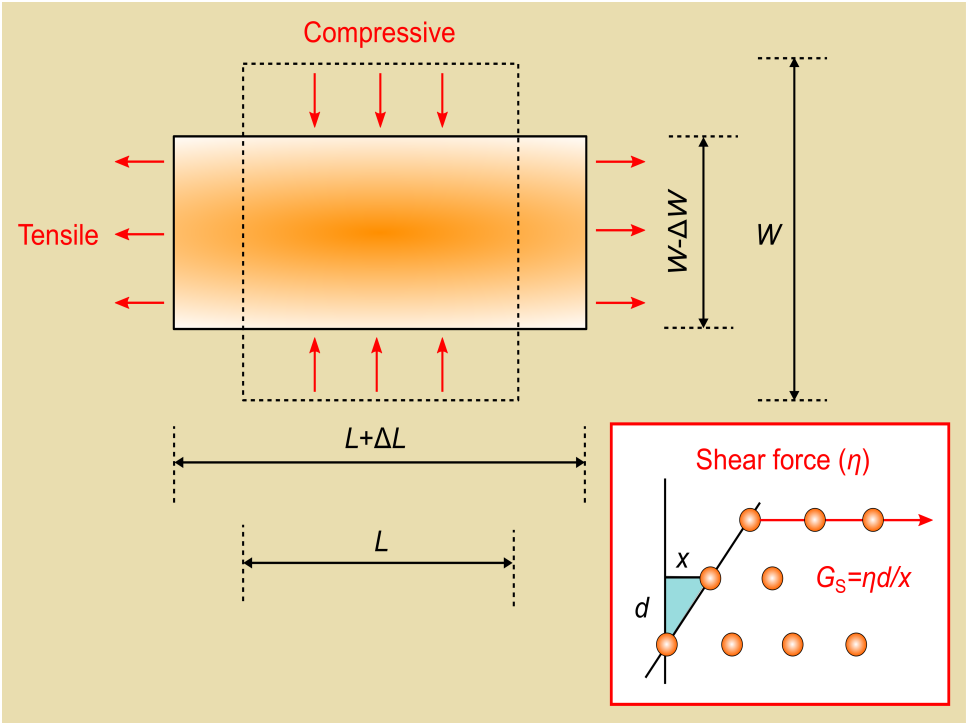

Figure 2.8: Poisson effect between transverse and longitudinal axial strains with the conserved volume of a bulk crystal. Poisson's ratio [$u_{\mathrm{P}} = (\Delta W/W)/(\Delta L/L)$] with a negative ratio of longitudinal strain (compressive) for axial tension (tensile). The inset represents a shear modulus by $G_{\mathrm{S}} = \eta d/x$, where η, d, and x are the shear stress (the force per the area), initial length, and transverse displacement, respectively.

mode [97]. The substrate steps are preferential sites for atomic adsorptions during epitaxy and thus play a significant role in the formation of two-dimensional layers. This growth mode is characterized by a steady advance of the steps in the vicinal direction, namely, adatoms diffuse on terraces and attach to the steps, causing the steps to advance [Fig. 2. 7(d)]. However, in this growth mode, step bunching is often characterized by the crowding of the steps and the creation of large terraces. Step bunching is related to the lower atomic coordination at the steps compared to atoms of the terraces. This causes an increase in the total surface energy of the system. Therefore, the minimization of the total energy can be achieved by step bunching, leading to the formation of wider terraces. Such bunching phenomena usually appear at annealed vicinal crystals or films grown on vicinal substrates at high temperature. Island formation on the vicinal substrates arises from the layer-by-layer modes through the nucleation and coalescence of islands.

These three modes, *i.e.*, step flow, step bunching, and island growth, across the vicinal substrates are predominately dependent on the growth temperature, terrace width of the vicinal substrates, the landing time, τ_{land}, between two consecutive incident atoms on the substrates (related to deposition flux in unit cells of monolayer/sec), and the life time, τ_{life}, of adatoms (before being incorporated into a step). In order to avoid such island formation on a vicinal substrate, the condition, $\tau_{\text{land}} > \tau_{\text{life}}$, is required. Otherwise, the adatoms on the terraces will increase in number over time to form islands as $\tau_{\text{land}} < \tau_{\text{life}}$.

2.1.4 Epitaxial thin films and strain engineering

The structure and composition of thin films are directly correlated with their functionalities (*e.g.* insulating/conducting films, anti-reflectors, dielectrics, mutiferroics, and capacitors) for a wide-range of applications. These are strongly influenced by growth conditions such as growth temperature, background pressure, incident material flux, elastic energy, underlying substrate, *etc.* Therefore, the understanding of the growth kinetics for the formation of thin films is mandatory to control growth mode and the resulting surface morphology. As discussed earlier (see Fig. 2.6.), within the kinetic model, the important factors that determine the surface morphology of films are the adatom surface diffusion coefficient (D_{s}), the energy barrier (E_{diff}) to hop between lattice sites and the energy barrier (the so-called $Ehrlich - Schwoebel$ barrier, E_{ES}) to cross a lower terrace [96, 97]. The diffusion distance, I_{diff}, of an adatom from its landing site can be described as

$$I_{\text{diff}} = \sqrt{D_{\text{s}}\tau}, \tag{2.18}$$

where τ is the residence time of the adatoms or clusters before they leave and are trapped at steps or island edges by diffusion. Thermally-activated adatoms diffuse along the surface with a diffusion coefficient, $D_{\text{s}} \cong D_{\infty}(-E_{\text{diff}}/k_{\text{B}}T)$, where E_{diff} is the diffusion barrier. For an atomic system, the pre-exponential factor is given by $D_{\infty} = f_{\text{n}}a^2$, where f_{n} and a are the attachment frequency and the surface lattice constant of the substrate (or the characteristic jump distance of adatoms), respectively. Thus, the substrates, substrate temperature, and surface structures

significantly influence the diffusion coefficient of the consecutive incident adatoms. For instance, the life-time of adatoms on the terrace area (L_{T}^2) of a vicinal substrate can be given by $\tau_{\mathrm{life}} = L_{\mathrm{T}}^2/2D$. The mean time of adatoms to land in the area, L_{T}^2, with a flux, F, for a unit cell is given by $\tau_{\mathrm{land}} = a^2/L_{\mathrm{T}}^2 F$. When a substrate temperature is high enough to detach atoms from the islands and in turn join the vicinal steps to minimize the free energy of the system, the diffusivity of the adatoms and/or small clusters and growth dynamics are significantly varied.

Epitaxial growth refers to alignment of crystallographic atomic positions along a single crystal substrate or an underlying single crystalline layer. If the type of film is the same as that of the substrate, the crystallographic growth is referred to as homoexpitaxy (Fig. 2.8a). If the types of the film materials are different with the substrate materials, the growth is known as heteroepitaxy (Fig. 2.8b). This growth mode typically depends on the strength of the atom-atom interactions and the atom-surface interactions between the overlayer and substrate, the quality of the single crystal substrate, the degree of vapour supersaturation of film materials at a growth temperature, and the lattice mismatch between the film and substrate. The lattice mismatch between a film layer and a substrate is defined as follows

$$f_{\mathrm{S}} = \frac{a_{\mathrm{sub}} - a_{\mathrm{bulk}}}{a_{\mathrm{sub}}}, \tag{2.19}$$

where a_{bulk} and a_{sub} are the in-plane lattice parameter of the unstrained film material and substrate, respectively. As the epitaxial layer is strained with the same in-plane lattice constants, a_x and a_y (cubic or tetragonal structures), the out-of-plane (z) is tetragonally deformed with a Poisson′s ratio, u, $[(\Delta W/W)/(\Delta L/L)]$ as shown in the inset of Fig. 2.8(c). This relationship is defined by the elastic moduli C_{11} and C_{12}:

$$a_z = a_{\mathrm{bulk}} + \frac{2C_{11}}{C_{12}}(a_{\mathrm{bulk}} - a_{x,y}), \tag{2.20}$$

where a_z and $a_{x,y}$ are the lattice constants for the out-of-plane (001) and in-plane (100) or (010) of the film. The C_{11} and C_{12} are given as $C_{11} = 2G((1\text{-}u)/(1\text{-}2u))$ and $C_{12} = 2G_S(u/(1\text{-}2u))$, respectively, where G_{S} is the shear modulus. When the thickness of the film increases, the strain energy is accommodated within the

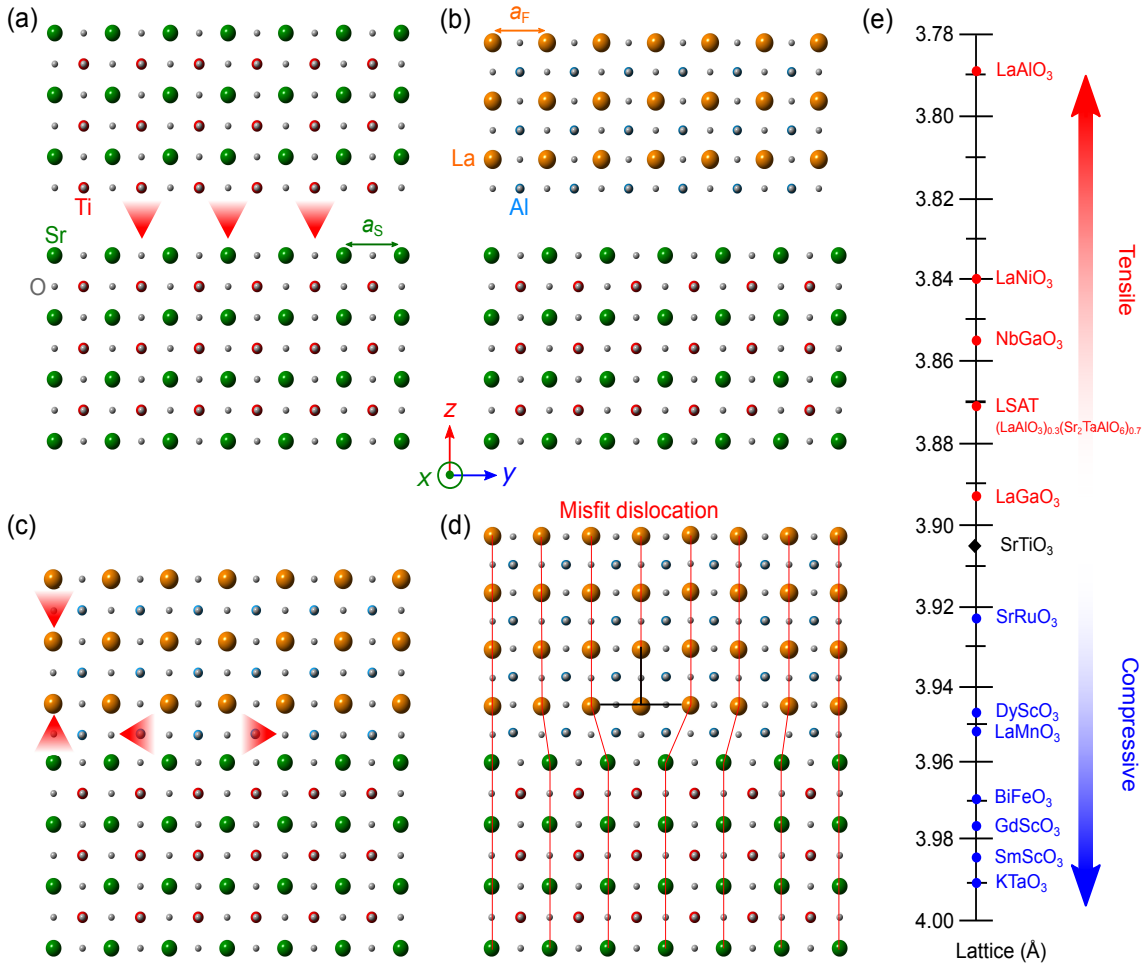

Figure 2.9: Schematics of (a) homoepitaxial and (b) heteroepitaxial film growths. (c) strained upper film(tensile strain in the in-plane of the film and compressive strain in the out-of-plane of the film) subject to the underlying layer/substrate. (d) The formation of a misfit dislocation (an edge dislocation) after the relaxation of lattice mismatch between the film and substrate. (e) The strain relationship between pseudotetragonal or pseudocubic a-axis lattice parameters of various perovskite oxides and $SrTiO_3$ substrates for the heteroepitaxy of thin film growth.

misfit film layer and further increases until the thickness reaches a critical thickness, strain relaxation occurs which gives rise to lattice defects and misfit dislocations. The strain, ε, of the misfit layer is defined as

$$\varepsilon = f_{\mathrm{S}}(1 - R_{\mathrm{relax}}) = \frac{a_{\mathrm{layer}} - a_{\mathrm{layer}}(\mathrm{bulk})}{a_{\mathrm{sub}}}, \tag{2.21}$$

where R_{relax} and a_{layer}(bulk) are a relaxation parameter and the in-plane lattice parameter of the epitaxial overlayer (bulk), respectively. A tensile strain (+ε) of the epitaxial film is given by a_{layer} – a_{layer} (bulk) > 0 and compressive strain (-ε) by a_{layer} – a_{layer}(bulk) < 0. In heterostructure systems with close lattice match, $|f_{\mathrm{S}}| \geq 1$ %, the epitaxial film overlayer follows the in-plane lattice spacing of the substrate within the layer-by-layer growth mode (a Frank-van der Merwe growth mode) up to the critical thickness. This is the so-called pseudomorphic growth. Hence, the relaxation factor of the epilayer is given by

$$R_{\mathrm{relax}} = \frac{a_{\mathrm{sub}} - a_{\mathrm{layer}}}{a_{\mathrm{sub}} - a_{\mathrm{layer}}(\mathrm{bulk})}. \tag{2.22}$$

Such thin film grwoth dynamics and strain relaxation processes have been observed in highly-mismatched heterostructures, *e.g.*, ZnO/Al_2O_3 (f_s: ≈18 %) and $Be_xZn_{1-x}O/Al_2O_3$ (> 18 %) as will be discussed in Chapters 5 – 7.

2.2 Band structure approximation and electronic properties of materials

2.2.1 Introduction

This thesis is concerned with the electronic properties of oxide-based semiconducting materials with respect to band gap modulation and lattice strain effects. Therefore, understanding the changes in their electronic band structure is required. The relation between the band structure, Fermi level (chemical potential), and the distribution of charge carriers at the surface or interface is important for the evaluation of variations in defect-associated energy levels within the band gap, subsequent band gap renormalization, band dispersion, and band bending in highly defective

or energetically reconstructed oxides. In this section, an overview of the theoretical approximations to the formation of electronic bands, the effect of defects or dopants, and charge carrier accumulation layer, and the associated band bending are presented.

2.2.2 Electronic band structure approximations

The energy band structure is formed by broadening of the electronic energy state in a crystal with a periodic potential. The band structure is dependent on the crystal composition and structure that also defines the shape of the first Brillouin zone (Γ-point). The motion of electrons in a many-body system needs to be formulated taking into account their own interactions (pair potentials) and potentials from the surrounding ions in a crystalline solid. These interactions are quantum-mechanically described by solving the many-body Schrödinger equation, which determines the time-independent electron energies of the system:

$$\hat{\mathcal{H}}|\Psi\rangle = E|\Psi\rangle \tag{2.23}$$

where $\hat{\mathcal{H}}$, E, and Ψ are the Hamiltonian operator of the system, eigenvalue (electron energy), and many-body wavefunction of the electrons. Disregarding the effect of spin-orbit coupling, the many-particle Hamiltonian is given by [98]

$$\hat{\mathcal{H}} = \sum_i \frac{\boldsymbol{p}_i^2}{2m_i} + \sum_j \frac{\boldsymbol{p}_j^2}{2M_j} + \frac{1}{2}\sum_{i',j} \frac{\boldsymbol{Z}_{j'}\boldsymbol{Z}_j e^2}{4\pi\epsilon_0|\boldsymbol{R}_j - \boldsymbol{R}_{j'}|} - \sum_{i,j} \frac{\boldsymbol{Z}_j e^2}{4\pi\epsilon_0|\boldsymbol{r}_i - \boldsymbol{R}_j|} + \frac{1}{2}\sum_{i',i} \frac{e^2}{4\pi\epsilon_0}\frac{1}{|\boldsymbol{r}_i - \boldsymbol{r}_{i'}|}, \tag{2.24}$$

where i and j label the electrons and ions, respectively. $\boldsymbol{p}$ is the momentum operator and $\boldsymbol{r}_\mathrm{i}$ and $\boldsymbol{R}_\mathrm{j}$ are the position of the i_th electron and j_th nucleus, respectively. m, M, and ϵ_0 represent the electron mass, ion mass, and the vacuum permittivity, respectively. The complex Hamiltonian, $\hat{\mathcal{H}}$, can be approximated by applying appropriate simplifications as described below. The electrons in a given crystal system can be divided into core electrons and outer-shell electrons. The core electrons are localized around the nuclei (ion cores). Since the ions are stationary compared to the outer-shell electrons, the mass (motion) of ions is much greater (slower) than that of the electrons ($i.e. M \gg m$). This allows for approximating the potentials of

the ions by a time-averaged adiabatic electronic potential. Hence, the total wave function is approximated by

$$\Psi = \psi_{\text{ions}}(\boldsymbol{R})\psi_e(\boldsymbol{r}, \boldsymbol{R}) \tag{2.25}$$

where $\psi_{\text{ions}}(\boldsymbol{R})$ is the wave function of the ions moving within their ionic potentials and $\psi_{\text{e}}(\boldsymbol{r}, \boldsymbol{R})$ is the wave function of all the electrons instantaneously dependent on the ionic position. The Hamiltonian of the system is thus described by the sum of three terms:

$$\hat{\mathcal{H}} = \hat{\mathcal{H}}_{\text{e}}(\boldsymbol{r}_i, \boldsymbol{R}_j) + \hat{\mathcal{H}}_{\text{ions}}(\boldsymbol{R}_j) + \hat{\mathcal{H}}_{\text{e-ions}}(\boldsymbol{r}_i, \Delta\boldsymbol{R}_j), \tag{2.26}$$

where $\hat{\mathcal{H}}_{\text{e}}$ ($\boldsymbol{r}_i$,$\boldsymbol{R}_j$) is the Hamiltonian of the electrons in the potential from the equilibrium position of the ions, $\hat{\mathcal{H}}_{\text{ions}}$ ($\boldsymbol{R}_j$) the Hamiltonian for the motion of ions, and $\hat{\mathcal{H}}_{\text{e-ions}}$ (r_i,$\Delta\boldsymbol{R}_j$) is the Hamiltonian for the change in the electronic energy associated with the displacement of the ions ($\Delta\boldsymbol{R}_j$) from their equilibrium positions. The last term is related to the normal modes of vibration of the solid system, commonly thermal vibration of ions, thus referring to as the electron-phonon interaction. Consequently, the simplified electronic Hamiltonian can be written by

$$\hat{\mathcal{H}}_{\text{e}} = \sum_i \frac{\boldsymbol{p}_i^2}{2m_i} + \frac{1}{2}\sum_{i',i} \frac{\text{e}^2}{4\pi\epsilon_0|\boldsymbol{r}_i - \boldsymbol{r}_{i'}|} - \sum_{i,j} \frac{\boldsymbol{Z}_j\text{e}^2}{4\pi\epsilon_0|\boldsymbol{r}_i - \boldsymbol{R}_j|}. \tag{2.27}$$

These three terms reflects the kinetic energy of electrons, the interaction of electrons, and the electron-ion interactions, respectively. To further simplify Eq. 2.27, the approximation requires the electron-electron interactions to be averaged as a constant repulsive component and a small perturbation (one-electron approximation). If the electron-electron interaction is negligible, each electron interacts independently with the lattice of ions. Furthermore, it can simply be considered that each electron experiences the same average potential, $V(\boldsymbol{r})$, with the surrounding ions in their equilibrium position. As a consequence, this approximation in the Schrödinger equation describing the identical motion of each electron is given by

$$\hat{\mathcal{H}}_{\text{e1}}\psi_n(\boldsymbol{r}) = \left[\frac{\boldsymbol{p}_i^2}{2m_i} + V(\boldsymbol{r})\right]\psi_n(\boldsymbol{r}) = E_n\psi_n(\boldsymbol{r}), \tag{2.28}$$

where $\hat{\mathcal{H}}_{\text{e1}}$, ψ_n ($\boldsymbol{r}$), and E_n are the one-electron Hamiltonian, the wave function, and the energy of an electron in the eigenstate, n. The electron eigenfunction, $\psi_{n\boldsymbol{k}}$

needs to be a periodic function with the same translational periodicity of V in a given crystal known as a Bloch wave function

$$\psi_{n\boldsymbol{k}}(\boldsymbol{r}) = \boldsymbol{u}_{n\boldsymbol{k}}(\boldsymbol{r})\exp(i\boldsymbol{k}\cdot\boldsymbol{r}), \tag{2.29}$$

where n labels the band index and $\boldsymbol{k}$ is the wavevector of the electron in the first Brillouin zone, respectively. $\psi_{n\boldsymbol{k}}(\boldsymbol{r})$ is defined by a plane wave of $\exp(i\boldsymbol{k}\cdot\boldsymbol{r})$ that satisfies the condition

$$\boldsymbol{u}_{n\boldsymbol{k}}(\boldsymbol{r}+\boldsymbol{R}) = \boldsymbol{u}_{n\boldsymbol{k}}(\boldsymbol{r}), \tag{2.30}$$

where $\boldsymbol{R}$ is a primitive translation vector of the Bravais lattice. The state of the electron can be determined by plotting the electron energy, E, as a function of wavevector, $\boldsymbol{k}$ using Eq. 2.26 to give the electronic band structure of the crystal. In order to understand fundamental physical properties of oxide semiconductors, which are intrinsically or extrinsically doped, their electronic band structures, the approximations introduced above are used to formulate the energy dispersions near the centre of the Γ-point, where the band extrema calculated in the reciprocal space usually occur.

2.2.3 Parabolic band approximation

This approximation is considered only for the states at which the energy of electrons are much larger than the $V(r)$, and by assuming the electrons are almost free. This allows the simplification of the energy dispersions at the band extrema which are the $\boldsymbol{k}$-space region of interest and to obtain the band gap energy transport, and other band structure parameters for a given semiconductor. The band dispersion at the Γ–point can be approximated by a Taylor expansion around the band extrema. The so-called parabolic approximation of energy dispersion for electrons and holes can be given by [99]

$$E_{\mathrm{e,h}}(\boldsymbol{k}) = E_{\mathrm{e,h}}(0) \pm \frac{\hbar^2\boldsymbol{k}^2}{2m^*}, \tag{2.31}$$

where $E_{\mathrm{e,h}}$ (0) is the energy at $\boldsymbol{k} = 0$, m^* is the electron or hole effective mass, and the $+$ and $-$ signs correspond to electron and hole energy, respectively. The

energy band gap defines as $E_g = E_C - E_V$, where E_C and E_V are the conduction band minimum (CBM) and valence band maximum (VBM), respectively. This free-electron approximation typically holds for non-degenerate wide band gap semiconductors, *e.g.*, ZnO and GaN, with neglectable interaction between the CBM and VBM. However, for certain cases of degenerate narrow gap semiconductors, *e.g.*, CdO, InN, InAs, and InSb, the non-parbolicity of the conduction band needs to be considered due to the interband interactions [9, 100–105].

2.2.4 $\boldsymbol{k \cdot p}$ perturbation theory

In many narrow band-gap semiconductors, an increase in the carrier concentration in the conduction band occurs by introducing a high level of intentional/unintentional doping and defects. This gives rise to the non-parabolicity of the conduction bands. The non-parabolicity of the conduction band in narrow band gap semiconductors is accompanied by interband interactions, whcih can be approximated by the $\boldsymbol{k \cdot p}$ perturbation theory. In this model, the electronic wavefunctions at any $\boldsymbol{k}$ in different energy bands are expressed by the sum of the periodic wavefunctions at the extrema. The $\boldsymbol{k \cdot p}$ model is based on the one-electron Hamiltonian using the Bloch theorem as follows [106]

$$\psi_{n\boldsymbol{k}}(\boldsymbol{r}) = u_{n\boldsymbol{k}}(\boldsymbol{r})\exp(i\boldsymbol{k}\cdot\boldsymbol{r}) = \left[\sum c_m \boldsymbol{u}_{m\boldsymbol{k}_0}(r)\right]\exp(i\boldsymbol{k}\cdot\boldsymbol{r}), \tag{2.32}$$

where $\boldsymbol{k}_0$ is the extrema. The Hamiltonian in the time-independent Schrödinger equation is given by [99]

$$\left[\hat{\mathcal{H}}_{e1} + \hat{\mathcal{H}}_1 + \hat{\mathcal{H}}_2 + V_{so} + V_{cf}\right]\boldsymbol{u}_{n\boldsymbol{k}}(\boldsymbol{r}) = E'_{n\boldsymbol{k}}\boldsymbol{u}_{n\boldsymbol{k}}(\boldsymbol{r}), \tag{2.33}$$

$$\hat{\mathcal{H}}_1 = \frac{\hbar\boldsymbol{k}\cdot\boldsymbol{p}}{m_0}, \tag{2.34}$$

$$\hat{\mathcal{H}}_2 = \frac{\hbar^2\boldsymbol{k}^2}{2m_0}, \tag{2.35}$$

where $\hat{\mathcal{H}}_{e1} = \frac{\boldsymbol{p}^2}{2m} + V_0\ (\boldsymbol{r})$ and $E'_{n\boldsymbol{k}} = E_{n\boldsymbol{k}} - \frac{\hbar^2\boldsymbol{k}^2}{2m}$. The V_{so} and V_{cf} are the spin-orbit and crystal-field potentials associated with magnetic effects, respectively. At the Γ-point [$\boldsymbol{k} = (0, 0, 0)$], the above equation is simplified as

$$\left[\hat{\mathcal{H}}_{e1} + V_{so} + V_{cf}\right]u_{n_0} = E_{n_0}\boldsymbol{u}_{n_0}(\boldsymbol{r}). \tag{2.36}$$

The solutions in Eq. 2.37 form a complete orthonormal set. Thus, the eigenvalues at any value of $\boldsymbol{k}$ near the Γ-point can be described by considering the $\boldsymbol{k}\cdot\boldsymbol{p}$ interaction between the valence band and conduction band as a perturbation. Applying the Kane model for zinc blende InSb, whose the extrema of the conduction band and three valence bands are at the Γ-point and doubly degenerate (considering only the $\boldsymbol{k}$-independent spin-orbit interaction), the 8 × 8 interaction matrix can be as simple diagonal matrix, formed of two 4 × 4 matrices, correspond to each spin state: [107]

$$H = \begin{bmatrix} \tilde{H} & 0 \\ 0 & \tilde{H} \end{bmatrix}, \tag{2.37}$$

in which,

$$\tilde{H} = \begin{bmatrix} E_s & 0 & \boldsymbol{kp} & 0 \\ 0 & E_p - \Delta_{\mathrm{so}}/3 & \sqrt{2}\Delta_{\mathrm{so}}/3 & 0 \\ \boldsymbol{kp} & \sqrt{2}\Delta_{\mathrm{so}}/3 & E_p & 0 \\ 0 & 0 & 0 & E_p + \Delta_{\mathrm{so}}/3 \end{bmatrix}, \tag{2.38}$$

where E_s and E_p are the eigenvalues of the Hamiltonian for the conduction band and valence band energies at the Γ-point. Δ_{so} is the spin-orbit splitting of the valence band, and $\boldsymbol{p}$ is Kane′s momentum matrix element defined by

$$\boldsymbol{p} = -\frac{i\hbar}{m_0}\langle S|p_z|Z\rangle = -\frac{i\hbar}{m_0}\int Sp_z Zd(\boldsymbol{r}), \tag{2.39}$$

$$\Delta_{\mathrm{so}} = i\frac{3\hbar}{4m_0^2c^2}\langle X|\frac{\partial V(\boldsymbol{r})}{\partial x}p_y - \frac{\partial V(\boldsymbol{r})}{\partial y}p_x|Y\rangle, \tag{2.40}$$

where $|S\rangle$ and $|X\rangle$, $|Y\rangle$, $|Z\rangle$ are the s-like and p-like basis wavefunctions, having the symmetry properties of atomic s and $p_{x,y,z}$ orbitals, respectively. The solution of the full set of equations over the basis functions gives the eigenvalues of the energy:

$$(E' - E_{\boldsymbol{s}})(E' - E_p)(E' - E_p + \Delta_{so}) - \boldsymbol{k}^2\boldsymbol{p}^2(E' - E_p + 2\Delta_{so}/3) = 0. \tag{2.41}$$

The dispersion of the conduction band is given by

$$E_{\mathrm{C}}(\boldsymbol{k}) = E' + E_{\boldsymbol{k}} = E' + \frac{\hbar^2\boldsymbol{k}^2}{2m_0^*}, \tag{2.42}$$

where E' is the highest eigenvalue of the Hamiltonian in Eqs. 2.37 and 2.38, and m_0^* is the effective mass of the conduction band edge. Given that the zero energy is

placed at the CBM.

$$E_{\mathrm{C}}(\boldsymbol{k}) = \frac{1}{2}\left[-E_{\mathrm{g}} + \sqrt{E_{\mathrm{g}}^2 + 4\boldsymbol{k}^2\boldsymbol{p}^2}\right] + E_{\boldsymbol{k}}, \tag{2.43}$$

where the Kane′s matrix element is simplified as

$$\boldsymbol{p}^2 = \frac{\hbar^2}{m_0}\left(\frac{m_0}{m_0^*} - 1\right) E_{\mathrm{g}}. \tag{2.44}$$

Applying Eq. 2.44 to conduction band, here a simplified model is the so-called "two-band" Kane model. Provided that the energy eigenvalues are small compared to the E_{g} and describing the momentum matrix element in terms of m_0^*. The dispersion relation of the conduction band is rearranged to

$$E(1 + \alpha E) = \frac{\hbar^2\boldsymbol{k}^2}{2m_0^*}, \tag{2.45}$$

where the energy is measured from the conduction band minimum and

$$\alpha = \frac{1}{E_{\mathrm{g}}}\left(1 - \frac{m_0^*}{m_0}\right)\left(1 - \frac{E_{\mathrm{g}}\Delta_{\mathrm{so}}}{3(E_{\mathrm{g}} + 2\Delta_{\mathrm{so}}/3)(E_{\mathrm{g}} + \Delta_{\mathrm{so}})}\right). \tag{2.46}$$

Given that the spin-orbit splitting of valence band is not comparable to the E_{g}, $E_{\mathrm{g}} \gg \Delta_{\mathrm{so}}$ and $E_{\mathrm{g}} \ll \Delta_{\mathrm{so}}$, and E, the dispersion is simplified as

$$E(1 + \alpha E + \beta E^2) = \frac{\hbar^2 k^2}{2m^*}, \tag{2.47}$$

where $\alpha = (1/E_{\mathrm{g}})$(1-$m^*/m_0$) and β = -(2/(E_{g}^2))(m^*/m_0)(1-m^*/m_0). For $m^* \gg m_0$, $\alpha \cong (1/E_{\mathrm{g}})$ which is known as the α-approximation. The value of α tends to zero for large E_{g}, leading to the parabolic dispersion of the conduction band. Thus, the density of the isotropic conduction band states is given by

$$g_{\mathrm{c}}(\boldsymbol{k}) = \frac{\boldsymbol{k}^2}{\pi^2}\left[\frac{dE_{\mathrm{C}}(\boldsymbol{k})}{d\boldsymbol{k}}\right]^{-1} = \frac{\boldsymbol{k}^2}{\pi^2}\left[4\boldsymbol{p}^2\left(E_{\mathrm{g}}^2 + 4\boldsymbol{k}^2\boldsymbol{p}^2\right)^{-1/2} + \frac{\hbar^2}{m_0}\right]^{-1}. \tag{2.48}$$

Considering the fact that the effective mass is a tensor quantity and energy-dependent $\boldsymbol{k}$-space ($\boldsymbol{k}_x$, $\boldsymbol{k}_y$, $\boldsymbol{k}_z$), the energy dependent conduction-band-edge effective mass in an isotropic conduction band is defined by

$$m^* = \hbar^2\boldsymbol{k}\left[\frac{dE_{\mathrm{c}}(\boldsymbol{k})}{d\boldsymbol{k}}\right]^{-1} = \hbar^2\left[4\boldsymbol{p}^2\left(E_{\mathrm{g}}^2 + 4\boldsymbol{k}^2\boldsymbol{p}^2\right)^{-1/2} + \frac{\hbar^2}{m_0}\right]^{-1}. \tag{2.49}$$

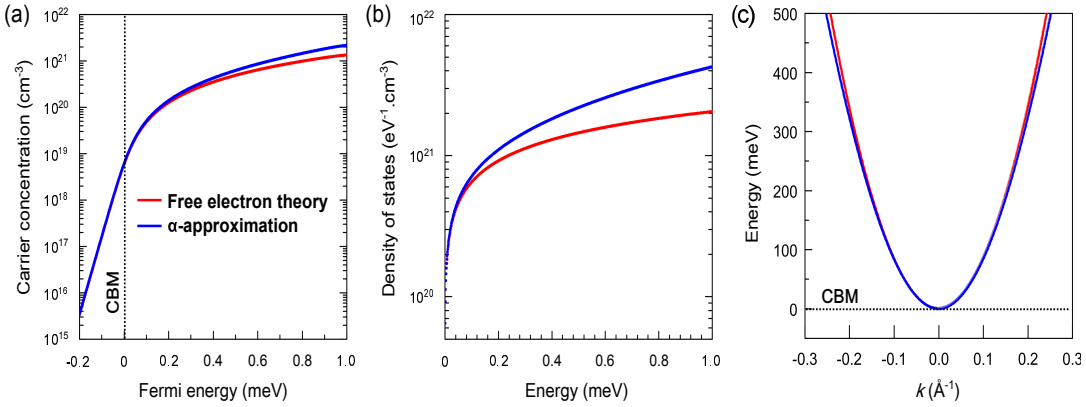

Figure 2.10: (a) The Fermi level difference in the band filling process tends to be significant at high carrier concentrations. (b) A higher (lower) curvature in the parabolic (non-parabolic) band with a lower (higher) density-of-states in the whole region. (c) Conduction band diagram for the parabolic band (free electron theory) and α-approximations.

The concentration of the non-parabolic conduction electrons, n, is given by

$$n = \int_0^\infty g_C(E) f_{FD} dE \tag{2.50}$$

where $f_{FD} = \frac{1}{\exp[(E-E_F)/k_B T]}$ is the Fermi-Dirac distribution function. Figure 2.10 compares variations in the electronic parameters of parabolic and non-parabolic conduction band approximations for a highly-doped wide band gap ZnO ($E_g = 3.37$ eV, $m^* = 0.45 m_0$).

2.2.5 Band filling and band gap renormalization

In this thesis, electrical and optical characteristics of heavily doped oxide thin films are discussed. In highly doped semiconductors, the increase in the charge carriers induce a concurrent effect associated with a band filling effect and the many-body effect. In highly-doped semiconductors, the increase in the electrons (holes) results in the filling of the conduction band (valence band), inducing many-body effects and the shrinkage of fundamental band gap (Fig. 2.11b). These effects influence the optical transitions, charge transport, and the screening length inside the materials. The band filling is known as the Burstein-Moss (BM) shift, which increases the optical gap energy [108].

$$\Delta E_{BM} = \frac{\hbar^2}{2m^*_{e-h}} \left(3\pi^2 n\right)^{2/3}, \tag{2.51}$$

where n is the carrier concentration, and $m^*_{\mathrm{e-h}}$ is the reduced effective mass, $(1/m^*_{\mathrm{e-h}})$ $= (1/m_{\mathrm{e}}) + (1/m_{\mathrm{h}})$. By the further increase in carrier concentration, band gap widening is counteracted by a band gap narrowing of many-body effect. The latter is the so-called band gap renormalization (BGN), which results from electron-electron interactions and electron-ion interactions. These interactions cause a downward (upward) shift of the conduction (valence) band by lowering the CBM for a highly doped n-type semiconductor as presented in Fig. 2.11c. The BGN is accounted for electron exchange and correlation energies, and carrier-carrier and carrier-ion coulomb interactions [109–111].

$$E_{\mathrm{BGR}}(E_{\mathrm{F}}) = \Delta E_{e-e}(E_{\mathrm{F}}) + \Delta E_{e-i}(E_{\mathrm{F}}), \tag{2.52}$$

where

$$\Delta E_{e-e}(E_{\mathrm{F}}) = -\frac{2e^2}{\epsilon_0\epsilon_{\mathrm{s}}\pi} - \frac{e^2\boldsymbol{k}_{\mathrm{TF}}}{2\epsilon_0\epsilon_{\mathrm{s}}}\left[1 - \frac{4}{\pi}\tan^{-1}\left(\frac{\boldsymbol{k}_{\mathrm{F}}}{\boldsymbol{k}_{\mathrm{TF}}}\right)\right], \tag{2.53}$$

$$\Delta E_{e-i}(E_{\mathrm{F}}) = -\frac{4\pi n e^2}{a^*\epsilon_0\epsilon_{\mathrm{s}}\boldsymbol{k}^3_{\mathrm{TF}}}. \tag{2.54}$$

Here, E_{F} and $\boldsymbol{k}_{\mathrm{F}}$ are the Fermi energy and the angular wave number, ϵ_0 and ϵ_∞ are the permittivity of vacuum and high frequency dielectric constant, respectively. The effective Bohr radius and Thomas-Fermi screening angular wave number are given by

$$a^* = \frac{4\pi\epsilon_0\epsilon_{\mathrm{s}}\hbar^2}{e^2 < m^*_{\mathrm{av}} >}, \tag{2.55}$$

$$\boldsymbol{k}_{\mathrm{TF}} = 2\left(\frac{\boldsymbol{k}_{\mathrm{F}}}{\pi r^*_{\mathrm{B}}}\right)^{1/2}, \tag{2.56}$$

where $< m^*_{\mathrm{av}} >$ is the density-of-state-averaged electron effective mass. Consequently, the energy band gap variations in highly degenerate semiconductors are determined by a combination of the BM and BGN effects as

$$E_{\mathrm{g,BM,BGM}} = E_{\mathrm{g0}} + \Delta E_{\mathrm{BM}} + \Delta E_{\mathrm{BGM}}, \tag{2.57}$$

where E_{g0} is the non-perturbed electronic band gap energy for non-degenerated semiconductors. The band gap can be also reduced by temperature effect via lattice expansion and electron-phonon interactions, in which its classical form can be described by the Varshni equation (Fig. 2.11a) [112].

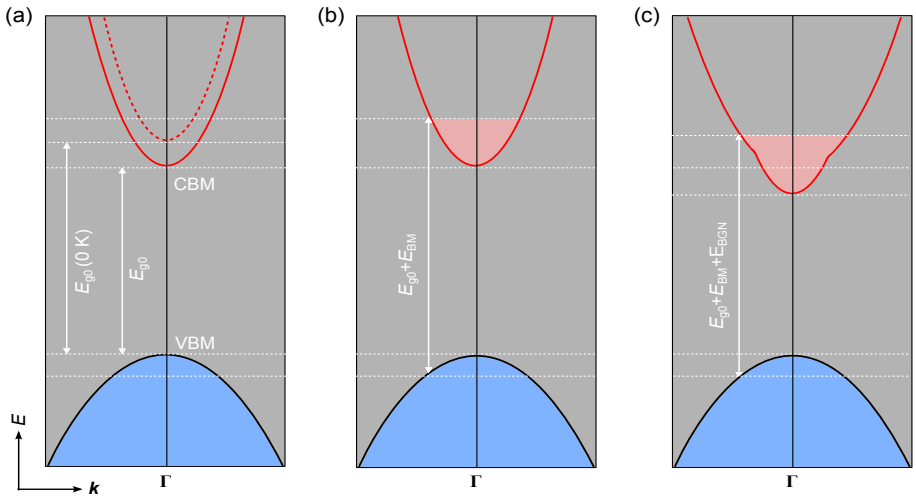

Figure 2.11: Schematic representations of band structures by (a) the band gap reduction due to a temperature effect, (b) conduction band filling effect (BM shift), and (c) BGN effect due to many-body interactions.

2.2.6 Charge neutralization and amphoteric defect model

In the surfaces or interfaces of practical material or heterostructured material systems, the perfect periodicity of lattice translational symmetry is often broken. The breaking symmetry of the crystals creates distinct states localized at the surface or interface, giving rise to the distribution of space charge. For example, the truncated surface of a material has atoms which are usually missed the nearest neighbors. This leads to surface reconstruction via atomic rearrangements (*e.g.* atomic dangling bonds) and/or chemisorption to minimize the total energy. Thus, the associated lattice defects (*e.g.* atomic interstitials and vacancies) or other extrinsic impurities cause charge depletion or accumulation layers at the surface and interface of the materials.

Attempts to approach such a space charge states in electronic aspects, the complex band structure of a one-electron lattice within the nearly-free electron approximation can be utilized solving the Schrödinger equation. In the Hamiltonian of such a model, a small periodic potential is used in terms of Bloch functions. This is added as a perturbation term satisfying the Bragg diffraction (Brillouin zone) boundary condition, $2\boldsymbol{k}_{\mathrm{i}} \cdot \boldsymbol{G} = |\boldsymbol{G}|^2$, where $\boldsymbol{G}$ is the reciprocal lattice vector and $\boldsymbol{k}_{\mathrm{i}} = (\pi/a) + i\boldsymbol{q}$ is wavevectors with real values. Solving the Schrödinger

equation within the nearly-free electron model together with the dispersion and periodic potential opens an energy gap at the Brillouin zone boundary. Meanwhile, to describe the localized states, at which the periodicity of a crystal is broken, the imaginary part, $i\boldsymbol{q}$, express the evanescent states that decay exponentially both into the vacuum and the bulk of the solid [113]. The solutions of the associated complex dispersion with real energies are present within the band gap of the materials, but are not able to be normalized in the bulk. Therefore, these states can be termed virtual gap states (ViGS) [114, 115]. The ViGS derive from the conduction and valence band states of the bulk, and thus their sign/nature depends on the Fermi level position relative to the branch point at which their character changes from predominantly donor-like close to the valence band to predominantly acceptor-like close to the conduction band [113]. In other words, the branch point energy of the ViGS is a state which has equal donor- and acceptor-character, and hence it is also described as the charge neutrality level (CNL). The CNL or branch-point energy is situated below the mid-gap energy at $\boldsymbol{q}_{\max}$ in the one-dimensional model. In order to predict the position of the CNL, many theoretical approaches have been developed. For example, empirical tight-binding calculations for many semiconductors have been performed and determined a linear relationship between the branch-point energy of the ViGS and dielectric band gap energy with a slop parameter 0.449±0.007 below the averaged mid-gap energy of the semiconductors. This was formed in good agreement with the one-dimensional model [113]. Later, Tersoff identified the averaged mid-gap energy, ($\bar{E}_{\mathrm{mid}}$), using a semi-empirical method as [116]

$$\bar{E}_{\mathrm{mid}} = \frac{1}{2}(\bar{E}_{\mathrm{C}} + \bar{E}_{\mathrm{V}}). \tag{2.58}$$

Based on this approach, the CNL is universal in most semiconductors. Thus, the role of the CNL is justification for competence to determine the preferential type of the semiconductors (either n-type or p-type). Unlike conventional semiconductors (*e.g.* Si and GaAs), where the CNL lies within the band gap [113, 117], most metal oxides have a large size and electronegativity mismatch between the metal cations (much larger, less electronegative atom) and the oxygen anion (smaller, high elec-

tronegative atom) [14, 17, 118]. These induce a single low lying conduction bands at the Γ-point, leading to n-type characteristics without intentional doping and the following difficulties for the realization of p-type conduction in many metal oxides. The origin of the n-type properties of the undoped metal oxides is primarily due to the formation of donor-like unintentional defects, *e.g.*, cation interstitials, anion vacancies, and impurities and associated localized states near the CBM [50]. However, n-type conductivity in the metal oxides is limited by increasing the prevalence of compensating defects as the Fermi level reaches the CNL in the conduction band. Such charge neutralization processes are associated with a self-compensation effect between the donor-like defects (dopants) and the acceptor-like defects (acceptors) in the surface or interface or the bulk of materials, based on an amphoteric model. This defect model, suggested by Walukiewicz, explains that variation in the formation energy of preferential defects relative to oppositely charged defects is dependent on the Fermi level with respect to the CNL [14]. Namely, the formation energy for donor (acceptor) native defects increases (decreases) with increasing the Fermi level, leading to the formation of donor (acceptor) defects is most favourable as the Fermi level is below (above) the Fermi stabilization energy as shown in Fig. 2.12. This model can be applied to interpret the energetic of native defect formation and doping limits in dilute semiconductors. Consequently, the concept and implication of the CNL and associated amphoteric defect formation are of primarily importance and widely applicable for understanding the electronic properties, bulk doing, and surface/interface space-charges in different semiconductor materials, and for designing/modifying their characteristics.

2.2.7 Space charge layers

As discussed for the existence of localized space-charge layers in materials, especially at the surface regions, their quantitative approximations are required. The space charge distribution of the localized areas, *e.g.*, the surface and metal-semiconductor interfaces as well as various heterointerfaces is dependent on the position of the Fermi level with respect to the CNL in the bulk (due to the Fermi

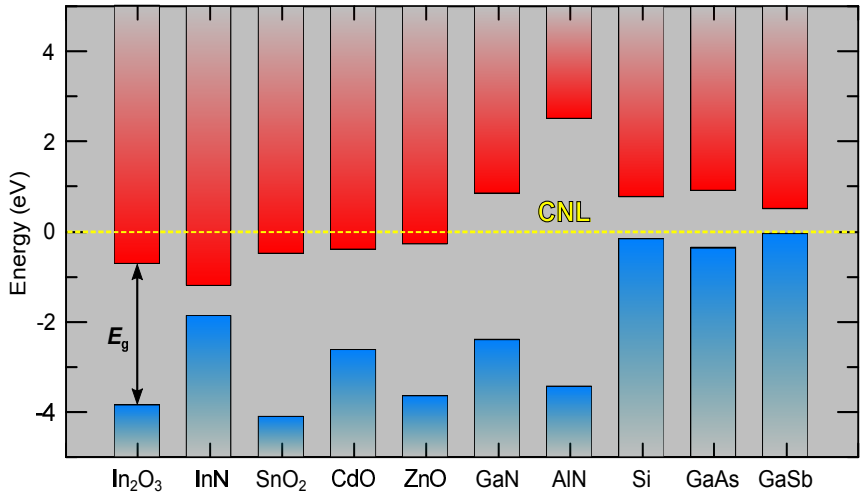

Figure 2.12: Line-up of conduction bands (red) and valence bands (dark blue) for various semiconductors relative to the CNL. This figure was adopted from [10, 14, 103, 119–122].

level pinning effect). This indicates a depletion or an accumulation of the majority carriers and band bending at the surface as shown in Fig. 2.13. Hence, the spatial band bending and width of the space charge layers are associated to the distribution of the free carriers for the charge neutrality together with their effective screening lengths.

The spatial dependence of the space charge region can be approximated by the band bending potential, $V(\boldsymbol{d})$, and electron density, $n(\boldsymbol{d})$, as a function of depth, $\boldsymbol{d}$, into the system satisfying Poisson′s equation as [113, 123]

$$\frac{d^2V}{d\boldsymbol{d}^2} = -\frac{e}{\epsilon_0\epsilon_s}[N_D^+ - N_A^- - n(\boldsymbol{d}) + p(\boldsymbol{d})], \tag{2.59}$$

where ϵ_s is the static dielectric constant of the material, $N_D^+(N_A^-)$ is the density of the bulk ionized donor (acceptor), and $n(\boldsymbol{d})$ $[p(\boldsymbol{d})]$ is the electron [hole] concentration in the space charge region, respectively. Regarding no band bending together with a constant Fermi energy in the bulk of the homogeneous material, the bending potential must satisfy the boundary condition given by

$$V(\boldsymbol{d}) \;\rightarrow\; 0 \text{ as } \boldsymbol{d} \;\rightarrow\; \infty \tag{2.60}$$

and the potential gradient is associated with variation in the sheet carrier density, N_s, from the surface to bulk of the material, which is derived from Gauss′s law:

$$\left.\frac{dV}{d\boldsymbol{d}}\right|_{\boldsymbol{d}=0} = \frac{e}{\epsilon_0\epsilon_s}N_s. \tag{2.61}$$

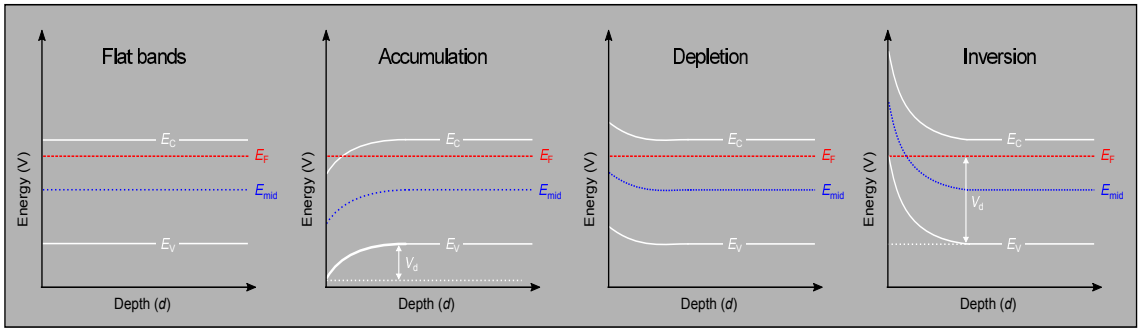

Figure 2.13: A schematic illustration of the band bending in the cases (a) flat bands, (b) charge accumulation, (c) depletion, and (d) inversion at the surface of an n-type semiconductor. The varied conduction band minimum (E_c) and valence band maximum (E_v), the Fermi energy (E_F), and the mid-gap energy (E_{mid}) are represented. The associated bending potentials, $V_{\boldsymbol{d}}$, are shown.

For an n-type (p-type) material, the downward (upward) band bending arises from $V(\boldsymbol{d})<0$ ($V(\boldsymbol{d})>0$) and positively (negatively) charged space charge region. This gives rise to the accumulation (depletion) of electrons at the surface of the material as shown in Fig. 2.13.

Within a modified Thomas-Fermi approximation (MTFA), Poisson′s equation is subject to the boundary conditions and can be solved in the one-electron Schrödinger equation together with the carrier densities, which correspond to the conduction and valence bands. The electron and hole densities are given by

$$n(\boldsymbol{d}) = \int_0^{\infty} g_{\mathrm{C}}(E) f_{\mathrm{FD}} f_{\mathrm{MTFA}}(\boldsymbol{d}) dE, \tag{2.62a}$$

$$p(\boldsymbol{d}) = \int_{E_{\mathrm{V}}}^{-\infty} g_{\mathrm{V}}(E) f_{\mathrm{FD}} f_{\mathrm{MTFA}}(\boldsymbol{d}) dE, \tag{2.62b}$$

where $g_{\mathrm{C}}(E)$ [$g_{\mathrm{V}}(E)$] is the conduction [valence] band density of states. Here, f_{FD} and $f_{\mathrm{MTFA}}(\boldsymbol{d})$ are the Fermi-Dirac function involving the depth-dependent potential and MTFA correction factor, respectively, given by [124, 125]

$$f_{\mathrm{FD}} = \frac{1}{1+\exp\left[(E-E_{\mathrm{F}}+V(\boldsymbol{d})/k_{\mathrm{B}}T\right]}, \tag{2.63a}$$

$$f_{\mathrm{MTFA}}(\boldsymbol{d}) = 1 - \mathrm{sinc}\left[\frac{2\boldsymbol{d}}{L}\left(\frac{E}{k_{\mathrm{B}}T}\right)^{\frac{1}{2}}\left(1+\frac{E}{E_{\mathrm{g}}}\right)^{\frac{1}{2}}\right], \tag{2.63b}$$

where $\mathrm{sinc}(x) = \sin(x)/x$. L is the thermal De-Broglie wave length (the Fermi length] of particles (Fermions) at a given temperature, $L = \hbar/(2m_0^* k_{\mathrm{B}}T)^{0.5}$ [$L = 1/\boldsymbol{k}_{\mathrm{F}}$], in the Maxwell-Boltzmann statistics (the Fermi-Dirac statistics) for non-degenerate

(degenerate) semiconductors. The correction factor, $f_{\mathrm{MTFA}}(\boldsymbol{d})$, physically represents the interference of incident and reflected electron standing wave functions due to the potential barrier at the localized region, ensuring a smooth decrease in the carrier concentration to zero. Consequently, applying the above MTFA model for the depth-dependent charge-profile calculations of a localized region in a material effectively enables the important inclusion of a significantly varied charge distribution with a potential barrier, *e.g.*, electron accumulation in a non-parabolic conduction band. This approximation has been applied in conjunction with experimentally obtained physical quantities (Hall carrier concentration and shifts of valence band minimum with respect to the Fermi level) for the determination of spatial band bending and carrier concentration variations within the highly degenerate interface of BZO film heterointerface (Chapters 6 and 7).

Chapter 3

Experimental Details and Simulation Models

3.1 Introduction

This chapter presents details of the growth methodology, the structural, optical, and electrical characterization techniques of the oxide thin films. The theoretical and practical background of each of the experimental technique is also introduced together with the respective simulation models.

3.2 Sputtering for the growth of oxide thin films

Thin film deposition techniques from the vapour phase can be classified mainly in one of two parts; physical vapour deposition (PVD) and chemical vapour deposition (CVD). The former is the case of sputtering (*e.g.* DC, RF, magnetron, and ion beam sputtering), evaporation (*e.g.* thermal and electron beam evaporation), and pulsed laser deposition (PLD). The latter is thermal, radiative, plasma, and metal-organic CVD (MOCVD). In this thesis, all of the films structured, *i.e.*, ZnO-based thin films, were prepared/grown using RF magnetron sputtering in the desirable ambient gas.

Sputtering is a physical vapour deposition technique used in a vacuum chambers which depends on the collision of generated plasma to eject the desired atoms and/or clusters from a solid target or material onto a chosen substrate. A glow discharge plasma of gas molecules (typically a noble gas such as Ar, with a typical pressure range around 10 – 1 mbar) is created by applying a voltage between two electrodes. The energetic particles are accelerated through plasma bombard onto the targets. The sputtered atoms/clusters are in non-thermodynamic equilibrium. The sputtering yield is defined by the average number of ejected atoms per incident ion. According to the momentum exchange between the ions and atoms at

the target, the yield usually relies on the energy and incident angle of ions, the masses of the ions, the masses and the surface binding energy of atoms of the target materials [126].

The yield and rate of material sputtering can increase employing magnetrons that utilize strong magnetic and electric fields below the cathode. This traps free electrons, which follow helical paths around the applied magnetic field above the surface of the target materials, and thus effectively confine the charged plasma particles/ions and their motion toward the surface of the materials. This leads to the increase in the probability of ionization by many orders of magnitude and it can allow lower sputtering pressure. This is the so-called magnetron sputtering as shown in Figure 3.1b. For the sputtering growth/deposition of oxide-based materials (insulators), a build-up of positive charge at the surface of sputtering materials/cathode occurs, however, such a charge build-up can be avoided by varying the sign of the anode-cathode bias (a high-rate of the RF switching with the added expense of RF power supplies and impedance matching networks: commonly 13.56 MHz) in a radio-frequency sputtering system. Note that at this high frequency the ions no longer follow the rapid switching and in turn the electrons effectively compensate/neutralize the positive charge build-up at the surface of insulating materials. This RF switching is also important as reactive O_2 gas is injected during the sputtering process of metallic sources, which can be readily oxidized. For instance, in this thesis, $Be_xZn_{1-x}O$ films were grown by co-sputtering of ZnO ceramic (2-inch diameter, 1/4-inch thickness, 99.99999 % purity, Kurt, USA) and Be metal (2-inch diameter, 1/4-inch thickness, 99.9 % purity, ESL, China) targets with the injection of additional O_2. The injected O_2 reacts with the ejected materials for compensation/improvement of the film stoichiometry as the loss of the anion usually occurs during the growth process (Fig. 3.1d). Since the formation of BeO is energetically favourable over the other possible reactions (see the discussion part of Chapters 6 and 7), it is expected to form at the surface of the metallic Be sputtering target during the sputtering processes. Therefore, an RF sputtering of the Be target was also applied instead of DC sputtering. The quality and characteristics of sputter-

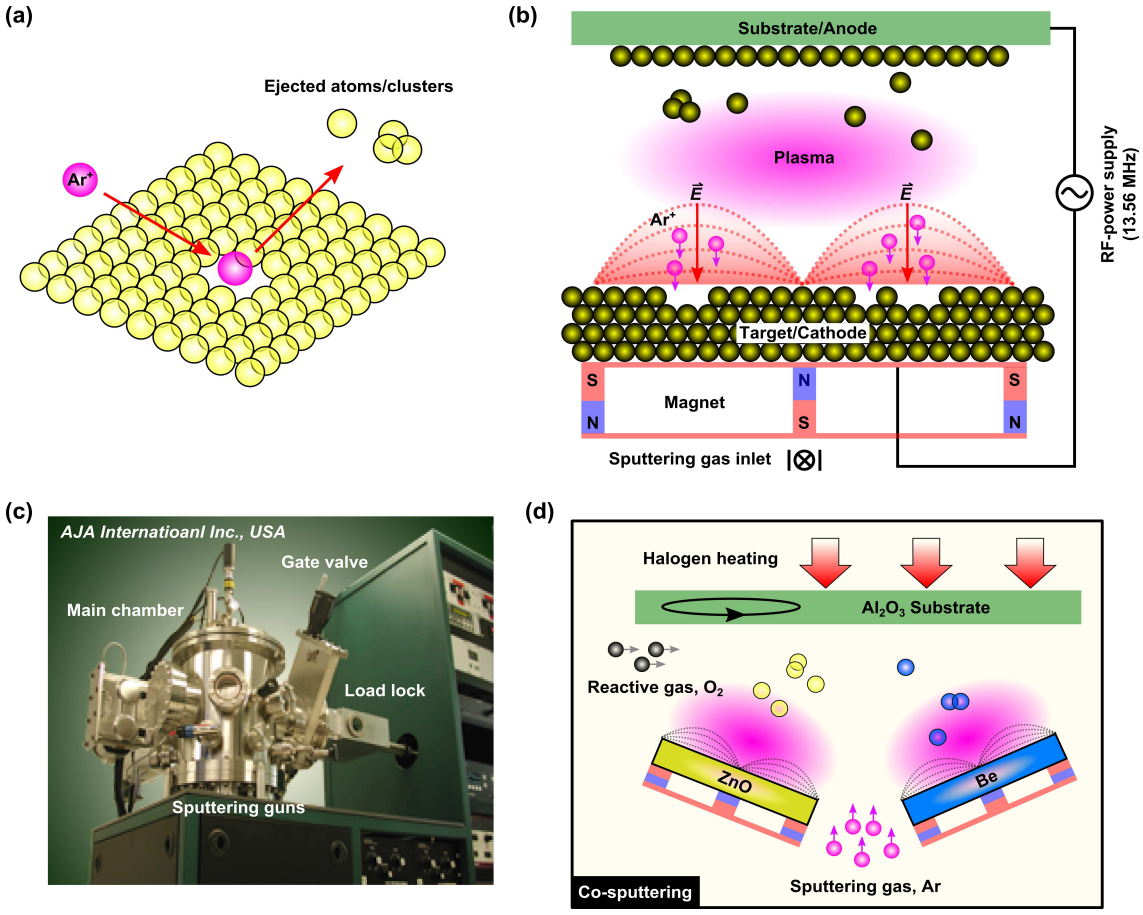

Figure 3.1: Schematic diagrams of the sputtering process (a) and magnetron sputtering (b) for the deposition of thin films using RF-power supply (13.56 MHz). (c) The image of a RF magnetron sputter system (18-inch Ø main chamber, AJA International Inc., USA), which has been used for the growth of oxide thin films in this thesis. (d) A schematic illustration of co-sputtering process using both 2-inch ZnO ceramic and 2-inch Be metal targets set up in different sputtering guns for the growth and synthesis of $Be_xZn_{1-x}O$ alloy films. The sputtering Ar gas and additional O_2 gas, which is reactive to the ejected atoms/clusters to form the most-likely stoichiometric oxide films, are supplied through different gas inlets and substrate temperature is set up by halogen heating. The substrate is rotated during the co-sputtering for the uniformity of thickness of the films.

grown films are primarily dependent on a combination of the RF power, reactive gas, partial pressure, and growth temperature. An optimized growth condition has been obtained by considering the growth variables: (*i*) RF power dependence of ion bombardment for the flux density and mobility of depositing atoms, (*ii*) oxygen partial pressure (a gas mixture of Ar 45 sccm:O_2 5 sccm) for film stoichiometry, (*iii*) the exponential decrease in the growth rate of films with growth temperature and Be composition for the control of alloy film thickness [a growth rate of $\approx$ 2.4 nm/min ($\approx$ 1.6 nm/min) for the growth of $Be_xZn_{1-x}O$ films at T_g = 200 °C (800 °C)], (*iv*) incident sputter-angles of the targets in each RF gun toward the surface of substrates for sputtering yield, (*v*) distance (15 cm) between the targets and the substrates for the minimization of surface damage, and (*vi*) the rotation of substrates (10 rpm) during the film growth for thickness uniformity of films. This has been used for the growth of the $Be_xZn_{1-x}O$ films presented in this thesis.

3.3 X-ray diffraction measurements

In order to investigate the structural properties of epitaxially grown oxide films or other oxide crystals, X-ray diffraction measurements are widely used for the analyses of lattice parameters of thin films, the degree of strain and relaxation, stoichiometricity, mosaicity and dislocation/planar defect densities of the films, the formation of ordered new phases (phase identifications), epitaxial relationship between the films and underlying layers (substrates) [127]. The X-ray beam incident on a given crystal is coherently scattered by the regular arrangement of atoms within the lattice of the material as the atoms scatter X-ray waves primarily through the core electrons of the atoms. The scattered amplitude of the X-ray beam is proportional to the Fourier transform of the electron density distribution of the materials (the structural factor of a crystal). The interference of the scattered X-ray beam can be constructive if the Bragg condition, $n\lambda = 2d_{hkl}sin\theta$, is satisfied ($n$ is an integer indicating the order of the reflection which defines a new lattice plane separation as $d'_{hkl} = \frac{d_{hkl}}{n}$, λ is the wavelength of X-ray, d_{hkl} is the lattice spacing between consecutive hkl Miller planes, and θ is the angle of incidence between the X-ray beam and

lattice planes of the crystal known as the Bragg angle). In order to compare different diffraction datasets obtained by different photon energies (*e.g.* between a lab X-ray source and a synchrotron light source), the λ dependence of the Bragg diffraction is corrected considering the geometric construction (Figs. 3.2a,b) and the scattering vector, Q, of the scattered photons, which transforms the measured/collected scattering data from angular space to reciprocal space. The transformation matrix is defined below

$$Q = \begin{pmatrix} Q_x \\ Q_y \\ Q_z \end{pmatrix} = \begin{pmatrix} \frac{2\pi}{\lambda}(sin\alpha_{\text{inc}} + sin\alpha_{\text{fin}}) \\ 0 \\ \frac{2\pi}{\lambda}(cos\alpha_{\text{fin}} - cos\alpha_{\text{inc}}) \end{pmatrix}, \tag{3.1}$$

where $2\pi/\lambda$ is the magnitude of the wavevector of the scattered photons, α_{inc}, and α_{fin} are the incident angle and final scattering angles with respect to the surface of lattice planes, respectively. In the X-ray diffraction geometry, the angle, ω, corresponds to the horizontal rotation of the specimens with respect to the incident beam and the detection angle is given by 2θ. Thus, these geometrical angles can be defined as

$$\omega = \alpha_{\text{inc}}, \tag{3.2}$$

$$2\theta = \alpha_{\text{inc}} + \alpha_{\text{fin}}. \tag{3.3}$$

Therefore, the transformation matrix can be rewritten as

$$Q = \begin{pmatrix} \frac{2\pi}{\lambda}(sin(\omega) + sin(2\theta - \omega)) \\ 0 \\ \frac{2\pi}{\lambda}(cos(2\theta - \omega) - cos(\omega)) \end{pmatrix} \tag{3.4}$$

For the case of a symmetric diffraction geometry ($\alpha_{\text{inc}} = \alpha_{\text{fin}}$), Eq. 3.4 reduces to

$$|Q| = Q_z = \frac{4\pi}{\lambda} sin(\omega). \tag{3.5}$$

Moreover, the lattice plane spacing, d_{hkl}, can be obtained using Eq. 3.5 in Q space by its substitution into Bragg′s Law:

$$d_{hkl} = \frac{2\pi}{|Q|}. \tag{3.6}$$

The above relations enable the determination of lattice parameters directly and independent of the experimental set of different X-ray energies. The XRD data presented in this thesis were obtained mostly by a Philips Panalytical X′pert Pro MRD and MPD using an X-ray source (Cu $K_{\alpha 1}$ = 1.5406 Å) operated at 40 kV/45 mA at the University of Warwick. In the MRD system, a highly intensive X-ray monochromatic beam was applied using a hybrid Ge crystal at the source together with divergence slits to collimate the incident beam. Some XRD data were collected by using a synchrotron light source (λ = 1.069 Å) from the beamline 5A of the Pohang Light Source II (PLS-II) in the Republic of Korea (Chapter 5).

In this thesis, X-ray diffraction measurements were used to examine composition-dependent and strain-induced variations in the lattice parameters of the oxide thin films. Finite domain or crystallite size, D_s, in a film versus the width of the diffraction curve can be obtained by using the Scherrer′s equation: $D_s = \zeta\lambda/B_{2\theta}\cos(\theta_B)$, where D_s is the diameter of the crystallite, ζ is the shape factor (a constant, 0.88, was used in this thesis) for the crystallites to represent a Lorenzian lineshape, λ is the X-ray wavelength, $B_{2\theta}$ is the full width at half maximum (FWHM) for the 2θ peak of the measured lattice plane, and θ_B is the Bragg angle [128]. However, this approximation on the Scherrer crystallite size needs to be considered with both the finite size of the samples, the existence of defects, and the instrumental resolution, which result in the diffraction peak broadening.

Both the asymmetric and symmetric Bragg reflections for the oxide films were compared to determine the degree of lattice strain and relaxation. In practical cases, grown films consist of defects and non-uniform crystal structures, *e.g.*, misaligned (tilted/twisted) grains with respect to the substrate surface normal, which correspond to the in-plane characteristics of the film layers. These in-plane structures can be characterized using ω-rocking curves, of which the position of the detector (2θ) is fixed and the films are rocked in ω. Thus, the mosaicity and crystal quality of both the textured (columnar structured) oxide films and epitaxial films were studied by measuring the ω-rocking curve of corresponding lattice planes and by the quantitative analyses of the FWHM of the measured ω-rocking curves.

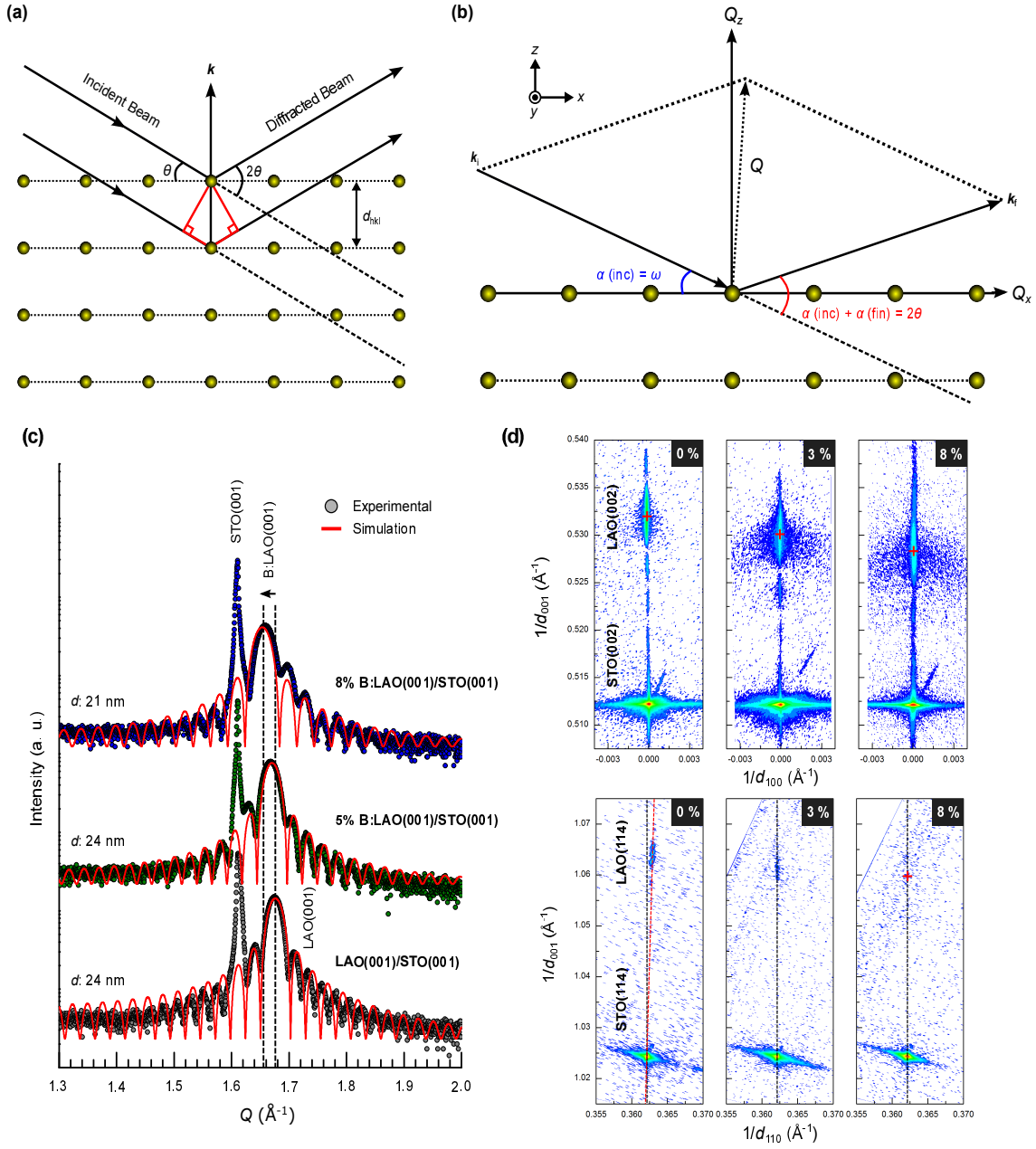

Figure 3.2: (a) Bragg′s Law for the case of symmetric diffraction, [$\theta = \alpha(\text{int}) = \alpha(\text{fin})$, where α(int) and α(fin) are the incident and final (scattered) angles]. (b) Geometric construction of the scattering vector, Q, for an angle dispersive set-up with α(int) and α(fin). The ω angle corresponds to the horizontal rotation of the specimen with respect to the incident beam and the detector angle is 2θ.(c) High-resolution XRD (001) Bragg peaks and finite thickness interference fringes for undoped and boron (B)-doped LAO films grown on STO(001) substrates as a function of B concentration. (d) Reciprocal space maps around the symmetric 002 and asymmetric 114 STO Bragg reflections of the films.

To evaluate the crystalline symmetry of the films/substrates and growth relationships between the films and substrates, azimuthal ϕ scans were carried out to determine the in-plane ordering of the films by analyzing the offset of the angular positions and the symmetry of corresponding reflections. The 30° rotation of the in-plane crystal orientation of both the ZnO and BZO film layers along the Al_2O_3 substrates occurs as ZnO $\{10\bar{1}0\}\|Al_2O_3$ $\{11\bar{2}0\}$. This is because the ZnO lattice aligns with oxygen sublattice of the substrate and thus leads to the reduction of the lattice mismatch from 32 % to 18 % (shown in Chapter 6). The thickness of these high quality epitaxial thin films grown on different material substrates was determined by the period of the interference fringes (or Kiessig fringes) as shown in Fig. 3.2c. The thickness fringes result from multiple scattering and extinction effects within the well-defined layer interfaces of the epitaxial films, that is, constructive and destructive interferences of X-rays reflected from the two interfaces as a consequence of the angular-dependent phase shift. Reciprocal space maps around symmetric (when the selected lattice plane parallel to the surface normal of the samples, a series of the rocking curves with each offset from one another by a value of $\Delta\omega$) and asymmetric reflections (since the selected lattice planes are not parallel to the surface normal, a series of coupled ω–2θ with an ω offset and thus the films can be tilted to measure the crystallographic directions) were collected using high resolution XRD scans to evaluate the degree of strain and relaxation in the oxide thin films along the mismatched substrates (Fig. 3.2d).

3.4 X-ray photoemission spectroscopy

X-ray photoemission spectroscopy (XPS) is a non-destructive surface sensitive technique for the characterization of electronic properties and chemical states at the surface of materials by directly obtaining the density of electronic states (DOS). This technique also allows the elemental quantification and chemical identifications of the surface by core level spectroscopy. The principle of XPS is based on the photoelectric effect discovered by H. R. Hertz in 1888, fully explained with the quantum nature of light by A. Einstein in 1905 [129, 130]. The design and functionality of the XPS

were developed together with a high resolution X-ray source and an electron analyser by K. M. Siegbahn in the 1960′s, which enable the characterization of core-levels with chemical shifts [131]. A schematic of the experimental setup for a typical XPS system is shown in Fig. 3.3. In the photoemission processes, when the surface of a sample is irradiated by incoming monoenergetic X-ray photons (monochromatic energy source) of a fixed energy, $h\nu$, greater than the sum of the electron binding energy, E_{B}, and the work function, Φ_{S}, of the sample, photoelectron are emitted from the valence and/or core levels in an ionization process (*i.e.* the electron leaves behind a hole). Then, the photo-excited electron acquires a kinetic energy, E_{k}, losing characteristic energy, which is the so-called work function of the sample (the minimum energy required for the electron to escape from the highest occupied state to the vacuum). In a practical XPS measurement, the binding energy of the electron, E_{B}, within the material can be approximately determined from its kinetic energy using the following relation:

$$E_{\mathrm{k}} = h\nu - E_{\mathrm{B}} - \Phi_{\mathrm{A}}, \tag{3.7}$$

where $h\nu$ is the incoming photon energy and Φ_{A} is the work function of the analyser. In order to acquire spectral information such as the binding energy (the energy difference between the initial state and the Fermi level), the transmission function of the analyser needs to be calibrated using a metallic sample (*e.g.* Au, Ag, or Cu) as the analyser has its own work function. In general, photoemission spectra are referenced to the Fermi level which corresponds to zero E_{B} of the electron and the E_{k} of the photo-excited electron is referenced to the vacuum level of the material. Metallic samples share the same ground potential with the analyser which has usually smaller work function compared to the sample work function. This work function difference causes a contact potential, $(\Phi_{\mathrm{S}} - \Phi_{\mathrm{A}})$, which gives rise to an acceleration of the electrons as they fly through the analyser. Thereby, the kinetic energy of all electrons increases by an amount of $(\Phi_{\mathrm{S}} - \Phi_{\mathrm{A}})$, namely, $E_k = h\nu - E_{\mathrm{B}} - \Phi_{\mathrm{S}} + (\Phi_{\mathrm{S}} - \Phi_{\mathrm{A}}) = \mathrm{h}\nu - E_{\mathrm{B}} - \Phi_{\mathrm{A}}$. The contact potential can be obtained by measuring a well-defined core level from a clean grounded-standard metal as a spectral calibration. Therefore, all measured XPS spectra and binding

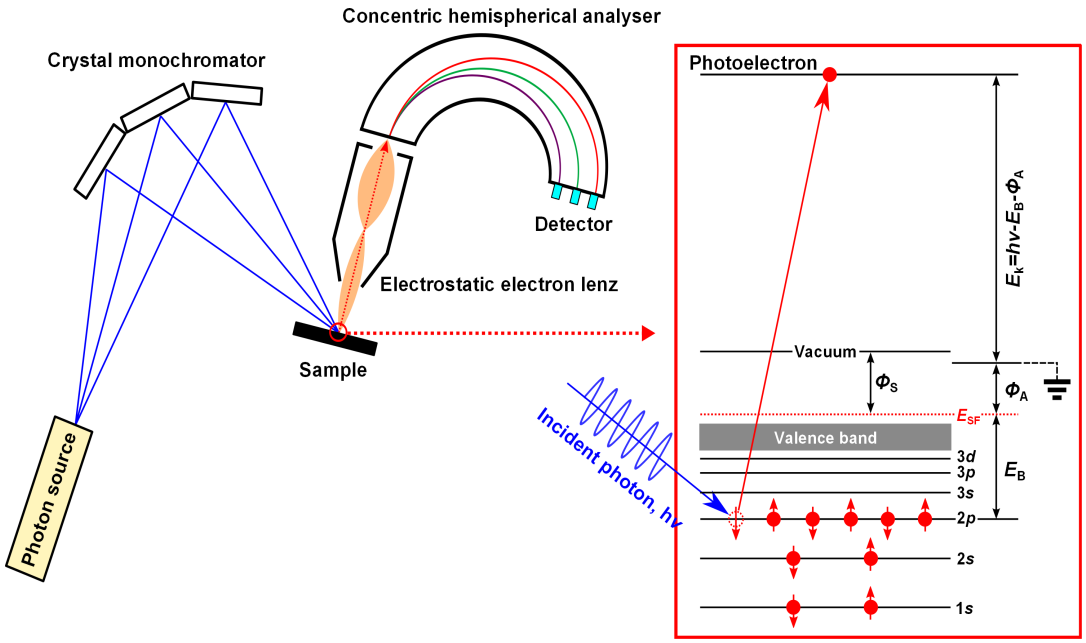

Figure 3.3: Schematics of a photoemission process and the trajectory of the emitted photoelectrons to the detector. Incoming monochromated X-ray photons with an energy, $h\nu$, impinge on the surface of the sample and release electrons with the kinetic energy of $E_k = h\nu - E_B - \Phi_A$. The electron analyser consists of an electrostatic input lens, a hemisphere, and a detection system. The different kinetic energies (pass energies along the path of the hemisphere) of the emitted photoelectrons are filtered by increasing the count rate with multiple channels in the hemispherical analyser.

energies presented in this thesis were calibrated relative to the position of the Fermi edge of an Ar^+-sputtered polycrystalline silver sample (Ag).

In photoemission spectroscopy, the range of accessible binding energies is dependent on the incident photon energy used for the excitation of photoelectrons. For instance, soft X-rays (typically $h\nu \leq 1000$ eV) can excite strongly bound core electrons for elemental analysis, whereas photons in the vacuum ultraviolet range (typically from gas discharge lines, $h\nu < 50$ eV) are used for the excitations of the valence electrons and weakly bound core electrons. This is related to ultraviolet photoemission spectroscopy (UPS). For photon energies of $h\nu > 2$ keV, this is much higher than a typical lab X-ray source, and is commonly called hard X-ray photoelectron spectroscopy. This enables an increase in the probing depth and bulk-like sensitivity, which is followed by an increase in photoelectron inelastic mean free path (IMFP) [132].

The photoemission process in solid-state materials can be divided into three

distinct steps: (i) the photo-excitation of an electron inside the solid by impinged a photon; (ii) propagation of the photoelectron toward the interface between the surface of the solid and vacuum; and (iii) escape of the electron through the surface into the vacuum. In the first step, an incident photon is absorbed and then electron-hole pair is formed inside the solid. In the sudden approximation, the photoexcitation of the electron can be expressed with the transition probability, P_{trans}, from the initial stage (Ψ_i) to the final stage (Ψ_f) using Fermi′s Golden Rule [98, 133].

$$P_{\text{trans}} = |\langle \Psi_f | \hat{\mathcal{H}} | \Psi_i \rangle|^2 \delta(E_f - E_i - h\nu), \tag{3.8}$$

where $\hat{\mathcal{H}}$ is the Hamiltonian for the interaction between the electron and photon. Hence, the obtained photocurrent is proportional to the transition probability, P_{trans}. The energy distribution of the photo-excited electrons, $N(E)$, can be written as

$$N(E) \propto \sum |\langle \Psi_f | \hat{\mathcal{H}} | \Psi_i \rangle|^2 f(E_i) \delta(E_f - E_i - h\nu) \delta(E - (E_f - \phi)) \delta(\boldsymbol{k}_i + \boldsymbol{G} - \boldsymbol{k}_f), \tag{3.9}$$

where $f(E_i)$ and $\boldsymbol{G}$ are the Fermi distribution function and the reciprocal lattice vector, respectively. The first and second delta functions fulfill the energy conservation of photo-excited electrons taking into account incident photon energy, the initial ($\boldsymbol{k}_i$) and final states ($\boldsymbol{k}_f$) of electrons, and the work function of the material. The third delta function term ensures the consevation of the momentum.

As for the second photoemission step, the photo-excited electrons propagate to the surface of the solid undergoing inelastic scattering with other electrons, plasmons or phonons. This causes electrons to lose energy, which reduces the chance of their escape from the surface. This corresponds to an increasing step-like background intensity of photoemission spectra toward the lower kinetics energies (higher binding energies). The final stage of the photoemission process is the escape of the photoelectrons from the surface with a kinetic energy which is larger than the surface potential barrier of the material. The total intensity of photoelectrons which are emitted from a distance, L, below the surface can be given by the Beer-Lambert law:

$$I(E) = I_0(E) \exp\left(-\frac{L}{\lambda sin\theta_{\text{TOA}}}\right), \tag{3.10}$$

where I_0 (E) is the initial intensity of the electrons with energy, E, λ is the IMFP of the electrons, and θ_{TOA} is the photoemission angle (the polar angle of the detector to the surface: a take-of-angle). The photoelectron IMFP in the material can be approximated by using a modified IMFP formula, namely, the TPP-2M formula considering the band gap, density, atomic mass, and stoichiometry of the material. At normal emission, the photoemission signal of 65 % (95 %) is within λ (3λ) of the surface. A typical escape depth of a photoelectron is less than 10 nm in an energy-dependent universal curve of λ. Since the effective path length to the surface can be obtained and predicted by IMFP, the depth-dependent chemical composition and the Fermi edge variation at the surface are obtainable by varying the incident photon energy and take-of-angle. This surface sensitive technique has been applied to investigate the degree of solute segregation and defect-mediated chemisorption as a function of θ_{TOA} at the surface of the transformed ternary oxide films in this thesis (presented in Chapters 6 and 7).

3.4.1 Spectral analysis

Photoemission spectra collected at high E_{B} range (a range of core levels of the constituent elements in a solid) allow the investigation of the chemical composition of a surface and to identify the chemical state of the detected elements. The position of the measured core levels in a photoemission spectrum can be used to ascertain the chemical environment of the element due to the characteristic set of binding energies expected in a material. Hence, small shifts in the binding energies of a particular peak indicate variations in the chemical states of the element.

By measuring the core level peak area, the relative concentration of the composing elements in the material can be determined. A quantitative elemental analysis is performed by considering a Shirley background (related to inelastic scattering of photoelectrons and a step-like background), the elemental relative sensitivity factors, and photo-ionization cross-sections [134–136]. In addition, the elemental composition needs to be corrected by the close-neighbor core-levels as it is more accurate in terms of electron kinetic energy and escape depth (related to IMFP of

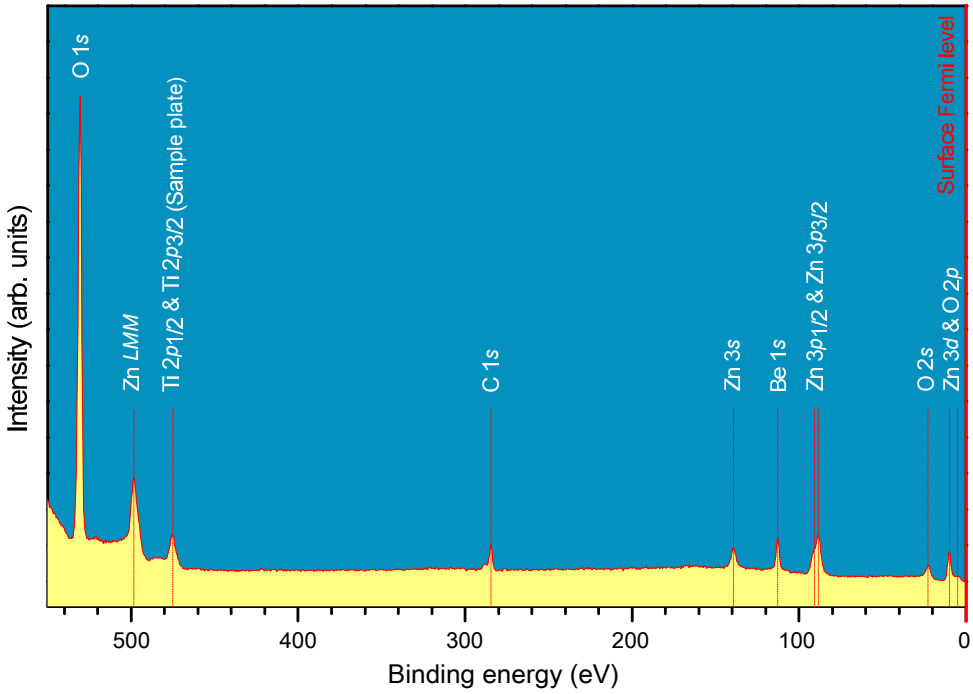

Figure 3.4: An XPS survey spectrum of a $Be_xZn_{1-x}O$ surface illuminated by monochromated Al K_α energy source ($h\nu$ = 1486 eV). The core states of elements are assigned by the positions of the obtained peaks. The Fermi level is referenced to the zero of the binding energy scale and the step-like background at higher binding energies is as a result of the inelastic scattering of the photoelectrons.

photo-excited electrons) [133, 137].

Each core level is labelled by a spectroscopic convention, $X\ nl_j$; where X is the elemental symbol; n is the principal quantum number; l ($s = 0$, $p = 1$, $d = 2$, $f = 3$,) is the orbital angular momentum quantum number; and $j = l \pm 1/2$ is the total angular momentum quantum number. The s-levels ($l = 0$) are characterized by single peaks in the spectrum due to their spherically symmetric orbitals. By contrast, core levels ($l \neq 0$) show doublet peaks due to spin-orbit effects caused by electromagnetic interaction between the electron spin (spin moment) and the magnetic field produced by the electron orbiting around the nuclei. Such spin-orbit coupling leads to a shift in each energy level in the energy spectrum by an energy separation of a doublet ($\Delta E_{\rm so}$):

$$\Delta E_{\rm so} \propto U(nl)\left[j(j+1) - s(s+1)\right], \tag{3.11}$$

where $U(nl)$ is the spin-orbit coupling constant. The doublet intensity ratio, corrected by the background intensity and experimental factors, should be equal to the

ratio of the relative degeneracy of the states $(2j + 1)$ as $I = (2J_- + 1)/(2J_+ + 1)$ and $I = 1/2$, $2/3$, and $3/4$ for p, d, and f doublets, respectively.

The shape of the core level peaks can also be influenced by the excitation of the conduction band surface plasmons. Hence, the Lorentzian line width of the core levels is due to the many-body interactions and the orbital lifetimes (recombination between electrons and holes). In addition, instrumental broadening arising from the experimental resolution (*e.g.* the finite resolution of the analyser, natural width of the photon beam, and thermal broadening) is described by a Gaussian function. The overall XPS core levels need to be convoluted by mixed Lorentzian-Gaussian (Voigt) line shapes. This process involves fitting the experimental peaks to a realistic Voigt function.

3.4.2 XPS measurements

The XPS data presented in this thesis were all collected by an Omicron SPHERA 125 concentric hemispherical analyser at the University of Warwick. The photoemission system consists of three connected ultrahigh vacuum (UHV) chambers for sample preparation, XPS, and angle-resolved photoemission spectroscopy (ARPES). The three UHV chambers are connected by a UHV sample transfer system to exchange and storage samples. The base pressure of the system is $< 3 \times 10^{-11}$ mbar, which is achieved and maintained using a combination of turbomolecular, sputter ion, and titanium sublimation pumps. The sample measurements were performed at room temperature using a monochromated Al K_α radiation ($h\nu = 1486$ eV; line width 0.25 eV). The photoelectrons travel through a 125 nm radius electrostatic hemispherical detection analyser (Omicron). The spectrometer contains 7 channeltrons optically coupled to the counting electronics. Survey spectra of the samples studied in this thesis were obtained with an overall energy resolution of ≈ 1.5 eV using a pass energy of 50 eV. The detailed valence band spectra and core level spectra were collected with an overall resolution of ≤ 0.6 eV and pass energies of < 10 eV. The energy scale of the spectrometer was regularly calibrated using the sputter-cleaned surface of metal samples (Ag, Au, and Cu) as discussed

earlier. The energy scale of the measured core levels in the samples was recorrected by an adventitious C 1s peak (E_{B} of 284.5 eV).

3.5 Optical spectroscopy

3.5.1 UV-visible absorption spectroscopy

Optical absorption features in materials directly correspond to their electronic band structures and so refer to excitation of electrons, *e.g.* electronic band-to-band transitions. For the case of an ideal, undoped, and direct band gap material, the fundamental electronic energy transition takes place from an initial occupied state (typically the highest valence band) to an unoccupied final state (typically the lowest unoccupied conduction band) by a given external energy greater than the band gap. The transmitted light through a material is collected by varying the incident photon energy. In a parabolic band approximation (*i.e.* parabolic dispersion relations for the conduction and valence bands), the direct interband energy transition takes place at the onset of significant absorption, until the photon energy is equal to the band gap of the material [138, 139]. The direct absorption coefficient, α, is usually given by a form of $\alpha(h\nu) \propto (h\nu - E_{\mathrm{g}})^{1/2}$, where $h\nu$ and E_{g} are the incident radiation energy and the band gap of the material, respectively. Using this relation, the band gap of the material can be determined by extrapolation of the linear portion to the horizontal background of the squared absorption coefficient, α^2, spectra as a function of the incident photon energy. For an indirect band gap material, an indirect energy transition is accompanied by a change in momentum, either by absorption or emission of a phonon to satisfy momentum conservation. However, the strength of the absorption for this transition is rather low. A distinct increase in the absorption coefficient can still be seen at a the given photon energy high enough to allow direct interband transitions. Moreover, for highly doped materials, in which the Fermi level is situated above (below) the conduction (valence) band, the corresponding band transition is no longer given by the band gap of the material as the transition for the electron states below the Fermi level is forbidden. This leads to a blue(red)-

shift in the absorption edge for the same momentum (corresponding to higher values of $\boldsymbol{k}$) in the conduction and valence bands. In this work, the transmittance spectra of wide band gap materials (*e.g.* ZnO and $Be_xZn_{1-x}O$), were obtained using a PerkinElmer Lambda 25 UV-visible spectroscopy with a spectral range of 1.1 eV to 6.5 eV at room temperature. The background absorption (caused by air molecules) and the intensity variation of the light sources (Tungsten-halogen visible lamp & Deuterium ultraviolet lamp), were accounted for performing a background scan for each set of measurements. In order to determine the band gap of the material, the optical absorption coefficient, α, is calculated using the overall transmittance, T_O (this coefficient is defined as the ratio of the radiation I transmitted by the sample to the incident radiation, I_0), data by the relation

$$T_O(h\nu) = \frac{(1-R)^2 \exp(-\alpha(h\nu)d)}{1-R^2\exp(-2\alpha(h\nu)d)}, \tag{3.12}$$

$$\alpha = \frac{1}{d\cos\theta} \ln \frac{2T_O R^2}{\sqrt{(1-R)^4 + 4T_O^2 R^2} - (1-R)^2}, \tag{3.13}$$

where d is the thickness of the samples, θ is the incident angle of light relative to the surface normal, and R is the reflectance at the air/sample interface, which is approximately equal to $[(n-1)/(n+1)]^2$, where n is the refractive index of the sample. The above equations take into account multiple internal reflections and the refractive index of the sample.

3.5.2 Fourier-transform infrared spectroscopy

In the infrared (IR) region, the optical spectrum represents low energy oscillations which mainly correspond to excited phonon vibrations and plasmon excitations (collective electron cloud oscillations in the conduction band) in a material. Since, in doped semiconductors and metals, the response of plasmas is associated with an oscillation of the free electron density with respect to the fixed positive ions and their associated damping energy, the effects of the corresponding plasma reflection can be apparent in the IR spectrum (especially in the mid-IR region). Therefore, the plasma energy (frequency), ω_p, is dependent on the free electron concentration, n, high frequency dielectric constant, $\epsilon(\infty)$, and the electron effective mass,

m^* [140, 141].

$$\omega_{\mathrm{p}}^2 = \frac{ne^2}{\epsilon_0 \epsilon(\infty) m_{\mathrm{av}}^*}, \tag{3.14}$$

where, e, ϵ_0, and $\epsilon(\infty)$ are the electronic charge, the vacuum permittivity, and the high frequency dielectric function, respectively. The energy-dependent electron effective mass should be averaged across the occupied conduction band states as the plasma oscillations are collective excitations of all the electrons (collective intraband oscillations). This can be described by

$$m_{\mathrm{av}}^* = \frac{\int_0^\infty g(E) m^*(E) f(E) dE}{\int_0^\infty g(E) f(E) dE}, \tag{3.15}$$

where $g(E)$ is the density-of-states and $f(E)$ is the Fermi-Dirac statistics. This equation has been applied to determine physical quantities such as m_{av}^* of highly degenerate samples in conjunction with the experimentally obtained ω_{p} and $\epsilon(\infty)$ via the reflectance spectra and simulations.

Light interaction with matter can be described in terms of the polarization and absorption (energy transfer to phonons and electrons) through their dielectric function. In this work, several different dielectric functions have been applied for the simulation of the reflectance spectra. Within the two-oscillator model, the complex dielectric function, $\tilde{\epsilon}(\omega)$, [the square of the refractive index, $\tilde{n}(\omega)^2$] consists of two terms which correspond to the lattice phonons and free electrons as given by the following equation

$$\tilde{\epsilon}(\omega) = \tilde{n}(\omega)^2 = \epsilon(\infty) + \frac{(\epsilon(0)\epsilon(\infty))\omega_{\mathrm{TO}}^2}{\omega_{\mathrm{TO}}^2 - \omega^2 - i\omega\gamma_{\mathrm{TO}}} - \frac{\epsilon(\infty)\omega_{\mathrm{p}}^2}{\omega(\omega + i\gamma_{\mathrm{p}}} \tag{3.16}$$

where $\epsilon(0)$ is the static dielectric constants, respectively. ω_{TO} (γ_{TO}) and ω_{p} (γ_{p}) are the frequency (correspondent damping = inverse life time) of a transverse optical phonon and plasma frequency, respectively [141, 142]. A common description of the lattice contribution to the IR dielectric function is defined by the sum of harmonic Lorentz oscillators:

$$\epsilon(\omega) = \epsilon(\infty) + \sum_{i=1}^{n} \frac{S_i \omega_{\mathrm{TO},i}^2}{\omega_{\mathrm{TO},i}^2 - \omega^2 - i\omega\gamma_{\mathrm{TO},i}}, \tag{3.17}$$

where S_i denote the oscillator strength. Considering anharmonic coupling effects of transverse optical (TO) phonon and longitudinal optical (LO) phonon modes in

polar materials, which are split due to the macroscopic electric fields associated with the longitudinal phonons, three independent oscillators need to be involved as a three oscillator model: [141]

$$\epsilon(\omega) = \epsilon(\infty)\left(\frac{\omega^2 + i\omega\gamma_{\mathrm{LO}} - \omega_{\mathrm{LO}}^2}{\omega^2 + i\omega\gamma_{\mathrm{TO}} - \omega_{\mathrm{TO}}^2} - \frac{\omega_{\mathrm{p}}^2}{\omega(\omega + i\gamma_{\mathrm{p}})}\right), \tag{3.18}$$

where ω_{LO} and γ_{LO} are the frequency and the broadening of a longitudinal optical phonon, respectively. This model describes two LO and TO phonon modes are along with the classical Drude model for the free carrier response. The corresponding coupling of the IR-active LO and TO phonon modes can be described using a factorized model with Lorentzian broadening

$$\tilde{\epsilon}(\omega) = \epsilon(\infty)\prod_{i}^{l}\frac{\omega^2 + i\omega\gamma_{\mathrm{LO},i} - \omega_{\mathrm{LO},i}^2}{\omega^2 + i\omega\gamma_{\mathrm{TO,i}} - \omega_{\mathrm{TO},i}^2} - \frac{\omega_{\mathrm{p}}^2}{\omega(\omega + i\gamma_{\mathrm{p}})} \tag{3.19}$$

If ω_{p} lies in the range of or close to the LO modes, the plasmon strongly interacts with the lattice phonons and, therefore, LO-phonon-plasmon (LPP) coupling effects need to be considered. The dielectric function of the material with free carriers can be transformed into a factorized expression similar to that for anharmonic effects of plasmon excitations with LO phonons in multi-phonon-mode materials (m species of plasmon and l lattice phonon bands):

$$\epsilon_j^{\mathrm{LPP}} = \epsilon_j^{\mathrm{LPP}}(\infty)\frac{\prod_{i=1}^{m+l}(\omega^2 + i\omega\tilde{\gamma}_{\mathrm{LPP},ij} - \tilde{\omega}_{\mathrm{LPP},ij}^2)}{\omega\prod_i^m(\omega + i\gamma_{\mathrm{p},ij})\prod_i^l(\omega^2 + i\omega\gamma_{\mathrm{TO},ij} - \omega_{\mathrm{TO},ij}^2)}, \tag{3.20}$$

where $\omega_{\mathrm{LPP},ij}$ and $\gamma_{\mathrm{LPP},ij}$ are the eigenfrequencies and broadening parameters of the coupled free carriers and lattice phonon modes (the LPP modes), respectively. The screened frequency of the lower ($i = 1$) and higher ($i = 2$) LPP modes are given by

$$\tilde{\omega}_{\mathrm{LPP},i} = \left\{\frac{1}{2}\left[\omega_{\mathrm{LO}}^2 + \omega_{\mathrm{p}}^2 + (-1)^i\sqrt{(\omega_{\mathrm{LO}}^2 + \omega_{\mathrm{p}}^2)^2 - 4\omega_{\mathrm{p}}^2\omega_{\mathrm{TO}}^2}\,\right]\right\}^{\frac{1}{2}}. \tag{3.21}$$

As thin films as multi-layered samples usually consist of different layer thicknesses and refractive indices, the multiple interference effects within the stratified medium need to be taken into account using a general transfer matrix method. Light reflection across a heterostructured sample within a stratified medium is illustrated in Fig. 3.6a. The refractive indices of the film and substrate are denoted as n_2' and

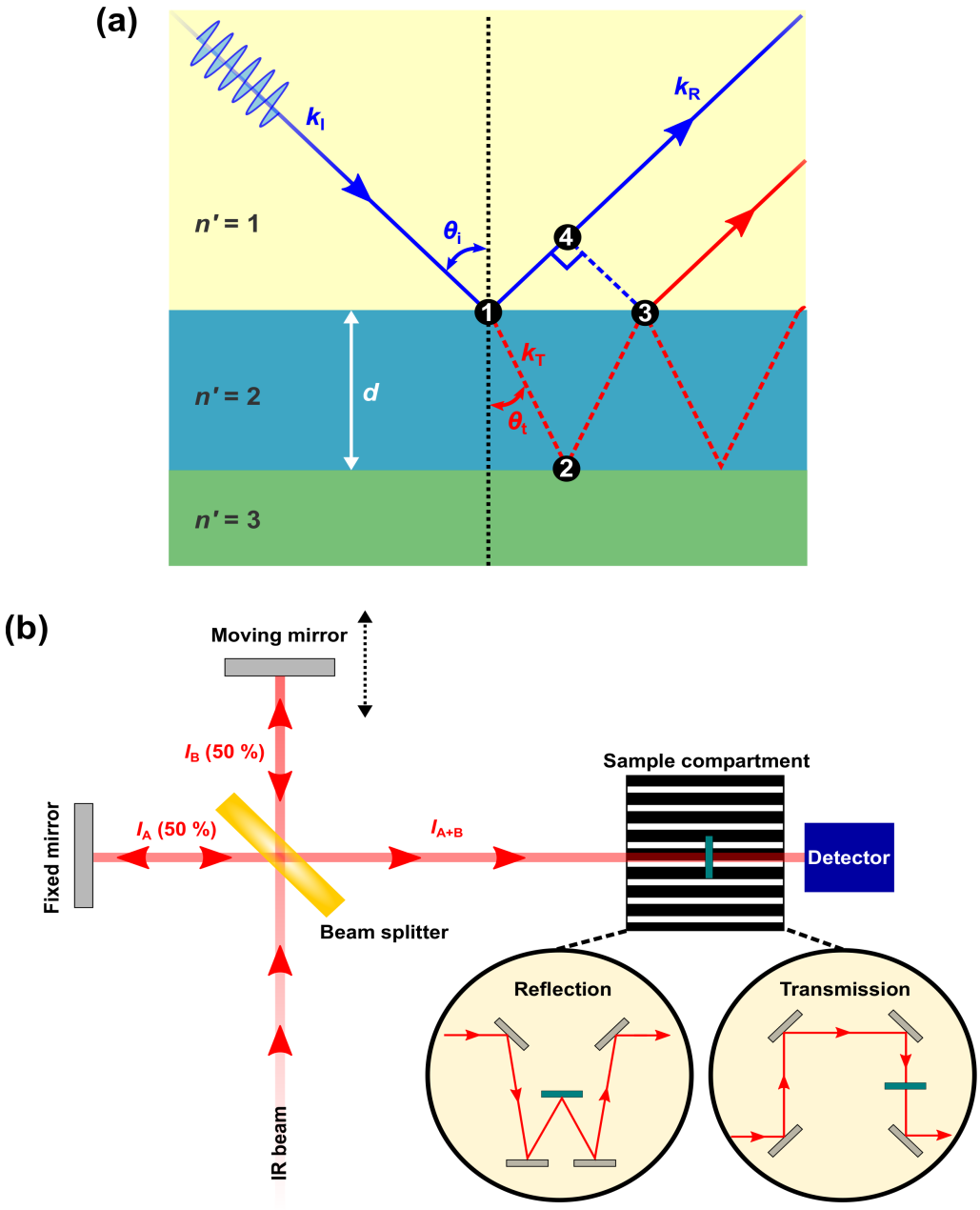

Figure 3.5: (a) Schematic representation of the reflections from a film/substrate interface. The incident radiation, k_i, propagates the film layer with a thickness of d at the incident angle, θ_i, and transmitted angle, θ_t, with respect to the surface normal. The path difference, Γ, between the resulting reflections can be defined as $\Gamma_R = n_2'(D_{12} + D_{23}) - D_{14}$, where n_2' is the refractive index of the film and D_{ij} represent the distance between i and j. (b) Schematic of an FTIR spectrometer: the Michelson interferometer, sample compartment, and detector. The geometry of the beam path in the sample compartment for reflectivity and transmission measurements at an incident angle of 11°.

n_3', respectively, and film thickness is d. The incident angle of light is θ_i and the transmitted angle is θ_t. As light propagation takes place at an angle, θ, to the surface normal, the amplitude coefficients of reflection (reflectivity, $\tilde{r}$) and transmission (transmitivity, $\tilde{t}$) at each interface can be extracted based on the Fresnel equations at any interface [143]. Using Snell's law, the complex Fresnel coefficients are treated separately by the two perpendicular polarizations ($\tilde{r}_\parallel$ and $\tilde{r}_\perp$) with respect to the plane of incidence as

$$\tilde{r}_\parallel = \frac{n_2'\cos\theta_i - n_1'\cos\theta_t}{n_2'\cos\theta_i + n_1'\cos\theta_t}, \tag{3.22a}$$

$$\tilde{r}_\perp = \frac{n_1'\cos\theta_i - n_2'\cos\theta_t}{n_1'\cos\theta_i + n_2\cos\theta_t}, \tag{3.22b}$$

$$\tilde{t}_\parallel = \frac{2n_1'\cos\theta_i}{n_2'\cos\theta_i + n_1'\cos\theta_t}, \tag{3.22c}$$

$$\tilde{t}_\perp = \frac{2n_1'\cos\theta_i}{n_2 n_1\cos\theta_i + n_2'\cos\theta_t}. \tag{3.22d}$$

The total reflectivity of the stratified sample can be evaluated by taking into account reflections for all of the underlying interfaces and is determined as the following geometric sum

$$\tilde{r} = \tilde{r}_{12} + \tilde{t}_{12}\tilde{r}_{23}\tilde{t}_{21}\exp(i\sigma) + \tilde{t}_{12}\tilde{r}_{23}\tilde{r}_{21}\tilde{r}_{23}\tilde{t}_{21}\exp(i\sigma) + \cdots, \tag{3.23}$$

$$= \tilde{r}_{12} + \tilde{t}_{12}\tilde{r}_{23}\tilde{t}_{21}\exp(i\sigma)\sum_{n=0}^{\infty}\left(\tilde{r}_{23}\tilde{r}_{21}\exp(i\sigma)\right)^n, \tag{3.24}$$

$$= \tilde{r}_{12} + \frac{\tilde{t}_{12}\tilde{r}_{23}\tilde{t}_{21}\exp(i\sigma)}{1 - \tilde{r}_{23}\tilde{r}_{21}\exp(1\sigma)}, \tag{3.25}$$

where $\sigma = \frac{\Gamma_R \omega}{c} = 2\pi k\tilde{n}_2' d\cos\theta_t$ accounts for the phase change arising from the light traveling across the layers. $\Gamma_R = n_2'\ (D_{12} + D_{23})$-$D_{14}$ is the path difference between subsequent reflections. $\tilde{k}$ is the wave number of the incident light. If unpolarised light is used, the total reflectance of the sample can be calculated by averaging over the two polarized reflectances

$$R = \frac{1}{2}(R_\parallel + R_\perp) = \frac{1}{2}\left(|\tilde{r}_\parallel|^2 + |\tilde{r}_\perp|^2\right) \tag{3.26}$$

In this work, the reflectance spectra of the multi-layered samples were recorded using a Bruker vertex 70v FTIR spectroscopy capable of producing polarized light and variable-angle measurements. The energy range of the IR measurements covers

the far-IR (80 – 600 cm^{-1}), mid-IR (420 – 5000 cm^{-1}), and near-IR/visible (4000 – 22000 cm^{-1}) spectral regions separately using different beam splitters and detectors. The geometry of the optics is illustrated in Fig. 3.6b. The experimental spectra from different samples were fitted using the appropriate dielectric functions and the transfer matrix methods to identify the phonon modes, free-carrier-associated plasma frequencies, and layer thickness within the samples.

3.6 Hall effect measurements

Hall effect measurements are widely applied to determine the electrical properties of semiconductors. These properties include the averaged sheet carrier concentration, the carrier type (n- or p-type) and the mobility of majority carriers, and the sheet resistance. A typical Hall bar geometry is shown in Fig. 3.6a. A force is generated on the carriers transversely across the bar as the Lorentz force, $F = q(E + v \times B)$, where q and v is the charge and velocity, respectively, while the an electric current flows along the longitudinal direction (x-direction) in applied electric field [144]. This forces the charge carriers to move in the y-direction, resulting in the charge accumulation at the edges and the built-up of an electric field in a steady state, which is the so-called Hall field. The Hall field direction is dependent on the type of carriers, *i.e.*, the Hall field direction of the positive charge carriers will be opposite to that for negative charge carriers. The magnitude of the induced Hall field is defined as $E_y = v_x \boldsymbol{B}_z$. By externally-controlled parameters such as applied current density (J_x) and the magnetic field ($\boldsymbol{B}_z$), while the Hall coefficient (R_H) is defined by

$$R_H = \frac{E_y}{J_x \boldsymbol{B}_z} = \frac{v_x}{J_x}, \tag{3.27}$$

where $v_x = \mu_e E_x$ and $J_x = ne\mu_e E_x$ when the electrons are majority charge carriers for the conductivity of a sample. The Hall coefficient is usually rearranged as;

$$R_H = \frac{\mu_\mathrm{e} E_x}{ne\mu_\mathrm{e} E_x} = \frac{1}{ne}. \tag{3.28}$$

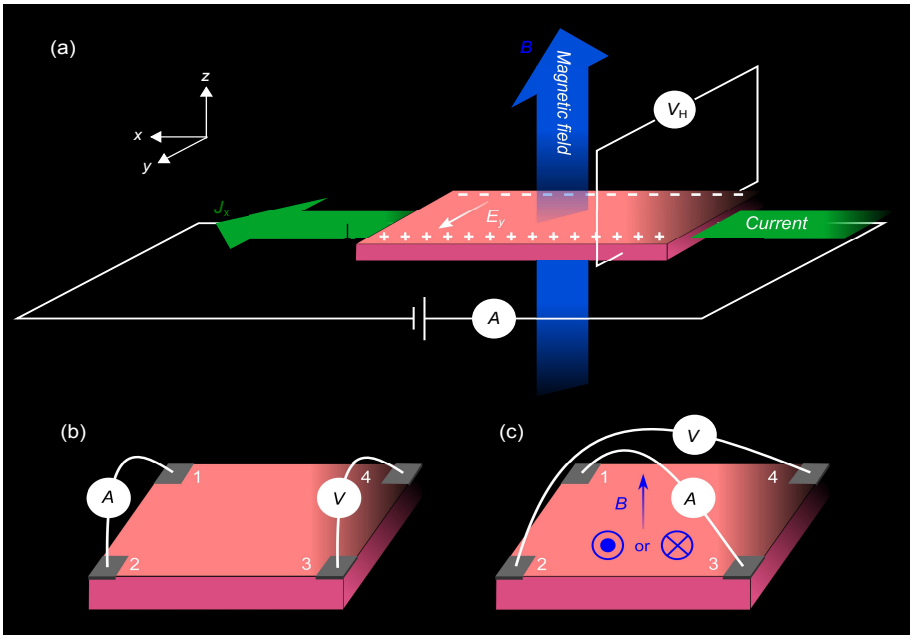

Figure 3.6: (a) A Hall bar geometry for the Hall effect measurements applying current flowing, J_x, along x-direction and magnetic field, $\boldsymbol{B}$, perpendicular to surface normal. The induced carrier motions, the subsequent charge build-up, an electric field, E_y, and a Hall voltage, V_H, across the bar. (b) and (c) represent the van de Pauw configuration for resistance and Hall measurements, respectively. Note that the layer should be electrically isolated from underlying layers or substrates as the results obtained normally show average values.

In many compensated semiconductor samples, where both electrons and holes co-exist, R_H is given by

$$R_H = \frac{1}{|\mathrm{e}|}\frac{(p\mu_\mathrm{h}^2 - n\mu_\mathrm{e}^2)}{(p\mu_\mathrm{h} + n\mu_\mathrm{e})^2}, \tag{3.29}$$

where n (p) and μ_e (h) are the electron (hole) concentration and mobility, respectively.

In practical cases, the applied current, I, magnetic field, $\boldsymbol{B}$, and Hall voltage, V_H, are known parameters unlike the current density of the charge carriers and the induced electric field strength. Therefore, the sheet carrier density, n_s, of the sample can be determined using the following relation:

$$n_\mathrm{s} = \frac{I\boldsymbol{B}}{eV_H}. \tag{3.30}$$

The bulk carrier concentration, n, can be obtained by $n = n_\mathrm{s}/d$, where d is the sample thickness. The V_H and n_s are also related to the carrier mobility through the sheet resistance, $R_\mathrm{s} = V_H/(I\boldsymbol{B}\mu) = 1/(en_\mathrm{s}\mu)$. As a current flows between

contacts 1 and 2, I_{12}, and a voltage is across contacts 3 and 4 (Fig. 3.6b), $R_{\rm s}$ can be determined by the van der Pauw equation:

$$\exp\left(-\frac{\pi R_{12,34}}{R_{\rm s}}\right)+\exp\left(-\frac{\pi R_{23,41}}{R_{\rm s}}\right)=1, \tag{3.31}$$

where $R_{12,34}$ ($R_{23,41}$) $= V_{34}/I_{12}$ (V_{41}/I_{23}). To determine a more accurate sheet resistance, the measured resistances should be averaged, switching the current and voltage contacts in the reciprocity theorem, $R_{12,34} = R_{21,43} = R_{34,12} = R_{43,21}$. The Hall voltage, V_H, between a set of diagonal contacts measured with the current flowing across a set of diagonal contacts on the other opposite corners and a constant B perpendicular to the surface normal as shown in Fig. 3.6(c). In this measurement configuration, eight Hall voltages are acquired for two diagonal sets by which an averaged $V_{\rm H}^{\rm av}$ can be calculated as the following equation:

$$V_H^{\rm av}=\frac{V_{13}^P-V_{13}^N+V_{14}^P-V_{24}^N+V_{31}^P-V_{31}^N+V_{42}^P-V_{42}^N}{8}, \tag{3.32}$$

where $V^{\rm P\ or\ N}$ relies on the polarity of the applied magnetic field, $\pm B$, to receive the corresponding p-type or n-type characteristics of a sample for the summation in $V_{\rm H}^{\rm av}$. Consequently, the averaged sheet carrier density and mobility can be determined applying each set of currents and voltages for the averaged sheet resistance and Hall voltage.

Part of the resistance and Hall measurement data presented in this thesis were achieved using an Ecopia HMS-3000 Hall effect measurement system at the University of Warwick. The measurements were performed at room temperature in the van der Pauw configuration. The current injection was from 1 nA to 20 mA and a permanent magnet of 0.55 T was applied. In order to ensure Ohmic contacts to avoid any charge depletion effects at the surface of the oxide samples, the mesa etching process was performed at all corners of the samples using ion-beam milling and then appropriate contact metals were applied depending on the type of the samples. The Ohmic behavior was then verified measuring the resistance of all the samples. Variable temperature (5 K – 300 K) Hall effect measurements were carried out to investigate defect-associated carrier distribution and their transport properties in the highly doped samples. These measurements were performed separately at the

University of Warwick and at the University of Iceland.

3.7 Atomic force microscopy

Atomic force microscopy (AFM) is a useful method to study the topographic features of thin films. AFM images provide a direct insight to the film growth processes (*e.g.* nucleation-and-growth mechanism and roughness on the films) and secondary structural evolution at the surface of the films. The AFM tip is atomically sharp (approximately 20 nm at the tip) and is made of Si_3N_4 mounted at the end of a flexible cantilever. AFM measurements typically ensure a height resolution of around 2 Å and lateral resolution of less than 100 Å, which allows microscopic morphological studies (*e.g.* a quantification of the surface roughness of the films through a root-mean-squared (RMS) value and height range).

In AFM, a scanning tip is attached to a cantilever arm which measures its deflection using an incident laser source that reflects off the back of the cantilever. The deflection is caused by the change in the interaction between the tip and the surface of a film while the tip scans across the surface. Each interaction gives rise to a motion/force on the tip of the cantilever from a given zero position, which is monitored by the laser reflected from the back of the cantilever. The reflected laser is recorded on a four-quadrant position sensitive photodiode. In this work, AFM was performed mainly in the tapping mode to prevent any damage to the surface of the films unlike the case in a contact mode. AFM tapping mode is operated as a dynamic mode by the vibration of the cantilever above its resonant frequency maintaining a constant tip height from the surface. Namely, the tip height is maintained using a piezoelectric crystal to remain a constant vibrational amplitude which is equivalent to the constant distance between the tip and film surface. Hence, variations in the frequency of oscillation (changes in the applied voltage) correspond to topographical variations at the surface of the film.

In this work, calibration work for the AFM results has been carried out using a standard reference sample (see Figure 3.8) to obtain more accurate size information for grains or particles at the surface of the films. All of the obtained AFM images

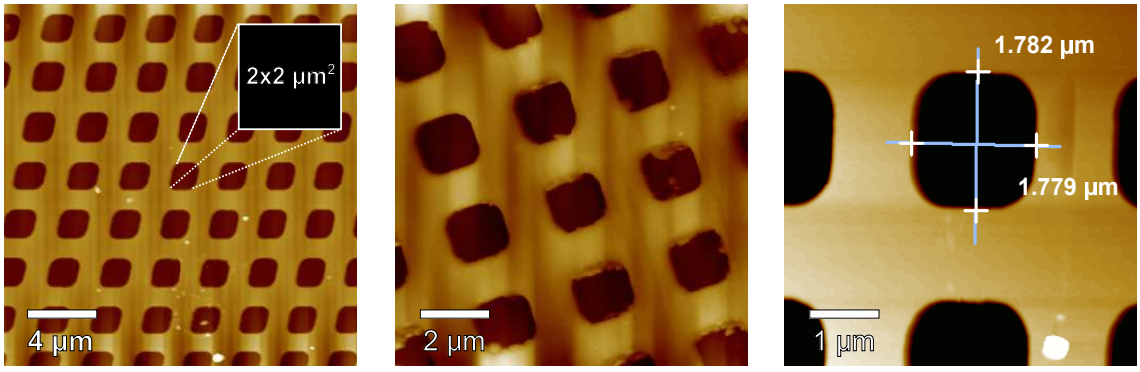

Figure 3.7: AFM topographic images for a standard reference sample for a size calibration in x- and y-directions, which was measured in a tapping mode. The inset of black square box (2×2 μm^2) corresponds to the actual planar area of the square pitches in the obtained images.

were reprocessed using Nanotec (WSxM 5.0) and Gwyddin softwares.

3.8 Other characterization techniques

3.8.1 Transmission electron microscopy

The resolution, δ_T, of an ordinary optical microscopy is approximated according to the Rayleigh′s criterion $\delta_T = 0.61\lambda/n\sin\beta$, where λ is the wave length of light (depending on the acceleration voltage of the electron gun in the de Broglie wave length), n is the refractive index of the viewing medium, and β is the semi-angle of collection of the magnifying lens (objective lens). As $n\sin\beta$ (the so-called numerical aperture) can be approximated to unity, δ_T is half the wave length of radiation. The resolution can be given as $\delta_T = 1.22\lambda/\beta$, where $\lambda \cong 1.22/E^{0.5}$ (E is the energy of electrons.). Therefore, applying high electron energies > 100 keV, a high resolution can be obtained with much smaller $\lambda < 0.04$ Å, which is much less than the diameter of an atom. High resolution transmission electron microscopy (HRTEM) enables the investigation of material properties on the atomic scale. In this thesis, the microstructural properties of the grown, post-treated oxide thin films, an oxide nanoparticles were investigated performing cross-sectional TEM and HRTEM measurements. This gives direct microstructural information such as orientation relationship, atomic stacking faults, twins, anti-phase boundaries, and the distri-

bution of planar defects (grain boundaries). Furthermore, scanning transmission electron microscopy (STEM) which relies on atomic density, specimen thickness, and defect-/strain-associated atomic planes was used to visualize the induced displacement/distribution of different weight of constituent atoms in the oxide films in a contrast view [145]. Energy dispersive X-ray spectroscopy equipped in TEM was employed for composition analysis for selected areas of the samples. TEM measurements for the $Be_xZn_{1-x}O$ samples were performed by Prof. Chel-Jong Choi at Chonbuk National University in South Korea using Field emission TEM, Tecnai G2 F30 S-Twin with an acceleration voltage of 300 kV.

3.8.2 Scanning Electron Microscopy

Scanning electron microscopy (SEM) typically consists of an electron gun, a focusing column, a sample stage, and various different electron detectors. The electron energy is adjusted in a range of 1 – 30 keV to achieve different depths of interaction between electrons and sample surface followed by the IMFP of electrons. This is because the electron scattering event at the surface is dependent on the energy of the incident electrons, the incident angle with respect to the surface of the sample, and the atomic number and density of the elements in the sample. Secondary electrons (SEs) arise from the emission of the valence electrons in the sample excited by the incident electron beam. Since, only the SEs generated at the surface of the sample are emitted, such SE emission can allow a surface sensitive measurement. Moreover, SE emission is larger in an oblique incidence of the electron beam, and by measuring the difference in the incident angle of the electron beam, the distinct brightness of the sample surface can be obtained. Therefore, the SEs collected by several detectors are used for detailed imaging of the topography of the sample surface. However, SEs with lower energies (< 10 eV) are strongly influenced by any charging effect due to the accumulation of static electric charges at the surface of a non-conductive sample. This gives rise to an anomalous contrast in SEM and, hence, requires additional treatment before measuring insulating surfaces (*e.g.* coating of metallic or carbon layers) to prevent any charging effects. This microscopy technique

was applied to study the surface morphologies and thicknesses of the oxide samples presented in Chapters 5 and 7. The SEM images in this work were acquired using a Zeiss SuPRA 55-VP FEGSEM at the University of Warwick and a Jeol JSM-5800 at Chonbuk National University in the Republic of Korea.

3.8.3 Photoluminescence

Photoluminescence (PL) spectroscopy is a non-destructive characterization technique and a powerful tool to investigate optical excitation processes across characteristic radiative transition channels. The optical carrier excitation from an initial occupied state to a final unoccupied state can be obtained by the absorption of a given laser energy which should be higher than the energy of the transition channel within the electronic structure of the material. When electron-hole pairs (so-called excitons, which are typically electrostatically bound within a characteristic length, the exciton Bohr radius) are generated as a result of the induced electron excitations, a number of processes can subsequently occur. These include recombination of the carriers from the excited state into the electronic ground state together with a characteristic luminescence [42,146]. The driving force of such simultaneous emission processes is primarily associated with restoring of the carriers to a thermal equilibrium state with their characteristic carrier lifetime. In the case of wide band gap semiconductors, the lifetime of the exciton emission is usually very short, on the order of several tens to hundreds of picoseconds, whilst the lifetime of the visible emission is much longer in the microsecond range [147]. The carrier lifetime and luminescence efficiency are generally dominated by the non-radiative lifetime, which is dependent on the associated defects in a sample [148]. Hence, the study of band-to-band and defect-associated luminescence from a sample provides critical information such as its chemical composition, the electronic band gap, and the impurity and defect levels. Furthermore, temperature-dependent luminescence from free excitons, donor-/acceptor-bound excitons, donor-acceptor-pairs, two-electron-satellites, and phonon replica gives valuable information about their thermal activation (thermal ionization of excitons) and quenching behavior to determine their binding energies

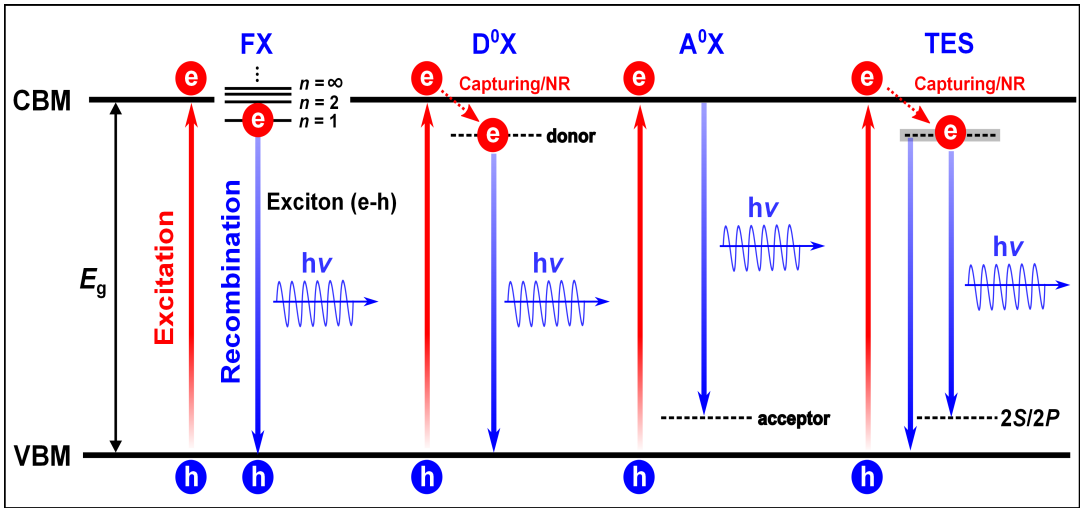

Figure 3.8: Schematic diagrams of the recombination mechanisms: (*i*) The photon energy, $E_{h\nu}$ equals the band gap energy, $E_{\rm g}$, for free exciton recombination from the band-to-band transition (from conduction band minimum, CBM, to valence band maximum, VBM; (*ii*) The $E_{h\nu}$ is reduced by the electron trapping/non-radiative relaxation together with the presence of donor or acceptor states (neutral donor-bound exciton: D^0X, neutral acceptor-bound-exciton: A^0X); (*iii*) Two-electron satellite (TES), *i.e.* two-electron transitions of neutral-donor-bound exciton, as the exciton collapses and the neutral donor returns to the ground state, or it may pick up an energy from the exciton, leaving the electron on the donor in an excited state, in the final state.

and chemical origins [149, 150]. Various types of luminescent exciton transitions including the trapping and relaxation processes are shown in Fig. 3.8.

In direct band gap ZnO, $\rm Zn_i$ typically act as a shallow donor. These defects create localized energy states located at $\approx$ 30 meV just below the conduction band edge [51,151]. Electrons given by the donor-like defects are predominantly located in the conduction band at room temperature, however, at sufficiently low temperatures ($T \leq 110$ K), the donors trap the electrons at the localized states within the band gap by a weak attractive potential, which is referred to as a donor-bound electron (a neutral donor state, D^0). A free exciton, FX, can also be trapped/bound to the donor and the excited state is named as a donor-bound exciton, D^0X. Thus, the PL energy of D^0X can be defined by

$$h\nu(D^0X) = E_{D^0X}(T) = E_{FX}(T) - E_{\rm B}, \tag{3.33}$$

$$E_{FX}(T) = E_{\rm g}(T) - E_{\rm ex}. \tag{3.34}$$

Here, $E_{\rm B}$ is the bound exciton localization energy, $E_{\rm g}(T)$ is the temperature-dependent

band gap energy of ZnO and FX is binding energy created by an electrostatic coulomb force between electron and hole, $E_{\mathrm{ex}} = R_y^* \frac{1}{n^2} = 13.6\ \mathrm{eV}\ \frac{m^*_{\mathrm{e-h}}}{n^2 \epsilon_0^2}$ $(n = 1, 2, 3, \cdots)$, where R_y^* is the excitonic Rydberg energy ($R_y^* \approx 60$ meV in ZnO) and n is the main quantum number.

Various characteristic deep level emission bands have been observed in ZnO-based materials. While the UV emission is usually associated with the band-edge transition or exciton recombination as shown in Fig. 3.9, the emissions in the visible ranges originate from localized states of intrinsic or extrinsic defects within the band gap of ZnO. These have been the subject of extensive controversy over the last two decades. In particular, for the green emission at 2.4 eV, a number of distinct hypotheses have been suggested; including a deep donor state around 0.9 to 1.3 eV below the CBM caused by oxygen vacancies [8, 152]. An acceptor level of oxygen interstitials [energy states around 0.72 eV for ϵ(0/-) and around 1.59 eV for ϵ(-/2-) above the VBM], which the conduction electrons are recombined to holes on these defects [50]. Red band emissions around 1.70 eV have been assigned to an optical transition between shallow donor states (related to $\mathrm{Zn_i}$) and deep levels (related to $\mathrm{V_{Zn}}$) as a donor-acceptor pair (DAP) transition [151].

PL measurements were performed using a CW He-Cd laser ($\lambda = 325$ nm) at the University of Iceland. For deep level emission measurements, a complementary long-pass optical filter with a cut-off wave length of 420 nm was used to increase the dynamic range of deep level emissions in the samples and remove the laser line and its second order diffraction. All of the PL measurements in this thesis were performed using a constant optimized exposure for absolute comparison of the luminescence intensity from the samples.

Chapter 4

Particle Pinning Effects on the Band Modulation of $Be_xZn_{1-x}O$ Alloys

4.1 Introduction

Wide band gap oxides have received a great deal of interest due to their potential use in optoelectronic applications, including ultraviolet (UV) laser diodes (LDs), light-emitting diodes (LEDs), high-mobility transistors, and gas sensors [3, 4, 30–32, 153]. The quantum confinement effect (QCE) and the fractional quantum Hall effect (FQHE) are phenomena that have been observed in well-designed oxide heterostructures and can add to the wealth of potential applications [154]. In order to design such quantum structures, it is essential to understand the band gap engineering of oxides and the nature of oxide-based heterointerfaces. In addition, various charge states can occur at such surfaces and interfaces (either charge accumulation or depletion), as a result of the surface termination, the formation of surface defects, *e.g.*, oxygen vacancies (V_O) or cation interstitials, the presence of unintentional impurities such as hydrogen, H_i) or other chemisorbed species [10, 155, 156]. ZnO-based materials have many applications and exhibit many interesting optical and electronic properties, including a large exciton binding energy ($\approx$ 60 meV) at room temperature, and high transparency in both ultra-violet (UV) and visible spectral ranges [157]. Beside these promising properties (a possibility of lower optical pumping thresholds of exciton-related recombination in many UV optical applications), the effective band gap engineering is prerequisite to design the quantum structures mentioned above for the advancement of highly efficient ZnO-based optoelectronics. To fabricate energy barrier layers in the quantum-structured ZnO-based devices, the wider band gap modulation of ZnO above 3.37 eV has been conducted by substituting Mg mole fraction forming $Zn_{1-x}Mg_xO$ [158]. However, the solubility limit of

Mg in the alloy regime occurs together with a structural transition around $x = 0.35$. This is due to non-identical crystal structure between hexagonal ZnO and cubic MgO. Later, $Be_xZn_{1-x}O$ alloys have been suggested as a competitive candidate by Ryu and a successful band gap tuning of hexagonal $Be_xZn_{1-x}O$ alloys was accomplished in the entire wide-range band gap energy from 3.37 eV for ZnO to 10.6 eV for BeO [159]. A $Be_xZn_{1-x}O$-based multi-quantum-well structure was designed by periodically stacking ZnO wells with $Be_{0.2}Zn_{0.8}O$ barriers, resulting in UV light emission generated from a conventional LED structure [32]. However, non-linear and deconfined emission features from the LED devices were observed with localized energy states. Compositional fluctuations and local segregation of Be were claimed by Be diffusion to the ZnO interfaces in the quantum well device structures [59]. Therefore, understanding the growth mechanisms of $Be_xZn_{1-x}O$ films is key to improving device performance. However, the lack of fundamental understanding of growth characteristics for highly mismatched $Be_xZn_{1-x}O$ alloys has been still remained with respect to the effects of internal strain, thermodynamic instability, and highly-mismatched underlying substrate. In this chapter, the influence of Be concentration on the microstructure of $Be_xZn_{1-x}O$ ternary films (from $x = 0$ to 0.77) are extensively demonstrated. The (0002) X-ray diffraction peak shows a systematic shift from 33.86° to 39.39°, and optical spectroscopy shows a blue-shift of the band gap from 3.24 to beyond 4.62 eV towards the deep UV regime as Be concentration increases. These are indicative of the incorporation of Be into the host ZnO lattice. During the band gap modulation, structural fluctuations (*e.g.* phase separation and compositional fluctuation of Be) in the ternary films are observed along with a significant change in the mean grain size. X-ray photoemission spectroscopy shows higher concentrations of metallic Be states found in the alloy films with the smaller grain size. Correlation between these two observations indicates that Be segregates to near the grain boundaries. A model structure is proposed through simulation, where an increase in grain growth driving force dominates over the Be particle pinning effect. This leads to further coalescence of grains, reactivation of grain growth, and the uniform distribution of Be composition in the $Be_xZn_{1-x}O$ alloy films.

4.2 Experimental details

$Be_xZn_{1-x}O$ alloy ($0 \leq x \leq 0.77$) thin films of thickness in the range of 178 – 198 nm were prepared on $Al_2O_3(0001)$ substrates in an oxygen partial pressure (P_{O_2}) of 2×10^{-3} mbar at a growth temperature of 400 °C using the radio-frequency (RF = 13.56 MHz) magnetron co-sputtering (base pressure: $1.6{\times}10^{-8}$ mbar). During the film deposition, Ar (O_2) gas flow was kept constant at 45 (5) sccm. In order to vary the Be concentration in the films, the RF power to the Be metal target (99.9 % purity, 2-inch diameter, 1/4-inch thickness) was adjusted from 0 to 80 W, while the RF power of the ZnO ceramic target (99.999 % purity, 2-inch diameter, 1/4-inch thickness) was fixed at 100 W. Films were prepared with almost constant thickness by controlling the deposition time under fixed conditions. Prior to film growth, both ZnO and Be targets were sputtered in the vacuum chamber using a RF power of 50 W in 30 min to remove target surface contaminants. The structural and optical properties of the films were evaluated by X-ray diffraction (XRD; $\lambda = 1.5406$ Å) and UV-visible spectroscopy measurements. Tapping mode atomic force microscopy (AFM) was used to observe the surface morphologies of the films. To determine the surface electronic structure and chemical state of the films as a function of Be composition, X-ray photoemission spectroscopy (XPS) was performed in ultra-high vacuum (UHV) using an Omicron SPHERA hemispherical analyser and monochromatic Al K_α source ($h\nu = 1486.6$ eV). Photo-excited electrons from the film surfaces were collected using a take-off angle of 90° (normal to the surface of the films). Surface charging during XPS measurements, resulting from the insulating nature of the samples, was compensated for by using a low energy electron flood gun (Omicron CN10). The binding energy (E_B) scale was calibrated using the C 1s position (284.5 eV) and the overall energy resolution was 0.6 eV. Elemental composition ratios were extracted including the electron mean free path correction and using Scofield cross sections [160]. Peaks were fitted using a Shirley background and Voigt (convolved Lorentzian-Gaussian) functions.

4.3 Results and discussion

4.3.1 Optical and structural properties

The change in the cut-off wavelength of the transmittance spectra for the $Be_xZn_{1-x}O$ alloy films as a function of Be fraction is shown in Figure 4.1a. The spectral range available (220 – 850 nm) was insufficient to measure the cut-off for the films with the highest Be content due to the wider band gap energies ($E_g > \approx$ 6 eV). However, there was clearly a continuous shift of the spectra into the deep UV energy region and a high transparency of over 85 % as the Be concentration increased. Based on these transmittance spectra and excluding reflectivity, the absorption coefficients, α, of the films were evaluated from $T_O = A\exp(-\alpha d)$, where T_O is the transmittance of the film, A is a constant and d is the film thickness. Consequently, by taking a linear extrapolation of the leading edge from the plot of α^2 versus $h\nu$, the optical band gap energies in the limit of the spectral region were determined to range from 3.24±0.01 to 4.62±0.06 eV for Be concentrations up to $x = 0.51$ (see the inset of Fig. 4.1a). Tailing of the absorption edge was found as Be concentration increased. This is commonly associated with a decrease of the crystalline quality of the material [161, 162].

As shown in Fig. 4.1b, changes in the optical band gap energies exhibited a non-linear dependence on the Be composition due to a large bowing effect. Values of the bowing parameters, b, were calculated to be 4.8±0.2, 4.6±0.4, 6.0±0.3, 7.8±0.3 and 9.5±0.2 eV for $x = 0.05$, 0.16, 0.32, 0.41, and 0.51, respectively. The large values, b, can be attributed to the considerable difference in atomic size and large chemical mismatch between Zn^{2+} and Be^{2+}. Moreover, the larger increase of b at higher Be compositions could be associated with additional band repulsion between the O $2p$ and the Zn $3d$ orbitals in the electronic band structure of the Be-rich alloys. The orbital interaction possibly results in an up-shift of valence band and in turn, a large band gap reduction [163, 164]. The lattice strain effect on the redistribution of the density of states in the hexagonal symmetry of largely mismatched films, also requires consideration. Consequently, the optical results confirm that the band

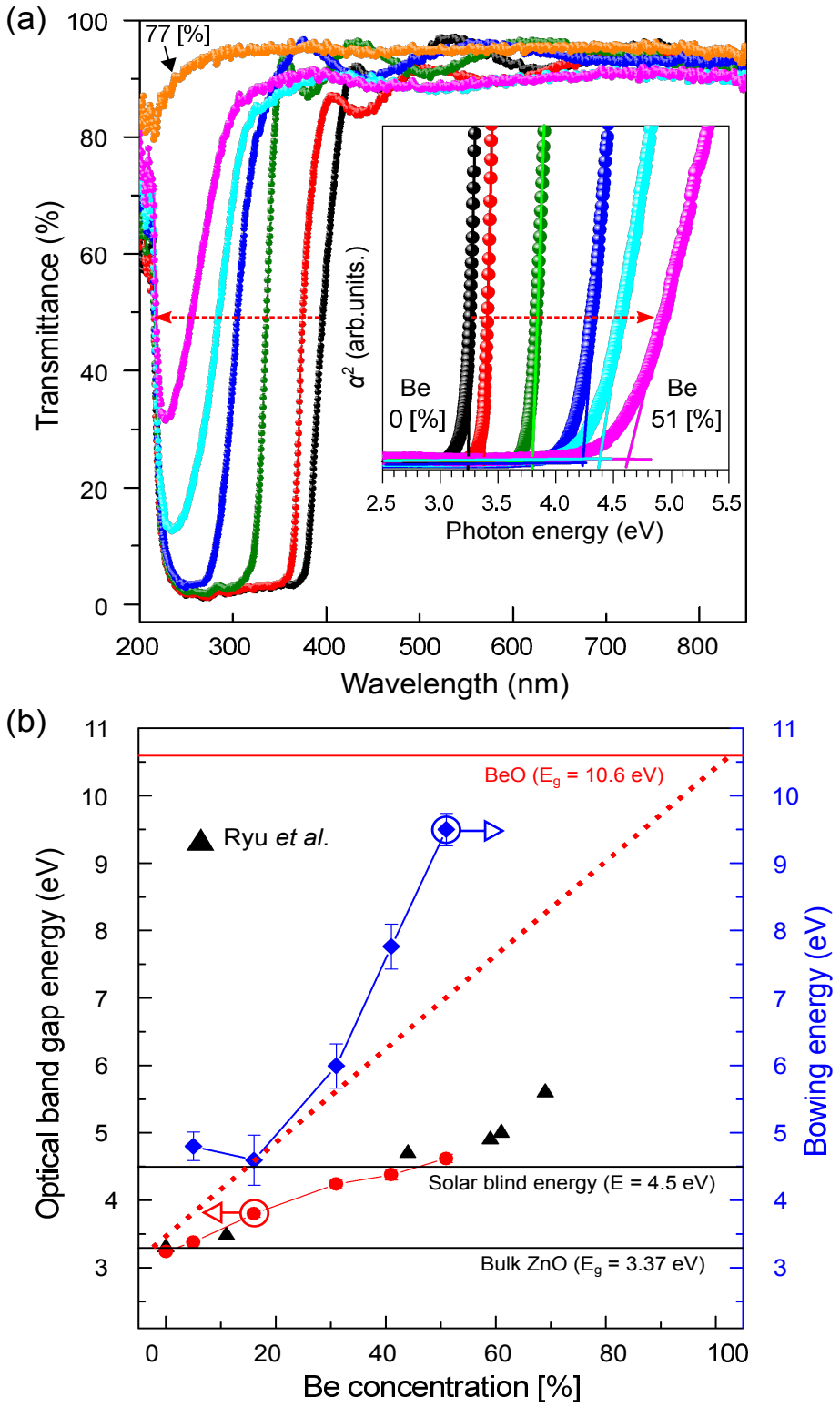

Figure 4.1: (a) Transmittance spectra of the $Be_xZn_{1-x}O$ films with an increase in the Be concentration [%], from $x = 0$ to 0.77, [Inset of (a)] the curve of α^2 vs photon energy ($h\nu$) for the films compositions $x = 0$ to 0.51, and (b) a comparison of band gap energies with the previous report with bowing parameters, b, for the $Be_xZn_{1-x}O$ alloys.

gap of ZnO can be tuned by incorporating Be into the host lattice although some structural deterioration should be expected. However, it is noted that the calculated optical values might be overestimated due to spectral merging that allowed the local distribution of Be to affect the optical spectroscopy measurement.

X-ray diffraction (XRD) patterns of the $Be_xZn_{1-x}O$ thin films grown on $Al_2O_3(0001)$ substrate, taken in the θ–2θ geometry are shown in Fig. 4.2a. All films were shown to be preferentially oriented along the c-plane (0001) of the wurtzite phase. In addition, $(10\bar{1}0)$ and $(10\bar{1}1)$ growth orientations were also observed. There was a significant shift in the (0002) diffraction peak position as the Be concentration increased. This suggests a structural change from the undoped ZnO structure (33.9°) towards a hexagonal BeO-type structure (41.1°). From this shift, a decrease in c-axis lattice parameter was deduced from 5.23 for to 4.80 Å as shown in Fig. 4.2b, confirming the lattice compression required for incorporating Be^{2+} into ZnO. Calculations based on Vegard′s law confirmed the Be fraction in the alloy films as x = 0.05, 0.16, 0.31, 0.41, 0.51, and 0.77 [165]. This revealed that Be atoms were well-substituted into Zn sites and that the c-axis oriented hexagonal structure was thus primarily maintained in all films. Broadening of the (0002) diffracted peak was also observed as the Be composition was gradually increased, suggesting a deterioration in the crystal quality of the film. This is also indicative of a reduced crystallite size with increasing Be content in the alloy films. It is known that adatom diffusion on a surface to island edges can be kinetically restricted by strain concentration near step edges during island growth. Since the strain-induced energy barrier to adatom movement at an island edge is proportional to the lattice mismatch, smaller coherent islands tend to be formed in a higher lattice-mismatched system [166]. Substantial elastic strain energy generated from the lattice mismatch between the $Be_xZn_{1-x}O$ films and the substrate would be further increased with the addition of more Be. This is due to the smaller atomic size of Be and causes smaller crystallites to form as the excess strain is relaxed. Hence, for a large lattice mismatch (more than 18 %) at the $Be_xZn_{1-x}O$ film/substrate interface, it is assumed to initiate three-dimensional (3D) grain growth to minimize the total energy configuration (strain

energy + surface energy). This leads to the formation of smaller crystallites and misaligned (tilted/twisted) lattice domains with random orientations [70, 167]. As a result, growth features with smaller grains were induced by the incorporation of atomically smaller Be into the host and the subsequent increase in lattice mismatch strain. Furthermore, since grain growth in films is driven by a reduction of total energy at grain boundaries, the grain boundary migration during film grain growth could play a crucial role in the formation of crystalline $Be_xZn_{1-x}O$ films. This point will be discussed in more detail later.

In the range from Be concentration, $x = 0.16$ to 0.41, the asymmetrically split (0002) peaks and extra peaks between the $(10\bar{1}0)$ and (0002) orientations are clearly observed (Fig. 4.2a). These two distinct peaks are shifted towards each other as the Be concentration increases and merge to form a single peak at a concentration of around $x = 0.51$. This peak then reduces in intensity and, disappears at the highest Be concentration of $x = 0.77$, where only an hexagonal (0002) peak was observed. Structural fluctuations may be attributed to a non-uniform distribution of Be atoms, as well as a higher level of lattice stress from grain boundaries and the substrate interface during film growth. In previous theoretical studies, phase separation in the $Be_xZn_{1-x}O$ alloy system was also expected due to the large enthalpy of alloy formation arising from the large mismatch between ZnO and BeO [168, 169].

4.3.2 Surface morphology and chemical composition

Topographic AFM images (10×10 μm^2) of the $Be_xZn_{1-x}O$ films grown on *c*-axis oriented Al_2O_3 substrates are shown in Fig. 4.3a. The images indicate that all films exhibited a granular microstructure corresponding to a three-dimensional (3D) columnar growth mode. Grain size varied and were randomly distributed on the film surfaces up to $x = 0.51$. For $x = 0.77$, a smaller grain size became dominant as shown in the 1×1 μm^2 scan of the $Be_{0.77}Zn_{0.23}O$ film (right-bottom image in Fig. 4.3a). The distribution of grain sizes on the film surfaces was consistent with XRD measurements, which indicated a coexistence of different growth orientations and a broadening of the (0002) diffraction peak [167]. The average grain size for the films

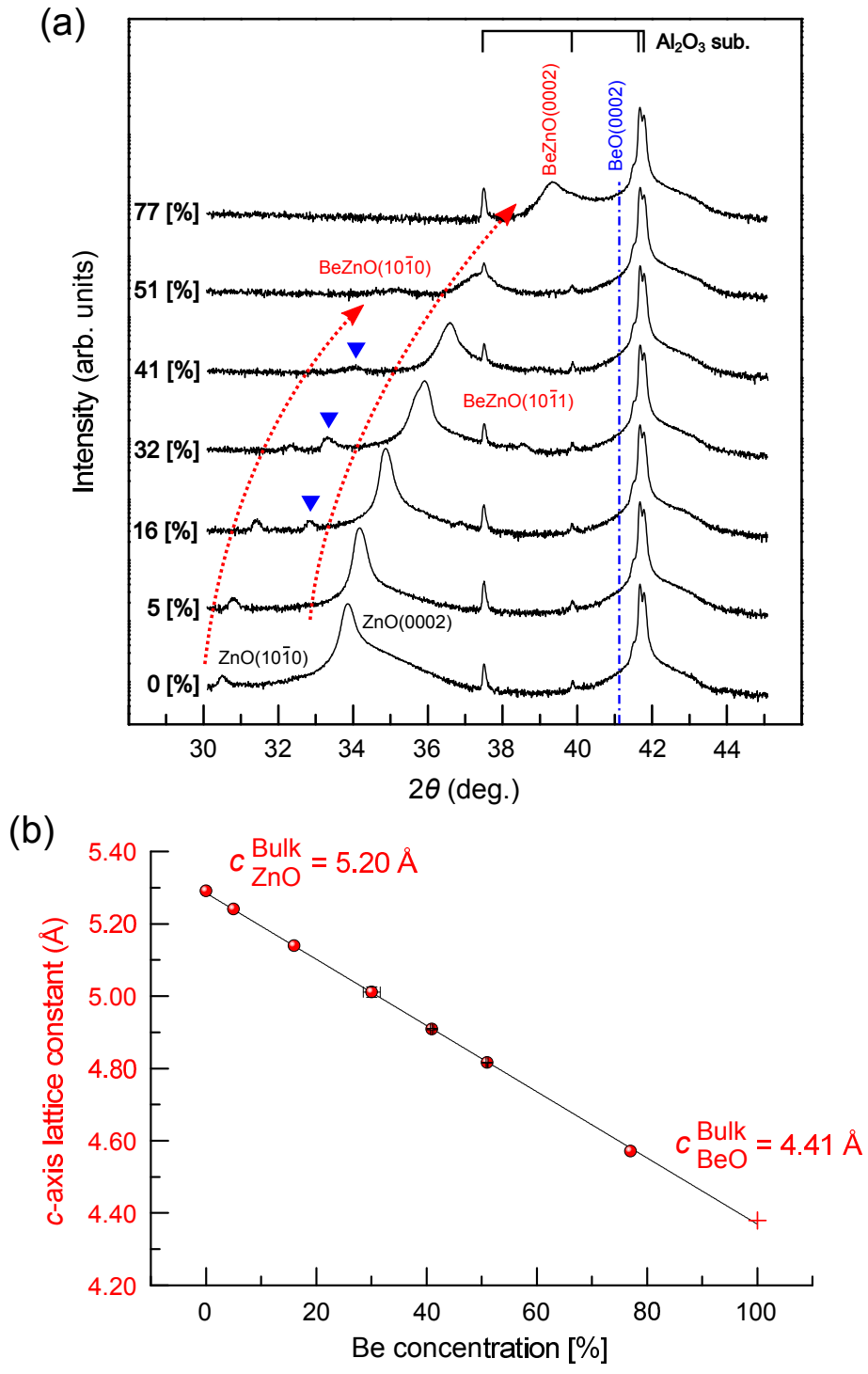

Figure 4.2: (a) XRD θ-2θ scans of the $Be_xZn_{1-x}O$ films as a function of Be concentration (%), and additional peaks appearing between $Be_xZn_{1-x}O(10\bar{1}0)$ and (0002) plane reflections are signified by blue-triangles. (b) c-axis lattice parameters of the films as a function of Be content (%).

were found to decrease from ∼68.6 nm for $x = 0$ to ∼27.8 nm at $x = 0.31$.

An increase of grain size followed at higher values of x to ∼76.0 nm at $x = 0.77$. It should be noted that the average grain size obtained from AFM analysis differed from that obtained from XRD using the Scherrer formula (Particle size, D. This is depicted in Fig. 4.3c [170]. Further insight into this can be obtained by analysis of the AFM phase images (Fig. 4.3b). It was found that the average grain size appeared larger due to a set of fine-grains along grain boundaries combining as Be concentration increased from $x = 0.31$ to 0.77. This is shown by spectral images of the selected grains (A and B) and revealed that the formation of the larger grains was a consequence of fine grain coarsening at the grain boundary junctions. XPS spectra from the Be 1s and Zn 3p core levels for the $Be_xZn_{1-x}O$ films are shown in Fig. 4.4a. A spin-orbit split Zn 3p doublet was observed at approximately 89 eV [171]. The Zn 3p core level peak showed broadening and a shift to the higher E_B with increasing Be concentration. This is attributed to a distribution of Zn ions in different net-charge states in the wurtzite alloy coordination, the presence of a variety of surface species (*e.g.* surface hydroxylation on polar surfaces: Zn-O-H), and the increased of number of Zn ions in defect states [11, 172]. These imply an increased surface area to volume ratio on decreasing the crystallite size, and a non-stoichiometric wurtzite environment as the Be concentration increases. As seen in Fig. 4.4b, the XPS spectrum for the undoped ZnO film showed a broad feature (≈ 100 to ≈ 120 eV) originating from screening effects of photo-excited electrons from surface plasmon excitation and inelastic collision processes (*e.g.* electron-electron and electron-phonon scatterings). This implies that the film surface possessed free-electron carriers due to native defects/unintentional impurities (*e.g.* V_O, Zn_i, and H_i) as is typical in undoped ZnO. This could have also contributed to a surface band bending effect [9, 10, 155]. The relative intensity of the plasmon peak to Zn 3p peak decreases continuously as the Be concentration increases. This reveals both a reduction of free carriers and the deterioration of crystallinity in terms of the number of photo-excited electrons with a relatively long-path distance on the film surfaces. So, the surface plasmon effect in Be 1s core-level on the $Be_xZn_{1-x}O$ film surfaces

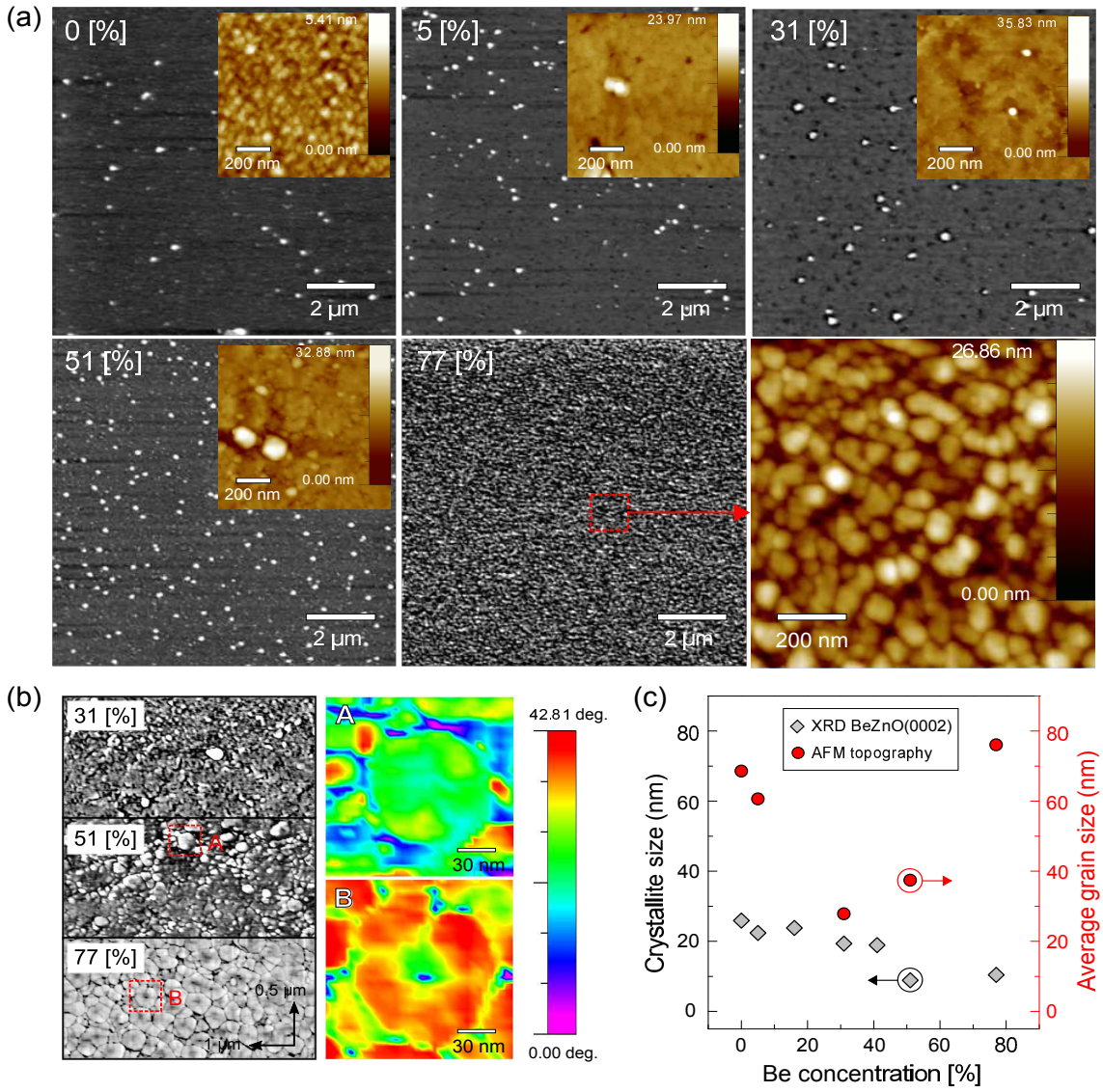

Figure 4.3: (a) AFM topography (10×10 μm^2) images of the $Be_xZn_{1-x}O$ films for $x = 0$, 0.05, 0.31, 0.51, and 0.77, and a (1×1 μm^2) image of the $Be_{0.77}Zn_{0.23}O$ film. All of the insets are AFM topography (1×1 μm^2) images. (b) Phase images (1×0.5 μm^2) of the selected $Be_xZn_{1-x}O$ films composed by Be concentration (%), $x = 0.31$, 0.51, and 0.77, magnified spectrum images (right-top and -bottom) for selected areas -A and -B ($x = 0.51$ and 0.77), respectively. (c) The profile of crystallite size (based on FWHM values of the (0002) XRD diffraction peaks for the films) and average grain sizes (AFM) as a function of Be concentration (%).

Table 4.1: Parameters (E_B, Lorentzian percentage of the Voigt line shape (L), and full width at half maximum (FWHM)) of Be 1s core level fitting, quantification values (%) of Be-O bonding (Be_O) and metallic Be bonding (Be_M), [$Be_{O/M}$/(Be+Zn+O)], and the ratio of Be_O/(Zn+Be_O) for the $Be_xZn_{1-x}O$ alloy films as a function of Be concentration obtained from the XPS spectra (Al K_α $h\nu$ = 1486.6 eV). The quantification analysis of atomic compositions (O, Zn, and Be) for all films was determined from the areas of the O 1s, Zn 3s, and Be 1s.

Sample	Bonding	E_B (eV)	L (%)	FWHM (eV)	Percentage (%)	Be_O/(Zn+Be_O) (%)
Be 5 %	Be_O	114.2	8	2.2	4.3	10
	Be_M	111.2	8	3.2	1.8	
Be 31 %	Be_O	114.4	8	2.3	17.8	40
	Be_M	111.2	8	3.7	11.2	
Be 51 %	Be_O	114.2	8	2.1	31.8	60
	Be_M	111.0	8	3.7	4.5	
Be 77 %	Be_O	114.3	8	1.8	44.8	80
	Be_M	111.1	8	3.0	1.6	

at high Be content was negligible, allowing the Be 1s core level to be fitted by two components at E_Bs at 111.1±0.1 and 114.2±0.1 eV, respectively (denoted in Fig. 4.4b). Those two distinct components were associated with metallic Be (Be_M) and Be-O bond (Be_O) states on the surface [173,174]. The BeO peak intensity increased continuously, again suggesting that Be was well-incorporated into the host lattice. This is consistent with the above XRD and optical spectroscopy measurements. The highest ratio of Be_M to Be_O was observed at a Be concentration of $x = 0.31$. Then, a continuous decrease of the ratio was observed with further addition of Be up to $x = 0.77$. All fitting parameters and the relative percentages of BeM and BeO for the Be 1s core level spectra found by evaluating the O 1s, Zn 3s, and Be 1s core-levels for all $Be_xZn_{1-x}O$ films are presented in Table 4.1. The surface BeO composition relative to the Zn composition [BeO/(Zn+BeO)] was higher compared to the film bulk. One possible explanation is that this is caused by a surface segregation process through the removal of surface Zn and/or O atoms to minimize the surface free energy [11, 48, 175].

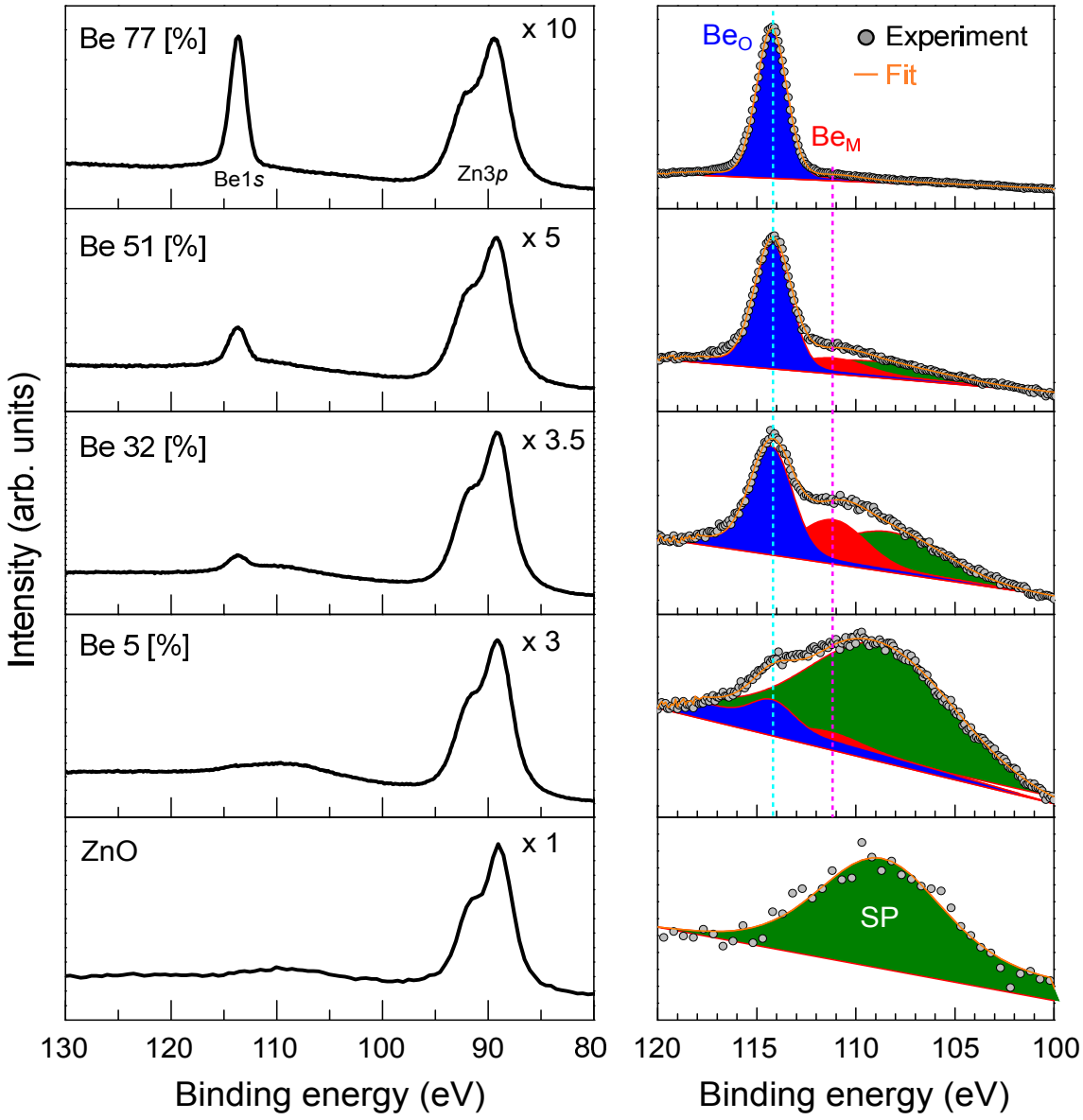

Figure 4.4: (a) Be 1s and Zn 3p XPS spectra of the $Be_xZn_{1-x}O$ alloys as Be fraction, x, increases. (b) Experimental Be 1s core level spectra for all films are fitted using Be-O bonding (Be_O), metallic Be (Be_M), and surface plasmon (SP) components using a Shirley background and Voigt line shapes (solid lines).

4.3.3 Particle pinning model and discussion

A possible mechanism for this type of grain growth of crystalline $Be_xZn_{1-x}O$ on Al_2O_3 substrates can be described by a model first suggested by Zener [176]. The model describes the formation of secondary phase particles, in this case metallic Be, at grain boundaries, which pin the boundaries and restrict the grain wall motion. This grain boundary drag caused by Be particles at grain boundaries would lead to the formation of smaller grains during growth as illustrated in Fig. 4.5a. It should be noted that the original Zener′s model [176] was used to describe a three dimensional array of grains and, therefore, the model below has been modified to account for the planar nature of film growth in this case. It was found that the Be concentration in the alloy films significantly affected grain structure and size. It is common in grain growth that the grain size depends on the migration of grain boundaries arising from the difference in grain curvatures (pressure; P_{g}), which are due to the chemical potential difference, $\Delta\mu$, described by [68, 70, 177]

$$\Delta\mu \approx \frac{2\gamma}{D} = P_{\mathrm{g}}, \tag{4.1}$$

where γ and D are interfacial energy at the boundary and mean grain size, respectively. Here, the matrix grain boundary mobility is interrupted by pinning of solute particles occupying areas of the grain boundary [176]. Pinning particles at grain boundaries reduce the Gibbs free energy, restricting the movement of the matrix grain boundaries during growth.

A pinning particle of circumference, $2\pi r\cos\theta$, is placed at the grain boundary, as illustrated in Fig. 4.5a, where r is the radius of particle [68]. The maximum pinning pressure, P_{p}, of the particles can be expressed as

$$P_{\mathrm{p}} = \frac{3f}{2\pi r^2} \cdot 2\pi r\cos\theta\gamma\sin\theta \approx \frac{3f\gamma}{2r}, \tag{4.2}$$

where f is the volume fraction of the particles in the unit area of a random plane. The first term is the mean number of the particles intersecting a unit area of a random plane and the second term is the maximum particle pinning force with a drag angle of $\theta = 45^\circ$ at the grain boundary. In the above equations, the two driving

pressures (P_g and P_p) counterbalance each other, and the pinned grain size, D_{max}, is approximately determined by

$$D_{max} = \frac{4r}{3f}. \tag{4.3}$$

Metallic Be particles favour lower energy sites at grain boundaries rather than in the matrix of the grain, subsequently inhibiting the grain boundary mobility. This results in a reduction of grain size as shown in Fig. 4.5b. In a similar case, Ingham [178] reported that metallic Al atoms at grain boundaries restricted ZnO grain growth in the formation of spinel crystallites as $ZnAl_2O_4$. In this work, AFM and XPS showed that the mean grain size was inversely proportional to the amount of metallic Be on the film surface. Furthermore, it can be assumed that by increasing the Be content in the films, the volume fraction of Be particles at grain boundaries is increased. There was, however, an inconsistency in crystallite size and mean grain size measured by XRD and AFM as seen in Fig. 4.3c. This discrepancy could be reconciled by considering the change in the Be pinning pressure at grain boundaries with an increase in Be pinning particle size. However, this would drive an Ostwald ripening of the Be particles at grain boundary interfaces, resulting in a coarsening of the particles and in turn decreasing the pinning pressure, P_p [179].

When the driving pressure of grain growth is sufficient to overcome pinning pressure of Be particles, movement of the grain boundaries occurs to allow coalescence. Interestingly, it appeared that a two-step coalescence process occurs at a Be concentration of $x = 0.77$. Initially, fine-sized grains coarsened, concave inwards and form an eight-junction grain boundary that minimized interface energy between the grains. A set of these coarsened fine-grains then combines in a triple-junction boundary favouring a distinctly shaped grain growth to produce an abnormal grain growth mode. At the same time, Be particles could encounter the lattice matrix grains due to a mass transport driven by the Be concentration gradient. Eventually, the Be concentration would become uniformly distributed across the fine grains via the grain boundary junctions leading to a reduction in metallic Be states, as shown by XPS measurements.

The approximate sizes of the Be pinning particles depends on the volume

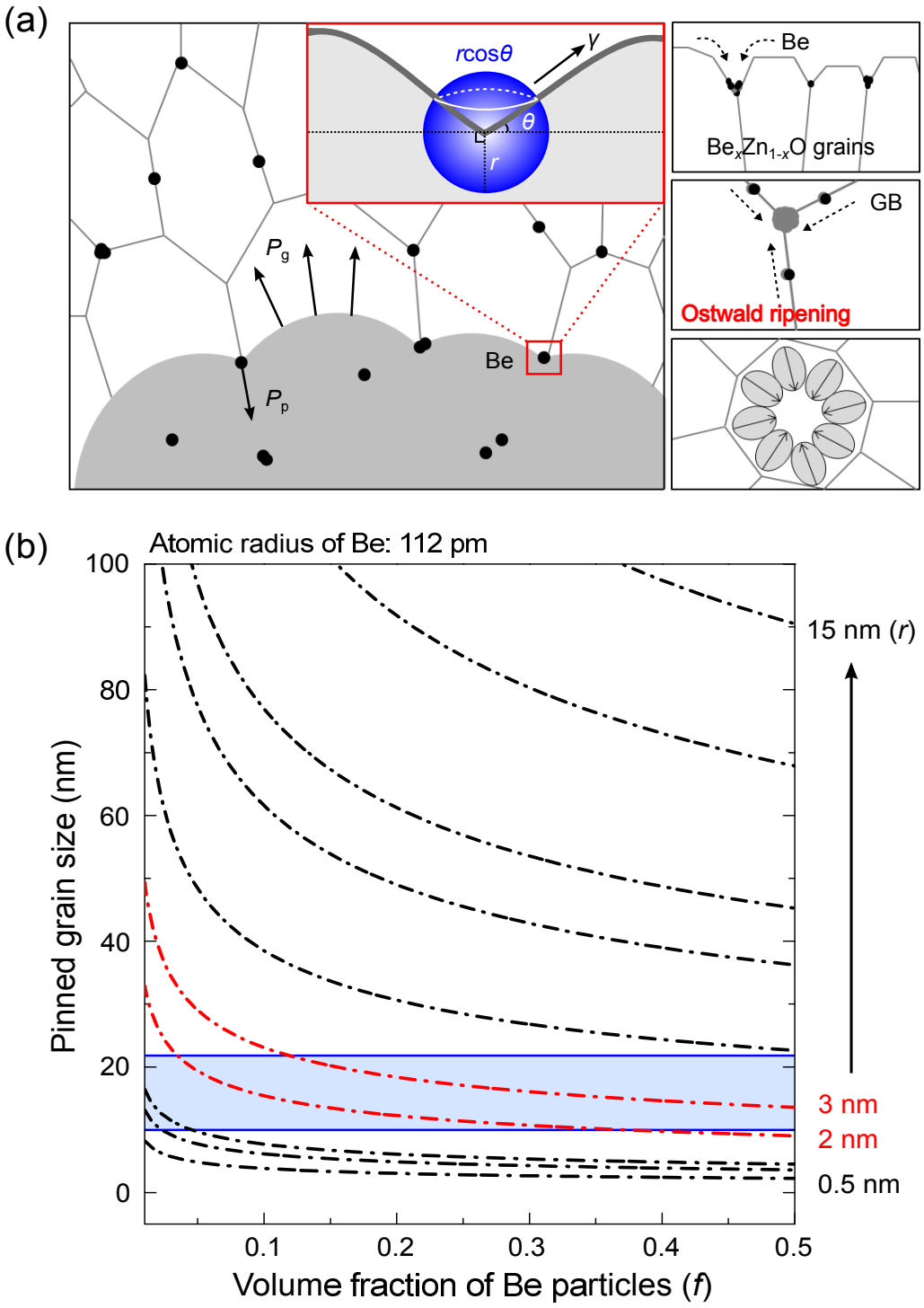

Figure 4.5: (a) Schematic for the grain growth model for crystalline $Be_xZn_{1-x}O$ pinned by Be particles, [70] and (b) pinned grain size D_p as a function of volume fraction f of Be pining particles, for values of the Be particle radius, r, from 0.5 to 15 nm. The shaded region between the two solid-blue lines represents the pinned grain size range with Be particle size of 2–3 nm, which is consistent with the experimental results.

fraction of the particles and the pinned grain size as depicted in Fig. 4.5b. Zener first proposed such a model with a random distribution of second phase particles at random boundary intersections, *i.e.*, the volume fraction, f^1, of the particles is represented by a random dispersion in both the planar (2D) and volume (3D) cases [176]. In the model proposed here, since it is most likely that Be pinning particles are located at grain boundaries, rather than in the bulk of the $Be_xZn_{1-x}O$ matrix, the model has been modified to require a non-random distribution of Be particles in a 3D system. Hillert [180] also suggested an applicable pinning model in which a 3D volume fraction of particles lead to modified parameters, as given by

$$\tilde{D}_{\max} = \frac{3.6r}{3f^{0.33}}, \tag{4.4}$$

where $\tilde{D}_{\max}$ is the pinned maximum grain size in a 3D system. Using this modification, the simulated plots (denoted by the red dot-dashed line in Fig. 4.5b) that showed pinning of grain sizes for Be particle sizes of 2 – 3 nm, are in good agreement with the AFM data. Note that in this approximation several plausible interactions (*e.g.* Be particle drag, Be solute precipitation, and re-dissolution) between grain boundaries and the Be solute have been considered.

Another aspect of this study was the possible coupling between grain size being restricted by Be particles at grain boundaries and the resulting surface variation on the films. This could have played a significant role in the compositional fluctuations of Be and, hence, the grain boundary structures. As the $Be_xZn_{1-x}O$ grain matrix encounters by Be particles, the surface curvature of the matrix grain would give rise to a local distribution of Be. In addition, an increased grain boundary area would promote an increase in the effective surface area (higher surface-to-volume ratio), encouraging surface chemisorption such as oxygen. This would lead to the formation of charge trapping/scattering centres, and thus potential barriers for charge transport [181, 182]. Therefore, the variation in the surface properties during grain growth was a matter of concern as it could cause substantial non-uniformity in the film properties and make application of $Be_xZn_{1-x}O$ in quantum structures or, indeed, other heterostructures problematic.

4.4 Conclusion

In summary, crystalline $Be_xZn_{1-x}O$ films ($0 \leq x \leq 0.77$) have been grown on *c*-axis Al_2O_3 substrates by a RF co-sputtering method. A band gap modulation in the $Be_xZn_{1-x}O$ films has clearly been confirmed while maintaining a hexagonal crystal structure. A continuous decrease in the *c*-parameter of the hexagonal structure was observed from 5.23 Å to 4.80 Å, and an optical band gap shift towards the deep UV region (from 3.24 eV to over 4.62 eV) was also observed. Variations in the grain growth of $Be_xZn_{1-x}O$ films on highly-mismatched substrates were observed and showed that the Be concentration in the films affected the distribution of grains in terms of orientation, size, and composition. In order to interpret the variation of grain growth kinetics with changing Be concentration, a modified Zener model has been developed that describes metallic Be particles driving a pinning effect on grain boundary motion. It was suggested that grain boundary drag as a result of Be pinning particles, induced local Be compositional fluctuations leading to smaller grain sizes. Conversely, coalescence of Be pinning particles at grain boundaries, along with increased Be volume fraction, could give rise to a re-enhancement of the grain growth driving force. This could lead to the formation of a coarse-grained array through the development of specific grain boundary junction-types. The grain boundary junctions also act as a channel for uniform distribution of Be within the crystalline $Be_xZn_{1-x}O$ ternary alloy films.

Chapter 5

Growth and thermal instability of crystalline $Be_xZn_{1-x}O$ alloy films

5.1 Introduction

An understanding of the phase stability of $Be_xZn_{1-x}O$ alloys is key to realizing effective band gap engineering in this material and for potential optoelectronic applications as presented in Chapter 4 [183]. To achieve homogeneous incorporation of Be in the host ZnO, several important factors should be considered: (*i*) an internal strain effect from different bond lengths between Zn-O (1.99 Å) and Be-O (1.65 Å) and a lattice mismatch of almost 20 %; (*ii*) a large difference in thermal expansion coefficients [2.49 and 3.98×10^{-6} K^{-1} (5.35 and 7.18×10^{-6} K^{-1}) at 300 K and 700 K for *c*-axis ZnO (*c*-axis BeO), respectively]; and (*iii*) substantial strain from the lattice mismatch between the alloy film and underlying substrate, *e.g.*, Al_2O_3 ≈18 %) and Si (111) ≈15 %) [184,185]. These effects can readily induce phase separation and compositional splitting in the ternary alloy system. Hence, in order to obtain a homogeneous and stable alloy phase, it is essential to study the synthesis of the $Be_xZn_{1-x}O$ alloys under various growth conditions. A few such studies have already been reported for the growth and thermodynamic properties of the alloy films in highly-mismatched system [186–188].

In this chapter, the effect of growth temperature on the synthesis of $Be_xZn_{1-x}O$ thin films grown on $Al_2O_3(0001)$ substrates has been demonstrated to interpret the thermodynamic characteristics of this highly-mismatched system. A single-phase hexagonal $Be_xZn_{1-x}O$ film was obtained with the highest Be incorporation, $x = 0.25$, at $T_g = 400$ °C. For higher growth temperatures, $T_g \geq 600$ °C, phase segregation and compositional fluctuation were observed in the films as presented by X-ray diffraction (XRD) peak splitting and broad multi-photoluminescence emis-

sion bands. The structural fluctuations following high-temperature synthesis of the $Be_xZn_{1-x}O$ alloys were addressed by considering Be concentration variations under strain relaxation and thermally-driven Be displacement during the alloy film growth.

5.2 Experimental details

The BeZnO alloy films were all grown on $Al_2O_3(0001)$ substrates by radio-frequency (RF = 13.56 MHz) magnetron co-sputtering. Oxygen partial pressure (P_{O2}) was 2×10^{-3} mbar and growth temperatures were in the range of T_g = 200–800 °C. The sputtering of the ZnO and Be targets was carried out in a gas mixture of Ar 45 sccm:O_2 5 sccm. A low-temperature (T = 200 °C) ZnO seed layer (less than 5 nm; this thickness was estimated by a growth rate of the ZnO film ($\approx$ 1 nm/min) at the given film growth condition (RF power = 50 W and deposition time = 5 min) was employed prior to growth of the main alloy film). The main film growth was performed with the RF power of 100 W for the ZnO target and the RF power of 40 W for the Be target. In order to prepare the alloy films with similar thicknesses in the range of $\approx$ 210 – 280 nm. Film thicknesses were determined by cross-sectional scanning electron microscopy (SEM) as shown in Fig. 5.1a. Synchrotron radiation X-ray scattering measurements (λ = 1.069 Å) were performed at beamline 5A of the Pohang Light Source II(PLS-II) in the Republic of Korea to investigate the structural variation of the alloy films grown at different T_g. The variation in the (0002) Bragg reflections of the BeZnO alloy films was evaluated using $Q_z = 4\pi\sin\theta/\lambda$, where q_z and θ are the peak position in the reciprocal space and incident photon angle, respectively. An undoped ZnO film prepared at T_g = 800 °C was measured in the same experimental condition as a reference sample. HRTEM was carried out using a Tecnai G^2 F30 S-Twin (FEI) with an acceleration voltage of 300 kV to characterize the microstructure of the BeZnO alloy film grown at T_g = 400 °C. Photoluminescence (PL) spectra of the alloy films were measured using a He-Cd laser (λ = 325 nm) at 5 K.

5.3 Results and discussion

5.3.1 Synchrotron X-ray diffraction

The synchrotron X-ray θ-2θ diffraction profile of the $Be_xZn_{1-x}O$ films grown at different growth temperatures from 200 to 800 °C is shown in Figure 5.1b. The (0002) peak position of the undoped ZnO thin film, grown at T_g = 800 °C, was at q_z = 2.40 $Å^{-1}$. For the $Be_xZn_{1-x}O$ film grown at T_g = 200 °C, three distinct diffraction peaks were found at q_z = 2.26, 2.46, and 2.66 $Å^{-1}$, respectively, which correspond to the $(10\bar{1}0)$, (0002), and $(10\bar{1}1)$ plane reflections. However, the $Be_xZn_{1-x}O$ film grown at T_g = 400 °C indicated a single (0002) peak with the largest shift to q_z = 2.49 $Å^{-1}$ with respect to that of the ZnO(0002) peak. This results from a single wurtzite-phase and the highest Be composition in the alloy film. For $T_g \geq$ 600 °C, significant phase separation occurred as the (0002) peak splits into Zn-rich and Be-rich phases. Additional broadening of the (0002) peak was also observed in the alloy films.

In order to further examine the structural variation of the alloy films as a function of T_g, ω-rocking curves of the BeZnO (0002) Bragg reflection were measured as shown in Fig. 5.1c. A non-smooth rocking curve with broken lines and a large full-width at half maximum (FWHM) were seen in the $Be_xZn_{1-x}O$ film at T_g = 200 °C, implying incoherent nucleation and misaligned crystallites on the underlying substrate. This is usually caused by insufficient energy for atomic movement during low-temperature film growth [27]. By contrast, a symmetric rocking curve was found with the smallest FWHM of 4.66° for the alloy film grown at T_g = 400°C (Fig. 5.1c). However, for $T_g \geq$ 600 °C, a superposition of both sharp and broad components in the rocking curves were observed with an increase in FWHM to 11.16°. In the previous studies [26, 27], it was reported that such a narrow component generally reflects a two-dimensional (2D) coherent layer well-aligned with the underlying substrate in the early stages of growth. On the other hand, the broad component represents the mosaicity of the film with misaligned grains (tilted or twisted) with respect to the substrate normal. Since a large lattice mismatch at

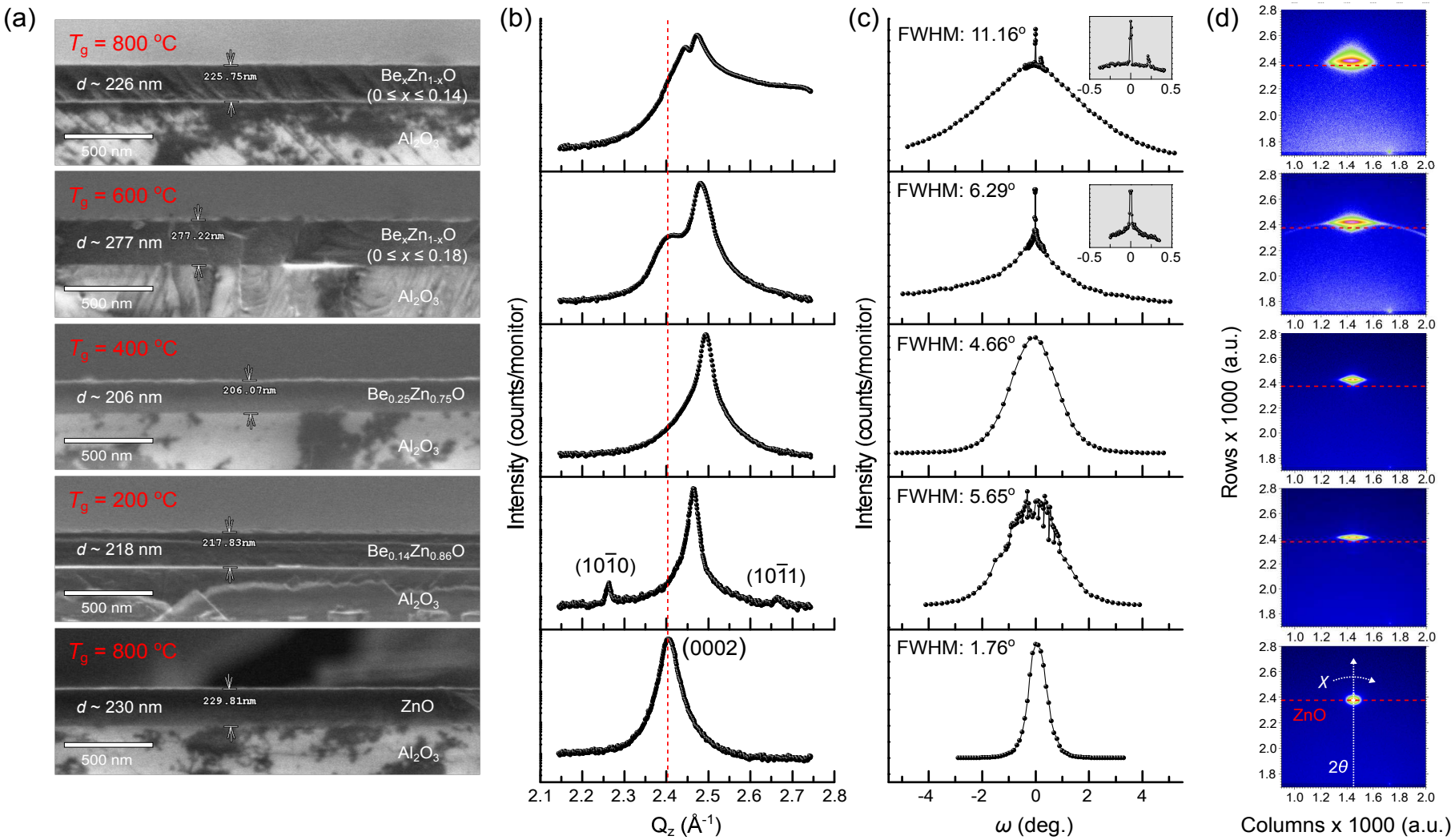

Figure 5.1: (a) Cross-sectional SEM images for the undoped ZnO (T_g = 800 °C) and $Be_xZn_{1-x}O$ films (T_g = 200, 400, 600, and 800 °C) with thicknesses of ≈ 206–277 nm, grown on Al_2O_3 substrates. (b) Synchrotron radiation XRD θ-2θ patterns of $Be_xZn_{1-x}O$ (0002) compared to that of undoped ZnO (0002) by the vertical red-dashed line, (c) the ω-rocking curves of $Be_xZn_{1-x}O$ (0002) Bragg reflection, and (d) two-dimensional (2D) X-ray scattering images of the ZnO film grown at T_g = 800 °C and the alloy films grown at different T_g (200–800 °C). The horizontal red-dashed lines in (d) indicate the 2θ position of the undoped ZnO film in the 2D X-ray reflection area.

the $Be_xZn_{1-x}O/Al_2O_3$ interface occurs, it is expected that the formation of a three-dimensional (3D) columnar structure of the films is favourable during the growth to minimize lattice strain. The narrow component could be associated with the partial distribution of well-aligned *c*-axis alloy domains with the substrate normal.

As can be seen in the inset of Fig. 5.1c, multiple narrow components in the rocking curve were observed at $T_g \geq 600$ °C. This is suggestive of the partial distribution of *c*-axis alloy domains with multiple in-plane alignments as well as different Be compositions. Furthermore, if the narrow component originates from the low temperature ZnO seed layer in a two-step growth mode (2D-3D transition) [27], all of the diffraction peaks should involve ZnO-related diffraction, while these peaks were not observed in films grown at $T_g \leq 400$ °C. Hence, the sharp components are believed to be due to well-aligned *c*-axis alloy domains in the alloy films. Meanwhile, the broad component in the rocking curve becomes wider as T_g increased to 800 °C. This results from further mosaic spreading and means that the film crystallinity deteriorated through the temperature-driven relaxation process. Therefore, thermodynamics plays a crucial role in the mobility of Be and strain relaxation. This initiates both phase separation and compositional fluctuation in the synthesis of $Be_xZn_{1-x}O$ alloy on a highly-mismatched substrate.

Two-dimensional XRD (2D-XRD) images of the $Be_xZn_{1-x}O$ films as a function of T_g are illustrated in Fig. 5.1d. The 2D-XRD image of the undoped ZnO film shows a focused spot, indicating a uniform in-plane lattice arrangement and isotropic crystallinity. Diffraction rings were observed for the $Be_xZn_{1-x}O$ films grown at $T_g = 200$ and 600 °C. This is due to a random distribution of misaligned in-plane lattices and low crystal quality for the alloy films. For $T_g \geq 600$ °C, the 2D x-ray reflection area was remarkably spread to include the undoped ZnO-related area (denoted by the horizontal red-dash lines). This is indicative of phase separation to Be-depleted and Be-rich phases, and further distribution of misaligned lattice planes along the out-of-plane (2θ) and in-plane (χ) directions, causing the compositional inhomogeneity and structural deterioration of the alloy films. As a result, the most focused 2D spot was found at $T_g = 400$ °C, corroborating the single crystalline

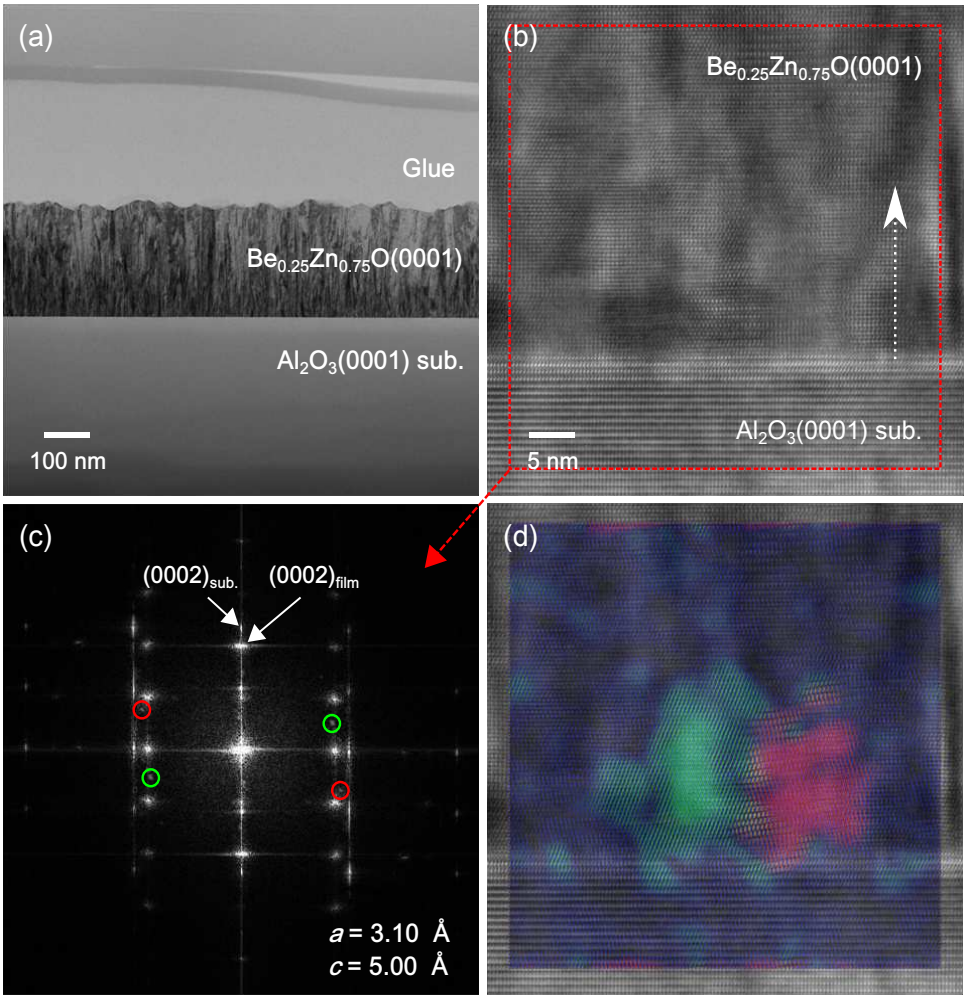

Figure 5.2: (a) Cross-sectional TEM image of the $Be_{0.25}Zn_{0.75}O$ film grown on Al_2O_3 (0001) substrate at T_g = 400 °C. (b) HRTEM image along the $[11\bar{2}0]$ zone axis of the wurtzite alloy film and (c) FFT image (corresponding to the area inside the red-dash square) of the interface region between the alloy film and substrate. (d) A superposition of the HRTEM with the masked red and blue areas corresponding to the extra-spots (denoted by red-and blue-opened circles) in the FFT.

nature with the most uniform Be composition in the alloy film.

5.3.2 Transmission electron microscopy

Transmission electron microscopy (TEM) was performed to investigate the microstructural properties of the $Be_xZn_{1-x}O$ film grown on Al_2O_3 (0001) substrate at T_g = 400 °C. The cross-sectional TEM image of the alloy film showed a 3D columnar structure with a number of misfit dislocations at the heterointerface as illustrated in Fig. 5.2a. It is known that a columnar structure typically arises from

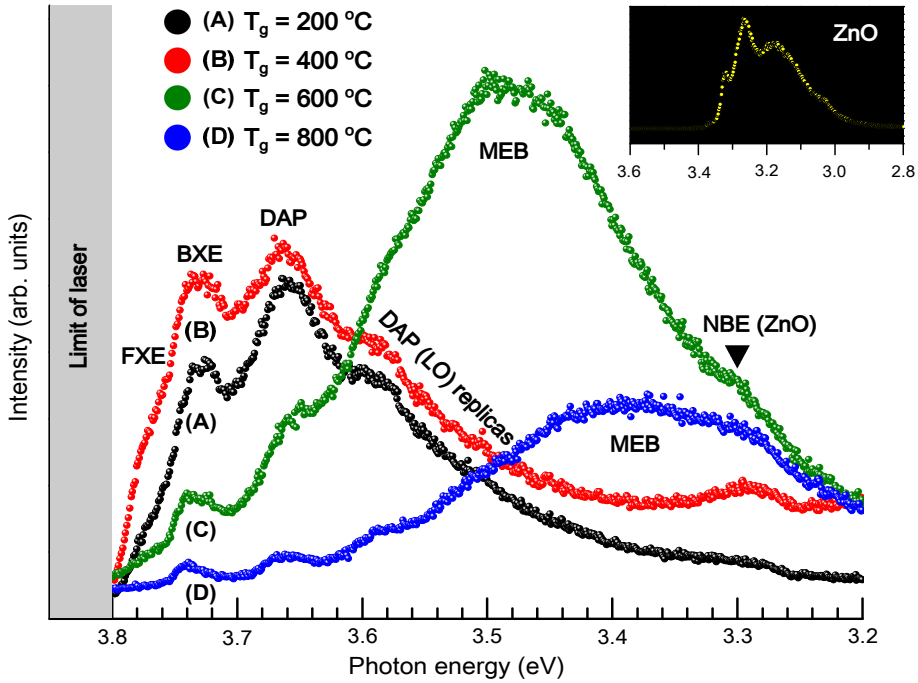

Figure 5.3: Photoluminescence spectra of the $Be_xZn_{1-x}O$ films grown at different temperatures (T_g: (A) 200 °C, (B) 400 °C, (C) 600 °C, and (D) 800 °C). The inset shows the photoluminescence spectrum of the ZnO film (T_g = 800 °C). All measurements were performed at T = 5 K.

the nucleation and coalescence of islands accompanied by lattice strain during the growth process [189, 190]. Figures 5.2b and c show the cross-sectional HRTEM of the wurtzite $Be_xZn_{1-x}O$ along the $[11\bar{2}0]$ direction and corresponding Fast Fourier transform (FFT) image for the red-dash square in the HRTEM image. The digital diffraction patterns, obtained from the FFT, displayed typical diffraction patterns of ZnO and Al_2O_3 for the $<11\bar{2}0>$ and $<10\bar{1}0>$ zone axes, respectively. This reveals that the prime domains of the alloy film are well-aligned along the substrate with a typical epitaxial relationship of $[0001]Be_xZn_{1-x}O \| [0001]Al_2O_3$ and $[10\bar{1}0]Be_xZn_{1-x}O \| [11\bar{2}0]Al_2O_3$, consistent with our previous study [101].

5.3.3 Photoluminescence

Photoluminescence (PL) spectra of the $Be_xZn_{1-x}O$ films grown at different temperature (T_g) are shown in Fig. 5.3. All of the spectra indicate excitonic emission features at T = 5 K. The band emission energy region of the alloy films is blue-shifted compared to that of undoped ZnO which is normally in the range of around

3.2 – 3.4 eV [42]. This is due to the incorporation of Be into the ZnO, which results in the widening of the band gap. No specific origin of each exciton-related recombination centre in BeZnO alloys has been yet determined, but is due to the change in the electronic band structure and the following ionized energy levels related to defects, *e.g.* Zn_i and hydrogen impurities [191,192]. The PL spectra were subdivided into distinct regions: (*i*) the free-exciton emission (FXE), 3.795–3.754 eV; (*ii*) the different bound exciton emissions (BXE) containing many types of donor/acceptor-bound excitons and the correlated donor-acceptor pairs (DAP), 3.754–3.615 eV; and (*iii*) the DAP longitudinal optical (LO)-phonon replicas by an energy separation of $\approx$ 75 meV with respect to the DAP energy, 3.615–3.488 eV [42, 193–195]. In addition, an emission band at a photon energy of around 3.3 eV was observed in all films, which is close to the energy region of the near-band-edge emission (NBE) for undoped ZnO. The alloy films grown at relatively lower temperature ($T_g \leq 400$ °C) showed distinct band-edge emission lines. The strongest excitonic emission bands with the highest energy $\approx$ 3.76 eV (FXE) was seen in the $Be_{0.25}Zn_{0.75}O$ film at $T_g = 400$ °C. This is consistent with previous results, indicating a high crystallinity of the alloy films grown at this temperature. In contrast, for the high-temperature ($T_g \geq 600$ °C)-grown films, additional large broad emission bands were found near the NBE emission bands of the BeZnO films. Broad emission bands attributed to compositional fluctuation under strain relaxation have been reported in other ternary systems, e.g. $In_xGa_{1-x}N$ and $Mg_xZn_{1-x}O$ [196, 197].

In the above synchrotron XRD measurements, randomly-distributed intermixing alloy phases separated into mainly Zn-rich and Be-rich alloy phases was also observed in the high-temperature-grown alloy films. Hence, the multi-emission band (MEB) shown in Fig. 5.3 is due to the presence of localized energy states originating from a broad distribution of the local composition of Be in the alloy films. The intensity of undoped ZnO-related emission for the ternary films grown at $T_g \geq 600$ °C increased compared to the alloy films grown at low T_g, which is consistent with the XRD results. Therefore, the PL results shown in Fig. 5.3 provide evidence for the compositional fluctuation/splitting of Be in the relatively high-temperature-grown

$Be_xZn_{1-x}O$ films.

5.3.4 Discussion

These experimental observations clearly indicate that high-temperature growth of the $Be_xZn_{1-x}O$ films on a highly-mismatched substrate causes: (*i*) Be compositional fluctuation; (*ii*) phase separation; and (*iii*) increased film mosaicity. These are all associated with the atomic movement of Be and strain relaxation at different T_g. It is worth noting the different types of strain induced by the different lattice mismatch of ZnO/BeO and between the alloy film and underlying substrate. As a result, during the growth, it is expected that the interface region has more elastic strain energy than the upper layers of the film. With such an elastic strain distribution near the interface, Be atoms tend to move up into the more relaxed regions by a compositional pulling effect [198]. Subsequently, less Be composition can be present in the interface region, giving rise to the formation of an undoped ZnO-like interface. As T_g increases, this relaxation process is promoted by providing more energy for Be movement. As a result, the Be composition in the film is divided roughly into Be-depleted and Be-rich regions in the $Be_xZn_{1-x}O$ alloy films grown at $T_g \geq 600$ °C. Further relaxation with higher T_g can lead to more mosaic spread in the alloy films. In addition, thermally-driven Be atoms moving to more relaxed areas are randomly dissociated from the alloy lattices. This causes increasing structural deterioration in the alloy film. Based on further investigation presented in Chapters 6 and 7, it was found that the dissociation/diffusion of Be in $Be_xZn_{1-x}O$ alloy films is induced by thermal annealing of over $T = 600$ °C [101]. Klingshirn *et al.* [58, 59] predicted the diffusion of Be and the resulting segregation in local areas of $Be_xZn_{1-x}O$/ZnO-based QW structures. Hence, we suggest that the compositional inhomogeneity and phase separation of the $Be_xZn_{1-x}O$ alloys originate by the coupling of strain relaxation and displacement of Be during the high-temperature synthesis.

5.4 Conclusion

In summary, the influence of the growth temperature on the formation of crystalline $Be_xZn_{1-x}O$ films grown on c-Al_2O_3 substrates has been investigated using synchrotron XRD, TEM, and PL measurements. The XRD and HRTEM results show that a single-phase $Be_xZn_{1-x}O$ alloy film with the highest Be composition, $x = 0.25$, was obtained at $T_g = 400$ °C. For $T_g \geq 600$ °C, phase separation into Zn-rich and a Be-rich phases were observed together with compositional inhomogeneity of Be in the alloy films. This corresponds to the XRD BeZnO(0002) peak splitting and broad PL emission bands. These results are attributed to a compositional pulling or gradient effect and wider distribution of mosaic structure in the high-temperature-grown films. The structural fluctuation is caused by strain relaxation in conjunction with thermal displacement of Be during the high-temperature growth of the $Be_xZn_{1-x}O$ alloy films on the highly-mismatched substrate.

Chapter 6

Formation of a Degenerate Interface in Highly-Mismatched BZO

6.1 Introduction

Wide band gap ZnO-based materials have many versatile properties such as large exciton binding energy (60 meV), unintentional n-type conductivity, high transparency in the near ultra-violet and visible ranges, and the high natural abundance) [4–8, 33, 58, 199]. These materials also provide opportunities for the fabrication of many optoelectronic devices such as laser diodes (LDs), light emitting diodes (LEDs), high electron mobility transistors (HEMTs), UV sensors, and their nanoscale structures in device applications [3, 5, 30, 153, 200]. However, there are persistent issues in using ZnO-based materials which include: conversion to p-type conductivity due to the position of the charge neutrality level (CNL), *i.e.*, the energy at which defect states change from donor-type to acceptor-type with reference to the Fermi level, being above conduction band minimum; thermal instability at high temperature (above 600 °C); and the distribution of thermally-created defects such as interstitial Zn (Zn_i), Zn vacancy (V_{Zn}), interstitial oxygen (O_i), and oxygen vacancy (V_O) [119, 201, 202]. The formation of such intrinsic defects, which creates states in the band gap of ZnO, strongly depends on the experimental conditions, namely, thermodynamic equilibrium [8].

$Be_xZn_{1-x}O$ ternary alloys have also been considered as promising candidate for the effective band gap engineering of ZnO [183]. This is because both ZnO and BeO possess wurtzite (WZ) crystal structures with a large difference in band gap energy. However, highly different physiochemical nature (*e.g.* atomic size, electronegativity, and formation enthalpy) of constituent atoms in the alloy system and mechanical stress of their heterostructures readily induce phase fluctuation un-

der thermodynamic equilibrium. Therefore, thermodynamic phase stabilization of highly mismatched alloys causes phase separation and the formation of multi-phase crystallinity [27, 169, 190, 203, 204]. Understanding the thermodynamics of Be and following phase transitions in the alloy system is essential to control such solid-state reactions and the resulting physical and chemical properties of the material.

In this chapter, the influence of thermal treatment on an inhomogeneous $Be_xZn_{1-x}O$ (BZO) film grown on $Al_2O_3(0001)$ and annealed at temperatures (T_A) up to 950 °C is explored. Thermal annealing induces significant recrystallization via strain relaxation and atomic redistribution to form a multi-phase crystalline film. This results in the considerable micro-segregation and mass transport of BeO and ZnO phases within the film combined with the formation of a crystalline ZnO interface layer. X-ray photoemission spectroscopy (XPS) along with infrared (IR) reflectance measurements and simulations clearly show the out-diffusion of Be atoms and precipitation of lattice point defects in the BZO films with increasing T_A. Highly conductive layers emerge at the BZO/Al_2O_3 interface for $T_A \geq 800$ °C. As a consequence, carrier concentration, conductivity, and density-of-state averaged effective masses of the degenerate interfaces are separately determined by applying a two-layer model for the high-temperature annealed BZO films. Accumulation of Be (Zn) at the surface (interface) is addressed by the migration of cations during high-temperature annealing based on a counter-diffusion mechanism to elucidate the formation of the highly degenerate interface layer in the alloy film.

6.2 Details of experiments and theoretical calculations

The BZO ternary film were grown on an $Al_2O_3(0001)$ substrate at 500 °C, in a partial pressure (P_{O2}) of 2×10^{-3} mbar (Ar 45 sccm:O_2 5 sccm gas mixture) by radio-frequency (RF) magnetron co-sputtering (base pressure: 1.6×10^{-8} mbar). For the film growth, the RF power of 100 W was supplied to the ZnO ceramic target and the RF power of 40 W was supplied to the Be metallic target. The as-grown film was thermally treated at various temperatures between 600 °C and 950 °C for 60 min with N_2 gas flowing. All annealing temperatures were set up with

a ramping rate of 20 °C/min. Structural changes for the as-grown and thermally-annealed films were characterized by high-resolution X-ray diffraction and powder X-ray diffraction using Panalytical X′Pert Pro MRD and Panalytical X′Pert Pro MPD equipped with an incident beam hybrid monochromator giving pure Cu $K_{\alpha 1}$ radiation (HRXRD: $\lambda = 1.5406$ Å). Surface morphology was studied with tapping-mode AFM measurements. A Perkin-Elmer Lambda 25 UV/Vis spectrometer was used to determine the optical band gap energy of the as-grown and annealed BZO films.

XPS measurements were performed in ultra-high vacuum (UHV: base pressure $= 3 \times 10^{-11}$ mbar) using an Omicron SPHERA hemispherical analyser and a monochromatic Al K_α X-ray source ($h\nu = 1486.6$ eV). Photoelectrons emitted from the film surfaces were collected at normal emission. During the XPS measurements, the surface charging effects were compensated using a low energy electron flood gun (Omicron CN10). The overall energy resolution was 0.47 eV and the E_B scale was calibrated using the adventitious C $1s$ peak ($E_B = 284.5$ eV). The transmission function of the analyser was calibrated using Ag, Au, and Cu foils. The XPS spectra were fitted using a Shirley background and Voigt function. Also, compositional ratios for each element (Zn, O, Be, and C) in the ternary films were determined correcting for the electron mean free path and using Scofield cross-sections [135].

Far- and Mid-IR reflectance measurements at an incident angle of 11° relative to the film surface normal were recorded using a Bruker Vertex 70v Fourier-transform infrared (FTIR) spectrometer. Because of the optical anisotropy of the polar crystal, s-polarized far-IR and mid-IR reflectance spectra for the films were obtained by Polyethylene (50 – 600 cm^{-1}) and ZnSe (460 – 8000 cm^{-1}) polarizers. The reflectance spectra were simulated utilizing a stratified medium consisting of 3 layers (4 layers) for as-grown and annealed, $T_A \leq 700$ °C, (annealed, $T_A = 800$ – 950 °C) samples with coherent interference. The electrical properties of the films were characterized by performing variable temperature (5 – 300 K) Hall-effect measurements in the van der Pauw configuration. Indium solder was used to make ohmic contacts to all of the etched corners of the 5×5 mm^2 samples. Field emission transmission electron

microscopy (FETEM, a Tecnai G^2 F30 S-Twin), equipped with energy dispersive X-ray spectroscopy (EDX, EDAX Genesis), was used with an acceleration voltage of 300 kV to characterize the microstructural properties and performed elemental profiling of the annealed BZO sample at $T_A = 950$ °C. In order to examine the defect distribution in the BZO films as a function of T_A, variable temperature photoluminescence (T = 12 – 300 K) measurements were carried out using a He-Cd laser ($\lambda = 325$ nm). A complementary long-pass optical filter with a cut-off wave length of 420 nm was also used to increase the dynamic range of the deep level associated emissions from the samples. In order to understand the formation of secondary phase BeO nanoparticles at the surface of the BZO films during high temperature annealing processes, the enthalpy of formation for bulk of both ZnO and BeO was also considered.

The total energies of atoms (Zn and Be), molecules (O_2), and solids (ZnO and BeO) were obtained by first-principles density functional theory calculations within the local density approximation using the Cambridge Sequential Total Energy Package plane-wave code. A plane-wave basis set with a kinetic energy cutoff of 400 eV was employed and the electron-ion interactions were treated by ultrasoft pseudopotentials. After the geometrical optimization of each unit cell structure, the obtained equilibrium lattice parameters for ZnO (BeO) were $a = 3.185$ Å (2.723 Å) and $c = 5.149$ Å (4.424 Å), respectively. The free energies, E^F_{ZnO} (E^F_{BeO}), for the formation of ZnO (BeO) were determined by

$$E^F_{ZnO} = \mu_{ZnO} - (\mu_{Zn} + \mu_O), \tag{6.1a}$$

$$E^F_{BeO} = \mu_{BeO} - (\mu_{Be} + \mu_O), \tag{6.1b}$$

where μ_{ZnO} (μ_{BeO}) is the chemical potential of ZnO (BeO), and μ_{Zn} (μ_{Be}) and μ_O are the chemical potential of Zn (Be) bulk and the chemical potential of O in an O_2 molecule, respectively.

6.3 Results and discussion

6.3.1 Recrystallization and atomic distribution in BZO films.

XRD 2θ-ω scans of the BZO (0002) reflection for the BZO films thermally treated as a function of T_A (600–950 °C) is shown in Fig. 6.1a. Clearly resolved diffraction peaks from the BZO(0002) reflection were found on the as-grown film, corresponding to multi-phase crystallinity with a non-uniform Be concentration in the film. Note that the in-plane lattice of the as-grown BZO film is biaxially strained subject to the highly mismatched c-plane Al_2O_3 substrate. Thereby, the (0002) peak position for the as-grown film is lower than that of bulk ZnO ($c = 5.20$ Å) although the lattice shrinkage is induced by the Be incorporation (≤ 6 %) into the ZnO [38]. A transition from multiple diffraction peaks to a single peak was observed with increasing T_A above 700 °C. Moreover, the position of the BZO (0002) diffraction peak gradually shifted towards higher 2θ. The lattice constant, c, of the BZO film annealed at $T_A = 950$ °C was determined to be $c = 5.19$ Å, which is close to that of bulk ZnO. This is indicative of a low Be composition (or even no Be) in the BZO films for high T_A. Examination of the BZO(0002) and $(10\bar{1}2)$ ω-rocking curves gives an insight to the mosaicity of the BZO films as presented in Fig. 6.1b. Figure 6.1c shows the variation in FWHM of the plane reflections as a function of T_A. The rocking-curve widths were reduced for T_A beyond 900 °C. It is known that the rocking curve widths of the (0002) and $(10\bar{1}2)$ planes reflect the associated density of structural defects, which are screw-type and edge-type threading dislocations, respectively [205–208]. Therefore, this result indicates a decrease in the number of structural defects with a significant reduction of the film mosaicity (out-of-plane tilting and in-plane twisting) as T_A increased. Figure 6.1d exhibits Φ scans along the azimuthal circle of Al_2O_3 $\{10\bar{1}4\}$ and BZO $\{10\bar{1}2\}$ reflections for the as-grown and annealed BZO films.

For all films, the scan across the BZO {10-12} indicated a six-fold symmetry, confirming a WZ crystal structure. By the offset of the angular positions of the BZO $\{10\bar{1}2\}$ from the three Al_2O_3 $\{10\bar{1}4\}$ reflections, an in-plane growth relation-

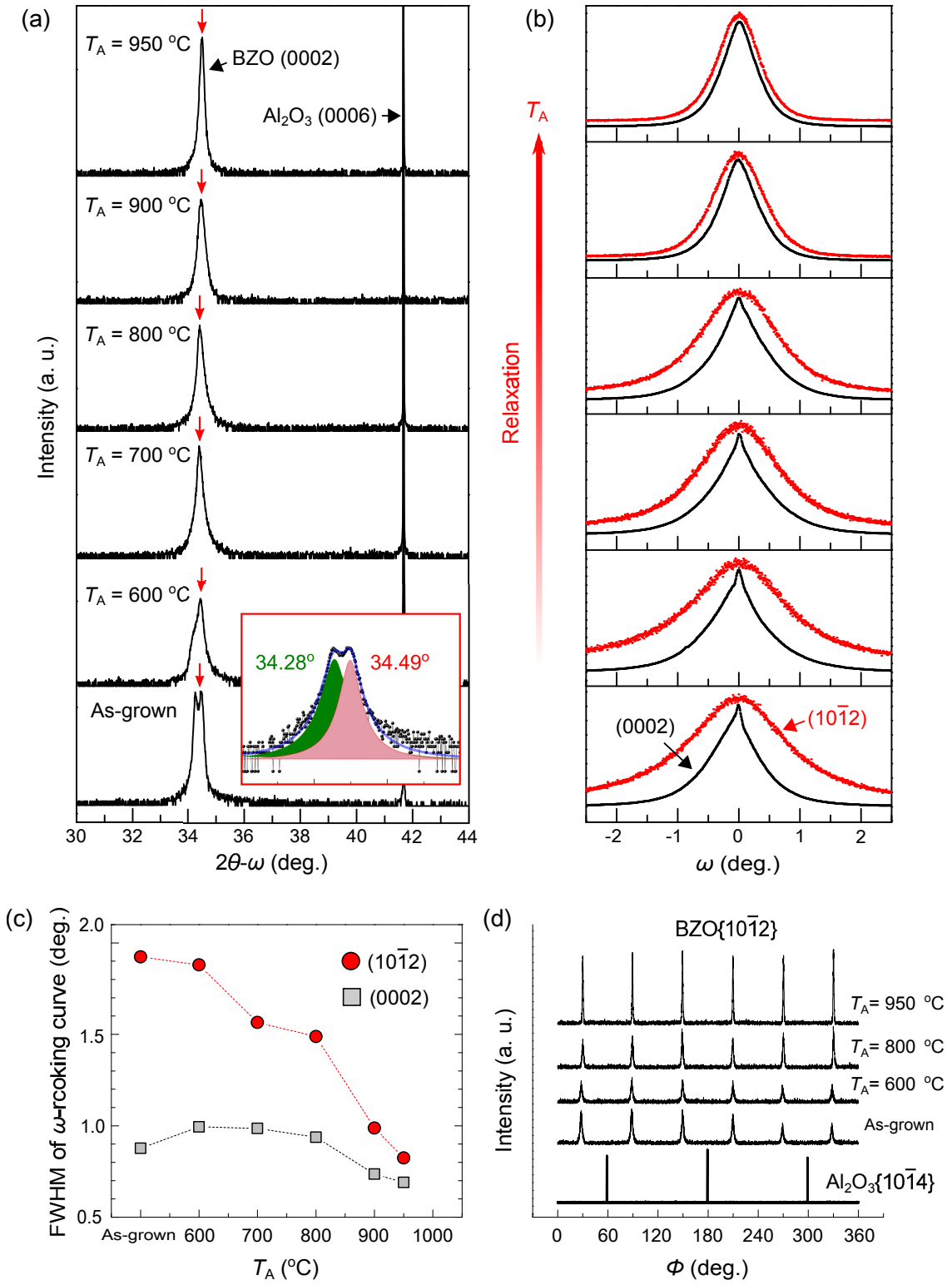

Figure 6.1: (a) HRXRD $2\theta - \omega$ (0002) diffraction patterns of the as-grown and annealed BZO films (T_A = 600–950 °C). (b) The ω-rocking curves of $Be_xZn_{1-x}O$ (0002) and (10$\bar{1}$2) Bragg reflections as a function of T_A. (c) Profiles of the FWHMs of the rocking curves for (0002) and (10$\bar{1}$2) BZO as a function of T_A. (d) Φ-scans across the off-normal ZnO {10$\bar{1}$2} reflection and the Al_2O_3 {10$\bar{1}$4}.

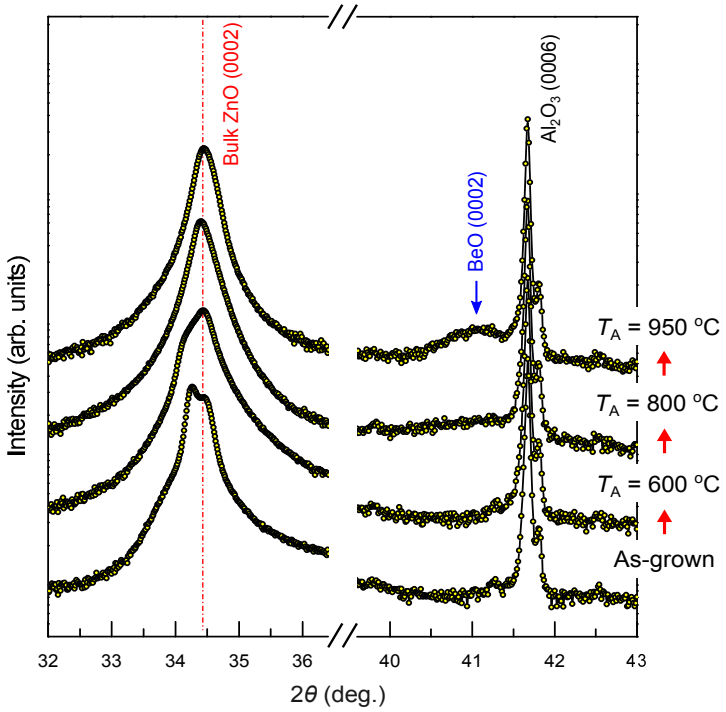

Figure 6.2: PXRD 2θ diffraction patterns of the as-grown and annealed BZO films (T_A = 600–950 °C). Extra diffraction peaks are found at $2\theta \approx 41°$, which correspond to the formation of WZ BeO crystallites in the annealed BZO film ($T_A \geq 800$ °C).

ship, BZO $\{10\bar{1}0\}\|Al_2O_3$ $\{11\bar{2}0\}$, was determined as a 30°-twisted film growth. This is typically observed in heteroepitaxial ZnO thin film on $Al_2O_3(0001)$ by molecular beam epitaxy, pulsed laser deposition, or sputtering [205,209,210]. Additionally, the FWHMs of the BZO $\{10\bar{1}2\}$ peaks decreased from 2.84° to 1.22° with increasing T_A, indicative of the enhancement of the BZO film crystallinity with the increase of T_A. Consequently, the XRD results reveal that the thermal treatment led to recrystallization of the BZO films through the redistribution of Be and strain-relaxation. Note that the HRXRD results showed no phase separation feature induced by Be out-diffusion and segregation. To further resolve the recrystallization of the BZO films, powder XRD (PXRD) measurements for the samples were performed, as shown in the Fig. 6.2 below. From these results, extra diffraction peaks were observed around $2\theta = 41°$ which increased gradually for $T_A \geq 800$ °C. These peaks correspond to the increase in WZ BeO(0002) diffraction feature as T_A increases and is due to the formation of WZ BeO crystallites in the annealed films.

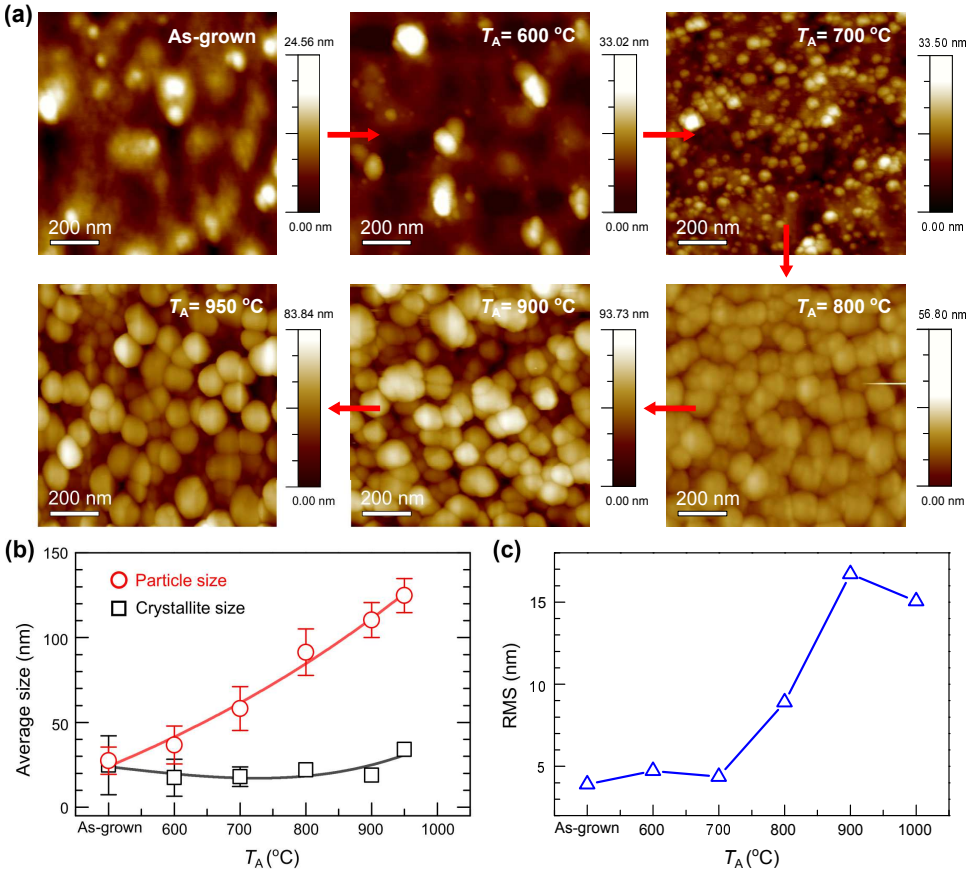

Figure 6.3: (a) AFM topography (1×1 μm^2) images of the as-grown and annealed BZO films (T_A = 600–950 °C). (b) Profiles of the crystallite size (XRD), average particle size (AFM), and (c) the root mean square (RSM) value of the average-surface roughness as a function of T_A.

AFM topographic images (1×1 μm^2) of the surface morphology for the as-grown and annealed BZO films are shown in Fig. 6.3a. The surface of the as-grown film exhibits a three-dimensional columnar microstructure with a distribution of different grain sizes. The varied grain sizes on the highly lattice-mismatched films are typically caused by the anisotropic growth with misaligned grains along the substrate normal to reduce the total energy [190]. The formation of nanoparticles at the surface of the film was clearly seen at T_A = 600 °C. As T_A increased, the small particles migrate toward the larger ones. This is Ostwald ripening and is driven by the difference in their chemical potentials to minimize surface free energy. The nanoparticles are preferentially located near grain boundaries, which are energetically more favourable for nucleation [68].

For $T_A \geq 800$ °C, the above growth process results in a continuous increase in

the mean size of the spherical nanoparticles (NPs) from ≈ 27 to 124 nm (Fig. 6.3b). Additionally, by comparing crystallite sizes calculated using XRD patterns of the BZO(0002) and applying the Debye-Scherrer formula (in the range of approximately 23 – 36 nm), the average NP sizes from AFM showed large discrepancies with increasing T_A (as shown in the upper panel of Fig. 6.3b). This reveals competing recystallization processes in the BZO films during thermal annealing, which lead to thermally-enhanced coalescence of grains in the bulk and the nucleation-and-growth of NPs at the surface. The root-mean-square (RMS) of surface roughness increased steeply with T_A to a maximum value of 15.4 nm as illustrated in the bottom panel of Fig. 6.3b. This is due to the distribution of the grown NPs at the vicinity at the surface. This surface recrystallization is associated with atomic segregation, bulk and surface diffusion, and nucleation-and-growth at the surface during thermal annealing. A detailed mechanism for the formation and behavior of the NPs at the surfaces of the annealed BZO films is presented in Chapter 7.

From the XRD and AFM results, significant recrystallization of the as-grown multi-phase BZO film on an Al_2O_3(0001) substrate was observed, showing a visible structural transition as T_A increases. Transmission electron microscopy (TEM) measurements were performed in order to understand the microstructural properties of the recrystallized BZO film at $T_A = 950$ °C. Figure 6.4a shows cross-sectional TEM images of an annealed BZO film. The total thickness of the film was found to be 152±8 nm. The recrystallized film consists of three distinct regions: (*i*) nanoparticles (NPs) at the surface [top inset], (*ii*) bulk film, and (*iii*) intermixing layer at the film layer-substrate interface. The crystallized NPs, which are WZ phase BeO, have the calculated lattice constants, $a = 2.63$ Å and $c = 4.27$ Å. The T_A dependent size and distribution of the NPs at the surface were also observed in AFM (Fig. 6.3a).

Figure 6.4b shows the high resolution TEM (HRTEM) image along the <11$\bar{2}$0>-zone axis for the interface region of the annealed film at $T_A = 950$ °C. The structural properties of the three different regions were examined separately by selecting the red-square areas I, II, and III, respectively, seen in Fig. 6.4. The associated Fast-Fourier transform (FFT) of the red-square I shows typical spots of WZ structure.

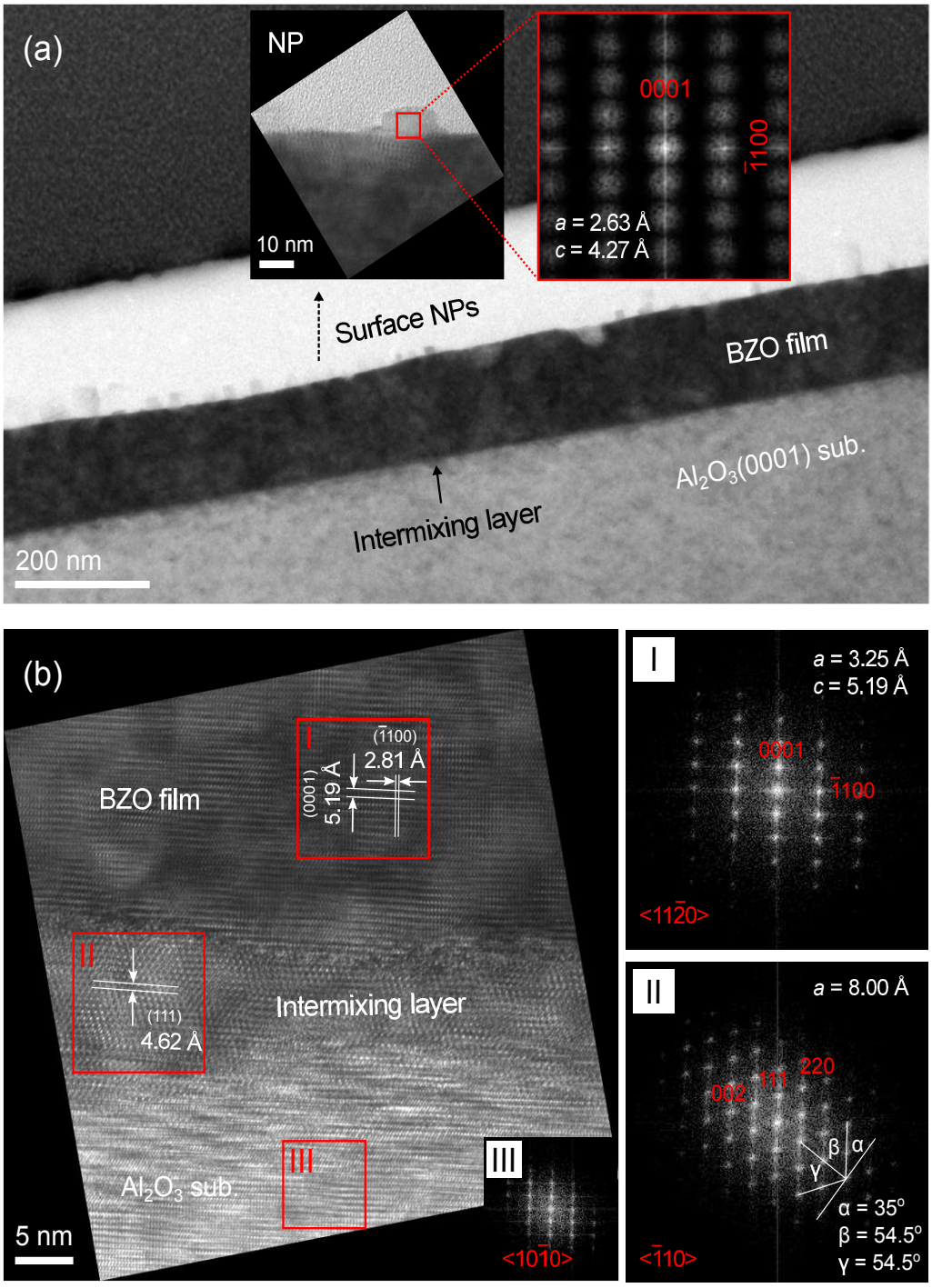

Figure 6.4: (a) Cross-sectional TEM image of the annealed BZO film on an Al_2O_3(0001) substrate (T_A = 950 °C). The annealed film is formed of (*i*) surface nanoparticles (NPs) [the top inset], (*ii*) main film, and (*iii*) intermixing layer. The insets are high resolution TEM image of the NP and Fast-Fourier transform (FFT) associated to the red-square area in the HRTEM image. (b) HRTEM image along the <11$\bar{2}$0>-zone axis of the BZO/Al_2O_3 interface region. The selected red-squares I, II, and III represent the main film, intermixing layer, and substrate, respectively. The corresponding FFTs of the red-square areas I and II indicate WZ and face-centered cubic (FCC) structures. The extracted lattice constants are shown in the images I and II.

The lattice constants of the film were determined to be $a = 3.25$ Å and $c = 5.19$ Å by extracting the plane spacing of 0001 and $\bar{1}100$. These are almost identical to that of bulk ZnO ($a = 3.25$ Å and $c = 5.20$ Å) (see the up-right FFT image I in Fig. 6.4b) [211]. This is indicative of a very low B composition in the annealed BZO film ($T_{\mathrm{A}} = 950$ °C) near the BZO/Al_2O_3 interface.

Crystallization of a new interfacial layer (≤ 10 nm thick) was found at the BZO/Al_2O_3 interface region as denoted by the red-square II of Figure 6.4b. The corresponding FFT pattern displays a face centered cubic (FCC) structure with interaxial angles between the planes as shown in the bottom-right image II of Figure 6.4b. The lattice constant obtained, $a = 8.00$ Å, is close to that of $ZnAl_2O_4$, $a = 8.086$ Å [168,212]. The formation of such a layer is believed to be caused by an interfacial solid-state reaction of ZnO and Al_2O_3 at the high annealing temperatures. This results in crystallization of spinel $ZnAl_2O_4$ or a Zn-deficient phase $Zn_xAl_yO_z$, at the interface depending on the degree of the atomic diffusion of Zn and O into Al_2O_3, *i.e.*, $(ZnO)_n$+$(Al_2O_3)_m$. Furthermore, the orientation relationship between the annealed BZO film, the thermally crystallized $ZnAl_2O_4$, and the Al_2O_3 substrate were determined to be present with $[0001]_{\mathrm{BZO}} \| [111]_{\mathrm{ZnAl_2O_4}} \| [0001]_{\mathrm{Al_2O_3}}$ and $[10\bar{1}0]_{\mathrm{BZO}} \| [\bar{1}\bar{1}2]_{\mathrm{ZnAl_2O_4}} \| [11\bar{2}0]_{\mathrm{Al_2O_3}}$.

Figure 6.5a displays cross-sectional scanning transmission electron microscopy (STEM) image of the annealed BZO film ($T_{\mathrm{A}} = 950$ °C). The STEM image is created by merging the bright-field (phase contrast in grey) and annular dark-field (Z-contrast in green) images to obtain a clear visualization of the spatial distribution of elements. The contrast in the bright field image is correlated to the mass-thickness and diffraction, while the intensity, I, of the Z-contrast dark field imaging by elastically scattered incoherent electrons is proportional to atomic number, Z, according to $I \approx Z^{\alpha}$, where α is a parameter ($\alpha \leq 2$) [145]. The STEM image enables an examination of atomic distribution and chemical composition in the main film and the intermixing layer. Vivid contrast is observed between the surface and near interface region (Fig. 6.5a). This is due to the accumulation of lighter Be atoms (larger Zn atoms) at the surface (interface) relative to the Zn (Be)

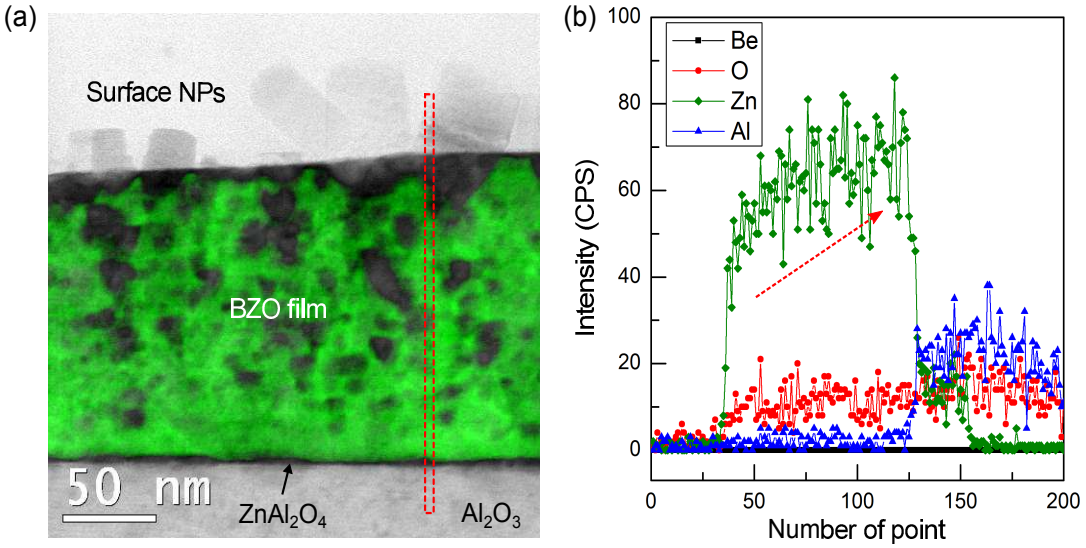

Figure 6.5: (a) Cross-sectional STEM image of the BZO film annealed at $T_A = 950$ °C. The image is presented by merging bright-field (grey) and annular dark-field (green) images. (b) Energy dispersive X-ray spectroscopy (EDS) line scan across the annealed BZO film. The EDS line profiles for the constituent elements (Be, O, Zn, and Al) across the sample correspond to the red vertical dashed line in (a).

concentration. Moreover, the density of partially distributed darker spots (in the dark field image) increases toward the surface of the film, implying an increase in the number of Be and/or BeO clusters closer to the surface. The intensity at the interfacial layer (based on the bright-field STEM) is seen to be darker than that of the substrate region (Al_2O_3) which is caused by the intermixing of ZnO and Al_2O_3 and the resulting spinel $ZnAl_2O_4$ or $Zn_xAl_yO_z$ layer formation mentioned earlier.

To further resolve the chemical compositions in the sample, energy dispersive X-ray spectroscopy (EDS) measurements were performed as shown in Fig. 6.5b. The EDS line profiles for each element (Be, O, Zn, and Al) across the specimen correspond to the red vertical line in Fig. 6.5b. Note that the signal intensity of Be and light atoms is generally underestimated in EDS as the detector is equipped with a Be window [213]. Apart from the limits of the concentration analysis for lighter elements in the sample within the EDS characteristics, an upward gradient in the intensity of Zn was clearly found moving toward the interface, denoted by the red arrow in Fig. 6.5b. This is indicative of an increase in the atomic concentration of Zn toward the interface, which corroborates the locally brighter region in the film

close to the interface, relative to the surface and substrate areas, in the Z-contrast STEM image (Fig. 6.5a). The atomic intermixing of Zn, Al, and O as a result of ZnO diffusion to the top surface of Al_2O_3 substrate was also verified from the EDS profiles of the interface region.

6.3.2 Surface chemical composition and VB photoemission

Monochromatic XPS measurements were performed to investigate the variation of Be composition and electronic structure as a function of T_A at the surfaces of the BZO films. Figure 6.6a shows the normalized XPS spectra of Zn 3s and Be 1s core-levels for the as-grown and annealed BZO films at T_A = 600 °C, 800 °C, and 950 °C. Be 1s peak located at a BE of 114.25±0.15 eV is attributed to a chemical bonding of the Be-O state (metallic Be states, $E_B \approx 111$ eV) [190]. This results from the incorporation of Be atoms in Zn sites forming a $Be_xZn_{1-x}O$ alloy for the as-grown film. Moreover, the Be 1s peak intensity gradually increased with respect to Zn 3s with increasing T_A, suggesting segregation of Be to the surface and the subsequent formation of BeO phases as observed in the TEM results. By comparing the relative XPS core-level intensities of the Zn 3s and Be 1s peaks, it was observed that the Be composition to Zn (Be/(Zn+Be)) at the surfaces of the ternary films was increased from 24.6 % to 51.3 % with increasing T_A, up to 950 °C, as shown in Fig. 6.6b. This Be enrichment could be caused by two factors during the thermal treatment process: (*i*) atomic replacement of interstitially distributed Be atoms into Zn sites, and (*ii*) out-diffusion of Be atoms towards the surface region.

Utilizing the optical measurements of the BZO films, the absorption edges were obtained by extrapolation of the linear portion to horizontal background of the absorption coefficient (α^2) spectra (this will be detailed in Chapter 7). These results show a continuous decrease of the optical band gap energy with increasing T_A as illustrated in Fig. 6.6d. Therefore, it is believed that the increased Be composition at the film surface is primarily associated with thermally-induced out-diffusion of Be atoms. This also supports the surface segregation of Be and the droplet/NP formation, which was observed in the TEM and AFM results. Figure 6.6c displays

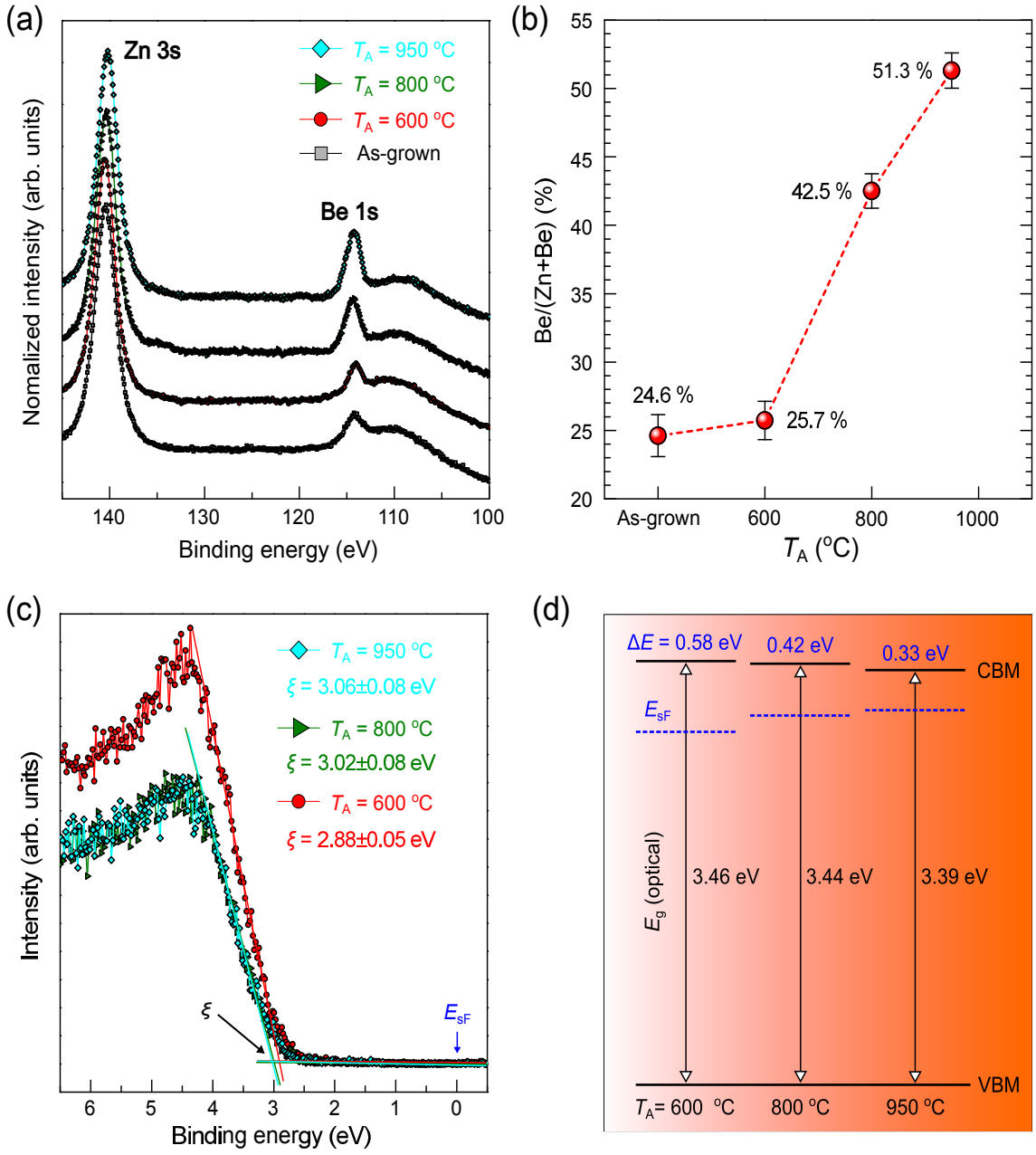

Figure 6.6: (a) Normalized XPS spectra of Zn 3*s* and Be 1*s* core-levels. (b) the relative ratio (%) of surface Be concentration to Zn [Be/(Zn+Be)] for the as-grown and annealed BZO films (T_A = 600 °C, 800 °C, and 950 °C). (c) Valence band (VB) photoemission spectra for the surface of the annealed films. The values of ξ indicate the separation of the VB maximum and surface Fermi level (E_{sF}). (d) A diagram of E_{sF} under a change of the band gap energy for the BZO films annealed at T_A = 600 °C, 800 °C, and 950 °C. The values of ΔE denote the separation of the optical band gap (E_g) to E_{sF} for the annealed films.

the valence band XPS spectra as a function of T_A for the BZO films. The position of the surface Fermi level (E_{sF}) in the films was determined by extrapolating a linear fit to the sharp edge of the VB spectra. Since the external electrons supplied by a charge neutralizer cause a shift in the near VB region, E_{sF} of the as-grown (insulating) film must be discounted. These data indicate that the VB edges of the BZO films shifted towards higher BE with respect to E_{sF} as T_A is increased. This corresponds to an upward shift of E_{sF}. Considering the band gap energy (E_g) change from 3.46 eV at T_A = 600 °C to 3.39 eV at T_A = 950 °C, E_{sF} for the BZO films moves towards the conduction band minimum (CBM) as ΔE (E_g – E_{sF}) decreases (Fig. 6.6d). This is suggestive of thermally-induced excess donors near surface accompanying the reduction of the band gap energy in the films as T_A is increased.

6.3.3 IR reflectance measurement and simulation models

IR reflectance measurements were carried out to determine the film thicknesses, IR-active BZO phonon modes and electron plasma frequencies (assigned to the free carrier excitations). According to an irreducible representation of lattice vibration modes for WZ BZO (space group: C_{6v}^4) at the centre (Γ-point) of the Brillouin zone, IR active A_1 and E_1 phonon branches are polarized along the z-direction and xy-plane, respectively [214, 215]. Both branches are composed of pronounced transverse-optical (TO) and longitudinal optical (LO) phonon modes, due to the macroscopic electric field associated with the LO phonons in a WZ structure [141, 142]. Based on the anisotropic dielectric response of the BZO films, s-polarized light has been used to attain $E \perp c$, where E is the electric field of incident light, obtained parallel to the surface. The s-polarized reflectance spectra of the BZO films (the as-grown and annealed, T_A = 600 °C) were simulated using the classical Drude model (ϵ_D) for carrier response and the modified expression, which involves the factorized model (ϵ_L) for the host lattice response and a model function (ϵ_{IM}) describing IR-active impurity [141]. Details of the reflectance simulations are shown in Chapter 3.

The reflectance spectra of the as-grown and annealed samples at $T_A \leq 700$ °C

Table 6.1: The best-fit parameters used in the IR simulations for the BZO films, where T_A, ϵ (∞), E_1 (TO), E_1 (LO), ω_p, d are annealing temperature, high frequency dielectric constant, E_1 transverse optical phonon frequency, E_1 longitudinal optical phonon frequency, the plasma frequency, and layer thickness, respectively.

T_A (°C)	BZO sample	ϵ (∞)	E_1 (TO) (meV)	E_1 (LO) (meV)	ω_p (meV)	d (nm)
As-grown	Film layer	3.55±0.05	59.2±0.5	78.5±0.04	...	212±8
600	Film layer	3.55±0.05	57.0±0.3	77.5±0.05	16±12	209±6
700	Film layer	3.62±0.02	54.3±0.1	76.1±0.05	42±8	208±8
800	Film bulk layer	3.62±0.02	53.2±0.1	75.9±0.05	68±6	192±4
	Interface layer	3.85±0.05	51.5±0.8	73.7±2	295±5	10±2
900	Film bulk layer	3.66±0.03	52.2±0.1	75.3±0.05	86±4	139±2
	Interface layer	3.92±0.05	51.2±0.9	73.5±3	320±4	20±1
950	Film bulk layer	3.80±0.02	51.8±0.1	74.8±0.03	95±6	114±3
	Interface layer	3.96±0.05	51.0±0.8	73.1±2	332±1	29±2

were modelled taking a three-layer stratified medium as vacuum/film/substrate. By contrast, the samples annealed at $T_A \geq 800$ °C were modelled assuming a four-layer stratified medium by dividing the film into bulk and interface layers. The experimental data and simulations together with schematics of the sample layers are shown in Fig. 6.7a. A factorized model was used to simulate the Al_2O_3 substrate, where the dielectric constants and phonon modes are used as input parameters. The effect of thermally nucleated NPs at the surface was accounted for by taking their incoherent optical response in the IR reflectance simulation. The extracted parameters are collected in Table 6.1.

Figure 6.7b shows plots of the phonon energy of E_1(TO) and (LO) modes for the BZO films as a function of T_A. The results show that both the E_1(TO) and (LO) bulk phonon energies are gradually red-shifted to lower phonon energies with increasing T_A. As a consequence, Be substitution in the ZnO lattice, and higher lattice vibration energies (phonon energies) were seen compared to that of undoped ZnO (see Fig. 6.7a). This is due to the smaller reduced mass and stronger bonding of Be-O compared to Zn-O in the WZ lattice. This corroborates the decrease of the lattice phonon energies attributed to out-diffusion of Be during the annealing

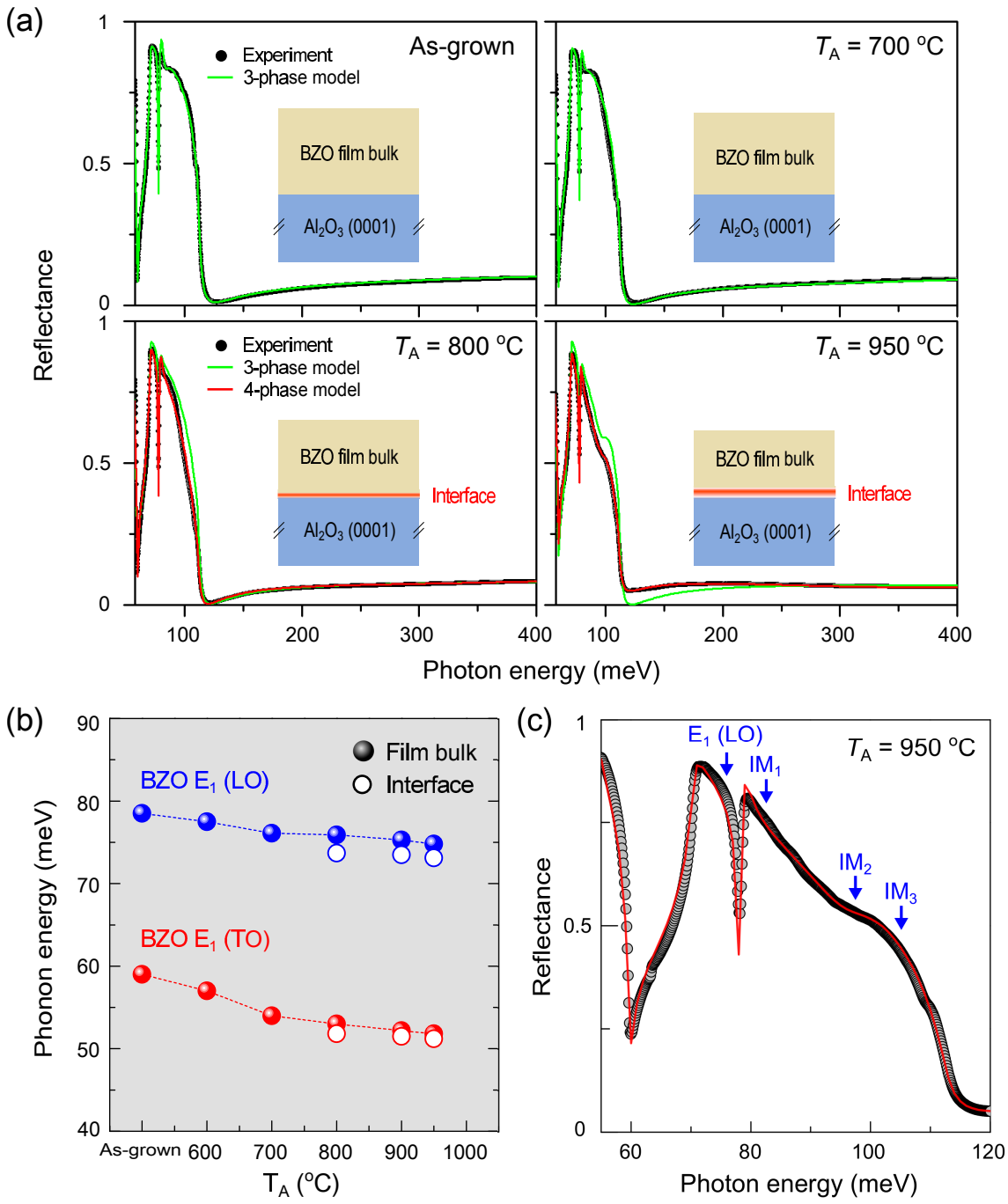

Figure 6.7: (a) Experimental IR reflectivity spectra (black-circle) plotted with the simulated spectra (green- and red-solid line). The insets represent schematics of the three-phase model for the as-grown and 700 °C annealed, and four-phase model for T_A = 800 °C and 950 °C. (b) Variation of the phonon mode frequencies, E_1(TO) and (LO), of the BZO film bulk (closed circle) and interface (open circle) layers as a function of T_A. (c) Three impurity modes of the BZO films annealed at T_A = 950 °C.

process.

The phonon energies of the interface layer for $T_A \geq 800$ °C are also close to those of the undoped ZnO [E_1(TO) = 50.8 meV and E_1(LO) = 72.7 meV] [43]. This implies a lower Be concentration at the interface compared to the bulk region. As mentioned above, three additional impurity modes were observed at IM_1 = 82.6 meV, IM_2 = 98 meV, and IM_3 = 106 meV (Fig. 6.7c). No specific origin of these impurity modes has been reported to date. The perturbation of the host lattice phonon modes arises from the local potential of impurities. Hence, within this model, these modes could possibly be attributed to local multi-phonon modes associated with BeO segregation and intrinsic lattice defects [216, 217]. The polarity splitting parameters (broadening constants) of these impurity modes increased (decreased) with T_A, suggesting an increase in local segregation of BeO and defect density within the annealed BZO films.

6.3.4 Temperature dependent carrier concentration and the double-charge layer approximation

The IR reflectance simulations are summarized in Table 8.1 and show that the thickness of the layers within the BZO films varies as a function of T_A. These results indicate that the total and bulk thicknesses significantly decrease when $T_A \geq 800$ °C, while the interface layer thickness increases. This effect is shown in Fig. 6.8a, and could be due to thermally-dissociated Zn-O bonds or an increase in density of textured grains. The effect of thermal treatment on the thickness variation in BZO films with different Be concentration was investigated (will be shown in Chapter 7). A high dissociation ratio in the undoped ZnO films was observed as T_A above 800 °C, accompanying by a sudden decrease in film thickness. As a consequence, the thickness reduction in the BZO films is attributed mostly to thermally-induced lattice dissociation of Zn-O bonds during the annealing process.

In order to account for the distribution of carriers within the films, the plasma frequency of each layer is plotted as a function of T_A in Fig. 6.8b. A monotonic increase in the plasma frequency was observed in both film and interface layers with

the increase of T_A. As the plasma frequency is proportional to the carrier concentration, a higher concentration was expected for higher T_A according to Eq. 6.3. This is consistent with the results of room-temperature (RT) Hall effect measurements shown in Fig. 6.8b. It is worth noting that there is a large difference between the plasma frequency of the film bulk and interface layers for $T_A \geq 800$ °C, and reveals that the interface layer could well be degenerate.

Hence, variable temperature Hall effect measurements were performed in the range of 5 – 300 K for the BZO films annealed at $T_A = 600$ °C, 800 °C, and 950 °C, as illustrated in Fig. 6.8c. The annealed BZO film ($T_A = 600$ °C) with no interface layer showed an anomalous temperature-dependent carrier concentration with a mobility below 10 $cm^2V^{-1}s^{-1}$ across the entire temperature range. This unusual behavior could result from defect, grain boundary, or alloy scattering due to disorder in the phase-segregated alloy, as observed in the XRD and AFM data. In contrast, the annealed BZO films at $T_A = 800$ °C and 950 °C showed temperature-independent Hall carrier concentration (n_H) and mobility (μ_H) values, supporting the existence of a degenerate layer at the BZO/substrate interface.

By considering the classical freeze-out of carriers in the non-degenerate bulk region, the majority of carriers at low temperatures must come from the interface region. Hence, the sheet carrier density (n^s_{Int}) and mobility (μ_{Int}) in the interface layers were obtained by a linear extrapolation of the Hall data to 0 K. The interface carrier concentration, n_{Int}, was calculated from n^s_{Int}/d, where d is the thickness of the interface layer obtained from the IR reflectance simulations. The carrier concentration of the interface of the annealed BZO films at $T_A = 800$ °C and 950 °C were determined to be $n_{Int} = 7.54 \times 10^{19}$ cm^{-3} and 2.16×10^{20} cm^{-3} and $\mu_{Int} = 43.80$ and 39.05 $cm^2V^{-1}s^{-1}$, respectively. The interface conductivities ($\sigma_{Int} = n_{Int}e\mu_{Int}$) were calculated to be $\sigma_{Int} = 5.3 \times 10^2$ $S{\cdot}cm^{-1}$ and 1.4×10^3 $S{\cdot}cm^{-1}$, respectively. The carrier concentration and conductivity of the double-layer films have been calculated by a parallel conduction model, [218]

$$n_B = \frac{(\mu_H n_H + \mu_{Int} n_{Int})^2}{\mu_H^2 n_H + \mu_{Int}^2 n_{Int}}, \tag{6.2}$$

where n_B is the carrier concentration of the film bulk region. The corrected RT

bulk carrier concentration of the films with T_A = 800 °C and 950 °C were found to be $n_B = 1.70 \times 10^{18}$ cm^{-3} and 5.06×10^{18} cm^{-3}, respectively. By comparing the carrier concentrations and conductivities of the interfaces with those of the bulk, it is apparent that the interface values are much higher. Furthermore, the carrier concentrations in the interfaces (the bulk) are above (below) the Mott-transition level ($n \approx 6 \times 10^{18}$ cm^{-3}) of undoped ZnO [219].

6.3.5 Discussion

The highly conductive layer, found at the BZO/Al_2O_3 interface, formed after high-temperature treatment, $T_A \geq 800$ °C, imposes degenerate semiconducting characteristics on all the BZO films. By using the physical quantities obtained from the analyses above, the density-of-states-averaged effective mass of conduction electrons, m^*_{av}, was calculated using, [141]

$$m^*_{av} = \frac{n_{Int} e^2}{\omega_p^2 \epsilon(0) \epsilon(\infty)}, \tag{6.3}$$

where e is electronic charge, $\epsilon(0)$ is the permittivity of free space, $\epsilon(\infty)$ is high frequency dielectric constant. Values of $\epsilon(\infty)$ in the range of 3.85 – 3.96, obtained from the IR reflectance simulations, were used for the interfaces formed at T_A = 800 °C and 950 °C. The $\epsilon(\infty)$ and m^*_{av} values vary with carrier concentration at the interfaces. The m^*_{av} of the interface layers were determined to be $0.31m_0$ and $0.68m_0$ for carrier concentrations of $n_{Int} = 7.54 \times 10^{19}$ cm^{-3} and 2.16×10^{20} cm^{-3}, respectively. This seems reasonable as the Fermi level position increases with carrier concentration. Variation of the average effective mass with carrier concentration has been found previously in highly doped ZnO and doped $Mg_xZn_{1-x}O$ alloys [108,220]. Such a high carrier concentration at the interface, above the Mott-transition level, causes strong band-filling effects (Burstein-Moss shift), along with the correlated band gap renormalization as a result of many-body effects [109, 110]. Hence, the degenerate interface layer is important in deriving the physical properties of both BZO films and all ZnO-based materials.

Here, we discuss possible atomic diffusion and phase transformation models for the metastable BZO films as a function of T_A to further interpret the formation of

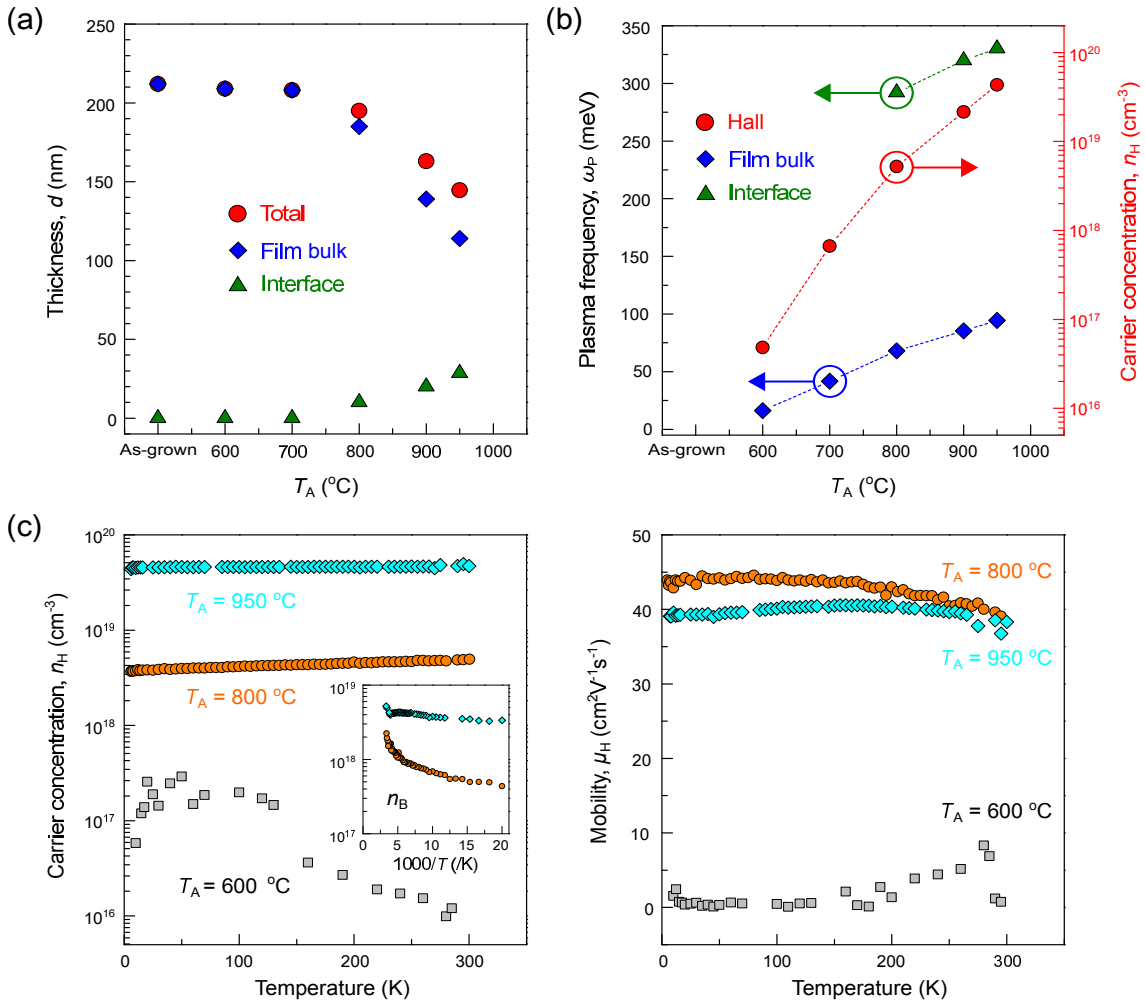

Figure 6.8: (a) Thickness (d) variation on the total, film bulk, and interface with increasing T_A (presented in Table I). (b) Plots of plasma frequencies (ω_P) for the film bulk and interface layers, and carrier concentration (n_H) as a function of T_A. (c) Temperature-dependent n_H and mobility (μ_H) for the BZO films annealed at T_A = 600 °C, 800 °C, and 950 °C. The inset in (c) shows corrected film bulk carrier concentration (n_B) versus inverse temperature for the BZO films annealed at T_A = 800 °C and 950 °C.

the multi-layer structure and degenerate interface layer [68, 213, 221]. Diffusion and segregation of Be were observed throughout the film with the resulting formation of secondary phase BeO NPs at the surface and grain boundaries. The phase separation phenomenon is caused when the annealing temperatures exceed the solubility limit of Be into host ZnO as a phase miscibility gap, as observed in our previous study [204]. The driving force for such segregation processes is energy minimization, *i.e.* the surface energy, interfacial energy, and elastic energy, etc of the metastable alloy system as Be atoms migrate from the bulk to the surface region [204, 222–224]. The high-temperature annealing ($T_{\mathrm{A}} \geq 800$ °C) leads to outward diffusion of Be together with the bond-breaking of Zn-O. Note that the vapour pressure of Be is much lower than that of Zn, meaning that Be is less likely to evaporate from the surface. Hence, the initial depletion of Zn atoms at the surface and grain boundaries preferentially occurs as a result of evaporation, and in turn an enrichment of Be. This gives rise to a supersaturation condition for the nucleation of the secondary phase NPs forming at the surface and grain boundary regions, which are preferential pathways for atomic mass transport. The diffused/segregated Be atoms can be preferentially oxidized to the more thermodynamically stable BeO, rather than ZnO as the free energy for the formation of the BeO [$E^{\mathrm{F}}_{\mathrm{BeO}} = -5.839$ eV at 0 K] is much lower than that of ZnO [$E^{\mathrm{F}}_{\mathrm{ZnO}} = -3.438$ eV at 0 K], obtained by density functional theory calculations. Therefore, the diffused/segregated Be atoms react with thermally diffused oxygen to form much energetically favourable BeO at the surface and grain boundaries, rendering to further nucleation-and-growth and minimizing their free energies.

This results in the distribution of the secondary phase BeO NPs at the surface and grain boundaries as presented in STEM. In other words, it is hard to recrystallize ZnO near Be-rich regions because Be acts as an effective oxygen trap to reduce the overall surface free energy. Furthermore, the grown BeO NPs, placed at the path way of mass transport, could passivate for the sublimation of residual Zn atoms from the film. These cause the excess of Zn interstitials in the annealed film. Concurrently, the induced outward diffusion of Be atoms creates vacancies, *e.g.*, $\mathrm{V_{Be}}$, near the interface, resulting in a vacancy flux, $J_{\mathrm{V}} = J_{\mathrm{Be}} - J_{\mathrm{Zn}}$, where J_{Be}

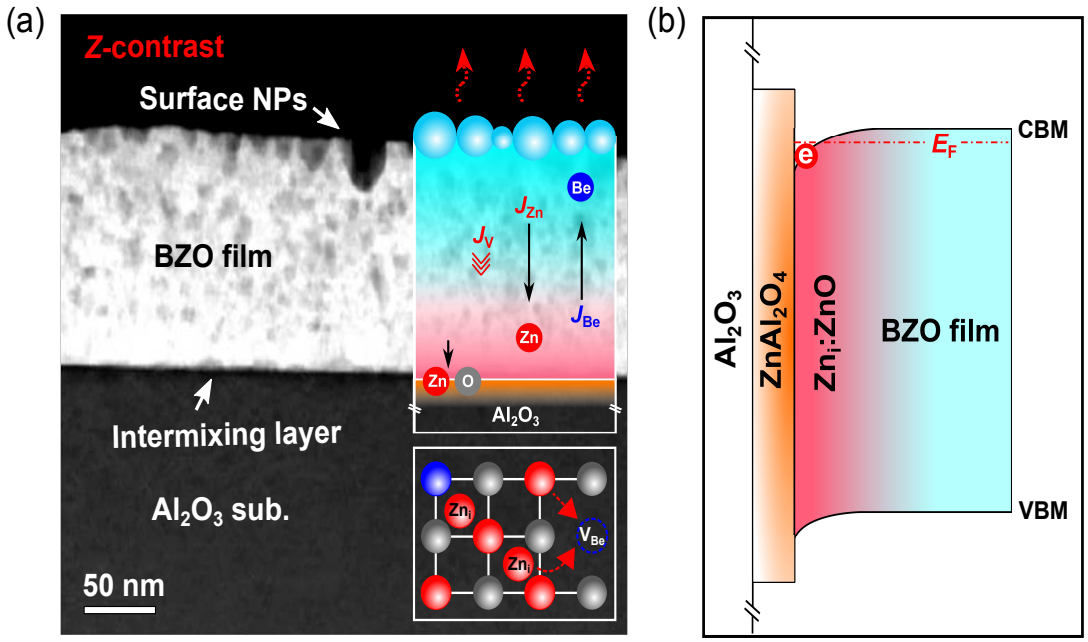

Figure 6.9: (a) Z-contrast dark-field STEM image for the BZO film annealed at T_A = 950 °C. The inset shows schematics of the atomic counter-diffusion mechanism in the BZO film, and the formation of surface BeO NPs and BZO/Al_2O_3 intermixing during solid-state reactions by thermal annealing. The Be flux (J_{Be}) is greater than the Zn flux (J_{Zn}) and thus the vacancy flux (J_V) toward the interface region. The bottom image represents the recrystallized surface associated with Be (blue-sphere) diffusion, while Zn (red-sphere) diffusion to the interface region of the film. (b) Schematic representation of the band line-up at the BZO film/Zn_i:ZnO/$ZnAl_2O_4$/Al_2O_3 heterostructure.

and J_{Zn} are diffusion fluxes of Be and Zn [168, 225]. This gives rise to the inward migration of Zn atoms towards the interface to minimize the chemical potential gradient [226,227]. As a result, a Zn concentration gradient from the surface towards the interface is observed from the Z-contrast STEM and EDS measurements (Fig. 6.5.). In the high-temperature recrystallization processes, such inward diffusing Zn atoms effectively compensate for atomic vacancy sites, both V_{Zn} and V_{Be}. This defect compensation with high T_A corresponds to an improvement of the crystalline quality of the film, observed in XRD. However, in the simultaneous occurrence of the atomic diffusion and following recrystallization, no significant correlation between the distribution of O and cation density gradient was found in the high-temperature annealed film. This is seen in the almost constant EDS intensity of O throughout the film, and hence diffusion proceeds predominantly by counter-diffusion of Be and Zn with the most likely equivalent distribution of oxygen [213]. Consequently, such

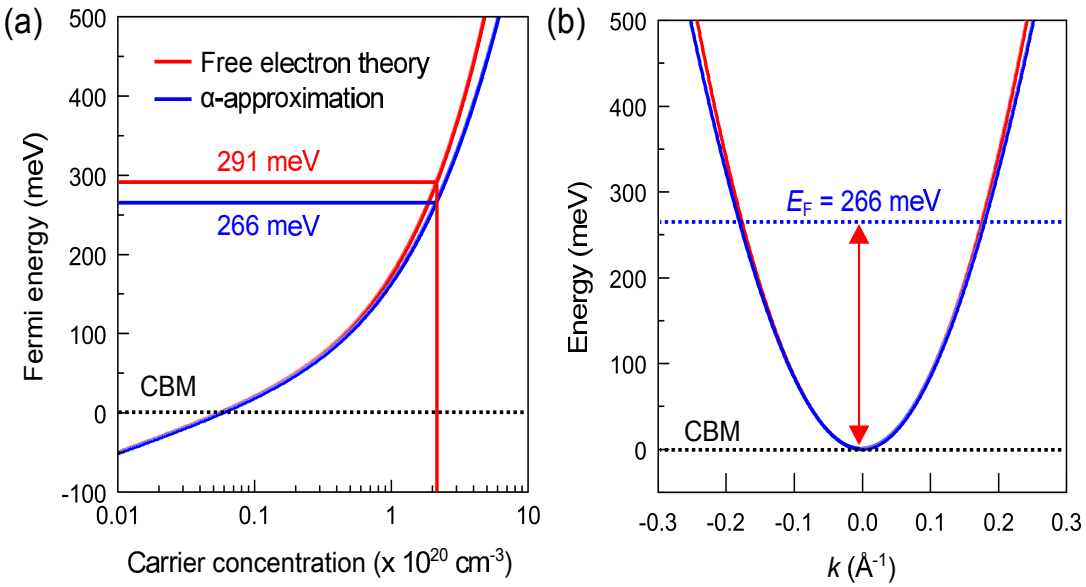

Figure 6.10: (a) Plots of Fermi energy versus carrier concentration for the degenerate interface layer of the annealed BZO film (T_A = 950 °C) approximated using Free electron theory (parabolic band structure), α-approximation (non-parabolic band structure), and Fermi-Dirac carrier statistics. The Fermi levels, E_F, were determined to be 291 meV (266 meV) above the conduction band minimum, CBM, for a parabolic (non-parabolic) conduction band. (b) The energy dispersions in the two models show no significant difference in the $\boldsymbol{k}$-space of interest.

cation counter-diffusion of Be and Zn (competition and repulsion) primarily and separately contributes to the formation of the Be-rich surface and Zn-rich interface in the high-temperature annealed alloy film (Fig. 6.9a). The diffusion of Zn and O (either in the form of ZnO or Zn and O ions) into Al_2O_3, as a unilateral atomic transfer, was also observed in the reaction interface, forming spinel $ZnAl_2O_4$ and Zn-deficient phase $Zn_xAl_yO_z$ [228].

Based on these diffusion processes at high T_A, an accumulation of Zn is formed, which creates a Zn-rich ZnO (Zn_i:ZnO) interface region within the film. Several groups have reported that Zn_i act as a source of donors due to shallow defect states ($\approx$ 31 – 37 meV) below the CBM, while V_O defects create deep level states in the band gap of ZnO [8,51,192]. In spite of the many studies claiming that interstitial hydrogen behaves as a shallow donor in n-type ZnO, we assert that this is not the case here. This is because the samples have been annealed at $T_A \geq 600$ °C, where hydrogen rapidly diffuse from the sample [8, 229]. Hence, we believe that the interface conductivity is primarily associated with the distribution of Zn_i. Due

to the high accumulation of such shallow donor-like defects, the defect bands are expected to merge with the conduction band, leading to band gap renormalization and a highly conductive interface layer in the high-temperature annealed alloy films, schematically illustrated in Fig. 6.9b [110]. The Fermi level is located above the CBM as a result of downward band bending associated with the accumulation of electrons [9]. The band lineup presented in Fig. 6.9b is an idealistic representation as the effects of local Be composition and charged dislocations [12] in that the Fermi energy has been disregarded, and the bulk considered to be most likely ZnO. The Fermi level position for the highest conductive interface layer obtained in this study is calculated to be 266 meV above the CBM (Fig. 6.10.). The conductivity of 1.4×10^3 S·cm^{-1} achieved for the degenerate interface layer is close to the highest values achieved in Al/Ga doped ZnO films for similar carrier concentrations [54,230]. However, a simultaneous increase in the concentration of negatively-charged compensating defects, especially V_{Zn}, should occur due to lowering of their formation energies as the Fermi level increases close to the CNL ($E_{CNL} \approx 250 - 300$ meV above the CBM) in ZnO [10, 201].

For Fermi energies above this level, the formation of *p*-type defects such as V_{Zn} becomes energetically more favourable, based on the amphoteric defect model [14, 100]. In recent works [54, 56], the suppression of acceptor-like defects under self-compensation processes has been proposed by intentional doping to form dopant-defect complexes, *e.g.*, Ga_{Zn}-V_{Zn}, remaining a high carrier concentration and a mobility in a heavily doped ZnO. In the cation counter-diffusion processes, sufficiently driven by high temperature annealing, the inward diffused Zn atoms significantly reduce the oppositely charged compensating defects under recrystallization. This also leads to a high conductivity for the interface region of the annealed BZO film. The ratio of Be concentration to Zn, and the reaction time will be other important parameters to control the accumulation of donor-like defects.

Controlling the distribution of defects through atomic counter-diffusion processes in $Be_xZn_{1-x}O$ alloys and even in other oxides will be essential and promising in future applications such as nanoscale transparent conductive transistors, and in

the fabrication of core-shell alloy nanostructures such as quantum wells in nanowires and hollow nanotubes/nanoparticles.

6.4 Conclusion

We have demonstrated the effect of thermal treatment on a multi-phase crystalline BZO film. Thermal treatment (T_{A} = 600 – 950 °C) leads to recrystallization of the metastable alloy film along with the atomic redistribution and strain-relaxation. Thermally-induced lattice dissociation and out-diffusion (inward) of Be (Zn) result in a pronounced microstructural segregation and precipitation of donor-like defects such as $\mathrm{Zn_i}$. These observations are accompanied by a decrease in the band gap energy and lattice phonon energy of the BZO films. For $T_{\mathrm{A}} \geq 800$ °C, highly conductive layers with thicknesses in the range of 10 – 29 nm are generated at the near-interface region of the BZO film/$\mathrm{Al_2O_3}$ substrate. The plasma frequency of the interfaces range from 295 meV to 332 meV, corresponding to carrier concentrations from $n_{\mathrm{Int}} = 7.54 \times 10^{19}$ cm^{-3} to 2.16×10^{20} cm^{-3}.

The interface regions with such high carrier concentrations show degenerate characteristics with high conductivities in the range of $\sigma_{\mathrm{Int}} = 5.3 \times 10^2$ – 1.4×10^3 S·cm^{-1}. IR reflectance simulations and a parallel conduction model enable determination of the average effective mass of the conduction electrons in the interface layers which ranges from $0.31\mathrm{m_0}$ to $0.68\mathrm{m_0}$. As a result, the degenerate interface layers are found to significantly influence the electronic and optical properties of the BZO films. Such nanoscale interface conductivities achieved in the high-temperature annealed BZO films are comparable to the highest values obtained in doped ZnO. A cation counter-diffusion mechanism is proposed to interpret the high accumulation of donor-like defects and the subsequent formation of the degenerate interface layer within the annealed alloy films. This study extensively contributes to the understanding for the thermodynamics of defect engineering of metastable $\mathrm{Be}_x\mathrm{Zn}_{1-x}\mathrm{O}$ alloys, and opens up a new era for wide band gap oxide-based alloy applications.

Chapter 7

Self-Assembled Passivation of Semiconducting Oxides

7.1 Introduction

For the next generation of optoelectronic devices, oxide-based applications such as transparent electronic circuitry have recently received a great deal of interest. These materials have both high optical transparency, excellent thermal and electrical characteristics often under severe environmental conditions [1, 231]. Various wide band gap metal oxide semiconductors such as doped and undoped In_2O_3, SnO_2, TiO_2, and ZnO and their related ternary alloys have been extensively employed as integrated materials in a number of transparent optoelectronic applications [45, 232–234]. However, the intrinsic physical and chemical properties of these materials are strongly influenced by surface effects associated with stoichiometry, mechanical stress, and chemical interactions with environmental species [8, 100, 235].

Thermal vulnerability of these oxides also causes atomic diffusion, lattice distortions, and the subsequent formation of charged defects even under thermodynamic equilibrium [236, 237]. More crucially, interactions of environmental species with the dissociated oxide surfaces are facilitated by chemisorption. This leads to structural rearrangement of cation and anion sites and differing charge distribution states across the oxide surface. Such variations in the ionic positions and charge densities can create additionally surface states, which vary the inherent semiconducting characteristics (*e.g.* uniformity of carrier density and carrier transport) and limit the high-performance of oxide-based optoelectronics such as metal-oxide-based memory devices [238–240]. Hence, passivation of the surface of oxide materials to protect against thermal degradation and physiochemical coupling with ambient gas molecules is essential for the design of inert surfaces in the device architec-

ture [241, 242].

Phase transformations in metastable oxides and their mismatched heterostructures can modify initial material properties that potentially impact on macroscopic atomic diffusion, mechanical and thermal properties of the oxides [243–245]. These phase transformations occur by the minimization of the total free energy (Gibbs free energy) in the phase diagram, which is driven by overcoming an energy barrier under pressure and temperature [72,73]. This leads to the formation of new phases, secondary crystallization or mixed phases and/or spinodal decomposition [75, 76]. Constituent atoms diffuse towards either surface or interface areas, resulting in the nucleation of a secondary phase due to the chemical potential difference between the diffused/segregated solute and a solid phase under supersaturation [246, 247]. At this point, the particles can nucleate and grow preferentially at energetically favourable sites, *e.g.*, non-equilibrium sites: point defects/defect clusters, dislocations, and grain boundaries, rendering lower free energy by the crystal nucleation [68, 78]. Hence, interactions between the new phase and the surface of the thin film/nanocrystals significantly influence the thermodynamics and kinetics of its nucleation-and-growth, as well as the physical and chemical properties. Hence, understanding such phase transition phenomena and the growth kinetics of these secondary phase particles in various metal oxides is essential to realize and control their functionalities, *e.g.*, the size dependence for the control of surface-to-volume ratio of particles and an effective distribution of particles of different radii [88,94,248]. Moreover, with particle coarsening features, *e.g.*, combined/competitive growth stages between the nucleation and curvature-induced coarsening of these nanoparticles, effective methods have been developed to fabricate desirable nanocrystals with uniform size distributions [84, 249–251]. This enables the designing of novel nanostructures with distinct chemical and physical properties with numerous potential applications, for example, in nanoelectronics and energy storage media.

In this chapter, a novel approach to the passivation of reactive oxide surfaces by spontaneous formation of functional secondary phase nanoparticles (NPs) is demonstrated. This is achieved as a result of a phase transformation on a thermally-

recrystallized metastable oxide. Using the example of beryllium zinc oxide (BZO), the detailed kinetic mechanisms found in the alloy is presented and discussed. This is as a result of the surface Be concentration dependence on the nucleation-and-growth and the size-distribution of NPs. The functionalities of the NPs include passivation against thermal dissociation and surface chemisorption, are detailed experimentally and theoretically. The thermodynamic characteristics of the constituent atoms and physiochemical reactions at the surface of the transformed BZO observed experimentally have been also simulated by density functional theory (DFT) calculations of the atomic compensation and relaxation energies at the model metastable surfaces.

7.2 Experimental details and computational methods

7.2.1 Film growth and thermal treatments

Undoped ZnO and BZO(0.02 & 0.06) films were grown on Al_2O_3(0001) substrates by RF co-sputtering. Oxygen partial pressure was 2×10^{-3} mbar (base pressure = 1.8×10^{-8} mbar), the gas mixture was Ar 45 sccm:O_2 5 sccm, and growth temperature was 500 °C. Change in Be concentration of the BZO films were controlled by linearly adjusting the RF power to the Be metal target (99.9 %, 2-inch diameter, 1/4-inch thickness) from 30 to 40 W, while the RF power of the ZnO ceramic target (99.999 %, 2-inch diameter, 1/4-inch thickness) was fixed at 100 W. Prior to the film growth, surface contaminants of all the targets were removed using an RF power of 50 W. All the as-grown films were thermally treated at various temperatures between 600 °C and 950 °C for 60 min in a continuous flow of N_2 gas. All annealing temperatures were attained at a ramping rate of 20 °C/min.

7.2.2 Characterizations

Structural determination of the films were carried out by high-resolution and powder X-ray diffraction using a Panalytical X′Pert Pro MRD and a Panalytical X′Pert Pro MPD, respectively, with an incident beam hybrid monochromator giving pure Cu $K_{\alpha 1}$ radiation (λ = 1.5406 Å). Optical absorption was measured at normal incidence using a Perkin-Elmer Lambda 25 UV/Vis spectrometer, and sur-

face morphology was studied with tapping-mode AFM. XPS measurements were performed in ultra-high vacuum as detailed in Chapter 3 using a monochromatic Al K_α X-ray source ($h\nu$ = 1486.6 eV). For increased surface sensitive measurements, the emitted photoelectrons were collected with variable take-off angle (TOA, θ_{TOA}), $30^\circ \leq \theta_{\mathrm{TOA}} \leq 90^\circ$. Surface charging effects were compensated using a low energy electron flood gun. The binding energy scale was again calibrated to the C 1s core-level peak with the overall energy resolution of 0.47 eV. The XPS spectra were fitted using a Shirley background subtraction and Voigt line shapes. Compositional ratios of the elements (Zn, O, Be, and C) in the films were determined after correcting for the inelastic mean free path of photo-emitted electrons via the TPP-2M formula [133] and applying Scofield photoionized cross-sections [135].

Far- and Mid-IR reflectance spectra at an incident angle of 11° with respect to the surface normal were recorded in the range of 50 – 8000 cm^{-1} using a Bruker Vertex 70v Fourier transform infrared (FTIR) spectrometer. The thickness of the films was determined by simulating the reflectance spectra in a stratified medium with associated complex dielectric functions. The IR reflectance simulations were carried out utilizing the classical Drude model and factorized model considering the longitudinal-optical phonon-plasmon coupling, impurity modes, and the anharmonic effects in the complex dielectric function of the films.

Field emission transmission electron microscopy (FETEM, a Tecnai G2 F30 S-Twin) was used with an acceleration voltage of 300 kV to characterize the microstructural properties of the annealed BZO samples at T_{A} = 950 °C. Defect distribution in the ZnO and BZO films were plotted as a function of T_{A} by variable temperature (T = 12–300 K) photoluminescence measurements using a He-Cd laser (λ = 325 nm). The electrical properties of the films were characterized by performing variable temperature (T = 5–300 K) Hall effect measurements in the van der Pauw configuration. Indium solder was used to make ohmic contacts to all of the etched corners of the 5 × 5 mm^2 samples.

7.2.3 Computational calculations

First-principle calculations were performed based on density functional theory (DFT) within a local density approximation using the Cambridge Sequential Total Energy Package (CASTEP) [252, 253]. A plane-wave basis set with a kinetic energy cut-off of 400 eV was employed and the electron-ion interactions were formulated using ultra-soft pseudopotentials. After geometrical optimization of the unit cell, the equilibrium lattice parameters for wurtzite ZnO were obtained to be $a = 3.185$ Å and $c = 5.149$ Å, respectively. A vacuum spacing of 20 Å was introduced in the z-direction to prevent inter-slab interactions. The surface was modelled by eight ZnO double layers allowing structural relaxation within a slab supercell of the four uppermost double layers. All calculations were carried out using 3×3 supercells composed of approximately 150 atoms. Numerical integrations over the Brillouin zone were performed only at the Γ-point due to the large size of the supercells. The atomic positions in all the supercells were continually relaxed to the residual forces below than 0.05 eV/Å. In the modelled ZnO slab supercells, any charge transfer from the uppermost O layer to the lowest Zn layer induced by the net dipole moment and electrostatic field across the slab was corrected by altering the valency of the Zn atoms on the lowest layer to +1.5 [47, 48]. Other surface stabilization processes accompanied by atomic reconstructions (atomic removals and/or the formation of islands) or additional H^+ and OH^- adsorption on the residual surface atoms were ruled out. The chemical adsorption energy, E_{ads}, (atomic substitution energy, E_{sub}) at the surface, namely, the energy released during chemisorption (substitution) corresponds to the binding energies of V_{ZnO} and H_2O (BeO). For quantitative evaluation, the average energy values are defined as

$$<E_{\text{ads}}> = (E_{\text{ads},N\text{H}_2\text{O}} - E_{N\text{V}_{\text{Zn-O}}} - N\mu_{\text{H}} - N\mu_{\text{OH}})/N, \tag{7.1a}$$

$$<E_{\text{sub}}> = (E_{\text{sub},N\text{BeO}} - E_{N\text{V}_{\text{Zn-O}}} + N\mu_{\text{O}} - N\mu_{\text{Be}})/N, \tag{7.1b}$$

$$E_{N\text{V}_{\text{Zn-O}}} = E_{\text{ZnO}}^{\text{Perf}} - N\mu_{\text{Zn}} - N\mu_{\text{O}}, \tag{7.1c}$$

where $E_{\text{ads},N\text{H}_2\text{O}}$ ($E_{\text{sub},N\text{BeO}}$) is the total energy of the ZnO slab supercells that contains N number of adsorbed H_2O (substituted BeO). $E_{N\text{V}_{\text{Zn-O}}}$ is the total energy

of the ZnO slab supercells with the N number of V_{Zn-O}, $E_{ZnO}^{Perf} - N\mu_{Zn}$ is the total energy of the ZnO supercell without any vacancies. μ defines the associated chemical potential. The average adsorption (substitution) energy gain per H_2O (BeO) is related to the change in the surface energy, $\Delta\gamma_{sur}$, via

$$\Delta\gamma_{sur} = E_{ads/sub} \cdot \theta_{VC}, \theta_{VC} = N/A, \tag{7.2}$$

where A is the surface area of the ZnO slab.

7.3 Results and discussion

7.3.1 Variations in the optical band gap energy and surface chemical composition with T_A

The BZO alloy films with different Be concentrations, $x = 0.02$ and 0.06, were grown on $Al_2O_3(0001)$ substrates, and are signified as BZO(0.02) and BZO(0.06). Be-concentration-dependent lattice shrinkage and band gap widening were observed in the as-grown BZO films as result of a chemical alloying of ZnO and BeO (Fig. 7.1.) [190]. To investigate the thermodynamics of the metastable BZO thin films, the strain relaxation and the subsequent phase transformations in the alloy films were systematically enforced by varying post-annealing temperatures, $T_A = 600 - 950$ °C.

In order to study the effect of annealing on the optical properties of the $Be_xZn_{1-x}O$ films ($x = 0.02$ and 0.06) compared to the undoped ZnO, the optical transmittance, T_O, of the films was used to calculate the absorption coefficient, α, by $T_O = A\exp(-\alpha D)$, where A is a transmission constant, and D is the film thickness [138]. Figure 7.2a shows α^2 as a function of photon energy for different Be concentration and T_A. The absorption edges were determined by linear extrapolation of the sharp onset to the horizontal portion of the spectra. The absorption edge of the as-grown films are shifted to higher energies with increasing Be composition along with an increase in the tailing of the spectra. These optical features are associated with a band gap widening induced by the incorporation of Be in the host ZnO lattice and Be-induced structural deterioration (see Fig. 7.1.).

Significant changes in the position and tailing of the optical absorption edge

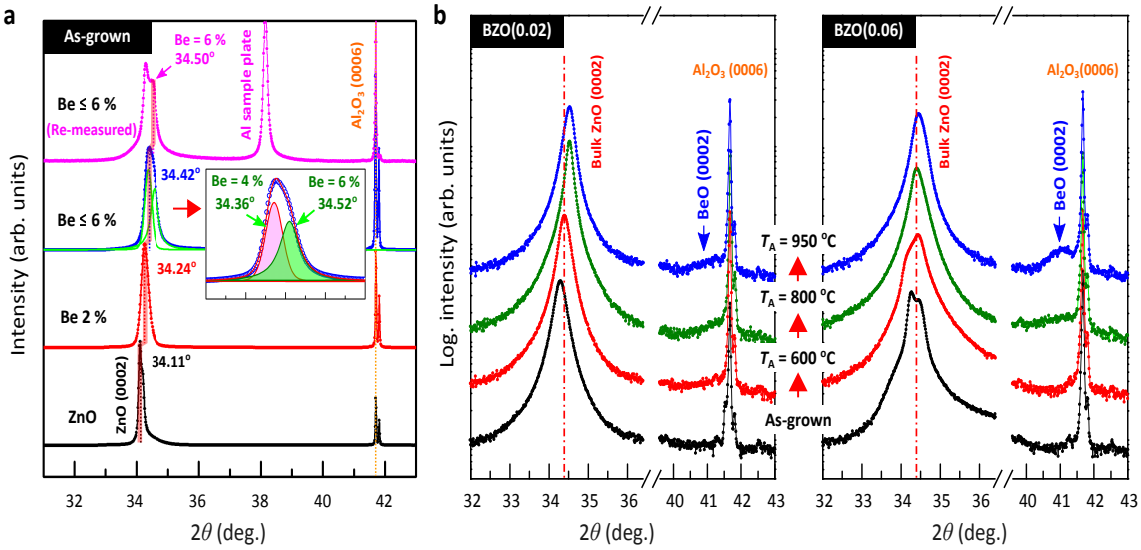

Figure 7.1: XRD θ-2θ patterns for (a) the as-grown ZnO and BZO(0.02 and 0.06) films and for (b) the as-grown and annealed BZO films on Al_2O_3(0001) as a function of T_A.

in the ZnO and $Be_xZn_{1-x}O$ films were observed with increasing T_A. As can be seen in Fig. 7.2b, the absorption edge, which corresponds to the optical band gap energy of the as-grown and annealed ZnO films, increases up to a temperature of 800 °C, while the energy decreased with further increasing T_A. The former is usually due to an increase in thermally-induced donor-like point defects and the subsequent conduction band-filling (Burstein-Moss effect) in the annealed films [108, 254]. The latter primarily arises from the thermal decomposition and the resulting structural deterioration of the ZnO lattice. This causes compensation of the conduction electrons through the introduction of the deep acceptor levels in the band gap together with tailing of the conduction band [54]. The red-shift of the optical band gap leads to an insulating behavior in the high-temperature-annealed ZnO films ($T_A \geq 900$ °C) and in turn no optical response was found at $T_A = 950$ °C. On the other hand, a continuous decrease in the optical band gap energy of both BZO films was found with T_A mainly due to loss of Be from the film bulk as a result of atomic redistribution and lattice strain relaxation presented in Chapter 6 [101]. However, it should be noted that the optical values obtained from the annealed alloy films are additionally affected by the many-body interactions, namely, electron-electron and electron-phonon interactions, which result in band gap renormalization [101, 109, 110].

Figure 7.2c shows the normalized XPS Zn 3s and Be 1s core level spectra for the BZO(0.02 and 0.06) films as a function of T_{A}. The spectral position of Be 1s at the binding energy of 114.3 eV indicates the chemical bonding of Be-O as a result of Be incorporation into the host ZnO [190]. The Be 1s peak intensity for both the alloy films gradually increases with T_{A} up to 950 °C. The atomic concentration of Be at the surface of the films was determined as a function of T_{A} by quantitative analysis of the intensity area of the O 1s, Zn 3s, and Be 1s core level peaks, taking into account the inelastic mean free path of photo-excited electrons and relative sensitivity factor for each element in the medium [133]. Figure 7.2d shows an increase in the ratio of Be to Zn, Be/(Zn+Be), from 0.10 [0.24] to 0.27 [0.51] for BZO(0.02) [BZO(0.06)] as T_{A} increased up to 950 °C. It is worthy of mention that the initial Be composition at the surface of the as-grown $\mathrm{Be}_x\mathrm{Zn}_{1-x}\mathrm{O}$ films is higher than that in the bulk (Fig.7.1b), due to surface segregation and removal of constituent atoms on the polar surface to reduce the surface energy [46,48]. Consequently, these opposing trends between the decrease in the optical band gap energy and the increase in the surface Be concentration with T_{A} are indicative of the out-diffusion of Be from the bulk to the surface through recrystallization, resulting in a lower Be composition in the bulk.

To further evaluate the atomic segregation/diffusion features at the surfaces of the BZO(0.02 and 0.06) films annealed at T_{A} = 950 °C, angle-dependent XPS measurements were carried out. The XPS spectra were collected by varying the TOA of photo-emitted electrons within the probing geometry (see the inset of Fig. 7.3a) to increase the XPS surface sensitivity. Figure 7.3a also shows the normalized XPS Zn 3s and Be 1s core level spectra for the annealed BZO films. The Be 1s peak intensity increases with decreasing θ_{TOA}, indicating the upward gradient of Be concentration conducive to the formation of surface NPs. From XPS quantitative analysis, the concentration gradient of Be at the surfaces was determined to range from 27 % [51 %] to 49 % [66 %] for the annealed BZO(0.02) [BZO(0.06)] as TOA decreased from $\theta_{\mathrm{TOA}} = 90°$ to 30° (Fig. 7.3b). In order to determine the depth-dependent Be composition at the surface, the inelastic mean free path, IMFP (λ), for the Be 1s core

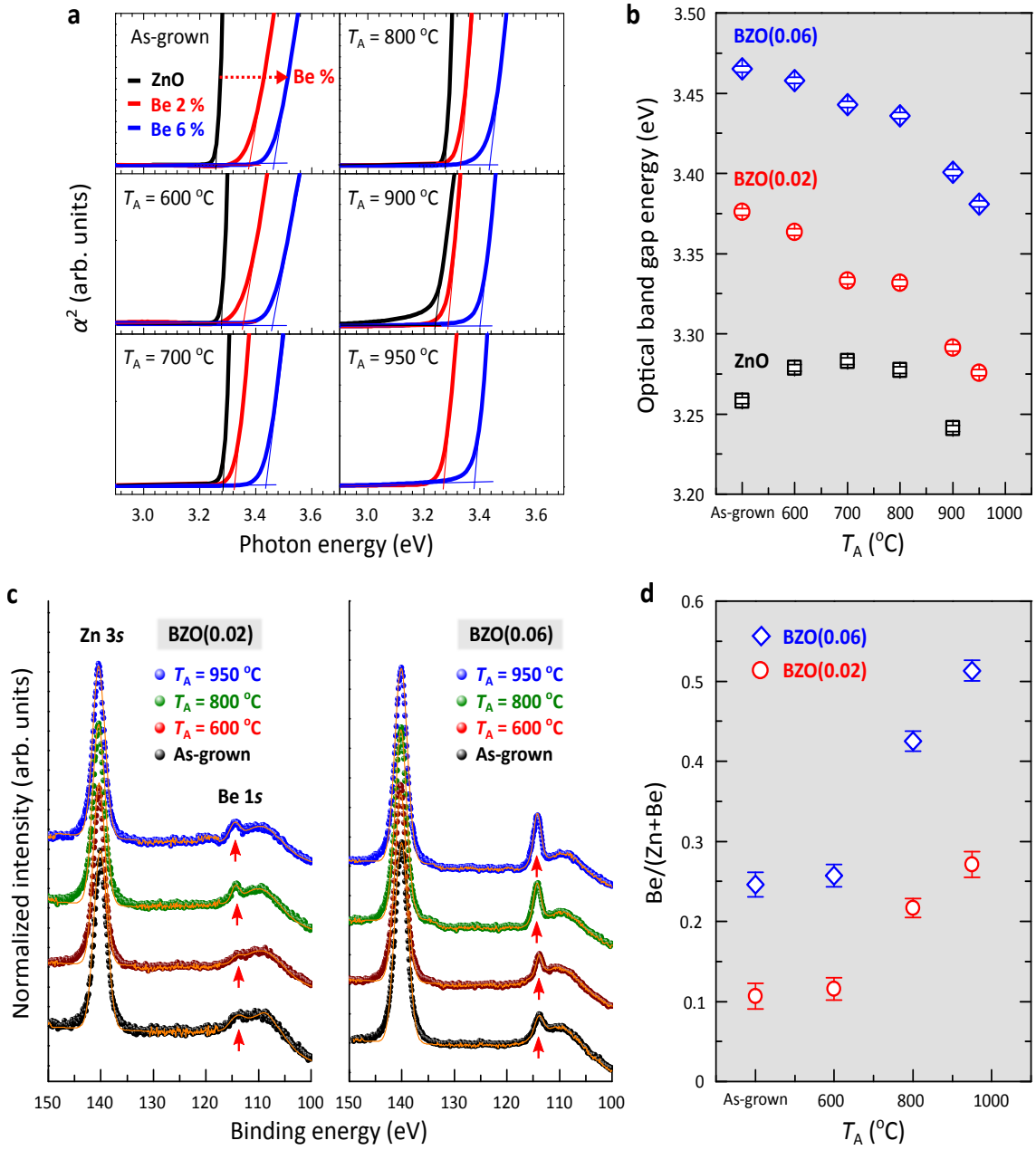

Figure 7.2: (a) Square of the absorption coefficient, α^2 as a function of photon energy obtained from the transmittance spectra of the as-grown and annealed ZnO and BZO(0.02 and 0.06) films with different T_A. (b) Comparison of the optical band gap energy of the films as a function of T_A. (c) Normalized XPS spectra of Zn 3*s* and Be 1*s* core levels for the as-grown and annealed ZnO and BZO films at different T_A. All the spectra were collected at normal emission and normalized to have the same intensity of the Zn 3*s* peaks. The red-arrows correspond to the binding energy of Be-O bond around $E_B \approx 114$ eV. (d) The profiles of Be to Zn ratio, Be/(Zn+Be), at the surface of the films with T_A.

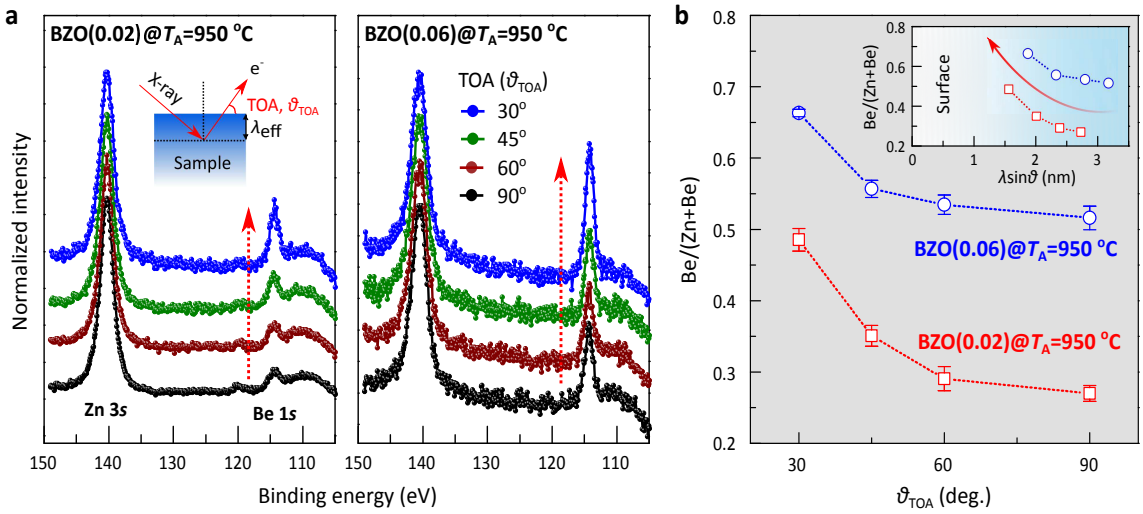

Figure 7.3: (a) Normalized XPS spectra of Zn 3*s* and Be 1*s* core levels with varied θ_{TOA} from 90° to 30° for the annealed BZO(0.02 and 0.06) films at $T_{\mathrm{A}} = 950$ °C. All the spectra were normalized to have the same Zn 3*s* peak intensity. The inset in the left panel is a schematic of the X-ray photoemission geometry. (b) The TOA dependence of the surface Be to Zn ratio, Be/(Zn+Be), for the annealed BZO films. The inset shows the depth profile of surface Be to Zn ratio. The TPP-2M formula was employed to calculate the effective inelastic mean free path, λ_{eff}, of photo-emitted electrons from Be 1*s* by Al K_α excitation energy using the approximated density of BZO medium.

level spectra was approximated as a function of varying the Be concentration and was calculated using the TPP-2M equation: Different densities in the surface region due to varying Be concentrations were considered in this approximation [133]. The depth profile of Be concentration in the NPs was attained using $\lambda_{\mathrm{eff}} = \lambda \sin\theta$ (nm), where λ_{eff} (effective IMFP) and θ_{TOA} are variable parameters, respectively, as shown in the inset of Fig. 7.3b. These results provide direct evidence of accumulation of BeO NPs at the surface of the transformed alloy films.

7.3.2 Formation of secondary phase NPs at the surface of the BZO films with T_{A}

On the basis of the transient atomic redistribution in the annealed BZO films, variations in the surface morphology with T_{A} were investigated. Figure 7.4a shows the AFM topographic images (1×1 μm^2) for thermal structural evolution at the surface of the BZO(0.02) films as a function of T_{A}. The formation of NPs was clearly seen with higher densities near grain boundaries for $T_{\mathrm{A}} = 600$ °C (see the inset for

the phase image, 0.5×0.5 μm^2). This is because mass transport mainly occurs along the grain boundaries rather than the basal surface of films and the atomically imperfect defects are active nucleation-and-growth sites [255, 256]. The surface NPs migrate towards bigger ones for $T_A = 800$ C due to Ostwald ripening (OR), driven by the difference in their chemical potentials [87, 251]. A continuous growth of NPs was observed at the surface ($T_A = 950$ C). As a result, the formation of NPs at the surface of the films is attributed to atomic segregation, bulk and surface diffusion, and the nucleation of NPs with subsequent clustering predominantly near the grain boundaries.

To further clarify the formation and crystalline nature of the NPs at the surface, TEM measurements were carried out for the annealed BZO(0.02 and 0.06) films at $T_A = 950$ C. Figure 7.4b shows the cross-sectional TEM images for the annealed BZO films. The thickness of the films was found to be 101±12 and 152±8 nm, respectively. The films consist of three distinct regions; (*i*) NP-distributed surface, (*ii*) the bulk film, and (*iii*) an interfacial layer. By comparing the images, it is seen that the density of NPs at the surface increased with an increase in Be concentration in the annealed BZO films. Dark field STEM measurements were performed to obtain the compositional configuration in the annealed BZO films. The upper image of Fig. 7.4c shows the *Z*-contrast STEM for the BZO(0.06) film annealed at $T_A = 950$ C. A pronounced contrast is observed between the surface and bulk of the film due to the accumulation of lighter Be atoms at the surface relative to the larger Zn atoms [145]. The darker spots in Fig. 7.4. are distributed across the main film with an upward density gradient to the surface. These again directly indicate the out-diffusion and local segregation of Be towards the surface of the film during high-temperature annealing. It was also found that the surface NPs were pinned at the surface as shown in the lower TEM image of Fig. 7.4c. To evaluate the crystalline feature of the surface NPs, high-resolution TEM and Fast-Fourier transform (FFT) were performed for the surface of the films (Fig. 7.4d). The filtered FFT images correspond to the red squares I and II in the NP and adjacent layers in the film, indicate that both crystalline phases have *c*-axis wurtzite structures. The

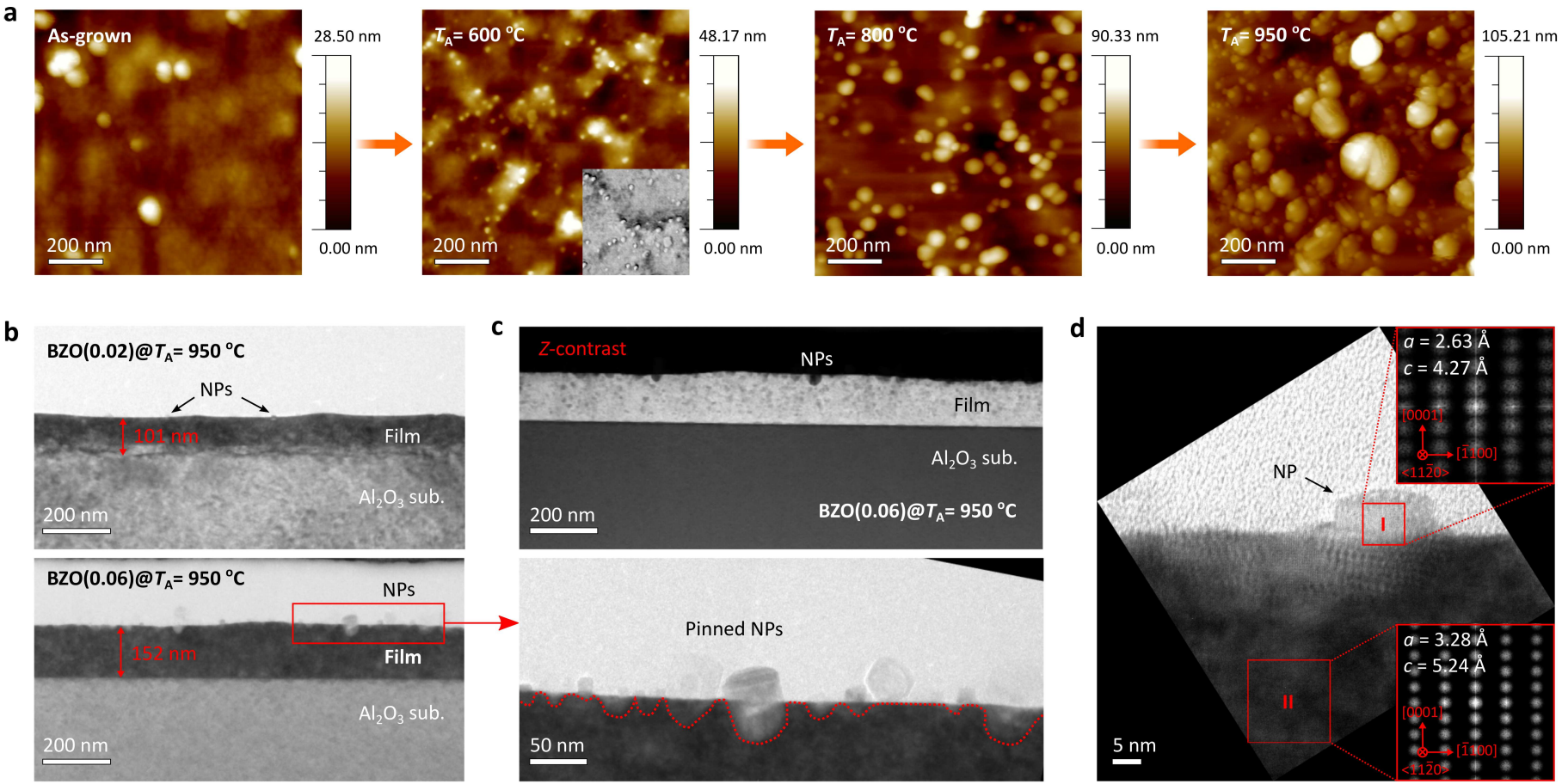

Figure 7.4: (a) AFM topography (1×1 μm^2) images for the as-grown and annealed BZO(0.02) films (T_A = 600 – 950 °C). The insets is a phase image (0.5×0.5 μm^2) of the film annealed at T_A = 600 °C. (b) Cross-sectional TEM images of the BZO(0.02 and 0.06) films annealed at T_A = 950 °C. The thickness of the films was determined to be 101±12 nm and 152±8 nm, respectively. (c) The top image is a Z-contrast dark field STEM image for the annealed BZO(0.06) film. The bottom is a magnified TEM image for the surface of the film corresponding to the red rectangular in the bottom image of (b). The red-dot line is a guide to the eye for the transparent NPs at the surface. (d) High resolution TEM image along with the <11$\bar{2}$0> zone-axis at the surface of the annealed BZO(0.06) film. The right-top and right-bottom insets are Fast-Fourier transforms (FFTs), which correspond to the red-square areas, I and II, inside the surface NP and the film layers underneath, respectively. The FFTs were filtered masking 0001 and 1$\bar{1}$00 reflections. The calculated a- and c-lattice parameters for each area, obtained by extracting the plane spacings, were denoted in the insets.

Table 7.1: The thicknesses (d) and thermal dissociation ratio (d_s/t) of the undoped ZnO, BZO(0.02), and BZO(0.06) films as a function of T_A.

	ZnO		BZO(0.02)		BZO(0.06)	
T_A (°C)	d (nm)	(d_s/t) (Å/sec)	d (nm)	(d_s/t) (Å/sec)	d (nm)	(d_s/t) (Å/sec)
As-grown	220±7	...	270±7	...	212±8	...
600	222±7	...	272±7	...	209±6	...
700	215±5	0.014	268±5	0.005	208±6	0.005
800	170±3	0.125	243±5	0.083	195±4	0.034
900	69±4	0.419	165±2	0.292	160±2	0.147
950	25±3	0.542	110±3	0.444	144±3	0.205

lattice parameters for the NPs were determined to be $a = 2.63$ Å and $c = 4.27$ Å based on the spacing of (0001) and $(1\bar{1}00)$ planes, while those for the surface layers of the film were $a = 3.28$ Å and $c = 5.24$ Å. The lattice parameters obtained for the NP are similar to that of hexagonal BeO ($a = 2.69$ Å and $c = 4.37$ Å) [257]. In addition, the lattice parameters of the film layers underneath are close to those of bulk ZnO ($a = 3.25$ Å and $c = 5.20$ Å). These results suggest that the surface NPs are mainly composed of Be and O forming BeO crystals as a result of the out-diffusion of Be from the bulk towards the top surface (Figs. 7.2 and 7.3).

7.3.3 Be-concentration-dependent film thickness and thermal dissociation

The thermal resistance on the thickness of the ZnO and BZO films was examined as a function of T_A by performing infrared (IR) reflectance measurements and simulation (Chapter 3) [101]. The thicknesses and the dissociation rates [the sublimated thickness of the films (d_s)/annealing time (t)] of the films with different T_A, obtained from the modelling, are presented in Table 7.1.

Figure 7.5a shows the thickness variations of the ZnO and BZO(0.02 and 0.06) films with different T_A. The plot is divided into region-I, $T_A \leq 700$ °C, and region-II, $T_A \geq 700$ °C. No significant change in the thickness of the films was found in region-I. By contrast, in region-II, the thickness of the undoped ZnO films decreased considerably as T_A increased up to 950 °C. The rate of the thickness

decrease in the BZO alloy films was lowered by increasing the Be concentration. This is indicative of Be-induced variations in thermal decomposition BZO relative to pure ZnO. Figure 7.5b shows Arrhenius plots of the dissociation rate of the films with respect to inverse annealing temperature, $1000/T_{\mathrm{A}}$; all values were deduced by the above thickness variation as a function of T_{A}. The activation energies, E_{A}, for dissociation of the films were extracted from decomposition kinetics by applying a zero-order rate law in a single direction, $d_{\mathrm{s}}/t = C_{\mathrm{A}}\exp(\text{-}E_{\mathrm{A}}/k_{\mathrm{B}}T_{\mathrm{A}})$, where C_{A} is the Arrhenius pre-exponential factor and k_{B} is the Boltzmann constant [69]. The Arrhenius kinetic parameters, E_{A} is proportional to the enthalpy of reaction [258]. This estimated E_{A} from the decomposition reaction rate of the undoped ZnO film to be 1.60±0.05 eV, which is close to the Zn-O bond strength of 1.64 eV/molecule [259]. Hence, the reduction of the film thickness is directly proportional to the thermal dissociation of the ZnO lattice during annealing. The thermal E_{A} of decomposition in the BZO films increased up to 2.12±0.18 eV with increasing Be concentration. This increase results from two correlated factors: (*i*) the effective coverage of atomic diffusion pathways (*e.g.* surface and grain boundary areas) by nucleated/grown BeO NPs preventing the thermal evaporation of diluted atoms and (*ii*) stronger bonding energy of BeO than that of ZnO [211].

The high-temperature lattice dissociation and atomic diffusion/sublimation were expected to produce lattice defects in the annealed films. Photoluminescence (PL) measurements performed at 12 K show deep level emissions in the as grown and annealed ZnO and BZO(0.06) films (T_{A} = 600, 800, and 950 °C) as shown in Fig. 7.5c. Two predominant deep band emissions (DBE) were found in both of the ZnO and BZO films around 2.09 and 1.88 eV, respectively. Amid the controversy of defect-associated DBE in ZnO, we assign these two bands to V_{Zn}-related defect emissions considering the above atomic dissociation processes in high temperatures and the subsequent formation of V_{Zn} clusters in the films. No strong emission of around 2.4 eV was attributed to V_{O}, however, it was observed from all the samples [260]. Similar emission features have been observed in annealed ion-implanted ZnO [149, 152, 202]. Thus, those two DBEs could be responsible for optical transi-

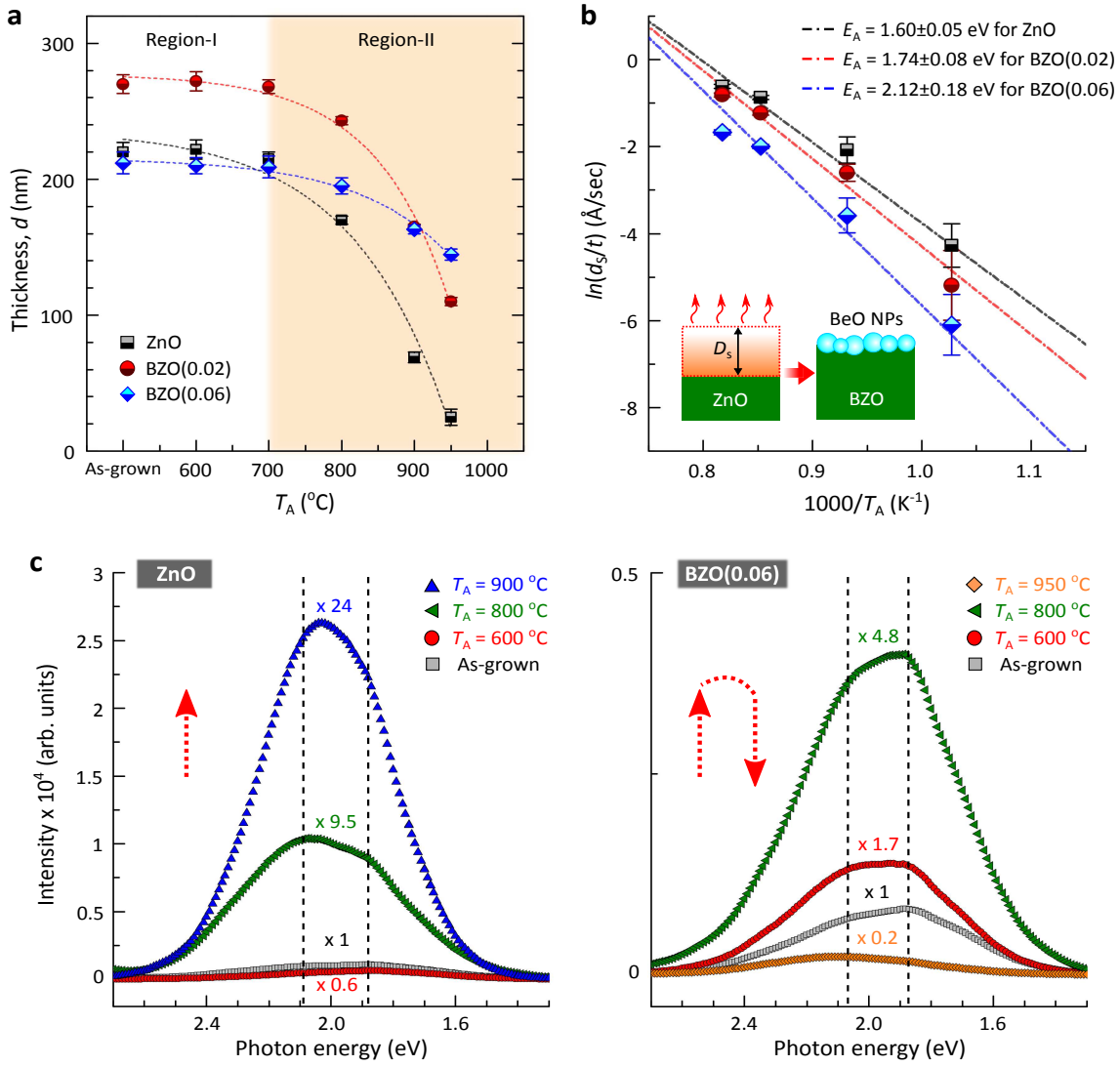

Figure 7.5: (a) Variations in the thickness of the undoped ZnO and BZO(0.02 and 0.06) films as a function of T_A. (b) Thermal dissociation rates with different T_A for ZnO [black-filled squares], BZO(0.02) [red-filled circles], and BZO(0.06) [blue-filled lozenges]. Data points are derived from D_s/t, where D_s and t are the sublimated thickness of the films and annealing time, respectively. Dash-dot lines represent the Arrhenius plots for thermal dissociation rates of the films with corresponding activation energies, E_A. (c) Low temperature (12 K) PL spectra for deep level emissions in the as-grown and annealed ZnO (T_A = 600, 800, and 900 °C) and BZO(0.06) films (T_A = 600, 800, and 950 °C).

tions from the ZnO/BZO conduction band (residual shallow donors such as Zn_i) to energy states of the vacancy cluster defects below by 2.1 eV (1.9 eV). The intensity of the defect-related DBE in the ZnO films is considerably increased by more than one order of magnitude for temperatures up to $T_A = 900$ °C. This reveals that high-temperature annealing facilitates the formation of V_{Zn} clusters, corroborating the thermal atomic dissociation and diffusion model together with the thickness reduction in the films for high T_A. On the other hand, the DBE intensity in the annealed BZO film increases up to $T_A = 800$ °C (lower intensity compared to that of ZnO), then, falls remarkably at $T_A = 950$ °C. Such a turn-over in the population of V_{Zn} has been addressed by counter-diffusion of cations, *i.e.*, outward (inward) diffusion of Be (Zn), and the following effective compensation of vacancy defects in the fully-transformed BZO alloy films (as discussed in Chapter 6).

7.3.4 Nucleation and growth of BeO NPs at the surface of the annealed BZO alloy films

The observation of thermally-induced recrystallization of these metastable BZO alloy films shows that annealing causes a phase transformation in the alloy in conjunction with lattice strain relaxation and a redistribution of the constituent atoms [101]. This corresponds with a shrinkage of the band gap energy in the bulk towards pure ZnO and an enrichment of Be at the surface. Such a phase transformation in a highly mismatched alloy system is typically due to the solubility limit of Be and low thermal stability under a miscibility gap, necessary to minimize the total free energy. During the annealing process, significant upward diffusion of Be occurs from the bulk to the surface together with the dissociation of Zn-O bonds. Hence, the constituent atoms, Zn, Be, and O, diffuse along the surface and grain boundaries that are effective pathways for atomic transport. Since the vapour pressure of Be is much lower than that of Zn, the out-diffusing Be atoms predominantly accumulate at the surface and at grain boundaries, while the dissociated Zn atoms evaporate. This leads to the observed increase of Be and the subsequent segregation at the surface, reaching the critical supersaturation level and giving rise to the secondary

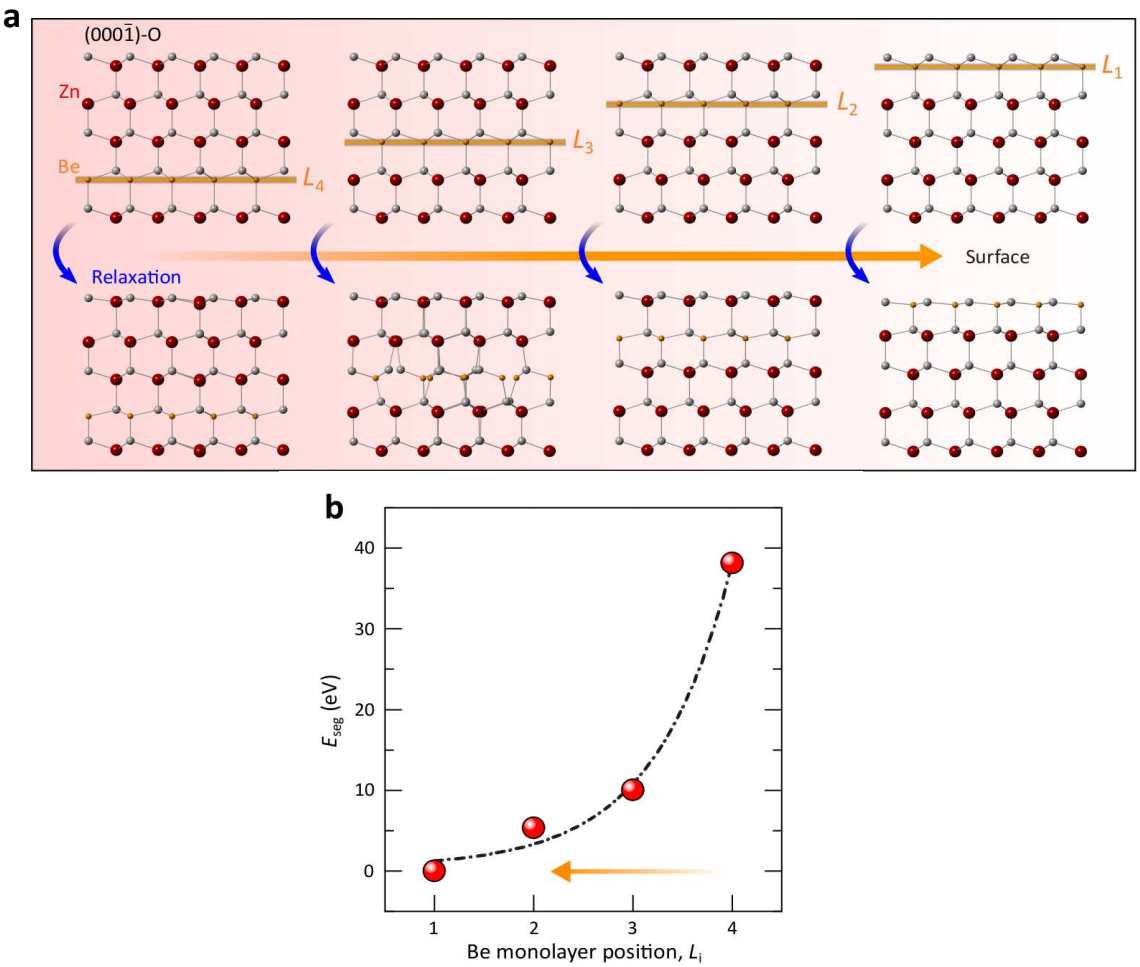

Figure 7.6: (a) Side views modelled for the four different atomic configurations with different full-Be monolayer positions (L_4–L_1) in O-terminated ZnO(000$\bar{1}$) slab supercells. Upper (lower) models represent as-constructed slab supercells (relaxed supercells). (b) The Be segregation energy profile calculated for four different atomic configurations corresponding to the position ($L_{i=1-4}$) of the Be monolayer within an O-terminated surface of wurtzite ZnO slab.

phase nucleation of BeO nanoparticle.

To simulate the energetics of the Be out-diffusion, density functional theory (DFT) calculations were performed modelling ZnO slabs with repeated substitution of Be into all Zn sites across a single cation monolayer from the uppermost surface, L_1, down to the inner layers; four cation-monolayers were taken into account, $L_1 - L_4$ (Fig. 7.6a). The Be segregation energies calculated by $E_{\text{seg}} = E(L_{i=1-4}) - E(L_1)$ show a significant increase when the substitute Be monolayer takes up lower Zn monolayer positions as illustrated in Fig. 7.6b. The tendency for Be segregation at the surface corresponds to the thermodynamic stabilization of the alloy

films, which is in good agreements with our experimental observation of Be transport toward the surface. Later, as the free energy, E^{F}, for the formation of BeO ($E^{\mathrm{F}}_{\mathrm{BeO}}$ = -5.839 eV at 0 K) is much lower than that of ZnO ($E^{\mathrm{F}}_{\mathrm{ZnO}}$ = -3.438 eV at 0 K), the diffused/segregated Be atoms preferentially react with thermally dissociated/diffused oxygen to form the energetically favourable BeO phase. These theoretical results corroborate the out-diffusion of Be, surface segregation, and the succeeding formation of secondary phase BeO NPs at the surface of the annealed BZO films.

In the classical nucleation theory (CNT), the kinetics of the BeO nucleation reactions is primarily described by: (*i*) the mobility of the Be and O atoms for structural attachments, which is significantly enhanced with temperature, and (*ii*) the total Gibbs free energy change, $\Delta G(R_{\mathrm{n}})$, for the formation of the nuclei [68, 84, 85, 88]. Assuming a spherical shape for BeO crystal within the parent BZO phase, $\Delta G(R_{\mathrm{n}})$ is given by

$$\Delta G(R_{\mathrm{n}}) = 4\pi R_{\mathrm{n}}^2\gamma - \frac{4}{3}\pi R_{\mathrm{n}}^3\Delta G_{\mathrm{V}} + \Delta G_{\mathrm{s}} - \Delta G_{\mathrm{d}}, \tag{7.3}$$

where R_{n} is the radius of the nucleus and γ is the surface tension (related to the free energy change for the formation of a solid BeO surface). The free energy change per unit volume, ΔG_{V}, of a BeO crystal for the formation of the nucleus dependent on the temperature (T) and solute supersaturation, S, according to $\Delta G_{\mathrm{V}} = k_{\mathrm{B}}T\ln(S)/v_{\mathrm{m}}$, where v_{m} is the molar volume of the bulk crystal. ΔG_{s} is a finite misfit strain energy per unit volume proportional to the volume of the inclusion and ΔG_{d}, the energy of pre-existing defects in the volume, means that some free energy is released through the destruction of the defects by the creation of the nucleus. The critical free energy of the stable BeO nucleus, ΔG_{c}, with respect to R yields an equilibrium size, R_{c}, from the relation, $d\Delta G(R)/dR = 0$. The critical radius, R_{c}, represents the minimum size of a stable BeO nuclei that allows them to endure and continue to grow; values below R_{c} would lead to dissolvation of the nuclei. Thus, nucleated BeO particles need to surpass a thermodynamic energy barrier ($\propto \gamma^3/\Delta G_{\mathrm{V}}^2$) for the growth of secondary phase nuclei.

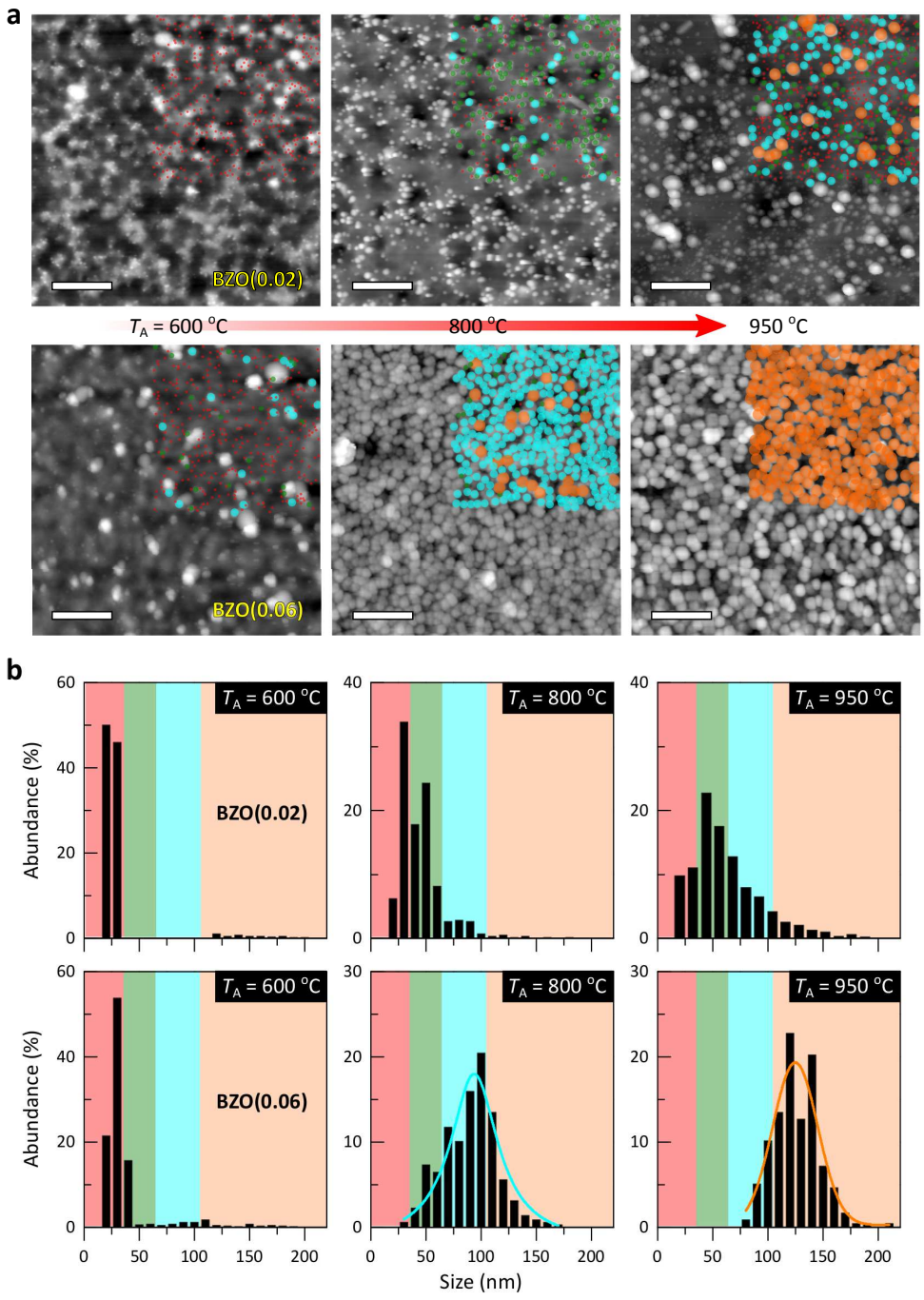

Figure 7.7: (a) Topographic AFM images (3×3 μm^2) for the surface morphology of the BZO(0.02) [upper panel] and BZO(0.06) [lower panel] films annealed at $T_A = 600 - 950$ °C. Scale bar, 600 nm. The size difference of the surface NPs in the top-right square area of each image are differentiated by color: red dots correspond to a size of $\sim$ 30 nm; green dots, $\sim$ 50 nm; blue dots, $\sim$ 100 nm; orange dots, $\sim$ 120 nm. (b) The relative particle size distributions of the grown NPs at the surface of the annealed alloy films.

In the classical approach to Ostwald ripening (OR) derived from Lifshitz, Slyozov, and Wagner (LSW) theory for particle growth under low supersaturation and quasi-steady-state limit, the driving force of OR is a decrease in the solubility of particles with increasing their radius, R_g. The growth of larger particles is at the expense of smaller dissolving particles due to the high solubility and surface energy of smaller particles [92, 93]. Furthermore, the surface reaction-limited particle growth normally gives rise to an asymmetric particle size distribution. Therefore, in most NP growth processes, nucleation and growth of particles concurrently occur throughout particle formation and hence the final particles show a broad size distribution as can be seen in Fig. 7.4a.

Here, the growth characteristics and associated size distribution of the secondary phase BeO NPs are investigated. These are originated from the thermally induced phase transformation of the BZO films according to the above nucleation-and-growth kinetic theory of NPs. Figure 7.7a shows AFM images (3×3 μm^2) of the temperature-dependent (T_A = 600 – 950 °C) variations in the growth and size distribution of the BeO NPs at the surface of the annealed BZO films (x = 0.02 and 0.06). The images show a gradual growth of the particles at the surface of the alloy films with T_A. More interestingly, distinct size distributions of the grown NPs are observed in the annealed alloy films with different initial Be compositions (Fig. 7.7b). The particle-size-distribution (PSD) of the NPs is broadened at the surface of low Be content alloy films as it displays a gradual growth of the particles at the surface of the films with T_A. This is associated with the typical OR effect in a transient growth regime. By contrast, the narrowing of the PSD together with increasing the average NP size are seen for the alloy films with high Be composition. PSD evolution of the NPs suggests that different NP growth characteristics induced by varied growth kinetic factors such as the supersaturation level, resulting from different Be concentrations at the surface as a function of T_A.

To interpret these distinct NP growth features with different surface Be concentrations, a correlation between the growth mode and PDS of the BeO NPs in the annealed BZO(0.06) films is deduced. As can be seen in Fig. 7.8a, the mean size,

$<G>$, of the BeO NPs is increased monotonically from $\sim$ 37 nm at T_{A} = 600 °C to $\sim$ 125 nm at T_{A} = 950 °C. This is accompanied by a linear increase in Be concentration and a narrowing of the PSD at the surface. The change in Be concentration ratio in Fig. 7.8a is defined by $C_f^{\mathrm{Be}}/C_i^{\mathrm{Be}}$, where C_f^{Be} and C_i^{Be} are the measured Be concentration in the annealed samples in the steady-state regime and the initial concentration of the as-grown sample, respectively. This reveals that the BeO NP growth rate, J_{G}, primarily depends on the degree of Be solute supersaturation at the surface. Therefore, Be acts as the growth rate controller assuming there is no concentration gradient in the oxygen for the diffusion process of Be and O atoms into a BeO compound precipitate of radius, R, within the steady-state approximation [261].

In the LaMer mechanism, the nucleation and growth stages for the formation of NPs are mainly dependent on two mechanisms: diffusion-controlled growth and reaction-controlled growth [92, 95]. In the former, all monomers participate in the nucleation processes and thus the mean NP size is dependent on S, while the latter mechanism is particle-size-dependent (the curvature-induced surface reaction of the particles). However, if the particle growth takes place in the transient growth regime before either OR or the equilibrium between the particles and monomers, the focusing of PSD is possible to continue in the diffusion-controlled growth mode by modifying the kinetics of the reactions (a steep drop of growth temperature or hot injection of participates or additional/continuous injection of participates). This would lead to inhibition of the nucleation of new NPs and the defocusing period of the NP growth. These effective approaches maintain the simultaneous diffusion-controlled particle growth and the resultant narrowing of the PSD, and have been widely applied for the mono-disperse formation of various colloidal particles [86–88]. In this study, given that a substantial amount of the out-diffused Be from the bulk (a high Be supersaturation) continuously participates in the growing of NPs. In the diffusion-controlled-particle-growth, the additional/continuous injection of Be solutes predominantly favours the focusing of the PSD of the BeO NPs with a larger mean size until the completion of the reaction/growth processes after the samples

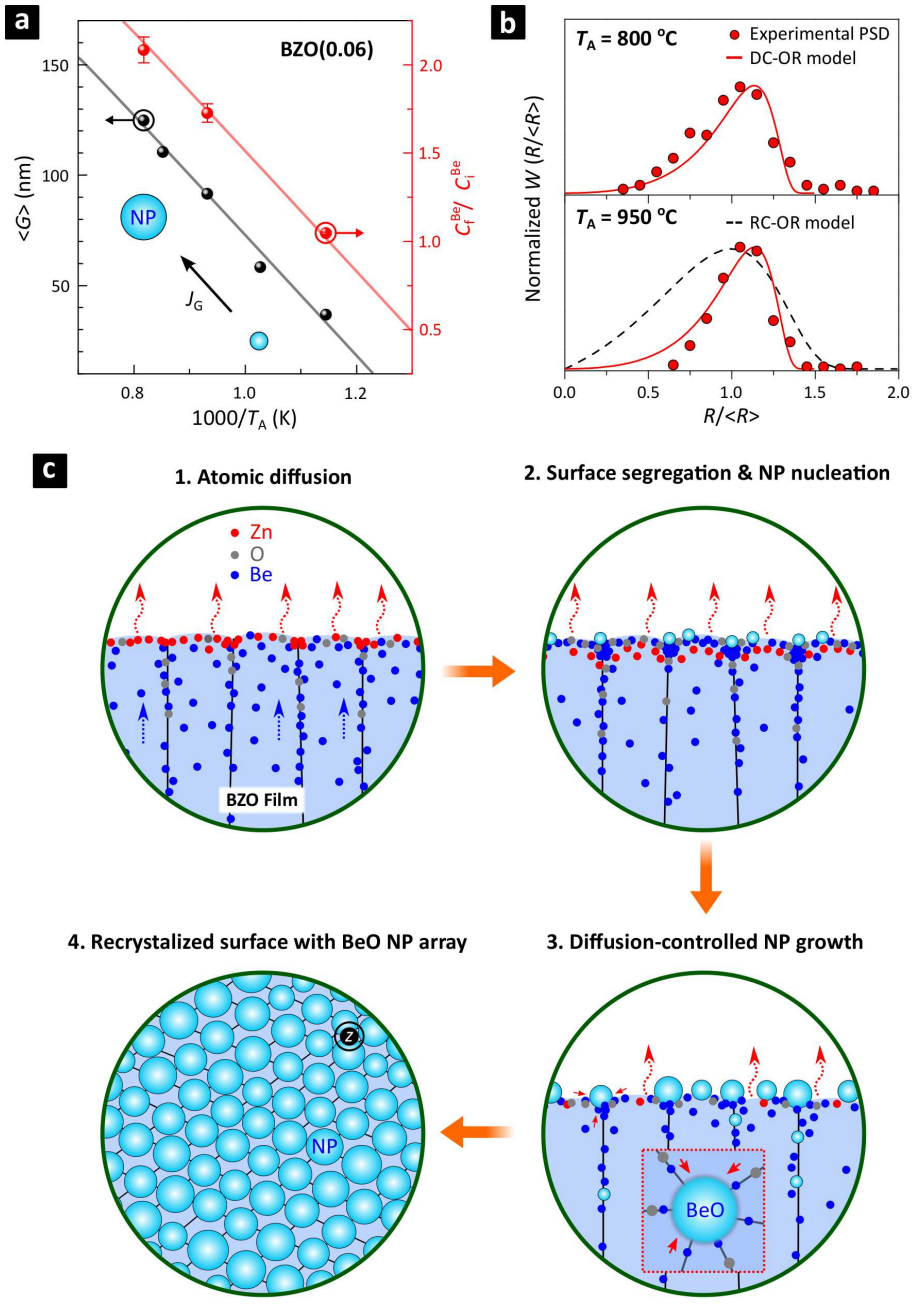

Figure 7.8: (a) Variations in the average size, $<G>$, of the grown BeO NPs and Be concentration ratio, $C_f^{\mathrm{Be}}/C_i^{\mathrm{Be}}$, at the surface of the annealed BZO(0.06) film as a function of reciprocal annealing temperature ($1000/T_{\mathrm{A}}$). (b) Stationary size distribution, W, of the NPs for two high-temperature-annealed alloy films as a function of particle radius ratio, $R_{\mathrm{g}}/<R_{\mathrm{g}}>$, where $<R_{\mathrm{g}}>$ is the average radius of the NPs. The limited PSDs are predicted from the associated size distribution function within the LSW theory for diffusion-controlled (solid line: DRL-OR) and reaction-controlled (dashed line: RRL-OR) Ostwald ripening. (c) Schematic representations of thermally driven out-diffusion of constituent atoms and the nucleation-and-growth processes of the secondary phase BeO NPs within the diffusion-controlled OR growth mode in a transformed BZO alloy film. This growth mode is enforced by the high Be supersaturation level at the surface together with the additional/continuous injection of Be solutes during the growth process, resulting in focusing of the NP size distribution.

were cooled down at room temperature. In Fig. 7.8b, such diffusion-controlled growth of the BeO NPs and the following PSD were predicted and characterized for the annealed BZO(0.06) films at $T_{\rm A}$ = 800 and 950 °C. This is performed by applying the stationary size distribution function in the diffusion rate-limited condition of OR (DRL-OR) based on the LSW theory that [87, 90]

$$W(Z) = \frac{(3^4 e/2^{5/3}) Z^2 e^{(-1/(1-(2Z/3)))}}{(Z+3)^{7/3}(1.5-Z)^{11/3}} \text{ for } \quad 0<Z<1.5,$$

$$W(Z) = 0 \quad \text{otherwise.} \quad (7.4)$$

Here, $Z \equiv R_{\rm g}/<R_{\rm g}>$ and $<R_{\rm g}>$ is the average particle radius; the cutoff is at Z = 1.5. The size focusing of the secondary phase BeO NP growth in the high-temperature annealed alloy films is predominantly associated with high Be solute saturation and simultaneous inclusion of the new arriving Be solutes from the bulk in the NPs within the stationary diffusion-controlled growth mode. The overall nucleation and-growth process forming the secondary phase BeO NPs at the surface of the thermally-transformed BZO films are schematically presented in Fig. 7.8c.

7.3.5 Passivation effects of surface NPs on chemisorption

Here, the influence of the secondary phase BeO NPs on physiochemical interactions between the surface of the annealed BZO films and environmental oxygen species (*e.g.* H_2O) is studied compared to the undoped ZnO films. Figure 7.9 shows O 1*s* spectra for the undoped ZnO and BZO films as a function of $T_{\rm A}$. The results reveal lower chemisorption at the surface of the high-temperature annealed BZO films and discernable spectral variation of O 1*s* peaks, compared to the ZnO films. For the BZO(0.02 and 0.06) films, the peak areas associated to Be-O bonds ($E_{\rm B} \approx$ 531.1 eV) is increased with $T_{\rm A}$, which is consistent with the increase in the peak area of Be 1*s* as a result of thermally-induced out-diffusion of Be to the surface of the alloy films. There is no significant change with $T_{\rm A}$ on the higher binding

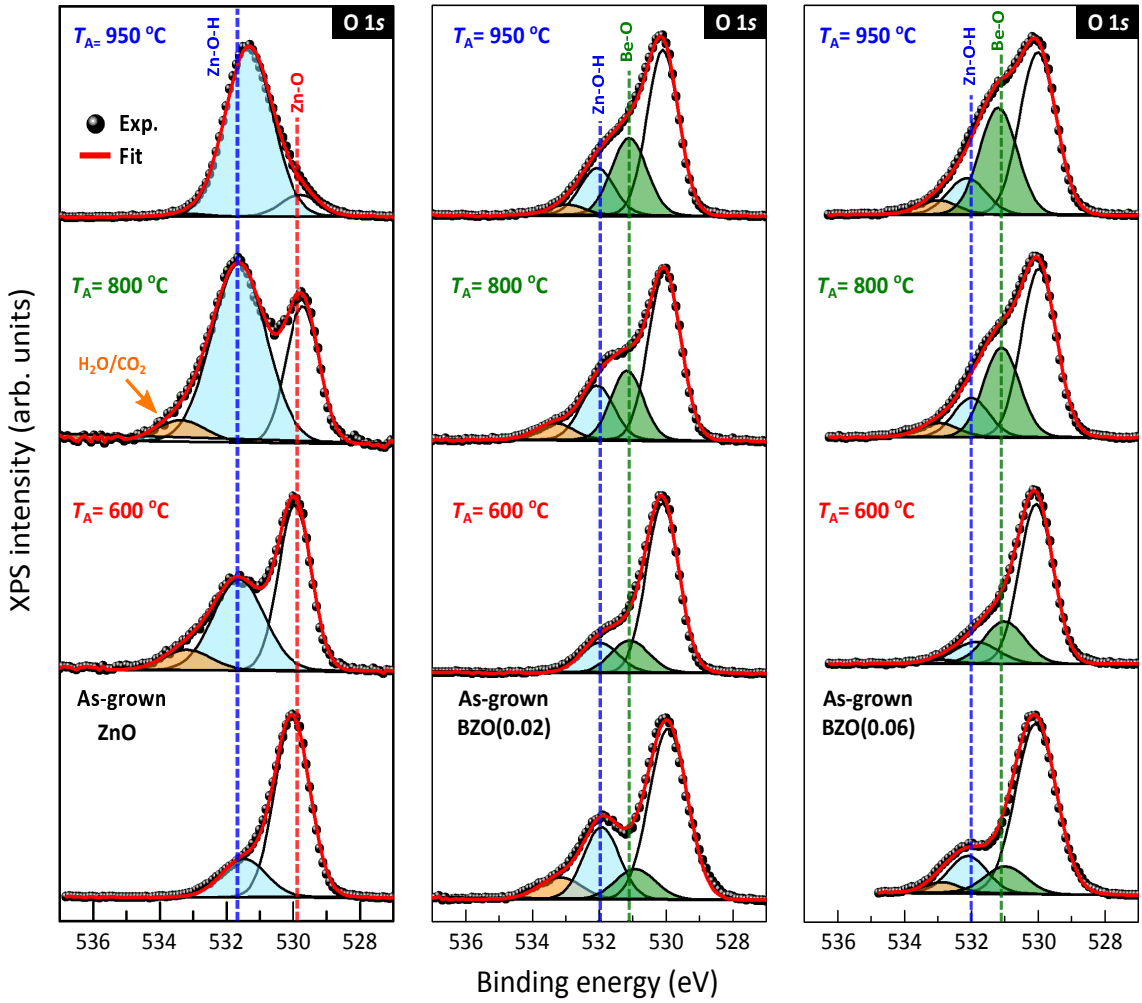

Figure 7.9: XPS O 1*s* core level spectra of the undoped ZnO and BZO(0.02 and 0.06) films with different T_A (600, 800, and 950 °C). All XPS spectra were collected at normal emission ($\theta_{TOA} = 90°$). Four distinct peak components were considered in the fitting of the BZO spectra due to additional Be-O bonds.

energy side ($E_B \approx 532 - 533$ eV) pertaining to surface chemisorption. Hence, these results clearly support surface passivation of the annealed alloy films by BeO NPs against defect-mediated chemisorptions-a feature not observed at the surface of the annealed ZnO films.

The ratio of O to Zn+Be, [O/(Zn+Be)], at the surface of the undoped ZnO and BZO(0.02 and 0.06) films for different T_A has been obtained by fitting the XPS core level spectra as depicted in Fig. 7.10a. The ratio of O anions to Zn and Be cations for the as-grown ZnO and alloy films was found to be around 1.20 – 1.33, respectively. The O-richness of the as-grown films is attributed to the stabiliza-

tion on unstable polar ZnO surfaces by surface atomic reconstructions and surface chemisorptions. The latter includes dissociative water species (H, O-H, H_2O) and other environmental species (CO_2) depending on polarity of the surface according to electron counting rules [46, 48]. A considerable increase in the ratio of O/Zn in the annealed ZnO films was observed varying from 1.33 to 5.14 up to $T_A = 950$ °C. Since, during high-temperature annealing, lattice defects and defect clusters such as V_{Zn} and V_O are produced, the increased defect density at the surface gives rise to an increase in the hydrophilicity and wettability at the surface of oxides by an increasing number of binding sites to accommodate adsorbates, *e.g.* hydroxyls and water molecules [262–264]. From the fitting of XPS O 1*s* core level spectra for the annealed ZnO films (Fig. 7.9), surface-chemisorption-related components such as hydroxides and water molecules at $E_B \sim 532$ – 533 eV to the Zn-O bond ($E_B \sim 530$ eV) was substantially increased for $T_A = 950$ °C. Therefore, we affirm that such an increase of O to Zn ratio is associated with both the evaporation of Zn and O atoms and the subsequent increase in thermally-induced surface defects. By contrast, the ratio O/(Zn+Be) of the BZO films reduced to 1 and remained constant, indicating that by increasing the Be concentration at the surface of the alloy films, this lowers and ultimately stop further chemical adsorption. This reveals that thermally created lattice vacancy-defects at the surface are compensated by atomic substitution, namely, $V_{Zn} + Be_{out-diff} \rightarrow Be_{Zn}$.

To gain further insight for such compensation processes (adsorption of oxygen species and atomic substitution) leading to the stabilization of the defective polar ZnO surfaces, appropriate models of the ZnO(000$\bar{1}$) surface structures for DFT calculations are shown in Fig. 7.10b. As high-temperature annealing causes dissociation of a number of Zn-O bonds which results in the thickness reduction of the undoped ZnO thin films, the Zn-O vacancy clusters (VCs) are expected to form at the surface [260]. Hence, different numbers, $N = 1$–9, of VCs were considered in the modelling of the ZnO slabs. The VCs (V_{ZnO}) are filled by two independent processes of dissociative H_2O adsorptions and BeO substitutions. Dissociated H^+ (OH^-) replaces V_{Zn} (V_O) sites for H_2O adsorptions, while Be^{2+} (O^{2-}) replaces V_{Zn}

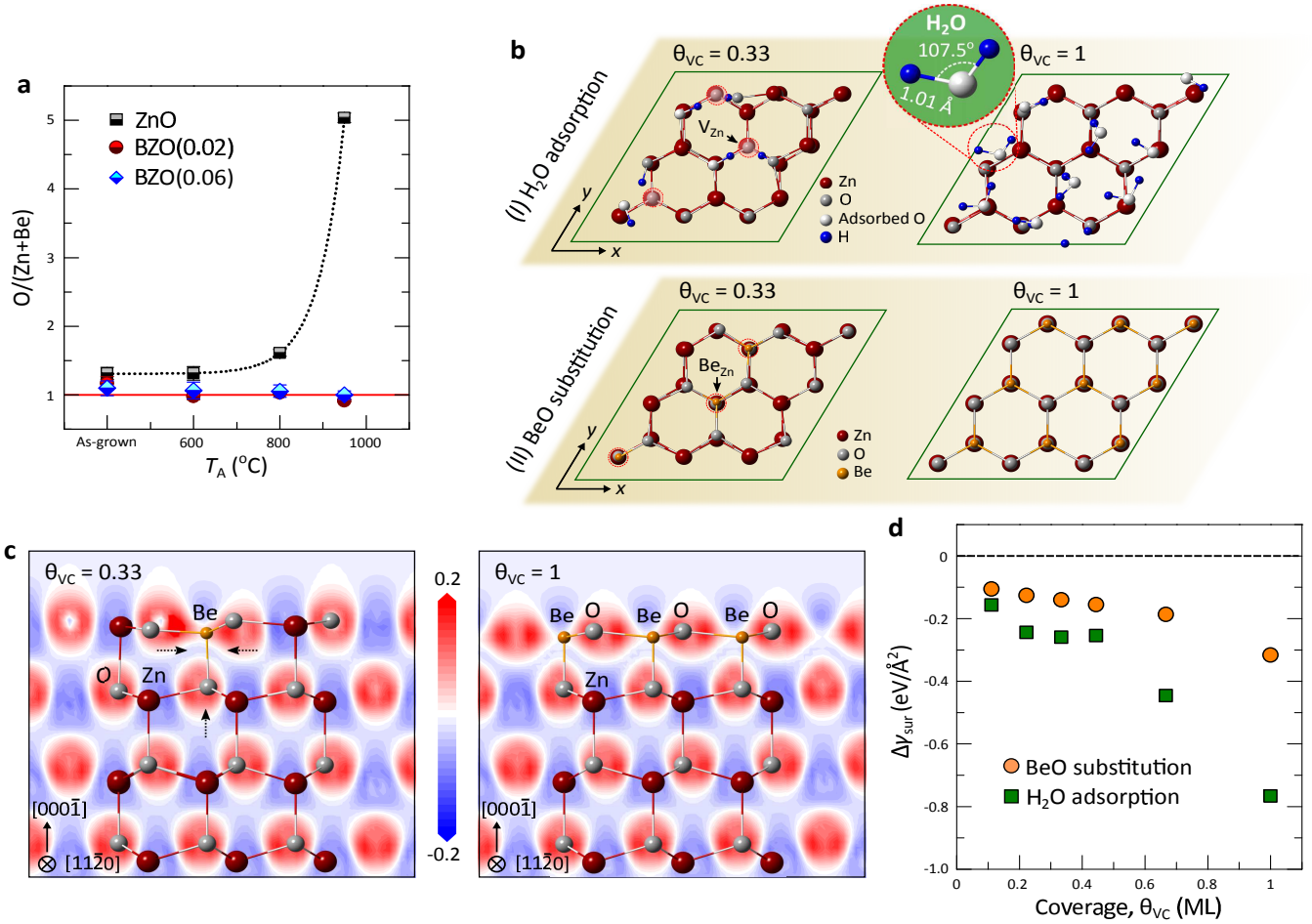

Figure 7.10: (a) Profiles of O to (Zn+Be) ratio for the as-grown and annealed ZnO and BZO(0.02 and 0.06) films at different T_A. The elemental ratios were obtained from the composition analyses by fitting the XPS spectra of the films. (b) Upper panel I: relaxed ZnO(000$\bar{1}$)-O surface structures with coverages, θ_{VC} = 0.33 and 1 of Zn-O VCs at the topmost ZnO double layer. Dissociated H_2O, *i.e.*, H and OH, replace V_{Zn} and V_O sites, respectively. For dissociative H_2O adsorptions, surface stabilization favours the formation of ionic O-H bonds adjacent to V_{Zn} at $\theta_{VC} \leq 0.44$, while the dominant formation of individual H_2O molecules occurs at $\theta_{VC} \geq 0.67$. Lower panel II: relaxed ZnO(000$\bar{1}$)-O surface structures with the same coverages at the topmost ZnO double layer. Be and O replace V_{Zn} and V_O sites, respectively. (c) Contour plots of charge-density difference along <11$\bar{2}$0> planes for the final atomic configuration of the BeO-substituted ZnO(000$\bar{1}$)-O surfaces with different coverage, θ_{VC} = 0.33 and 1. Blue and red regions represent charge depletion and accumulation, respectively. (d) Variations in the corresponding surface energy, $\Delta\gamma_{sub}$, of ZnO(000$\bar{1}$) as a function of the coverage, θ_{VC}, for both dissociated H_2O adsorption and BeO substitution.

(V_O) sites for BeO substitutions [49, 263]. These adsorption and substitution mechanisms are based on the balance between the energy gain through the saturation of the surface broken bonds by dissociated water and BeO, and the energy cost for the splitting of water molecules and the substitution of BeO. Therefore, the energy gain needs to be larger than the energy cost, leading to surface stabilization.

For the relaxation of the adsorbing surfaces at low coverage ($\theta_{VC} \leq 0.44$) of VCs, dissociated H atoms diffuse and couple with the topmost O dangling bonds adjacent to V_{Zn} due to their electrostatic attraction, leading to the dominant formation of O-H bonds (Fig. 7.10b). At high coverages ($\theta_{VC} \geq 0.67$), the dissociated O-H and H tend to form individual H_2O molecules on the surfaces. In the case of BeO substitutions, the local atomic bond length at the surface reduces due to the local impact of shorter Be-O bonds until the coverage of VCs by BeO substitutions reaches $\theta_{VC} = 0.33$. The surface atomic rearrangement subsequently saturates along the wurtzite crystal symmetry at the high coverage regime ($\theta_{VC} \geq 0.44$) reaching an equilibrium lateral bond distance of $d = 1.85$ Å and the c-bond length, $d_z = 1.79$ Å for the topmost surface double layer. As seen in Fig. 7.10c, strong Be-O bonds are formed at the top layer, leading to charge accumulation along the ligands. These atomic and charge redistributions on the BeO substitution are caused by the electronegativity and atomic size difference between the Zn and Be with respect to O. The more ionic bonding character of the substituted BeO is responsible for the strengthening of the defective surface. Furthermore, the surface energy change, $\Delta\gamma_{sub}$, determined as a function of the coverage, θ_{VC}, of H_2O/BeO on VCs clearly show a continuous decrease in $\Delta\gamma_{sub}$ as the number of VCs increases for both H_2O adsorptions and BeO substitutions (Fig. 7.10d). This implies that atomic vacancy defects and/or vacancy clusters facilitate the surface wettability of highly defective ZnO to lower the surface free energy. In the case of the transformed BZO alloys, water adsorptions at vacant sites on the surface are effectively restrained by BeO substitutions before exposing the surface defects to the atmosphere. The succeeding formation of thermally robust BeO NPs suppresses both the thermal sublimation of ZnO at the surface for high T_A and any further defect-mediated chemical adsorption.

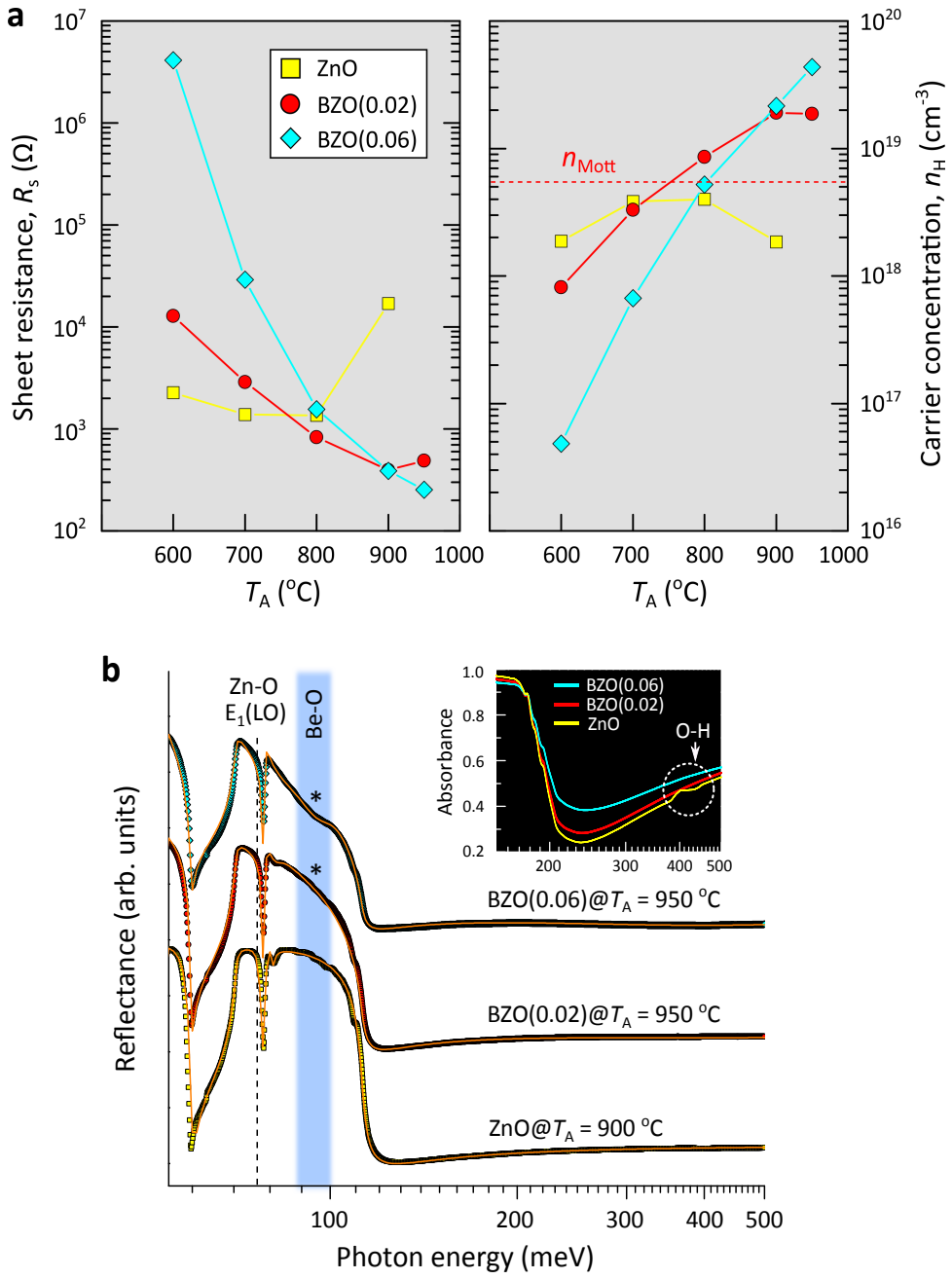

Figure 7.11: (a) Room temperature sheet resistance and carrier concentration of the ZnO and BZO(0.02 and 0.06) films annealed at different T_A. (b) Experimental IR reflectance plotted with the simulated spectra (orange lines) for the annealed ZnO (T_A = 900 °C) and BZO (T_A = 950 °C) films. An impurity mode (∗) in the IR reflectance spectra of the BZO films is found at ≈ 96 meV that is associated with BeO NPs. The adsorption peaks between 400 and 450 meV in the inset of (b) are due to surface O-H species.

7.3.6 Electrical characteristics of the annealed BZO films

Hall effect measurements were performed to investigate the effect of annealing on the electrical properties of the annealed ZnO and BZO(0.02 and 0.06) films as a function of T_A. Figure 7.11a shows room temperature (RT) sheet resistance (R_s) and Hall carrier concentration of the ZnO and BZO films annealed at different T_A. The R_s decreases to 1.38 kΩ for the ZnO film annealed at 800 °C. This decrease is primarily attributed to an increase in the carrier mobility due to the thermally driven grain growth in the film. The ZnO film annealed at T_A = 900 °C exhibits a higher $R_s \approx 17$ kΩ, (a lower Hall carrier concentration, $n_H = 1.8 \times 10^{18}$ cm^{-3} at RT) and the film annealed at T_A = 950 °C shows a highly insulating behavior. This is due to high-temperature-induced lattice dissociation, the subsequent increase of compensating lattice defects such as V_{Zn}, and surface effects, which are associated with coupling of grain boundaries and/or surface lattice defects and the related trap defects such as OH and O_2. In contrast, a continuous lowering (increasing) of R_s, up to 252 Ω, (carrier concentration, $n_H = 4.3 \times 10^{19}$ cm^{-3} at RT) was seen in the BZO(0.06) films annealed at T_A = 950 °C. The carrier concentration in the high-temperature ($T_A \geq 800$ °C) annealed BZO films is above the Mott-transition concentration of ZnO, $n_{Mott} = 5.7 \times 10^{18}$ cm^{-3}. To get further insights into the electrical behaviour of the films, IR reflectance measurements and simulation of the annealed ZnO (T_A = 900 °C) and BZO (T_A = 950 °C) films were performed and the results (Fig. 7. 11b) identify an impurity mode (≈ 96 meV) in the BZO films, which is related to Be-O phonon mode [101]. In addition, absorption peaks at 400 – 450 meV associated with surface O-H species were observed only in the annealed ZnO films as shown in the inset of Fig. 7b. Such oxygen species usually act as electron traps and build potential barriers at the surface defects, which cause charge compensation and a strong impedance opposing charge carrier transport at the surface of many oxides [233, 238, 240, 241]. Comparison with the electrical properties of the annealed ZnO films suggests that BeO NPs in the annealed BZO films prevent the adsorption of acceptor-like oxygen species by covering the surface lattice and planar defects, while annealing increases n-type donor sources such as

V_O or Zn_i [101,241]. This leads to a decrease (increase) in R_s (n_H) of the BZO films annealed at high temperatures which eventually forms highly conductive film layers with significant reduction in charge compensation.

7.3.7 Discussion

In this study, the spontaneous coverage and growth of secondary phase BeO NPs effectively enhances both the thermal-oxidation resistance and the durability of the active n-type ZnO layers within the phase-transformed BZO. The NPs prevent the formation of extrinsic acceptor surface states by inhibiting the physiochemical interactions between the induced lattice defects or planar defects and environmental oxygen species such as H_2O/OH^- and O_2/O^{2-}. This leads to the reduction of the associated charge compensation and significantly improves charge carrier concentration and carrier transport properties of the oxide material. Therefore, controlling the nucleation-and-growth and particle-size distribution of environmentally inert secondary phase NPs by thermodynamic phase transformation and solid-state reactions in metastable oxide alloys is key for effective passivation of reactive oxide surface. This novel phase transformation concurrently driven by strain relaxation and defect-mediated atomic compensation is also applicable to numerous metastable material systems subject to the structural interiors and material composition. Additionally, from a technological perspective, this facile method offers not only cost-effective process for the fabrication of environmentally robust oxide materials, but also provides a guideline to the design of future oxide optoelectronic applications obviating the need for post-surface-protective treatments.

7.4 Conclusion

Physiochemical interactions that occur at the surfaces of oxide materials can significantly impair their performance in many applications. As a result, surface passivation of oxide materials has been attempted via several deposition methods and with a number of different inert materials. Here, we demonstrate a novel way to passivate the surface of a versatile semiconducting oxide, ZnO. We use the method

of self-assembly, achieved via thermodynamic phase transformation means, to passivate the surface of ZnO thin films with BeO nanoparticles (NPs). This approach involves the use of BZO as a starting material that eventually yields the required coverage of secondary phase BeO NPs. Thermally induced phase transformation in metastable BZO films significantly initiates the evolution of secondary phase NPs and the functionalization of the surface. Transient diffusion of Be and segregation toward the surface of the annealed alloy films result in the nucleation-and-growth of BeO NPs. The particle growth kinetics, size and uniformity of the surface NPs, are predominantly dependent on the degree of Be segregation as a solute supersaturation level at the surface of the alloy film. A significant correlation was deduced between the uniform distribution of thermally-grown NPs at the surface, and variations in the film thickness and surface chemisorption. Crucial to our findings from this study is the effective passivation by thermally-grown NPs to prevent high-temperature thickness reduction and defect-mediated chemisorption in the annealed BZO films – (undesirable features that are observed in undoped ZnO). Hence, we affirm that the uniformity of the NP arrays pinned at the surface as a result of a sufficient phase transformation of the alloy films plays an efficient role in the passivation of thermal dissociation and surface chemical reactions. Such passivation will allow the use of semiconducting oxides in a variety of different electronic applications, while maintaining the inherent properties of the materials.

Chapter 8

Summary and Conclusions

In this thesis, we have primarily explored characteristics of the thermodynamic phase transformation and the associated functionalization on a metastable oxide alloy, $Be_xZn_{1-x}O$, for potential applications based on band gap and defect engineering of a wide gap material.

In Chapters 4 and 5, the growth dynamics of the $Be_xZn_{1-x}O$ alloys have been systematically investigated in terms of solute concentration and growth temperatures during their band gap modulation. The influence of Be concentration on the microstructure of $Be_xZn_{1-x}O$ ternary films (from $x = 0$ to 0.77), grown on $Al_2O_3(0001)$ substrates was demonstrated. With increasing Be concentration, the (0002) X-ray diffraction peak shows a systematic shift from 33.86° to 39.39°, and optical spectroscopy showed a blue-shift of the band gap from 3.24 eV to beyond 4.62 eV towards the deep UV regime, indicating that Be atoms are incorporated into the host ZnO lattice. During the band gap modulation, structural fluctuations (*e.g.* phase separation and compositional fluctuations of Be) in the ternary films were observed along with a significant change in the mean grain size. X-ray photoelectron spectroscopy indicates higher concentrations of metallic Be states found in the film with the smaller grain size. Correlation between these two observations indicates that Be segregates to near the grain boundaries. A model structure has been proposed, where an increase in grain growth driving force dominates over the Be particle pinning effect. This leads to further coalescence of grains, reactivation of grain growth, and the uniform distribution of Be composition in the $Be_xZn_{1-x}O$ alloy films.

The influence of growth temperature on synthesizing $Be_xZn_{1-x}O$ alloy films, grown on highly-mismatched $Al_2O_3(0001)$ substrates, was studied by synchrotron X-ray scattering, high-resolution transmission electron microscopy (HRTEM), and

photoluminescence measurements. A single-phase $Be_xZn_{1-x}O$ alloy with a Be concentration of $x = 0.25$, was obtained at the growth temperature, $T_g = 400$ °C, and verified by HRTEM. It was found that high-temperature growth, $T_g \geq 600$ °C, caused a phase separation. This results in a random distribution of intermixing alloy phases. The inhomogeneity and structural fluctuations observed in the $Be_xZn_{1-x}O$ films grown at high temperatures are attributed to a variation in Be composition and mosaic distribution via atomic displacement (Be pulling effect) and strain relaxation to minimize their free energy configuration.

Thermodynamic phase transformation of $Be_xZn_{1-x}O$ alloys have been extensively investigated in this study (Chapters 6 and 7). Significant counter-diffusion of constituent Be and Zn cations, *i.e.*, out-diffusion of Be towards surface and inward diffusion of Zn towards the interface between the alloy film and substrate, takes place. This corresponds to a monotonic decrease in the lattice phonon energies and band gap energy of the films. Such atomic redistribution induced by thermal annealing initiated the formation of a highly-conductive interface. Infrared reflectance simulations identified a highly conductive ZnO interface layer (thicknesses in the range of ≈ 10 – 29 nm for annealing temperatures, $T_A \geq 800$ °C). The highly degenerate interface layers with temperature-independent carrier concentration and mobility, significantly influence the electronic and optical properties (band filling effects and the subsequent many-body effects) of the BZO films. The density-of-states-averaged effective mass of the conduction electrons for the interfaces was calculated to be in the range of $0.31m_0$ and $0.67m_0$, while a conductivity as high as 1.4×10^3 S·cm^{-1} was attained, corresponding to the carrier concentration $n_{Int} = 2.16 \times 10^{20}$ cm^3 at the interface layers, and comparable to the highest conductivities achieved in highly doped ZnO. The origin of such a nanoscale degenerate interface layer is attributed to the counter-diffusion of Be and Zn, rendering a high accumulation of Zn interstitials and a giant reduction of charge-compensating defects.

On the basis of the above results, the effect of thermodynamics and phase transformations and particle nucleation-and-growth on a metastable $Be_xZn_{1-x}O$ ternary alloy, was demonstrated. During the thermally-driven relaxation processes,

the induced out-diffusion of Be and the subsequent segregation give rise to a supersaturation condition for the nucleation of BeO crystals at the surface of the alloy. The structural evolution of the secondary phase nanoparticles, the form of wurtzite BeO, at the surface of the annealed BZO films were characterized. The defect-mediated atomic compensation, and the associated limiting growth kinetics and the size distribution of the nanoparticles were investigated. Furthermore, the particle size distribution was strongly related to the supersaturation of Be solute at the surface of the annealed alloy films.

In order to interpret the solute concentration-dependent particle size distribution, a diffusion-controlled model of Ostwald ripening has been proposed together with an over-saturation/continuum injection of Be monomers for the size-focusing of the BeO NPs at the surface. Such narrowing of the size distribution has been simulated by a particle size distribution function based on LSW theory and the simulation results are in good agreements with the experimental observations. Sufficient size-focused distribution of the grown nanoparticles, pinned at the surface of the transformed alloy films, led to efficient passivation of surface chemical reactions and thermal dissociation, features not seen in undoped ZnO. The experimentally thermal and chemical resistance of the secondary phase nanoparticles in the transformed alloy films were simulated by first-principles calculations of compensation and relaxation energies in model metastable surfaces. The crucial findings presented in this study can open up a new approach using phase transformations in metastable materials into designing thermally and chemically robust oxide-based nanoparticles for advanced applications.

This novel approach for the formation of functional self-assembled nanoparticles and degenerate interface layer by the consequence of phase transformations in metastable oxides suggests a new criterion for the fabrication of environmentally resistant optoelectronics. The induced counter-diffusion behavior of constituent cations which has distinct diffusion characteristics in metastable oxides should be precisely controllable to tune their applications. To further resolve the quantitative kinetics of the secondary phase nanoparticle growth, critical parameters such as:

temperature-dependent solute diffusivities; activation energies for monomer diffusion; a resulting derived reaction constant for a time-dependent nanoparticle growth, needs to be acquired. Furthermore, the conductivity of degenerate interface layer can be modulated by employing n-dopants as doped BZO. Thermodynamically-induced diffusion competition between co-existing Zn and dopants could be crucial to control the desirable interface conductivity and levels of surface passivation. The novel methods presented in this thesis can provide guidelines for the design of environmentally robust oxide-based device architectures via thermodynamic phase transformation of various metastable oxides or other materials system.

Bibliography

[1] K. Nomura, H. Ohta, K. Ueda, T. Kamiya, M. Hirano, and H. Hosono, Science **300**, 1269 (2003).

[2] R. L. Hoffman, B. J. Norris, and J. F. Wager, Appl. Phys. Lett. **82**, 733 (2003).

[3] S. Chu, G. Wang, W. Zhou, Y. Lin, L. Chernyak, J. Zhao, J. Kong, L. Li, J. Ren, and J. Liu, Nat. Nanotech. **6**, 506 (2011).

[4] A. Tsukazaki, A. Ohtomo, T. Kita, Y. Ohno, H. Ohno, and M. Kawasaki, Science **315**, 1388 (2007).

[5] A. Tsukazaki, S. Akasaka, K. Nakahara, Y. Ohno, H. Ohno, D. Maryenko, A. Ohtomo, and M. Kawasaki, Nat. Mater. **9**, 889 (2010).

[6] N. Nakagawa, H. Y. Hwang, and D. A. Muller, Nat. Mater. **5**, 204 (2006).

[7] A. Ohtomo and H. Y. Hwang, Nature **427**, 423 (2004).

[8] A. Janotti and C. G. V. de Walle, Rep. Prog. Phys. **72**, 126501 (2009).

[9] P. D. C. King, T. D. Veal, D. J. Payne, A. Bourlange, R. G. Egdell, and C. F. McConville, Phys. Rev. Lett. **101**, 116808 (2008).

[10] P. D. C. King, T. D. Veal, A. Schleife, J. Zúñiga-Pérez, B. Martel, P. H. Jefferson, F. Fuchs, V. Muñoz-Sanjosé, F. Bechstedt, and C. F. McConville, Phys. Rev. B **79**, 205205 (2009).

[11] M. W. Allen, D. Y. Zemlyanov, G. I. N. Waterhouse, J. B. Metson, T. D. Veal, C. F. McConville, and S. M. Durbin, Appl. Phys. Lett. **98**, 101906 (2011).

[12] S. K. Vasheghani Farahani, T. D. Veal, A. M. Sanchez, O. Bierwagen, M. E. White, S. Gorfman, P. A. Thomas, J. S. Speck, and C. F. McConville, Phys. Rev. B **86**, 245315 (2012).

[13] K. M. Yu, W. Walukiewicz, J. Wu, W. Shan, J. W. Beeman, M. A. Scarpulla, O. D. Dubon, and P. Becla, Phys. Rev. Lett. **91**, 246403 (2003).

[14] W. Walukiewicz, Appl. Phys. Lett. **54**, 2094 (1989).

[15] L. Pavesi and P. Giannozzi, Phys. Rev. B **46**, 4621 (1992).

[16] J. I. P. Pankove and N. M. Johnson, *Semiconductors and Semimetals*, volume 34, Academic Press, Boston, 1991.

[17] C. G. Van de Walle and J. Neugebauer, Nature (London) **423**, 626 (2003).

[18] A. K. Singh, A. Janotti, M. Scheffler, and C. G. Van de Walle, Phys. Rev. Lett. **101**, 055502 (2008).

[19] W. M. Hlaing Oo, S. Tabatabaei, M. D. McCluskey, J. B. Varley, A. Janotti, and C. G. Van de Walle, Phys. Rev. B **82**, 193201 (2010).

[20] T. Koida, H. Shibata, M. Kondo, K. Tsutsumi, A. Sakaguchi, M. Suzuki, and H. Fujiwara, J. Appl. Phys. **111**, 063721 (2012).

[21] D. C. Look and R. J. Molnar, Appl. Phys. Lett. **70**, 3377 (1997).

[22] N. Reyren, S. Thiel, A. D. Caviglia, L. F. Kourkoutis, G. Hammerl, C. Richter, C. W. Schneider, T. Kopp, A.-S. Rüetschi, D. Jaccard, M. Gabay, D. A. Muller, J.-M. Triscone, and J. Mannhart, Science **317**, 1196 (2007).

[23] F. Y. Bruno, M. N. Grisolia, C. Visani, S. Valencia, M. Varela, R. Abrudan, J. Tornos, A. Rivera-Calzada, A. A. Ünal, S. J. Pennycook, Z. Sefrioui, C. Leon, J. E. Villegas, J. Santamaria, A. Barthélémy, and M. Bibes, Nat. Commun. **6**, (2015).

[24] S. Nakamura, Science **281**, 956 (1998).

[25] K. Sun, W. Wei, Y. Ding, Y. Jing, Z. L. Wang, and D. Wang, Chem. Commun. **47**, 7776 (2011).

[26] S. I. Park, T. S. Cho, S. J. Doh, J. L. Lee, and J. H. Je, Appl. Phys. Lett. **77**, 349 (2000).

[27] I. W. Kim and K. M. Lee, Nanotechnology **19**, 355709 (2008).

[28] J. H. You, J.-Q. Lu, and H. T. Johnson, J. Appl. Phys. **99**, 033706 (2006).

[29] G. E. Pike and C. H. Seager, J. Appl. Phys. **50**, 3414 (1979).

[30] Y. W. Heo, Y. W. Kwon, Y. Li, S. J. Pearton, and D. P. Norton, Appl. Phys. Lett. **84**, 3474 (2004).

[31] K. Nakahara, S. Akasaka, H. Yuji, K. Tamura, T. Fujii, Y. Nishimoto, D. Takamizu, A. Sasaki, T. Tanabe, H. Takasu, H. Amaike, T. Onuma, S. F. Chichibu, A. Tsukazaki, A. Ohtomo, and M. Kawasaki, Appl. Phys. Lett. **97**, 013501 (2010).

[32] Y. R. Ryu, T. S. Lee, J. A. Lubguban, H. W. White, B. J. Kim, Y. S. Park, and C. J. Youn, Appl. Phys. Lett. **88**, 241108 (2006).

[33] A. Ohtomo, M. Kawasaki, T. Koida, K. Masubuchi, H. Koinuma, Y. Sakurai, Y. Yoshida, T. Yasuda, and Y. Segawa, Appl. Phys. Lett. **72**, 2466 (1998).

[34] A. Brif, G. Ankonina, C. Drathen, and B.Pokroy, Adv. Mater. **26**, 477 (2014).

[35] D. J. Norris, A. L. Efros, M. Rosen, and M. G. Bawendi, Phys. Rev. B **53**, 16347 (1996).

[36] A. M. Smith and S. Nie, Acc. Chem. Res. **43**, 190 (2010).

[37] A. Janotti, D. Segev, and C. G. Van de Walle, Phys. Rev. B **74**, 045202 (2006).

[38] A. R. Denton and N. W. Ashcroft, Phys. Rev. A **43**, 3161 (1991).

[39] J. E. Bernard and A. Zunger, Phys. Rev. B **36**, 3199 (1987).

[40] S.-H. Wei, S. B. Zhang, and A. Zunger, J. Appl. Phys. **87**, 1304 (2000).

[41] R. Dingle, Phys. Rev. Lett. **23**, 579 (1969).

[42] B. Meyer, Phys. Rev. B **69**, 045416 (2004).

[43] K. Ellmer, A. Klein, and B. Rech, *Transparent Conductive Zinc Oxide: Basics and Applications in Thin Film Solar Cells*, Springer, 2008.

[44] R. F. Service, Science **276**, 895 (1997).

[45] K. Song, J. Noh, T. Jun, Y. Jung, H.-Y. Kang, and J. Moon, Adv. Mater. **22**, 4308 (2010).

[46] O. Dulub, U. Diebold, and G. Kresse, Phys. Rev. Lett. **90**, 016102 (2003).

[47] B. Meyer and D. Marx, Phys. Rev. B **67**, 035403 (2003).

[48] G. Kresse, O. Dulub, and U. Diebold, Phys. Rev. B **68**, 245409 (2003).

[49] H. Ye, G. Chen, H. Niu, Y. Zhu, L. Shao, and Z. Qiao, J. Phys. Chem. C **117**, 15976 (2013).

[50] A. Janotti and C. G. Van de Walle, Phys. Rev. B **76**, 165202 (2007).

[51] D. C. Look, J. W. Hemsky, and J. R. Sizelove, Phys. Rev. Lett. **82**, 2552 (1999).

[52] D. C. Look, G. C. Farlow, P. Reunchan, S. Limpijumnong, S. B. Zhang, and K. Nordlund, Phys. Rev. Lett. **95**, 225502 (2005).

[53] D. M. Hofmann, A. Hofstaetter, F. Leiter, H. Zhou, F. Henecker, B. K. Meyer, S. B. Orlinskii, J. Schmidt, and P. G. Baranov, Phys. Rev. Lett. **88**, 045504 (2002).

[54] D. C. Look, K. D. Leedy, L. Vines, B. G. Svensson, A. Zubiaga, F. Tuomisto, D. R. Doutt, and L. J. Brillson, Phys. Rev. B **84**, 115202 (2011).

[55] D. O. Demchenko, B. Earles, H. Y. Liu, V. Avrutin, N. Izyumskaya, Ü. Özgür, and H. Morkoç, Phys. Rev. B **84**, 075201 (2011).

[56] Y. Ke, S. Lany, J. J. Berry, J. D. Perkins, P. A. Parilla, A. Zakutayev, T. Ohno, R. O′Hayre, and D. S. Ginley, Adv. Funct. Mater. **24**, 2875 (2014).

[57] X. H. Pan, W. Guo, Z. Z. Ye, B. Liu, Y. Che, W. Tian, D. G. Schlom, and X. Q. Pan, Appl. Phys. Lett. **95**, 152105 (2009).

[58] Y. R. Ryu, T. S. Lee, J. A. Lubguban, A. B. Corman, H. W. White, J. H. Leem, M. S. Han, Y. S. Park, C. J. Youn, and W. J. Kim, Appl. Phys. Lett. **88**, 052103 (2006).

[59] C. Klingshirn, J. Fallert, H. Zhou, and H. Kalt, Appl. Phys. Lett. **91**, 126101 (2007).

[60] C. Yang, X. M. Li, Y. F. Gu, W. D. Yu, X. D. Gao, and Y. W. Zhang, Appl. Phys. Lett. **93**, 112114 (2008).

[61] J. M. Khoshman, D. C. Ingram, and M. E. Kordesch, Appl. Phys. Lett. **92**, 091902 (2008).

[62] W. J. Kim, J. H. Leem, M. S. Han, I. W. Park, Y. R. Ryu, and T. S. Lee, J. Appl. Phys. **99**, 096104 (2006).

[63] M. S. Han, J. H. Kim, T. S. Jeong, J. M. Park, C. J. Youn, J. H. Leem, and Y. R. Ryu, J. Cryst. Growth **303**, 506 (2007).

[64] L. Dong and S. P. Alpay, Phys. Rev. B **84**, 035315 (2011).

[65] C. K. Gan, X. F. Fan, and J.-L. Kuo, Comp. Mater. Sci. **49**, S29 (2010).

[66] I. W. Kim and K. M. Lee, Nanotechnology **19**, 355709 (2008).

[67] S. I. Park, T. S. Cho, S. J. Doh, J. L. Lee, and H. J. Jung, Appl. Phys. Lett. **77**, 349 (2000).

[68] D. A. Porter, K. E. Easterling, and M. Y. Sherif, *Phase Transformations in Metals and Alloys*, CRC Press, 3rd edition, 2008.

[69] B. V. L'vov, *Thermal Decomposition of Solids and Metals: New Thermochemical Approach to the Mechanism, Kinetics and Methodology*, Springer, 2007.

[70] M. Ohring, *Materials Science of Thin Films*, Academic Press, 2002.

[71] J. W. Gibbs, Trans. Conn. Acad. Arts Sci. **3**, 108 (1874 and 1877).

[72] R. S. McWilliams, D. K. Spaulding, J. H. Eggert, P. M. Celliers, D. G. Hicks, R. F. Smith, G. W. Collins, and R. Jeanloz, Science **338**, 1330 (2012).

[73] F. Coppari, R. F. Smith, J. H. Eggert, J. Wang, J. R. Rygg, A. Lazicki, J. A. Hawreliak, G. W. Collins, and T. S. Duffy, Nat. Geosci. **6**, 926 (2013).

[74] M. Einax, W. Dieterich, and P. Maass, Rev. Mod. Phys. **85**, 921 (2013).

[75] Z. Hiroi, H. Hayamizu, T. Yoshida, Y. Muraoka, Y. Okamoto, J. Yamaura, and Y. Ueda, Chem. Mater. **25**, 2202 (2013).

[76] H. B. Yu, K. Samwer, Y. Wu, and W. H. Wang, Phys. Rev. Lett. **109**, 095508 (2012).

[77] B. Fultz and J. J. Hoyt, *Alloy Physics*, Wiley-VCH, 2007.

[78] H. Kuhlenbeck, S. Shaikhutdinov, and H.-J. Freund, Chem. Rev. **113**, 3986 (2013).

[79] V. V. Slezov, *Kinetics of First-order Phase Transitions*, Wiley-VCH Verlag, 2009.

[80] M. Volmer and A. Weber, Z. Phys. Chem.-Stoch. **119**, 277 (1926).

[81] R. Becker and W. Döring, Ann. Phys. (Berlin) **24**, 719 (1935).

[82] Y. B. Zeldovich, J. Exp. Theor. Phys. **12**, 525 (1942).

[83] R. Kampmann and R. Wagner, *Decomposition of alloys: the early stages*, Pergamon Press, 1984.

[84] Y. Sun, Chem. Soc. Rev. **42**, 2497 (2013).

[85] J. Baumgartner, A. Dey, P. H. H. Bomans, C. Le Coadou, P. Fratzl, N. A. J. M. Sommerdijk, and D. Faivre, Nat. Mater. **12**, 310 (2013).

[86] X. Peng, J. Wickham, and A. P. Alivisatos, J. Am. Chem. Soc. **120**, 5343 (1998).

[87] D. V. Talapin, A. L. Rogach, M. Haase, and H. Weller, J. Phys. Chem. B **105**, 12278 (2001).

[88] S. G. Kwon and T. Hyeon, Small **7**, 2685 (2011).

[89] V. Radmilovic, C. Ophus, E. A. Marquis, M. D. Rossell, A. Tolley, A. Gautam, M. Asta, and U. Dahmen, Nat. Mater. **10**, 710 (2011).

[90] J. H. Yao, K. R. Elder, H. Guo, and M. Grant, Phys. Rev. B **47**, 14110 (1993).

[91] P. J. Skrdla, J. Phys. Chem. C **116**, 214 (2012).

[92] I. Lifshitz and V. Slyozov, J. Phys. Chem. Solids **19**, 35 (1961).

[93] R. J. Borg and G. J. Dienes, *The Physical Chemistry of Solids*, Academic Press, Inc., 1992.

[94] A. L. Rogach, D. V. Talapin, E. V. Shevchenko, A. Kornowski, M. Haase, and H. Weller, Adv. Funct. Mater. **12**, 653 (2002).

[95] V. K. LaMer and R. H. Dinegar, J. Am. Chem. Soc. **72**, 4847 (1950).

[96] G. Ehrlich and F. G. Hudda, J. Chem. Phys. **44**, 1039 (1966).

[97] W. Hong, H. N. Lee, M. Yoon, H. M. Christen, D. H. Lowndes, Z. Suo, and Z. Zhang, Phys. Rev. Lett. **95**, 095501 (2005).

[98] P. Y. Yu and M. Cardona, *Fundamentals of Semiconductors*, Springer–Verlag, 1999.

[99] B. K. Ridley, *Quantum Processes in Semiconductors*, Oxford University Press, 1993.

[100] M. Burbano, D. O. Scanlon, and G. W. Watson, J. Am. Chem. Soc. **133**, 15065 (2011).

[101] D. S. Park, S. K. Vasheghani Farahani, M. Walker, J. J. Mudd, H. Wang, A. Krupski, E. B. Thorsteinsson, D. Seghier, C.-J. Choi, C. J. Youn, and C. F. McConville, ACS Appl. Mater. Interfaces **6**, 18758 (2014).

[102] D. M. Detert, K. B. Tom, C. Battaglia, J. D. Denlinger, S. H. N. Lim, A. Javey, A. Anders, O. D. Dubon, K. M. Yu, and W. Walukiewicz, J. Appl. Phys. **115**, (2014).

[103] P. D. C. King, T. D. Veal, P. H. Jefferson, J. Zúñiga-Pérez, V. Muñoz-Sanjosé, and C. F. McConville, Phys. Rev. B **79**, 035203 (2009).

[104] S. C. Jain, J. M. McGregor, and D. J. Roulston, J. Appl. Phys. **68**, 3747 (1990).

[105] S. Huant and K. Karraï, Phys. Rev. B **37**, 6955 (1988).

[106] B. R. Nag, *Electron Transport in Compound Semiconductors*, Springer–Verlag, 1980.

[107] E. O. Kane, J. Phys. Chem. Solids **1**, 249 (1957).

[108] H. Fujiwara and M. Kondo, Phys. Rev. B **71**, 075109 (2005).

[109] A. P. Roth, J. B. Webb, and D. F. Williams, Phys. Rev. B **25**, 7836 (1982).

[110] B. E. Sernelius, K.-F. Berggren, Z.-C. Jin, I. Hamberg, and C. G. Granqvist, Phys. Rev. B **37**, 10244 (1988).

[111] A.-H. Lu, E. Salabas, and F. Schüth, Angew. Chem. Int. Ed. **46**, 1222 (2007).

[112] Y. Varshni, Physica **34**, 149 (1967).

[113] W. Mönch, *Semiconductor Surfaces and Interfaces*, Springer, Berlin, 2001.

[114] V. Heine, Phys. Rev. **138**, A1689 (1965).

[115] Y.-C. Chang, Phys. Rev. B **25**, 605 (1982).

[116] J. Tersoff, Phys. Rev. Lett. **52**, 465 (1984).

[117] W. Walukiewicz, J. Vac. Sci. & Technol. B **6**, 1257 (1988).

[118] C. Kilic and A. Zunger, Appl. Phys. Lett. **81**, 73 (2002).

[119] C. G. Van de Walle and J. Neugebauer, Nature (London) **423**, 626 (2003).

[120] P. D. C. King and T. D. Veal, J. Phys.: Condens. Matter **23**, 334214 (2011).

[121] P. D. C. King, T. D. Veal, C. E. Kendrick, L. R. Bailey, S. M. Durbin, and C. F. McConville, Phys. Rev. B **78**, 033308 (2008).

[122] T. D. Veal, P. D. C. King, S. A. Hatfield, L. R. Bailey, C. F. McConville, B. Martel, J. C. Moreno, E. Frayssinet, F. Semond, and J. Zúñiga-Pérez, Appl. Phys. Lett. **93**, 202108 (2008).

[123] P. D. C. King, T. D. Veal, and C. F. McConville, Phys. Rev. B **77**, 125305 (2008).

[124] H. Übensee, G. Paasch, and J.-P. Zöllner, Phys. Rev. B **39**, 1955 (1989).

[125] G. Paasch and H. Übensee, Phys. Status Solidi B **113**, 165 (1982).

[126] R. Behrisch and W. Eckstein, *Sputtering by Particle Bombardment*, Springer, 2007.

[127] P. F. Fewster, *X-Ray Scattering from Semiconductors*, Imperial College Press, 2000.

[128] A. L. Patterson, Phys. Rev. **56**, 978 (1939).

[129] H. Hertz, Ann. Phys. **31**, 983 (1887).

[130] A. Einstein, Ann. Phys. **322**, 132 (1905).

[131] K. Siegbahn, Surf. Sci. **217**, 111 (1982).

[132] W. Drube, J. Electron Spectrosc. Relat. Phenom. **190, Part B**, 125 (2013).

[133] S. Hofmann, *Auger- and X-ray Photoelectron Spectroscopy in Materials Science*, Springer Berlin Heidelberg, 2013.

[134] D. A. Shirley, Phys. Rev. B **5**, 4709 (1972).

[135] J. Scofield, J. Electron Spectros. Relat. Phenom. **8**, 129 (1976).

[136] S. Tougaard, Surf. Sci. **216**, 343 (1989).

[137] S. Tanuma, C. J. Powell, and D. R. Penn, Surf. Interface Anal. **21**, 165 (1994).

[138] J. I. Panlove, *Optical Processes in Semiconductors*, Dover Publications Inc., 1971.

[139] A. M. Fox, *Optical Properties of Solids*, Oxford University Press, 2001.

[140] K. H. Rieder, M. Ishigame, and L. Genzel, Phys. Rev. B **6**, 3804 (1972).

[141] A. Kasic, M. Schubert, S. Einfeldt, D. Hommel, and T. E. Tiwald, Phys. Rev. B **62**, 7365 (2000).

[142] N. Ashkenov, B. N. Mbenkum, C. Bundesmann, V. Riede, M. Lorenz, D. Spemann, E. M. Kaidashev, A. Kasic, M. Schubert, M. Grundmann, G. Wagner, H. Neumann, V. Darakchieva, H. Arwin, and B. Monemar, J. Appl. Phys. **93**, 126 (2003).

[143] M. Born and E. Wolf, *Principles of Optics*, Pergamon Press, 2002.

[144] L. J. van de Pauw, Philips Res. Rep. **13**, 1 (1958).

[145] S. Pennycook, Annu. Rev. Mater. Sci. **22**, 171 (1992).

[146] A. A. Toropov, O. V. Nekrutkina,d T. V. Shubina, Th. Gruber, C. Kirchner, A. Waag, K. F. Karlsson, P. O. Holtz, and B. Monemar, Phys. Rev. B **69**, 165205 (2004).

[147] T. V. Butkhuzi, T. G. Chelidze, A. N. Georgobiani, D. L. Jashiashvili, T. G. Khulordava, and B. E. Tsekvava, Phys. Rev. B **58**, 10692 (1998).

[148] M. Kubota, T. Onuma, A. Tsukazaki, A. Ohtomo, M. Kawasaki, T. Sota, and S. F. Chichibu, Appl. Phys. Lett. **90**, (2007).

[149] J. Grabowska, A. Meaney, K. K. Nanda, J.-P. Mosnier, M. O. Henry, J.-R. Duclère, and E. McGlynn, Phys. Rev. B **71**, 115439 (2005).

[150] W. Shan, W. Walukiewicz, J. W. Ager, K. M. Yu, H. B. Yuan, H. P. Xin, G. Cantwell, and J. J. Song, Appl. Phys. Lett. **86**, (2005).

[151] K. E. Knutsen, A. Galeckas, A. Zubiaga, F. Tuomisto, G. C. Farlow, B. G. Svensson, and A. Y. Kuznetsov, Phys. Rev. B **86**, 121203 (2012).

[152] Y. Dong, F. Tuomisto, B. G. Svensson, A. Y. Kuznetsov, and L. J. Brillson, Phys. Rev. B **81**, 081201 (2010).

[153] H. Long, G. Fang, S. Li, X. Mo, H. Wang, H. Huang, Q. Jiang, J. Wang, and X. Zhao, IEEE Electron Device Lett. **32**, 54 (2011).

[154] A. Tsukazaki, S. Akasaka, K. Nakahara, Y. Ohno, H. Ohno, D. Maryenko, A. Ohtomo, and M. Kawasaki, Nat. Mater. **9**, 889 (2010).

[155] M. W. Allen, C. H. Swartz, T. H. Myers, T. D. Veal, C. F. McConville, and S. M. Durbin, Phys. Rev. B **81**, 075211 (2010).

[156] A. Janotti and C. G. V. de Walle, Rep. Prog. Phys. **72**, 126501 (2009).

[157] R. F. Service, Science **276**, 895 (1997).

[158] A. Ohtomo, M. Kawasaki, T. Koida, K. Masubuchi, H. Koinuma, Y. Sakurai, Y. Yoshida, T. Yasuda, and Y. Segawa, Appl. Phys. Lett. **72**, 2466 (1998).

[159] Y. R. Ryu, T. S. Lee, J. A. Lubguban, A. B. Corman, H. W. White, J. H. Leem, M. S. Han, Y. S. Park, C. J. Youn, and W. J. Kim, Appl. Phys. Lett. **88**, 052103 (2006).

[160] J. Scofield, J. Electron Spectros. Relat. Phenom. **8**, 129 (1976).

[161] A. Meeder, D. Fuertes Marrón, A. Rumberg, M. Ch. Lux-Steiner, V. Chu, and J. P. Conde, J. Appl. Phys. **92**, 3016 (2002).

[162] R. C. Rai, M. Guminiak, S. Wilser, B. Cai, and M. L. Nakarmi, J. Appl. Phys. **111**, 073511 (2012).

[163] L. Dong and S. P. Alpay, Phys. Rev. B **84**, 035315 (2011).

[164] H. L. Shi and Y. Duan, Eur. Phys. J. B **66**, 439 (2008).

[165] A. R. Denton and N. W. Ashcroft, Phys. Rev. A **43**, 3161 (1991).

[166] Y. Chen and J. Washburn, Phys. Rev. Lett. **77**, 4046 (1996).

[167] C. V. Thompson and R. Carel, J. Mech. Phys. Solids **44**, 657 (1996).

[168] X. F. Fan, Z. Zhu, Y.-S. Ong, Y. M. Lu, Z. X. Shen, and J.-L. Kuo, Appl. Phys. Lett. **91**, 121121 (2007).

[169] C. K. Gan, X. F. Fan, and J.-L. Kuo, Comp. Mater. Sci. **49**, S29 (2010).

[170] W. Dang, Y. Fu, J. Luo, A. Flewitt, and W. Milne, Superlattices Microstruct. **42**, 89 (2007).

[171] S. B. Amor, M. Jacquet, P. Fioux, and M. Nardin, Appl. Surf. Sci. **255**, 5052 (2009).

[172] Y. Y. Tay, S. Li, C. Q. Sun, and P. Chen, Appl. Phys. Lett. **88**, 173118 (2006).

[173] A. Wiltner and C. Linsmeier, New J. Phys. **8**, 181 (2006).

[174] C. Linsmeier and J. Wanner, Surf. Sci. **454**, 305 (2000).

[175] D. P. Woodruff and T. A. Delchar, *Modern Techniques of Surface Sciene-Second Edition*, Cambridge University Press, 1944.

[176] C. Zener, Trans. AIME **175**, 15 (1948).

[177] J. E. Burke and D. Turnbull, Prog. Metal Phys. **3**, 220 (1952).

[178] B. Ingham, R. Linklater, and T. Kemmitt, J. Phys. Chem. C **115**, 21034 (2011).

[179] J. M. E. Harper, J. C. Cabral, P. C. Andricacos, L. Gignac, I. C. Noyan, K. P. Rodbell, and C. K. Hu, J. Appl. Phys. **86**, 2516 (1999).

[180] M. Hillert, Acta Metallurgica **13**, 227 (1965).

[181] W.-R. Liu, W. F. Hsieh, C.-H. Hsu, K. S. Liang, and S.-S. Chien, J. Appl. Cryst. **40**, 924 (2007).

[182] S. M. Hearne, E. Trajkov, D. N. Jamieson, J. E. Butler, and S. Prawer, J. Appl. Phys. **99**, 113703 (2006).

[183] Y. R. Ryu, T. S. Lee, J. A. Lubguban, A. B. Corman, H. W. White, J. H. Leem, M. S. Han, Y. S. Park, C. J. Youn, and W. J. Kim, Appl. Phys. Lett. **88**, 052103 (2006).

[184] L. Dong and S. P. Alpay, Phys. Rev. B **84**, 035315 (2011).

[185] H. Iwanaga, A. Kunishige, and S. Takeuchi, J. Mater. Sci. **35**, 2451 (2000).

[186] J. M. Khoshman, D. C. Ingram, and M. E. Kordesch, Appl. Phys. Lett. **92**, 091902 (2008).

[187] M. S. Han, J. H. Kim, T. S. Jeong, J. M. Park, C. J. Youn, J. H. Leem, and Y. R. Ryu, J. Cryst. Growth **303**, 506 (2007).

[188] C. Yang, X. M. Li, Y. F. Gu, W. D. Yu, X. D. Gao, and Y. W. Zhang, Appl. Phys. Lett. **93**, 112114 (2008).

[189] J. M. Yuk, J. Y. Lee, Y. S. No, T. W. Kim, and W. K. Choi, Appl. Phys. Lett. **93**, 021904 (2008).

[190] D. S. Park, J. J. Mudd, M. Walker, D. Seghier, A. Krupski, N. Fereshteh Saniee, C.-J. Choi, C. J. Youn, S. R. C. McMitchell, and C. F. McConville, CrystEngComm **16**, 2136 (2014).

[191] L. Dong and S. P. Alpay, Phys. Rev. B **84**, 035315 (2011).

[192] J. Sann, J. Stehr, A. Hofstaetter, D. M. Hofmann, A. Neumann, M. Lerch, U. Haboeck, A. Hoffmann, and C. Thomsen, Phys. Rev. B **76**, 195203 (2007).

[193] M. Brandt, H. von Wenckstern, G. Benndorf, M. Lange, C. P. Dietrich, C. Kranert, C. Sturm, R. Schmidt–Grund, H. Hochmuth, M. Lorenz, M. Grund-

mann, M. R. Wagner, M. Alic, C. Nenstiel, and A. Hoffmann, Phys. Rev. B **81**, 073306 (2010).

[194] C. Lin and A. Z. Li, J. Cryst. Growth **203**, 511 (1999).

[195] A. Yamamoto, Y. Moriwaki, K. Hattori, and H. Yanagi, Appl. Phys. Lett. **98**, 061907 (2011).

[196] S. Pereira, M. R. Correia, E. Pereira, C. Trager-Cowan, F. Sweeney, K. P. O'Donnell, E. Alves, N. Franco, and A. D. Sequeira, Appl. Phys. Lett. **81**, 1207 (2002).

[197] H. Matsui, H. Tabata, N. Hasuike, and H. Harima, J. Appl. Phys. **99**, 024902 (2006).

[198] S. Pereira, M. R. Correia, E. Pereira, K. P. O'Donnell, C. Trager-Cowan, F. Sweeney, and E. Alves, Phys. Rev. B **64**, 205311 (2001).

[199] W.-S. Choi, M. F. Chisholm, D. J. Singh, T. Choi, G. E. Jellison, and H. N. Lee, Nat. Commun. **3**, 689 (2012).

[200] K. Nakahara, S. Akasaka, H. Yuji, K. Tamura, T. Fujii, Y. Nishimoto, D. Takamizu, A. Sasaki, T. Tanabe, H. Takasu, H. Amaike, T. Onuma, S. F. Chichibu, A. Tsukazaki, A. Ohtomo, and M. Kawasaki, Appl. Phys. Lett. **97**, 013501 (2010).

[201] A. Schleife, F. Fuchs, C. Rödl, J. Furthmüller, and F. Bechstedt, Appl. Phys. Lett. **94**, 012104 (2009).

[202] H. L. Mosbacker, C. Zgrabik, M. J. Hetzer, A. Swain, D. C. Look, G. Cantwell, J. Zhang, J. J. Song, and L. J. Brillson, Appl. Phys. Lett. **91**, 072102 (2007).

[203] W.-R. Liu, B. H. Lin, S. Yang, C. C. Kuo, Y.-H. Li, C.-H. Hsu, W. F. Hsieh, W. C. Lee, M. Hong, and J. Kwo, CrystEngComm **14**, 1665 (2012).

[204] D. S. Park, A. Krupski, A. M. Sanchez, C.-J. Choi, M.-S. Yi, H.-H. Lee, S. R. C. McMitchell, and C. F. McConville, Appl. Phys. Lett. **104**, 141902 (2014).

[205] W.-R. Liu, W. F. Hsieh, C.-H. Hsu, K. S. Liang, and S.-S. Chien, J. Appl. Cryst. **40**, 924 (2007).

[206] B. Pecz, A. El-Shaer, A. Bakin, A.-C. Mofor, A. Waag, and J. Stoemenos, J. Appl. Phys. **100**, 103506 (2006).

[207] Y. Wang, X.L. Du, Z. X. Mei, Z.Q. Zeng, Q.Y. Xu, Q.K. Xue, and Z. Zhang, J. Cryst. Growth **273**, 100 (2004).

[208] K. Tamura, A. Ohtomo, K. Saikusa, Y. Osaka, T. Makino, Y. Segawa, M. Sumiya, S. Fuke, H. Koinuma, and M. Kawasaki, J. Cryst. Growth **214/215**, 59 (2000).

[209] Y. Chen, D. M. Bagnall, H.-J. Koh, K.-T. Park, K. Hiraga, Z. Zhu, and T. Yao, J. Appl. Phys. **84**, 3912 (1998).

[210] C. Liu, S. H. Chang, T. W. Noh, M. Abouzaid, P. Ruterana, H. H. Lee, D. W. Kim, and J. S. Chung, Appl. Phys. Lett. **90**, 011906 (2007).

[211] T. Yao and S.-K. Hong, *Oxide and Nitride Semiconductors: Processing, Properties, and Applications*, Springer, 2010.

[212] Y. Wang, Q. Liao, H. Lei, X.-P. Zhang, X.-C. Ai, J.-P. Zhang, and K. Wu, Adv. Mater. **18**, 943 (2006).

[213] H. J. Fan, M. Knez, R. Scholz, K. Nielsch, E. Pippel, D. Hesse, M. Zacharias, and U. Gosele, Nat. Mater. **5**, 627 (2006).

[214] T. C. Damen, S. P. S. Porto, and B. Tell, Phys. Rev. **142**, 570 (1966).

[215] J. M. Calleja and M. Cardona, Phys. Rev. B **16**, 3753 (1977).

[216] R. Cuscó, E. Alarcón-Lladó, J. Ibáñez, L. Artús, J. Jiménez, B. Wang, and M. J. Callahan, Phys. Rev. B **75**, 165202 (2007).

[217] K. Senthilkumar, M. Tokunaga, H. Okamoto, O. Senthilkumar, and Y. Fujita, Appl. Phys. Lett. **97**, 091907 (2010).

[218] R. L. Petritz, Phys. Rev. **110**, 1254 (1958).

[219] H. Tampo, A. Yamada, P. Fons, H. Shibata, K. Matsubara, K. Iwata, S. Niki, K. Nakahara, and H. Takasu, Appl. Phys. Lett. **84**, 4412 (2004).

[220] J. G. Lu, S. Fujita, T. Kawaharamura, H. Nishinaka, Y. Kamada, and T. Ohshima, Appl. Phys. Lett. **89**, 262107 (2006).

[221] F. L. Williams and D. Nason, Surf. Sci. **45**, 377 (1974).

[222] M. Es-Souni, Scr. Metall. Mater. **23**, 919 (1989).

[223] P. Bogus*l*awski and J. Bernholc, Phys. Rev. Lett. **88**, 166101 (2002).

[224] V. R. Stamenkovic, B. S. Mun, K. J. J. Mayrhofer, P. N. Ross, and N. M. Markovic, J. Am. Chem. Soc. **128**, 8813 (2006).

[225] K. N. Tu and U. Gösele, Appl. Phys. Lett. **86**, 093111 (2005).

[226] L. S. Darken, Trans. AIME **180**, 430 (1949).

[227] R. J. Baird, T. J. Potter, G. P. Kothiyal, and P. K. Bhattacharya, Appl. Phys. Lett. **52**, 2055 (1988).

[228] H. J. Fan, Y. Yang, and M. Zacharias, J. Mater. Chem. **19**, 885 (2009).

[229] N. H. Nickel, Phys. Rev. B **73**, 195204 (2006).

[230] K.-K. Kim, S. Niki, J.-Y. Oh, J.-O. Song, T.-Y. Seong, S.-J. Park, S. Fujita, and S.-W. Kim, J. Appl. Phys. **97**, 066103 (2005).

[231] J. F. Wager, Science **300**, 1245 (2003).

[232] L. Wang, M.-H. Yoon, G. Lu, Y. Yang, A. Facchetti, and T. J. Marks, Nat. Mater. **6**, 317 (2007).

[233] C. Prasittichai and J. T. Hupp, J. Phys. Chem. Lett. **1**, 1611 (2010).

[234] B. O′Regan and M. Gratzel, Nature **353**, 737 (1991).

[235] C. Soci, A. Zhang, B. Xiang, S. A. Dayeh, D. P. R. Aplin, J. Park, X. Y. Bao, Y. H. Lo, and D. Wang, Nano Lett. **7**, 1003 (2007).

[236] S. Ghosh, G. G. Khan, K. Mandal, A. Samanta, and P. M. G. Nambissan, J. Phys. Chem. C **117**, 8458 (2013).

[237] R. Meyer, R. Waser, J. Helmbold, and G. Borchardt, Phys. Rev. Lett. **90**, 105901 (2003).

[238] F. M. Hossain, J. Nishii, S. Takagi, A. Ohtomo, T. Fukumura, H. Fujioka, H. Ohno, H. Koinuma, and M. Kawasaki, J. Appl. Phys. **94**, 7768 (2003).

[239] W.-K. Hong, G. Jo, S.-S. Kwon, S. Song, and T. Lee, IEEE Trans. Electron Devices **55**, 3020 (2008).

[240] P.-K. Yang, W.-Y. Chang, P.-Y. Teng, S.-F. Jeng, S.-J. Lin, P.-W. Chiu, and J.-H. He, Proc. IEEE **101**, 1732 (2013).

[241] E. Thimsen, M. Johnson, X. Zhang, A. J. Wagner, K. A. Mkhoyan, U. R. Kortshagen, and E. S. Aydil, Nat. Commun. **5**, 5822 (2014).

[242] D. H. Levy, D. Freeman, S. F. Nelson, P. J. Cowdery-Corvan, and L. M. Irving, Appl. Phys. Lett. **92**, 192101 (2008).

[243] C.-C. Chen, A. B. Herhold, C. S. Johnson, and A. P. Alivisatos, Science **276**, 398 (1997).

[244] P. V. Kumar, N. M. Bardhan, S. Tongay, J. Wu, A. M. Belcher, and J. C. Grossman, Nat. Chem. **6**, 151 (2014).

[245] Y. W. Yin, J. D. Burton, Y.-M. Kim, A. Y. Borisevich, S. J. Pennycook, S. M. Yang, T. W. Noh, A. Gruverman, X. G. Li, E. Y. Tsymbal, and Q. Li, Nat. Mater. **12**, 397 (2013).

[246] S. Kashyap, T. J. Woehl, X. Liu, S. K. Mallapragada, and T. Prozorov, ACS Nano **8**, 9097 (2014).

[247] J. Tersoff, D. E. Jesson, and W. X. Tang, Science **324**, 236 (2009).

[248] H. Zhang and J. F. Banfield, Chem. Mater. **17**, 3421 (2005).

[249] L.-Y. Chen, J.-Q. Xu, H. Choi, H. Konishi, S. Jin, and X.-C. Li, Nat. Commun. **5**, 3879 (2014).

[250] E. Rabani, D. R. Reichman, P. L. Geissler, and L. E. Brus, Nature **426**, 271 (2003).

[251] N. T. K. Thanh, N. Maclean, and S. Mahiddine, Chem. Rev. **114**, 7610 (2014).

[252] M. C. Payne, M. P. Teter, D. C. Allan, T. A. Arias, and J. D. Joannopoulos, Rev. Mod. Phys. **64**, 1045 (1992).

[253] M. D. Segall, P. J. D. Lindan, M. J. Probert, C. J. Pickard, P. J. Hasnip, S. J. Clark, and M. C. Payne, Journal of Physics: Condensed Matter **14**, 2717 (2002).

[254] J. S. Manser and P. V. Kamat, Nature Photon. **8**, 737 (2014).

[255] J. M. Yuk, J. Y. Lee, Y. Kim, Y. S. No, T. W. Kim, and W. K. Choi, Appl. Phys. Lett. **97**, 061901 (2010).

[256] B. K. Min, W. T. Wallace, A. K. Santra, and D. W. Goodman, J. Phys. Chem. B **108**, 16339 (2004).

[257] T. Hanada, *Oxide and Nitride Semiconductors*, Springer Berlin Heidelberg, 2009.

[258] A. Michaelides, Z.-P. Liu, C. J. Zhang, A. Alavi, D. A. King, and P. Hu, J. Am. Chem. Soc. **125**, 3704 (2003).

[259] D.-K. Hwang, M.-S. Oh, J.-H. Lim, C.-G. Kang, and S.-J. Park, Appl. Phys. Lett. **90**, 021106 (2007).

[260] J. H. Bang, Y.-S. Kim, C. H. Park, F. Gao, and S. B. Zhang, Appl. Phys. Lett. **104**, 252101 (2014).

[261] S. Bhattacharyya and K. Russell, Metall. Trans. **3**, 2195 (1972).

[262] M. A. Henderson, Surf. Sci. Rep. **46**, 1 (2002).

[263] O. Bikondoa, C. L. Pang, R. Ithnin, C. A. Muryn, H. Onishi, and G. Thornton, Nat. Mater. **5**, 189 (2006).

[264] H. Hu, H.-F. Ji, and Y. Sun, Phys. Chem. Chem. Phys. **15**, 16557 (2013).